Borides and borophosphides at the nanoscale : liquid-phase synthesis and electrocatalytic water splitting properties

Edouard De Rolland Dalon

Sorbonne Université

Ecole doctorale de Physique et Chimie des Matériaux (ED 397)

Laboratoire de Chimie de la Matière Condensée de Paris

Borides and borophosphides at the nanoscale: liquid-phase synthesis and electrocatalytic water splitting properties

Par Edouard de ROLLAND DALON

Thèse de doctorat de Physique et Chimie des Matériaux

Dirigée par David Portehault

Présentée et soutenue publiquement le 22 septembre 2023

Devant un jury composé de :

M. Parola Stéphane	Professeur, ENS Lyon	Rapporteur
M. Tricard Simon	Chargé de recherche CNRS, INSA Toulouse	Rapporteur
Mme. Treguer-Delapierre Mona	Professeure, ICMCB Bordeaux	Examinatrice
Mme. Kabbour Houria	Chargée de recherche CNRS, ENS Lille	Examinatrice
M. Portehault David	Directeur de recherche CNRS, LCMCP Paris	Directeur de thèse

Acknowledgements

First of all, I would like to thank all the jury members, Dr. Stéphane Parola, Dr. Simon Tricard, Dr. Houria Kabbour and Dr. Mona Treguer-Delapierre who agreed to review my work of these three years of PhD and for the really interesting and useful scientific discussions we had.

I would also to express my gratitude to my thesis director Dr. David Portehault who accepted me for this thesis topic, believed in me and helped me to progress as scientist and researcher throughout the internship and the thesis.

This PhD would not have been possible without the financial support of the European Research Council for the GENESIS project, for which I am very grateful.

Special thanks are also due to all of the scientific collaborators who have contributed significantly to this thesis, in particular Capucine Sassoye, Gwanaëlle Rousse, Lise-Marie Lacroix, Melik Maksem, Pierre-Olivier Autran, Isabel Gomez Recio (also former member of our group), Mohamed Selmane, Isabelle Génois, Daniel Gutiérrez Martin.

My Gratitude also go to Dr. Tsou-Hsi-Camille Chan Chang for her pioneering work, really useful for the studies developed in this manuscript.

As the proverb says “alone we go faster, together we go further”, I want to thanks the current and former members of the NANO group for all the scientific collaborations and all of the good moments we have shared: Adeline, Alicia, Amandine, Marzena, Daniel, Emile, Anissa, Carlos, Fernando, Yang particularly but without forgetting Clara, Céline, Sushil, Anthony, Romain, Léna, Guillaume, Madeleine, Binghua and Corinne Chaneac, Sophie Carenco.

I would also like to thank the LCMCP members who all contribute to the functioning of this excellent laboratory and its friendly atmosphere. In particular, for the permanent members: Hélène Gervais, Corinne Pozzo di Borgo, Diana Lesueur, Christian Bonhomme, François Ribot, Christel Laberty-Robert, Laurence Rozes and again Capucine Sassoye. My gratitude also to my dear current and former colleagues: Ryma, Laurence, Agathe, Milad, Florence, Mariette, Fanny, Florent, Davide, Aurélien, Hajar, Amélie, Viviane, André.

A special mention also to all of my office colleagues not already mentioned, who have supported me in the all senses of the term, and among others, have tried desperately to get me to leave the office at a reasonable time, generally without success: Caroline, Melissa, Rhune, Nadège, Salem, Thomas, Laura.

Finally, to my dear Yuna, my roommate Po and all of my friends from the Sorbonne University and elsewhere, for the too rare but intense moments that we shared during my Ph.D. Irène, François Laura, Gauthier, Edwyn, Océane, Thibault, Aristote, Thomas (Mirail), Jerôme, Marie, Vianney, Fanny, Olivier, Marie-Astrid, Anne-Laure, Claire, Nicolas, Louis, Marc-Vianney, Ludovic, Thomas, Alexandre, Claire, Hugues.

Summary

Acknowledgements 1
Summary 3
Introduction 5
References 8
Chapter 1: Strategies for chemical transformations of nanocrystals 13
I) The nano-Kirkendall effect during post-synthesis transformation 14
II) Exchange reactions 15
a) Galvanic exchange 15
b) Ion exchange 17
III) Heteroelement incorporation 19
a) Metal insertion 19
b) s-block elements insertion 21
c) p-block elements insertion 21
d) Similarities between boride and phosphide materials 22
IV) Activate transformations by etching 24
Conclusion 24
References 26
Chapter 2: Molten salts-based conversion of nickel into nanocrystals of nickel borides 35
I) Introduction: the chemistry of borides 36
II) The incorporation of boron into nickel nanoparticles 37
a) Synthesis of Ni_3B and Ni_4B_3 nanocrystals 37
b) Investigation of the reaction mechanism by *in situ* X-ray diffraction 42
c) Role of aggregation 47
III) Solid-state reaction reference 48
Conclusion and perspectives 48
Annexes 50
References 60
Chapter 3: Nickel borides as water splitting electrocatalysts 65
I) Introduction: borides as electrocatalysts for water splitting 66
a) The water splitting process 66
b) HER/OER mechanism 67
c) The role of boron to enhance the catalytic activity 68
II) Nickel boride as ambivalent catalyst for overall water splitting reactions 70
III) Attempts to improve the dispersion of nanoelectrocatalysts 74
a) Reported strategy of activity improvement by roll milling 74
b) Influence of roll milling of catalyst inks on their electrocatalytic properties 75
Conclusion and perspectives 77
Annexes 78
References 87
Chapter 4: Synthesis and identification of key parameters for the synthesis of nickel borophosphides 93
I) Introduction: The challenge of crystalline nickel borophosphide nanomaterials 94
II) The one-pot approach from $Ni^{(0)}$ nanoparticles 95
a) Red phosphorus as P source 96
b) Trioctylphosphine as source of P 97
c) Partial conclusion: competitive reactivity of nickel nanoparticles versus B and P sources

.....98
III) Heteroelement (B/P) insertion in nickel boride or phosphide nanoparticles 98
a) Boron insertion into nickel phosphide nanoparticles 98
b) Phosphorus insertion into nickel boride nanoparticles 100
IV) The one-pot approach from a metal salt 103
a) Rietveld refinement on ternary Ni-B-P/ Ni_3P nanoparticles 104
b) Screening of the optimal conditions for Ni-P-B ternary phases 107
c) NaH as reducing agent 111
Conclusion and perspectives 112
Annexes 114
References 126
Chapter 5: Conversion of core-shell metal nanoparticles as a path towards bimetallic borides 129
I) Introduction: bimetallic nickel cobalt borides structures: a way to improve the properties 130
II) New route to homogeneous nickel cobalt boride 133
a) Synthesis of Ni-Co core-shell nanoparticles 134
b) Aiming at Ni-Co-B compositions 135
III) Key parameters of structural evolution 137
a) Effect of the boron-to-metal content 137
b) Structural evolution with the dwell time 138
c) Temperature effect on structural evolutions 144
IV) Bimetallic Nickel cobalt boride as water splitting catalyst 147
Conclusion and perspectives 148
Annexes 149
References 154
Chapter 6: The delicate conversion of iron into iron borides at the nanoscale 161
I) Introduction: Targeting iron borides as nanoscale materials 162
a) The interest of iron borides 162
b) Methods to reach nanoscaled iron borides 162
II) The role of surface ligands during the conversion of iron to iron boride 163
a) Core-shell iron-iron oxide nanoparticles and their tentative conversion into boride 163
b) Synthesis of crystalline Fe nanoparticles as precursors for boride synthesis 165
c) Synthesis of iron boride from Fe nanoparticles 166
d) Study of the reaction mechanism by *In situ* X-ray diffraction 167
e) Assessment of stability under air 169
III) Targeting Fe_2B 169
Conclusion and perspectives 169
Annexes 171
References 178
General conclusion and perspectives 181
Appendix 185

General introduction

Transition metal borides are of major interest in large families of applications, including magnetism[1–3], refractory materials[4,5], superconductors[6], catalytic reactions such as hydrodesulfurization[7,8] or hydrogenation[9] and electrocatalytic water splitting[10,11]. In most of these fields, this is the association of boron with metals atoms that modifies properties and enhances performances, by bringing covalence to the nature of bonding. Along the increase of the metal-to-boron ratio, boron tends to extend covalent B-B bonds into complex clusters and frameworks, which yields unique crystal structures and unique variations of properties. However, compared to other classes of materials such as carbides, sulfides or phosphides, which have been reported for some of the applications mentioned, the exploration of borides remains limited due to the complexity of their synthesis.

Indeed, due to the high degree of covalence in these materials, conventional synthesis methods are based on solid-state reactions between metal and elemental boron at temperatures above 1000 °C. These methods are not suitable for the elaboration of nanoscale materials as extensive crystal growth occurs at these temperatures. Unfortunately, decreasing the temperature generally leads to insufficient energy input for crystallization, hence amorphous phases, often poorly stable and with properties that differ from those of the crystals.

On the opposite, liquid-state approaches towards metal borides, generally based on molecular or ionic precursors, allow the combination of transition metals with boron in a one or a two-step synthesis[12–17]. In the former case, reactions occur in high temperature liquids[18–23]. In the latter case, an amorphous intermediate is formed following colloidal chemistry protocols, and an annealing step triggers the crystallization of borides[16,17,24,25]. In both cases, however, the size and morphology control over the boride nano-objects are inferior compared to the standards of colloidal synthesis[26,27]. A general method to achieve composition and morphology-controlled boride nanocrystals then remains unattained. Such control would be of high interest to understand and optimize the properties, to target new high interest or metastable boride compounds, and to pave the way to the combination of boride with other p-block elements.

Particularly, metal-rich borides and phosphides exhibit structural similarities. Like borides, metal-rich phosphides possess a high, although lower, degree of covalence in M-P and P-P bonds[12,28–32]. This explains why some application fields of phosphides are common to borides,

particularly for water splitting electrocatalysis[11,12,14,29,30,33,34]. This raises the possibility of complex electron transfers in borophosphides, which could further enhance the catalytic properties. Nevertheless, borophosphides are rare, even at the bulk scale. For instance, only two phases have been reported in the case of the nickel, and only through solid-state strategies[35,36].

Therefore, the aim of this thesis is to develop new approaches towards morphology-controlled nanostructures containing metals and p-block elements boron and/or phosphorus. The field of interest extends from single metals to borides and borophosphides of one or two metals. To overcome the limitations of the reported synthesis methods, our strategy relies on several pillars. First, inorganic molten salts are used to provide liquid media thermally stable over a wide temperature range, with a low viscosity, in order to accelerate reactions compared to solid-state processes, and to support homogeneous reactivity. The second pillar is the use metal nanoparticles as reagents, which act as nano-reactors in which boron and phosphorus atoms are incorporated. The high surface-to-volume ratio of the nanoparticles and small diffusion length within them should ensure high reactivity compared to conventional reagents.

Overall, this approach presents several advantages. The diffusion paths are shorter, the liquid state provides sufficient diffusion and structural changes can be accommodated more easily than in bulk solids. We demonstrate herein that the control of composition and morphology of the boride nano-objects is superior to other synthesis methods. Meanwhile, we put emphasis on reaction mechanisms and identification of reaction intermediates. For this purpose, we have combined *ex situ* techniques (total X-ray scattering coupled with pair distribution function analysis, transmission electron microscopy, X-ray photoelectron spectroscopy) and *in situ* X-ray diffraction to monitor the reaction pathways in the melt. We will also show that this synthesis approach provides materials with promising electrocatalytic properties for water splitting.

More in detail, this thesis is divided in six chapters:

In **Chapter 1**, we briefly review the state-of-the-art in post-synthesis modification methods of nanostructures, including the processes of controlled and selective chemical and structural transformations of nanocrystals. Since the reactivity of nanomaterials is different from that of bulk phases, a knowledge of the processes behind their transformation is essential to drive and understand the crystallization pathways studied throughout the different chapters. In particular, the possibility of B, P insertion in metal-containing nanostructures is discussed according to the reported synthesis methods and the structural similarities of borides and phosphides.

Chapter 2 presents the proof-of-concept of the synthesis of metal boride nanocrystals in molten salt medium by incorporation of boron into metal nanoparticles with the case study of nickel borides. We discuss the synthesis conditions towards pure Ni_3B and Ni_4B_3 nanocrystals with controlled morphology by using nickel nanoparticles as precursors. A detailed study of the specific crystallization mechanism revealed the presence of intermediate phases and possibly a non-classical crystallization pathway.

Chapter 3 focuses on the electrocatalytic properties of the nickel boride nanoparticles discussed in chapter 2 for water splitting half-reactions: the hydrogen evolution reaction and the oxygen evolution reaction.

Chapter 4 depicts the co-incorporation of boron and phosphorus into nickel nanoparticles to attain nickel borophosphide nanoparticles. Different reaction pathways are investigated in molten salts conditions by incorporating heteroelements (B, P) into nickel, nickel borides or nickel phosphides nanoparticles. In parallel, a redox approach in molten salts involving the reduction of nickel$^{(II)}$ in presence of B and P sources has been investigated.

Chapter 5 extends the concept of boron incorporation into pre-formed metal nano-objects, by discussing the synthesis of a new bimetallic nickel cobalt boride formed by the insertion of boron into core-shell Ni-Co nanoparticles. The specificity of the synthesis method combined with structural and thermodynamic considerations allowed to avoid phase depletion during crystallization, observed in methods involving redox reactions of Ni (II) sources. We present also preliminary results on the electrocatalytic activity of these materials for water splitting.

Chapter 6 presents another extension of the synthesis concept, by transformation of iron nanoparticles into iron boride nanocrystals. We highlight how the synthesis method to produce the initial metal nanoparticles plays an important role in their further conversion into borides

In addition, an appendix chapter is devoted to the use of molten salts to form ligand-free metallic nanoparticles. Indeed, when the particles are used as reactants, the absence of ligand could be beneficial in controlling reactivity and limiting side reactions. The synthesis is based on the properties of alkali halide liquid salts to provide a colloidal stability during a simple reduction of a metal precursor by a hydride. This work represents the first foray into the synthesis of metal nanoparticles in molten salts, and the use of induction heating for colloidal synthesis. It then paves the way to important extensions of the studies discussed in the previous chapters.

References

(1) Rades, S.; Kraemer, S.; Seshadri, R.; Albert, B. Size and Crystallinity Dependence of Magnetism in Nanoscale Iron Boride, α-FeB. *Chem. Mater.* **2014**, *26* (4), 1549–1552. https://doi.org/10.1021/cm403167a.

(2) Gabani, S.; Flachbart, K.; Siemensmeyer, K.; Mori, T. Magnetism and Superconductivity of Rare Earth Borides. *J. Alloys Compd.* **2020**, *821*, 153201. https://doi.org/10.1016/j.jallcom.2019.153201.

(3) Hamayun, M. A.; Abramchuk, M.; Alnasir, H.; Khan, M.; Pak, C.; Lenhert, S.; Ghazanfari, L.; Shatruk, M.; Manzoor, S. Magnetic and Magnetothermal Studies of Iron Boride (FeB) Nanoparticles. *J. Magn. Magn. Mater.* **2018**, *451*, 407–413. https://doi.org/10.1016/j.jmmm.2017.11.088.

(4) Matkovich, I.; Board, E. *Boron and Refractory Borides*; 1977. https://doi.org/10.1007/978-3-642-66620-9.

(5) Zhunkovskii, G. L.; Evtushok, T. M.; Grigor'Ev, O. N.; Kotenko, V. A.; Mazur, P. V. Activated Sintering of Refractory Borides. *Powder Metall. Met. Ceram.* **2011**, *50* (3–4), 212–216. https://doi.org/10.1007/s11106-011-9320-2.

(6) Zhao, B.; Wang, L.; Tao, Q.; Zhu, P. The Structure and Multifunctionality of High-Boron Transition Metal Borides. *J. Phys. Condens. Matter.* **2023**, *35* (17). https://doi.org/10.1088/1361-648X/acbad6.

(7) Skrabalak, S. E.; Suslick, K. S. On the Possibility of Metal Borides for Hydrodesulfurization. *Chem. Mater.* **2006**, *18* (13), 3103–3107. https://doi.org/10.1021/cm060341x.

(8) Linares, C. F.; Brunet, S. Improving the Hydrogenation Pathway from the Dibenzothiophene (DBT) Hydrodesulfurization (HDS) Reaction Using Alloys of Bulk NiXCoyborides. *React. Kinet. Mech. Catal.* **2023**, *136* (2), 901–917. https://doi.org/10.1007/s11144-023-02393-0.

(9) Feng, W.; Ma, Y.; Niu, L.; Zhang, H.; Bai, G. Confined Preparation of Ultrafine NiB Amorphous Alloys for Hydrogenation. *Catal. Commun.* **2018**, *109* (February), 20–23. https://doi.org/10.1016/j.catcom.2018.02.015.

(10) Jiang, W. J.; Niu, S.; Tang, T.; Zhang, Q. H.; Liu, X. Z.; Zhang, Y.; Chen, Y. Y.; Li, J. H.; Gu, L.; Wan, L. J.; Hu, J. S. Crystallinity-Modulated Electrocatalytic Activity of a Nickel(II) Borate Thin Layer on Ni3B for Efficient Water Oxidation. *Angew. Chemie - Int. Ed.* **2017**, *56* (23), 6572–6577. https://doi.org/10.1002/anie.201703183.

(11) Gupta, S.; Patel, M. K.; Miotello, A.; Patel, N. Metal Boride-Based Catalysts for Electrochemical Water-Splitting: A Review. *Adv. Funct. Mater.* **2020**, *30* (1). https://doi.org/10.1002/adfm.201906481.

(12) Carenco, S.; Portehault, D.; Boissière, C.; Mézailles, N.; Sanchez, C. Nanoscaled Metal Borides and Phosphides: Recent Developments and Perspectives. *Chem. Rev.* **2013**, *113* (10), 7981–8065. https://doi.org/10.1021/cr400020d.

(13) Chen, H.; Zou, X. Intermetallic Borides: Structures, Synthesis and Applications in Electrocatalysis. *Inorg. Chem. Front.* **2020**, *7* (11), 2248–2264. https://doi.org/10.1039/d0qi00146e.

(14) Lee, E.; Fokwa, B. P. T. Nonprecious Metal Borides: Emerging Electrocatalysts for Hydrogen Production. *Acc. Chem. Res.* **2022**, *55* (1), 56–64. https://doi.org/10.1021/acs.accounts.1c00543.

(15) Dinh, K. N.; Liang, Q.; Du, C. F.; Zhao, J.; Tok, A. I. Y.; Mao, H.; Yan, Q. Nanostructured Metallic Transition Metal Carbides, Nitrides, Phosphides, and Borides for Energy Storage and Conversion. *Nano Today.* **2019**, *25*, 99–121. https://doi.org/10.1016/j.nantod.2019.02.008.

(16) Masa, J.; Weide, P.; Peeters, D.; Sinev, I.; Xia, W.; Sun, Z.; Somsen, C.; Muhler, M.; Schuhmann, W. Amorphous Cobalt Boride (Co 2 B) as a Highly Efficient Nonprecious Catalyst for Electrochemical Water Splitting: Oxygen and Hydrogen Evolution. *Adv. Energy Mater.* **2016**, *6* (6), 1–10. https://doi.org/10.1002/aenm.201502313.

(17) Braun, M.; Chatwani, M.; Kumar, P.; Hao, Y.; Sanjuán, I.; Apostoleri, A. A.; Brix, A. C.; Morales, D. M.; Hagemann, U.; Heidelmann, M.; Masa, J.; Schuhmann, W.; Andronescu, C. Cobalt Nickel Boride as Electrocatalyst for the Oxidation of Alcohols in Alkaline Media. *JPhys Energy.* **2023**, *5* (2). https://doi.org/10.1088/2515-7655/acbb2a.

(18) Gouget, G.; Beaunier, P.; Portehault, D.; Sanchez, C. New Route toward Nanosized Crystalline Metal Borides with Tuneable Stoichiometry and Variable Morphologies. *Faraday Discuss.* **2016**, *191*, 511–525. https://doi.org/10.1039/c6fd00053c.

(19) Jothi, P. R.; Yubuta, K.; Fokwa, B. P. T. A Simple, General Synthetic Route toward Nanoscale Transition Metal Borides. *Adv. Mater.* **2018**, *30* (14), 2–7. https://doi.org/10.1002/adma.201704181.

(20) Portehault, D.; Devi, S.; Beaunier, P.; Gervais, C.; Giordano, C.; Sanchez, C.; Antonietti, M. A General Solution Route toward Metal Boride Nanocrystals. *Angew. Chemie - Int. Ed.* **2011**, *50* (14), 3262–3265. https://doi.org/10.1002/anie.201006810.

(21) Portehault, D.; Gómez-Recio, I.; Baron, M. A.; Musumeci, V.; Aymonier, C.; Rouchon, V.; Le Godec, Y. Geoinspired Syntheses of Materials and Nanomaterials. *Chem. Soc. Rev.* **2022**, *51* (11), 4828–4866. https://doi.org/10.1039/d0cs01283a.

(22) Gouget, G.; Debecker, D. P.; Kim, A.; Olivieri, G.; Gallet, J. J.; Bournel, F.; Thomas, C.; Ersen, O.; Moldovan, S.; Sanchez, C.; Carenco, S.; Portehault, D. In Situ Solid-Gas Reactivity of Nanoscaled Metal Borides from Molten Salt Synthesis. *Inorg. Chem.* **2017**, *56* (15), 9225–9234. https://doi.org/10.1021/acs.inorgchem.7b01279.

(23) Portehault, D.; Delacroix, S.; Gouget, G.; Grosjean, R.; Chan-Chang, T. H. C. Beyond the Compositional Threshold of Nanoparticle-Based Materials. *Acc. Chem. Res.* **2018**, *51* (4), 930–939. https://doi.org/10.1021/acs.accounts.7b00429.

(24) Pu, Z.; Liu, T.; Zhang, G.; Liu, X.; Gauthier, M. A.; Chen, Z.; Sun, S. Nanostructured Metal Borides for Energy-Related Electrocatalysis: Recent Progress, Challenges, and Perspectives. *Small Methods.* **2021**, *5* (10), 1–21. https://doi.org/10.1002/smtd.202100699.

(25) Chen, Z.; Duan, X.; Wei, W.; Wang, S.; Zhang, Z.; Ni, B. J. Boride-Based Electrocatalysts: Emerging Candidates for Water Splitting. *Nano Res.* **2020**, *13* (2), 293–314. https://doi.org/10.1007/s12274-020-2618-y.

(26) Kang, Y.; Tang, Y.; Zhu, L.; Jiang, B.; Xu, X.; Guselnikova, O.; Li, H.; Asahi, T.; Yamauchi, Y. Porous Nanoarchitectures of Nonprecious Metal Borides: From Controlled Synthesis to Heterogeneous Catalyst Applications. *ACS Catal.* **2022**, 14773–14793. https://doi.org/10.1021/acscatal.2c03480.

(27) Kovalenko, M. V.; Manna, L.; Cabot, A.; Hens, Z.; Talapin, D. V.; Kagan, C. R.; Klimov, V. I.; Rogach, A. L.; Reiss, P.; Milliron, D. J.; Guyot-Sionnnest, P.; Konstantatos, G.; Parak, W. J.; Hyeon, T.; Korgel, B. A.; Murray, C. B.; Heiss, W. Prospects of Nanoscience with Nanocrystals. *ACS Nano.* **2015**, *9* (2), 1012–1057.

https://doi.org/10.1021/nn506223h.

(28) Sun, H.; Meng, J.; Jiao, L.; Cheng, F.; Chen, J. A Review of Transition-Metal Boride/Phosphide-Based Materials for Catalytic Hydrogen Generation from Hydrolysis of Boron-Hydrides. *Inorg. Chem. Front.* **2018**, *5* (4), 760–772. https://doi.org/10.1039/c8qi00044a.

(29) Chunduri, A.; Gupta, S.; Bapat, O.; Bhide, A.; Fernandes, R.; Patel, M. K.; Bambole, V.; Miotello, A.; Patel, N. A Unique Amorphous Cobalt-Phosphide-Boride Bifunctional Electrocatalyst for Enhanced Alkaline Water-Splitting. *Appl. Catal. B Environ.* **2019**, *259* (August), 118051. https://doi.org/10.1016/j.apcatb.2019.118051.

(30) Masa, J.; Andronescu, C.; Antoni, H.; Sinev, I.; Seisel, S.; Elumeeva, K.; Barwe, S.; Marti-Sanchez, S.; Arbiol, J.; Roldan Cuenya, B.; Muhler, M.; Schuhmann, W. Role of Boron and Phosphorus in Enhanced Electrocatalytic Oxygen Evolution by Nickel Borides and Nickel Phosphides. *ChemElectroChem.* **2019**, *6* (1), 235–240. https://doi.org/10.1002/celc.201800669.

(31) Wang, W.; Liu, P.; Wu, K.; Zhang, K.; Li, L.; Qiao, Z.; Yang, Y. Synthesis of Ni-P-B Amorphous Nanoparticles with Uniform Size as a Potential Hydrodeoxygenation Catalyst. *New J. Chem.* **2015**, *39* (2), 813–816. https://doi.org/10.1039/c4nj01770f.

(32) Akopov, G.; Yeung, M. T.; Kaner, R. B. Rediscovering the Crystal Chemistry of Borides. *Adv. Mater.* **2017**, *29* (21). https://doi.org/10.1002/adma.201604506.

(33) Huang, C. J.; Xu, H. M.; Shuai, T. Y.; Zhan, Q. N.; Zhang, Z. J.; Li, G. R. A Review of Modulation Strategies for Improving Catalytic Performance of Transition Metal Phosphides for Oxygen Evolution Reaction. *Appl. Catal. B Environ.* **2023**, *325* (December 2022), 122313. https://doi.org/10.1016/j.apcatb.2022.122313.

(34) Menezes, P. W.; Indra, A.; Das, C.; Walter, C.; Göbel, C.; Gutkin, V.; Schmeißer, D.; Driess, M. Uncovering the Nature of Active Species of Nickel Phosphide Catalysts in High-Performance Electrochemical Overall Water Splitting. *ACS Catal.* **2017**, *7* (1), 103–109. https://doi.org/10.1021/acscatal.6b02666.

(35) Mikhalenko, S.; Chernogorenko, V.; Kuz'ma, Y.; Lavrov, Y.; Muchnik, S. Phase Equilibria in the Ni-B-P System. *Inorg. Mater.* **1985**.

(36) Tomashyk, V. Ternary Alloys Based on III-V Semiconductors. *Ternary Alloys Based on*

III-V Semiconductors. **2017**, pp 1–362. https://doi.org/10.4324/9781315116624.

Chapter 1: Strategies for chemical transformations of nanocrystals

This thesis is dedicated to the design of nanoparticles and nanostructures containing metals and p-block elements: boron and/or phosphorus. Various studies have shown the possibility to design nanostructures of borides and phosphides through one-step syntheses from molecular or ionic precursors[1–9]. Such methods usually yield nanostructures with size and morphology control that do not reach the standards of colloidal chemistry[1,7,9–11]. Several teams have shown that incorporation of phosphorus into metal nanoparticles enables to design metal phosphides with superior control of the morphology[8,12,13], since it is directly related to the morphology of the initial nanoparticles, obtained by colloidal chemistry in organic solvents. Such approaches have never been reported for borides. Interestingly, the structures and properties of metal-rich phosphides and borides present similarities. This suggests that the conversion of metal nanoparticles by boron incorporation may be achievable.

In this chapter, from a broader perspective, different methods for transforming nanocrystals are presented. Indeed, new crystal structures, nanostructures and properties, which are difficult or impossible to achieve through one-step syntheses may become within reach by post-synthesis methods[11,14–16]. Most of the methods for nanostructure transformation described thereafter are valid for some range of compositions such as metal chalcogenides, halides, oxides and few compounds of p-block elements[14–19]. Then, this chapter has several objectives. First, to explore the possibilities enabled by post-synthesis chemical transformations and to clarify the involved mechanisms; second, to comprehend the chemistry of boride and phosphide nanomaterials in order to propose reaction pathways towards precise morphological control, inspired by post-synthetic modifications of other families of nano-objects.

As the surface-to-volume ratio increases with reducing particle size, surface reactivity becomes predominant, which explains the higher reactivity of nanoparticles compared to a bulk analog. This is the reason why most recent developments in post-synthetic modification of solids have focused on nano-objects, to incorporate new elements, achieve more complex structures and thermodynamically metastable phases; unattainable in the bulk states or by direct synthesis of the nano-objects[15,20]. Note however that nano-objects often exhibit surface ligands, possible aggregation and crystalline defects[20], which may also modulate their reactivity.

I) The nano-Kirkendall effect during post-synthesis transformation

In most of the methods of chemical transformation of nanostructures addressed hereafter, a morphological transformation corresponding to the formation of a “void” within the particles

may be observed. The nano-Kirkendall effect may arise during a reaction between a nanoparticle and an external agent or by interdiffusion of atoms/ions for core-shell structures. These reactions imply diffusion of at least one kind of atoms/ions within a nanoparticle. If the incoming species diffuse slowly into the nanoparticle, then atoms/ions from the core diffuse to the surface to react with the incoming ones. The unbalanced atom/ion flux to the shell induces the formation of vacancies in the core. These vacancies affect the morphology by evolving into voids when there concentration is sufficient, thus yielding hollow nanoparticles[14,18,21,22].

II) Exchange reactions

Exchange reactions include strategies of galvanic replacement and ion exchange (**Figure 1**)[16,20].

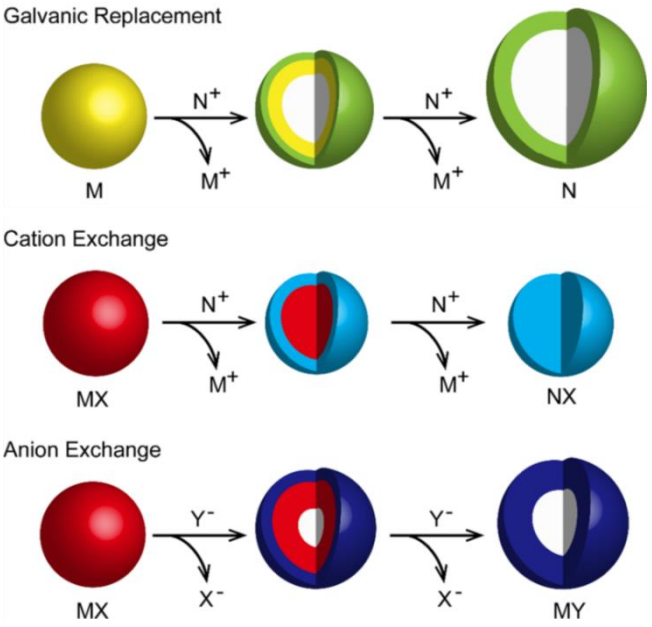

Figure 1. Schemes of exchange reactions in nanomaterials: galvanic replacement, cation exchange, anion exchange. The voids are represented by white areas. Adapted from [20].

a) Galvanic exchange

Galvanic exchange, also known as transmetalation, is based on the difference in redox potentials between two metals. The process consists in the redox reaction in a solvent between dispersed metal-containing nanoparticles and the dissolved oxidized form of another metal, with higher redox potential than the metal within the nanoparticles. Then, as in classical metallurgy, galvanic replacement occurs, where the lower redox potential metal is oxidized and transferred to the solution, while the reduction and/or incorporation of the substituting metal

takes place. During the deposition of the more noble metal (higher redox potential of the oxidized form), part of the initial nanoparticles act as sacrificial template during the substitution[18,20,23,24].

In terms of reaction pathway, two mechanisms take place simultaneously (**Figure 1**). Initially, an alloy shell is formed and grows on the nanoparticles. As this step proceeds, dealloying occurs and galvanic replacement becomes effective. In parallel, the dynamic process of alloying and dealloying induces the formation of pinholes responsible for the oxidation and dissolution in solution of the template metal from the center. The template is thus partially decomposed. In addition, in the final stage of dealloying, the structure may break up. To avoid this phenomenon, the galvanic exchange is usually stopped upstream. In general, noble metal salts containing Au, Pd, and Pt conduct the galvanic exchange on Ag, Cu, Al, Ni and Co used as template[18,25].

However, other nanoscale compositions have been reported by galvanic replacement including CoCu[26], FeCu[27] or RuM (M = Fe, Ni, Cu, Co) supported on TiO_2[28] . Recently, a group has presented the formation of two-dimensional Ni-Co-B amorphous nanolayers supported on reduced graphene oxide (rGO) by galvanic replacement of cobalt by nickel[29]. In chapter 5 of this manuscript, another strategy will be discussed[30] to form first core-shell nickel-cobalt nanoparticles and then a NiCo nanoalloy upon heating[31]. This strategy, in contrast to galvanic exchange, conserve the initial Ni: Co atomic ratio.

Galvanic exchange can be extended to metal oxides by replacing the metal ions of lower redox potential with metal ions of higher redox potential. A study[32] has demonstrated the general nature of this method by using galvanic substitution for the pairs Mn_3O_4 -Fe_2O_3 , Co_3O_4-SnO_2 and Mn_3O_4-SnO_2 as study cases. The galvanic substitution on these phases resulted in hollow cage nanostructures. Similar to the previous cases, these morphologies result from the reaction between the substituted oxide species and the substituent oxides, leading to a gradual precipitation on the surface of the nanocrystal while a void is formed in the center of the nanocrystal. Finally galvanic exchange is stopped before total depletion, resulting in a hollow cage-like morphology with the substituent oxide as a shell enclosing the remaining substituted oxide[20,32].

New synthesis routes are derived from galvanic substitution as in the case of layered structures. MAX phases, for examples, are composed of hexagonal layered structures of metal (M) carbides (X = C) or nitrides (X = N), interleaved by an A element, usually a 13-16 group element[33,34]. In these compounds, galvanic replacement was used to substitute Al atoms as the

A element by Zn atoms in Ti_3ZnC_2, Ti_2ZnC, Ti_2ZnN and V_2ZnC. Further galvanic exchange from Ti_3ZnC_2 yielded $Ti_3C_2Cl_2$[34,35]. Note that in this case, the diffusion of the incoming atoms is sufficiently fast into the MAX crystals to enable exchange into the core of the objects, without formation of any internal void.

Coupling of galvanic exchange with co-reducing agents constitute another synthesis route. The modification of the kinetics of reduction can provide a control of the morphology of the nanostructure. Thus, the use of hydroquinone as reducing agent during the synthesis by galvanic replacement of AgPd, AgPt and AgAu nanostructures resulted in the formation of hollow nanodendrites and nanoflowers[24]. Indeed, during galvanic replacement, the oxidized Ag was dissolved and replaced by the reduced metal precursor while a second process of precursor reduction by hydroquinone occurs.

b) Ion exchange

A distinction is made between anion and cation exchange reactions from nanoparticles[18].

- Cation exchange

Cation exchange corresponds to the replacement of cations within nanostructures by those in solution[14,36,37]. The anionic framework needs to be sufficiently stable to maintain the morphology rather than reconstruct the overall structure[6,13]. The reaction is generally topotactic as no deep modification of the crystal structure is observed[37]. Various cation exchange reactions have been observed in metal oxides, chalcogenides, phosphides, and arsenides using various metal cations (Cu^+, Ag^+, Cd^{2+}, Pb^{2+}, Zn^{2+}, $Sn^{2+/4+}$, Ga^{3+}, In^{3+},Mn^{2+}, Au^{3+}, Co^{2+}, Fe^{2+} and Ni^{2+} among other) [15]. A reported Fe^{2+} to Co^{2+} cation exchange in ferrite nanocrystals ($Fe^{II}Fe^{III}{}_2O_4$) preserved the nanocrystals in presence of trioctylphosphine (TOP) as surface ligand; essential to avoid the depletion into small polydisperse nanoparticles[38].

The exchange reaction is thermodynamically driven and can only occur if solvation or complexation sufficiently stabilize the outgoing cations into the solution. In all cases, the cation exchange starts by a nucleation event on a single domain on the surface, which initiates the solid-solid transformation[14,15]. In principle, the cation exchange reaction starts on sites of lower surface energy and low coverage by ligands[15]. Thereafter, the way of substitution in the nanomaterial can depend on several factors that impact the thermodynamic equilibrium of cation exchange, such as the solubility constants, the crystal structure and corresponding lattice

energies, the presence of ligands on specific sites, the relative solvation energies, the localization of the surface event and the hard-soft acid-base interactions[14,36,37].

As cation exchange occurs through a solid-solid phase transformation, adjusting its kinetics can allow metastable phases or kinetic products to be stabilized[14,37]. Stopping the reaction leads to a variety of achievable products and structures, including core-shell, patchy, doped, alloyed or phase-segregated structures (**Figure 2**)[37].

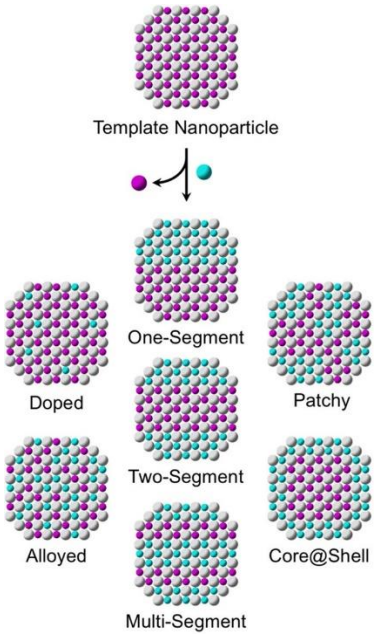

Figure 2. Examples of diverse structures reported by cation exchange reactions. Reproduced from [37].

Partial cation exchange with nanoscale $Cu_{1.8}S$ (roxbyite copper sulfide) has conducted to different behaviors as a function of the morphology of the initial material and the nature of the substituting cation. Partial exchange with Zn^{2+} in roxbyite spheres produced $Cu_{1.8}S$−ZnS sandwich spheres, while replacement of Zn^{2+} by Cd^{2+} led to Janus spheres with one hemisphere containing CdS and the other one $Cd_{1.8}S$. The use of roxbyite nanorods partially exchanged with Zn^{2+} introduced multiple ZnS bands separated by roxbyite domains[37,39].

- Anion exchange

As just discussed, in the case of cation exchange, the small size of the cations allows a rapid exchange and maintenance of the nanostructure, compared to the larger anions that are unable

to diffuse rapidly. The high energy barrier for anion diffusion then imposes higher temperatures and longer reaction times to enable anion exchange[14,15,18]. Anion exchange is then rarely topotactic as anions diffuse badly into cationic sublattices with narrow interstitial spaces and large energy barriers for diffusion from one site to the other. Deep morphological modifications, including Kirkendall voids, are therefore inherent to these reactions, but reversely enable complex nanostructures to be achieved. Nonetheless, several factors such as lattice mismatch, exposed crystal faces or the nature of ligands, enable to tune the reactivity[15,16]. To illustrate the role of ligands, the sulfidation of Fe_3O_4 into hollow Fe_3S_4 nanocrystals was performed by conventional anion exchange using H_2S to extract O^{2-} ions. By using a specific oxygen-extracting agent (here the (Z)-N-trimethylsilyl-octadec-9-en-1-amine containing an oxophilic group and a nucleophilic amine), O^{2-} removal and exchange was accelerated, the Kirkendall void was avoided, thus yielding Fe_3S_4 nanocrystals. This method was then successfully applied for the exchange of MnO into MnS and ZnO into ZnS with conservation of the morphology[16].

Anionic exchange has been reported for several elements of the groups of pnictogens, chalcogens and halogens (groups 15 ,16 and 17 of the periodic table). Nevertheless, the catalogue of achievable structures can be extended by controlling the anion exchange to stabilize intermediates as heterostructures and core-shell structures[15]. The controlled partial anionic exchange of hollowed cobalt oxydes (CoO_x) nanocrystals was conducted to form the cobalt oxysulfide $CoO_xS_{0.18}$ (x unidentified)[40]. The structure described as a distorted S-substituted CoO phase showed significant enhancement of the electrocatalytic activity towards the hydrogen evolution reaction compared to CoO_x.

III) Heteroelement incorporation

Another way of manipulating nanostructures is the incorporation of atoms/ions into the nanomaterial. This incorporation can be performed directly or after performing etching or substitution to trigger and control the reactivity.

a) Metal insertion

Alloying enables to design new compositions at the nanoscale. Metal incorporation generally induces morphological changes as a mechanism of interdiffusion occurs and follows the nano-Kirkendall effect, since it is rare that the two metals have the same diffusion coefficient (**Figure 3**) in the parent solid [22,41,42].

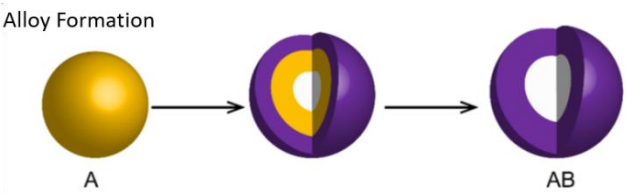

Figure 3. Mechanism of formation of an alloy at the nanoscale by reaction of a metal nanoparticle with atoms in solution. The void is represented by a white area. Adapted from [20].

As a case study, nanoparticles of an Au-Pd alloy containing some Kirkendall voids were prepared from Pd nanocubes brought into contact with metallic Au formed by reduction of a Au (I) precursor with oleylamine[22]. As the two metals are miscible, the alloy was formed upon heating. In this case, the use of the Au(I) precursor instead of a classical $Au^{(III)}$ precursor was deliberately chosen to minimize the galvanic replacement.

Similarly, the mechanism of interdiffusion can arise in core-shell bimetallic structures. The shell atoms can generally modify the surface of the core metal without altering the crystal facets[22,43]. Nanoscale high entropy alloys defined as a single-phase solid solution of at least 5 elements (PdCuPtNiCo) have been synthetized by this route from core-shell nanoparticles PdCu-PtNiCo[44]. Notwithstanding the high degree of control over the composition, the metals need to be miscible to form a single-phase alloy. Thus, PdCu-PtNiCo core-shell nanoparticles were converted into PdCuPtNiCo nanoalloy without depletion during annealing. In this case, several factors facilitated the diffusion such as high interfacial strains, which lower the diffusion barrier in addition to lattice distortions and low atomic diffusivity during mixing. We will use a similar process in chapter 5, to form a NiCo alloy from core-shell Ni-Co nanoparticles[30], for its subsequent conversion into a nickel cobalt boride. A combination of *in situ* XPS and TEM showed stepwise processes along a temperature ramp[31]: first, a desorption of oxide species occurs through a carbo-reduction process; then, migration of nickel atoms from the core to the shell while cobalt atoms migrate reversely yields the alloy without significant size variation .

Recently, our group reported an original approach towards the synthesis of metal silicide nanoparticles by incorporating metals (Ni and Fe) into pre-formed silicon nanoparticles [45]. The synthesis relies on two main pillars: molten salts to provide a liquid-state medium at high temperature and silicon (0) nanoparticles capable of reducing and incorporating the metal ion precursor into metal (0). Conversely, $Si^{(0)}$ is oxidized into volatile species of $Si^{(IV)}$. The size distribution of the resulting particles is maintained and the objects exhibit a homogeneous composition while an oxide layer is formed on the surface upon exposure to air.

b) s-block elements insertion

Reports on the insertion of alkali metals or alkaline earth metals into nanostructures generally aim at a reversible uptake process for applications in batteries. Indeed, further storage capabilities can be obtained with nanomaterials as they possess a higher surface to volume ratio, different ion solubilities and a modulated interfacial strain, which drives changes in surface redox states[46,47]. In addition, shorter diffusion pathways provide rapid insertion and extraction of the alkali element[48]. The reversible incorporation process is performed electrochemically from ion-containing solutions and yields insertion of alkali or alkaline earth cations. The reduction or oxidation of the desired element is then controlled by simply modifying the applied electrochemical potential[46,49–51]. Under these conditions, despite the small size of the s-block element studied, morphological changes are observed during the first insertion/extraction cycle. In the case of lithium as reversibly inserted element, volume expansion of the lattice of the nanomaterials is generally observed[49,50]. Replacement of Li^+ by larger Na^+ cations induces larger expansion, structural and morphological changes, as well as side reactions under electrochemical conditions, such as disproportionation[47,49]. It is worth mentioning that even with the incorporation of Ca^{2+}, no void formation have been reported[47–51]. In contrast, vacancies were observed in the structure of the reversibly inserted Li in Li_xFePO_4[48].

c) p-block elements insertion

Colloidal nanocrystals formed by p-block elements incorporation into existing metal nano-objects have been reported for carbon[19], the chalcogenides oxygen, sulfur and selenium[18,22,52] but most commonly for phosphides[1,18,22,53–56]. A recent study has reported the insertion of boron into nickel nanoparticles for the formation of Ni_2B and Ni_3B nanocrystals by solid-state mechanochemistry within 1-3 days of reaction at 400°C. Despite its simplicity, this method resulted into aggregated particles with a size range much larger than that of the initial nickel particles[6]. For these incorporation reactions, the incoming elements may exhibit slower inward diffusion and the outward diffusion of metal atoms, thus resulting in a nano-Kirkendall void. The resulting particles are enlarged and include a void in the center[1,14,18,22,52,53,57].

For phosphide synthesis, trioctylphosphine and white phosphorus (P_4) are the main sources of phosphorus for conversion of elemental Ni, Pd, Fe, Co, Cu, Zn, In, Pb nanoparticles[1,18,22,53–56]. No formation of Kirkendall void was observed in Ni_2P nanocrystals formed by decomposition of white phosphorus (P_4) on nickel nanoparticles [58,59] unlike some other methods, based on

trioctylphosphine (TOP) as source of phosphorus[1,18], due to the high reactivity of P_4 and then high flux of P atoms towards the inside of the particles.

In chapter 4, we address the incorporation of phosphorus within metal or metal boride nanoparticles. Due to safety concerns and unavailability of the highly reactive white phosphorus, a restricted-use chemical, we have used either trioctylphosphine, surface ligand used during the synthesis of phosphides[60], or red phosphorus, a phosphorus source less reactive than with phosphorus, but readily available user-friendly.

The mechanism of phosphidation of cobalt nanoparticles by TOP ligands was studied in details[18,53]. The conversion of ε-Co to Co_2P occurs through a two-step process. First, an amorphous shell of cobalt phosphide is formed by inward diffusion of phosphorus with negligible outward diffusion of cobalt. As the shell grows and Co_2P becomes the major phase, the diffusivity scale is reversed and the outward diffusion of cobalt allows the formation of a Kirkendall void. Thereafter, the subsequent conversion of Co_2P to CoP involves a different mechanism by cation exchange reaction. A de-intercalation of cobalt atoms from the interstitial sites occurs, while the anion lattice is maintained but deformed to form the CoP structure. TEM studies showed an increase of the void diameter before re-annealing. The percentage of hollow nanoparticles in the final product fell from 70 % in Co_2P to 30 % in CoP, suggesting that other mechanisms including either the Kirkendall process or fracturation of hollow nanoparticles and Ostwald ripening may be involved.

d) Similarities between boride and phosphide materials

Interestingly, the properties of bulk and nanoscale phosphides are often related to those of borides[1,3,61–63]. These similarities can be related to the nature of bonding and to crystal structures. Indeed, crystal and electronic structures in metal borides and metal phosphides depend on several factors such as the nature of the metal, and the stoichiometry.

The electronegativities of phosphorus (χ(P)= 2.19), boron (χ(B)= 2.04) and most transition metals are similar. For the first transition series, Fe, Co, Ni and Cu have a narrow χ range [1.83-1.90]. These small differences in electronegativity tend to reinforce the covalent character of the metal-B/P bond. However, more ionicity is observed in metal phosphides compared to metal borides due to the higher electronegativity difference. The resulting M-P bonds yield a relatively positive charge on the metal and a relatively negative on P [1,64]. More specifically, the formation of a metal-p-block element bond induces an electron transfer from the metal to the p-block element in accordance with their respective electronegativities. However, for both

elements, but more pronounced for boron, there is a reverse electron transfer corresponding to a back-donation to the *d*-band of the metal[1,7,63]. The metal is thus "ennobled" due to a filling to the *d*-band, with a trend towards the adoption of an electron configuration closer to that of a noble metal. As result, the stability of the metal is enhanced against oxidation as well as the chemical and thermal stability and the catalytic activity become closer to those of noble metals.

Besides, the properties and structures derive from the metal nature and content. According to DFT calculations, in metal-rich borides (usually MB_x; x< 6) and metal-rich phosphides (usually MP_x; x< 1:1), the proximity of metal atoms provides strong electron delocalization in the metal sublattice, thus yielding metallic properties[1,64,65].

In metal borides, strong, short and directional B-B covalent bonds form a sublattice. As the boron content in the boride phase increases, the sublattice tends to concatenate and evolve in geometry from isolated boron atoms, clusters and then framework in 2D by formation of chains of boron atoms and 3D dimensions composed of skeletons/backbones boron atoms. The decrease in the B-B bonds distances to a minimum of 175 pm, similar to that found in elemental boron, confirms the strengthening of the covalent sublattice[1,65]. In metal-rich phosphides, the phosphorus atoms interact poorly. Back-donation due to overlapping of metal and phosphorus orbitals also limits the ionic character of the M-P bonds. As the phosphorus content in the phase composition increases, the P-P interaction become stronger and the electrons are more concentrated around P due to the more ionic character of the compounds. Phases with high phosphorus content are semiconductors or insulators as they hinder electron delocalization of the metal sublattice[1,64]. Unlike boron, phosphorus can only form finite chain structures including a minimum P-P distance of 215 pm. In comparison, this hinder of electron delocalization is observed in higher boron contained phases as the boron substructure is more defined and covalent[1].

Depending on the application, metal-rich or boride/phosphide-rich phases may be more suitable. From an overall point of view, the structures and behavior of borides and phosphides diverge strongly for B/P-rich compositions. Conversely, metal-rich boride and phosphide phases exhibit close structures and properties[1,3], as will be discussed in chapter 4.

In terms of applications, both borides and phosphide phases have been particularly studied as water splitting electrocatalysts to supplant noble metals[1,61,62,64,66–68], as will be described in chapters 3 and 5, where we will investigate the properties of some materials synthesized into this work.

In summary, since the properties and reactivity of phosphorus and boron are related, the work hypothesis for this PhD work was that boron incorporation similar to phosphorus into metal-based nanoparticles would be possible. Due to the higher covalence in borides, we expected the need for higher temperatures to trigger incorporation, compared to phosphides. This has driven the choice of molten salts as reaction media, which provided a large temperature range to assess this reactivity. Thus, the formation of transition metal borides and borophosphides by incorporation of the p-block element into metal containing nanoparticles corresponds to the main approach developed in chapters 2,4,5,6.

IV) Activate transformations by etching

Selective etching strategies have been developed to remove specific atoms or compounds within nanoparticles or surface ligands. This process may induce deep structural reconstruction, which then changes the properties. For example, selective stripping of CsX (X = Cl, Br, I) from Cs_4PbX_6 nanocrystals to form $CsPbX_3$ induced lattice reconstruction, which then changed the properties from non-luminescent to highly luminescent nanocrystals[22].

Besides, selective etching can enhance the reactivity and activate chemical transformation pathways difficult to reach by other methods.

As case of study, a coordination-assisted etching using $K_3[Fe(CN)_6]$ as etching agent and ligand allowed to incorporate iron into $Co(OH)_2$ porous nanoplates with a controllable composition. The resulting nanoplates showed an enhancement of the electrocatalytic activity in oxygen evolution reaction[69].

On another side, a facet selective etching followed by deposition or galvanic replacement was reported for several noble metals[23]. As an illustration, Pd nanocubes were selectively etched with bromide along specific facets, which then served as actives site for galvanic replacement using H_2PtCl_6 to form Pt atoms and attain Pd-Pt concave nanocubes[23,70] .

Conclusion

The shorter range of cohesion in nano-objects and their high surface energy provides higher reactivity and flexibility compared to bulk solids. Post-synthesis chemical transformations of nano-objects then provide paths towards a wide variety of mechanisms and resulting

nanomaterials, with potentially complex structures and morphologies unreachable by classical pathways of nanoscale syntheses.

Along this chapter, we have addressed several post synthesis pathways of exchange reactions or incorporation of metal, s-block, p-block elements. We have seen that despite the great versatility of compositions and structures achievable, their control may be limited. Indeed, parameters such as the post-synthesis method, the composition, the morphology, synthesis conditions or a difference between inward and outward diffusion can influence the transformation. Then, understanding the mechanisms allows to find strategies such as the use of an etching agent or a specific ligand to drive the reaction.

A particular focus was placed on the possibility of boron incorporation in metal-containing nanostructures based on the reported phosphidation methods of metal containing nanostructures and the common features between borides/ phosphides structures. In the next chapters, we investigate this pathway and we address the electrocatalytic properties of the resulting nanomaterials.

References

(1) Carenco, S.; Portehault, D.; Boissière, C.; Mézailles, N.; Sanchez, C. Nanoscaled Metal Borides and Phosphides: Recent Developments and Perspectives. *Chem. Rev.* **2013**, *113* (10), 7981–8065. https://doi.org/10.1021/cr400020d.

(2) Chen, Z.; Duan, X.; Wei, W.; Wang, S.; Zhang, Z.; Ni, B. J. Boride-Based Electrocatalysts: Emerging Candidates for Water Splitting. *Nano Res.* **2020**, *13* (2), 293–314. https://doi.org/10.1007/s12274-020-2618-y.

(3) Sun, H.; Meng, J.; Jiao, L.; Cheng, F.; Chen, J. A Review of Transition-Metal Boride/Phosphide-Based Materials for Catalytic Hydrogen Generation from Hydrolysis of Boron-Hydrides. *Inorg. Chem. Front.* **2018**, *5* (4), 760–772. https://doi.org/10.1039/c8qi00044a.

(4) Jothi, P. R.; Yubuta, K.; Fokwa, B. P. T. A Simple, General Synthetic Route toward Nanoscale Transition Metal Borides. *Adv. Mater.* **2018**, *30* (14), 2–7. https://doi.org/10.1002/adma.201704181.

(5) Portehault, D.; Devi, S.; Beaunier, P.; Gervais, C.; Giordano, C.; Sanchez, C.; Antonietti, M. A General Solution Route toward Metal Boride Nanocrystals. *Angew. Chemie - Int. Ed.* **2011**, *50* (14), 3262–3265. https://doi.org/10.1002/anie.201006810.

(6) Hong, J.; Mutalik, S.; Miola, M.; Gerlach, D.; Mehrabi K, R.; Ahmadi, M.; Kooi, B. J.; Portale, G.; Rudolf, P.; Pescarmona, P. P.; Protesescu, L. Nickel Boride (NixB) Nanocrystals: From Solid-State Synthesis to Highly Colloidally Stable Inks. *Chem. Mater.* **2023**, *35* (4), 1710–1722. https://doi.org/10.1021/acs.chemmater.2c03478.

(7) Jiang, Y.; Lu, Y. Designing Transition-Metal-Boride-Based Electrocatalysts for Applications in Electrochemical Water Splitting. *Nanoscale.* **2020**, *12* (17), 9327–9351. https://doi.org/10.1039/d0nr01279c.

(8) Callejas, J. F.; Read, C. G.; Roske, C. W.; Lewis, N. S.; Schaak, R. E. Synthesis, Characterization, and Properties of Metal Phosphide Catalysts for the Hydrogen-Evolution Reaction. *Chem. Mater.* **2016**, *28* (17), 6017–6044. https://doi.org/10.1021/acs.chemmater.6b02148.

(9) Pu, Z.; Liu, T.; Zhang, G.; Liu, X.; Gauthier, M. A.; Chen, Z.; Sun, S. Nanostructured Metal Borides for Energy-Related Electrocatalysis: Recent Progress, Challenges, and

Perspectives. *Small Methods.* **2021**, *5* (10), 1–21. https://doi.org/10.1002/smtd.202100699.

(10) Kovalenko, M. V.; Manna, L.; Cabot, A.; Hens, Z.; Talapin, D. V.; Kagan, C. R.; Klimov, V. I.; Rogach, A. L.; Reiss, P.; Milliron, D. J.; Guyot-Sionnnest, P.; Konstantatos, G.; Parak, W. J.; Hyeon, T.; Korgel, B. A.; Murray, C. B.; Heiss, W. Prospects of Nanoscience with Nanocrystals. *ACS Nano.* **2015**, *9* (2), 1012–1057. https://doi.org/10.1021/nn506223h.

(11) Portehault, D.; Delacroix, S.; Gouget, G.; Grosjean, R.; Chan-Chang, T. H. C. Beyond the Compositional Threshold of Nanoparticle-Based Materials. *Acc. Chem. Res.* **2018**, *51* (4), 930–939. https://doi.org/10.1021/acs.accounts.7b00429.

(12) D'Accriscio, F.; Schrader, E.; Sassoye, C.; Selmane, M.; André, R. F.; Lamaison, S.; Wakerley, D.; Fontecave, M.; Mougel, V.; Le Corre, G.; Grützmacher, H.; Sanchez, C.; Carenco, S. A Single Molecular Stoichiometric P-Source for Phase-Selective Synthesis of Crystalline and Amorphous Iron Phosphide Nanocatalysts. *ChemNanoMat.* **2020**, *6* (8), 1208–1219. https://doi.org/10.1002/cnma.202000198.

(13) Henkes, A. E.; Vasquez, Y.; Schaak, R. E. Converting Metals into Phosphides: A General Strategy for the Synthesis of Metal Phosphide Nanocrystals. *J. Am. Chem. Soc.* **2007**, *129* (7), 1896–1897. https://doi.org/10.1021/ja068502l.

(14) Han, H.; Yao, Y.; Robinson, R. D. Interplay between Chemical Transformations and Atomic Structure in Nanocrystals and Nanoclusters. *Acc. Chem. Res.* **2021**, *54* (3), 509–519. https://doi.org/10.1021/acs.accounts.0c00704.

(15) Saruyama, M.; Sato, R.; Teranishi, T. Transformations of Ionic Nanocrystals via Full and Partial Ion Exchange Reactions. *Acc. Chem. Res.* **2021**, *54* (4), 765–775. https://doi.org/10.1021/acs.accounts.0c00701.

(16) Lim, Y.; Han, J. H.; Cheon, J. Chemical Transformations of Anisotropic Platelets and Spherical Nanocrystals. *Acc. Chem. Res.* **2021**, *54* (7), 1565–1574. https://doi.org/10.1021/acs.accounts.0c00802.

(17) Tan, J. M. R.; Scott, M. C.; Hao, W.; Baikie, T.; Nelson, C. T.; Pedireddy, S.; Tao, R.; Ling, X.; Magdassi, S.; White, T.; Li, S.; Minor, A. M.; Zheng, H.; Wong, L. H. Revealing Cation-Exchange-Induced Phase Transformations in Multielemental Chalcogenide Nanoparticles. *Chem. Mater.* **2017**, *29* (21), 9192–9199.

https://doi.org/10.1021/acs.chemmater.7b03029.

(18) Anderson, B. D.; Tracy, J. B. Nanoparticle Conversion Chemistry: Kirkendall Effect, Galvanic Exchange, and Anion Exchange. *Nanoscale.* **2014**, *6* (21), 12195–12216. https://doi.org/10.1039/c4nr02025a.

(19) Meffre, A.; Mehdaoui, B.; Kelsen, V.; Fazzini, P. F.; Carrey, J.; Lachaize, S.; Respaud, M.; Chaudret, B. A Simple Chemical Route toward Monodisperse Iron Carbide Nanoparticles Displaying Tunable Magnetic and Unprecedented Hyperthermia Properties. *Nano Lett.* **2012**, *12* (9), 4722–4728. https://doi.org/10.1021/nl302160d.

(20) Xu, L.; Liang, H. W.; Yang, Y.; Yu, S. H. Stability and Reactivity: Positive and Negative Aspects for Nanoparticle Processing. *Chem. Rev.* **2018**, *118* (7), 3209–3250. https://doi.org/10.1021/acs.chemrev.7b00208.

(21) Tianou, H.; Wang, W.; Yang, X.; Cao, Z.; Kuang, Q.; Wang, Z.; Shan, Z.; Jin, M.; Yin, Y. Inflating Hollow Nanocrystals through a Repeated Kirkendall Cavitation Process. *Nat. Commun.* **2017**, *8* (1), 1–8. https://doi.org/10.1038/s41467-017-01258-0.

(22) Chen, J.; Jiang, F.; Yin, Y. Manipulation of Interfacial Diffusion for Controlling Nanoscale Transformation. *Acc. Chem. Res.* **2021**, *54* (5), 1168–1177. https://doi.org/10.1021/acs.accounts.0c00743.

(23) Ahn, J.; Zhang, L.; Qin, D. Transforming Noble-Metal Nanocrystals into Complex Nanostructures through Facet-Selective Etching and Deposition. *ChemNanoMat.* **2020**, *6* (1), 5–14. https://doi.org/10.1002/cnma.201900378.

(24) Da Silva, A. G. M.; Rodrigues, T. S.; Haigh, S. J.; Camargo, P. H. C. Galvanic Replacement Reaction: Recent Developments for Engineering Metal Nanostructures towards Catalytic Applications. *Chem. Commun.* **2017**, *53* (53), 7135–7148. https://doi.org/10.1039/c7cc02352a.

(25) Pham, V. V.; Ta, V. T.; Sunglae, C. Synthesis of NiPt Alloy Nanoparticles by Galvanic Replacement Method for Direct Ethanol Fuel Cell. *Int. J. Hydrogen Energy.* **2017**, *42* (18), 13192–13197. https://doi.org/10.1016/j.ijhydene.2017.01.236.

(26) Nafria, R.; Genç, A.; Ibáñez, M.; Arbiol, J.; Ramírez De La Piscina, P.; Homs, N.; Cabot, A. Co-Cu Nanoparticles: Synthesis by Galvanic Replacement and Phase Rearrangement during Catalytic Activation. *Langmuir.* **2016**, *32* (9), 2267–2276.

https://doi.org/10.1021/acs.langmuir.5b04622.

(27) Liu, A.; Fu, J.; Liu, J.; Zhang, W. Copper Nanostructure Genesis via Galvanic Replacement and Kirkendall Growth from Nanoscale Zero-Valent Iron. *ACS ES&T Water*. **2022**, *2* (8), 1353–1359. https://doi.org/10.1021/acsestwater.2c00080.

(28) Zhou, G.; Dong, Y.; He, D. Bimetallic Ru–M/TiO 2 (M = Fe, Ni, Cu, Co) Nanocomposite Catalysts Facribated by Galvanic Replacement: Structural Elucidation and Catalytic Behavior in Benzene Selective Hydrogenation. *Appl. Surf. Sci.* **2018**, *456* (May), 1004–1013. https://doi.org/10.1016/j.apsusc.2018.06.206.

(29) Shi, M.; Hou, Y.; Du, X.; Guo, J.; Li, B.; Li, Y. 2D/2D-Ni-Co-B/RGO Nanolayers Prepared by Galvanic Replacement for Hydrogen Generation through NaBH4 Hydrolysis. *ACS Appl. Nano Mater.* **2023**, *6* (8), 6798–6809. https://doi.org/10.1021/acsanm.3c00515.

(30) Palazzolo, A.; Poucin, C.; Freitas, A. P.; Ropp, A.; Bouillet, C.; Ersen, O.; Carenco, S. The Delicate Balance of Phase Speciation in Bimetallic Nickel Cobalt Nanoparticles. *Nanoscale*. **2022**. https://doi.org/10.1039/d2nr00917j.

(31) Bonifacio, C. S.; Carenco, S.; Wu, C. H.; House, S. D.; Bluhm, H.; Yang, J. C. Thermal Stability of Core-Shell Nanoparticles: A Combined in Situ Study by XPS and TEM. *Chem. Mater.* **2015**, *27* (20), 6960–6968. https://doi.org/10.1021/acs.chemmater.5b01862.

(32) Oh, M. H.; Yu, T.; Yu, S. H.; Lim, B.; Ko, K. T.; Willinger, M. G.; Seo, D. H.; Kim, B. H.; Cho, M. G.; Park, J. H.; Kang, K.; Sung, Y. E.; Pinna, N.; Hyeon, T. Galvanic Replacement Reactions in Metal Oxide Nanocrystals. *Science*. **2013**, *340* (6135), 964–968. https://doi.org/10.1126/science.1234751.

(33) Rosli, N. F.; Nasir, M. Z. M.; Antonatos, N.; Sofer, Z.; Dash, A.; Gonzalez-Julian, J.; Fisher, A. C.; Webster, R. D.; Pumera, M. MAX and MAB Phases: Two-Dimensional Layered Carbide and Boride Nanomaterials for Electrochemical Applications. *ACS Appl. Nano Mater.* **2019**, 6010–6021. https://doi.org/10.1021/acsanm.9b01526.

(34) Portehault, D.; Gómez-Recio, I.; Baron, M. A.; Musumeci, V.; Aymonier, C.; Rouchon, V.; Le Godec, Y. Geoinspired Syntheses of Materials and Nanomaterials. *Chem. Soc. Rev.* **2022**, *51* (11), 4828–4866. https://doi.org/10.1039/d0cs01283a.

(35) Li, M.; Lu, J.; Luo, K.; Li, Y.; Chang, K.; Chen, K.; Zhou, J.; Rosen, J.; Hultman, L.; Eklund, P.; Persson, P. O. Å.; Du, S.; Chai, Z.; Huang, Z.; Huang, Q. Element Replacement Approach by Reaction with Lewis Acidic Molten Salts to Synthesize Nanolaminated MAX Phases and MXenes. *J. Am. Chem. Soc.* **2019**, *141* (11), 4730–4737. https://doi.org/10.1021/jacs.9b00574.

(36) Beberwyck, B. J.; Surendranath, Y.; Alivisatos, A. P. Cation Exchange: A Versatile Tool for Nanomaterials Synthesis. *J. Phys. Chem. C.* **2013**, *117* (39), 19759–19770. https://doi.org/10.1021/jp405989z.

(37) Schaak, R. E.; Steimle, B. C.; Fenton, J. L. Made-to-Order Heterostructured Nanoparticle Libraries. *Acc. Chem. Res.* **2020**. https://doi.org/10.1021/acs.accounts.0c00520.

(38) Sytnyk, M.; Kirchschlager, R.; Bodnarchuk, M. I.; Primetzhofer, D.; Kriegner, D.; Enser, H.; Stangl, J.; Bauer, P.; Voith, M.; Hassel, A. W.; Krumeich, F.; Ludwig, F.; Meingast, A.; Kothleitner, G.; Kovalenko, M. V.; Heiss, W. Tuning the Magnetic Properties of Metal Oxide Nanocrystal Heterostructures by Cation Exchange. *Nano Lett.* **2013**, *13* (2), 586–593. https://doi.org/10.1021/nl304115r.

(39) Fenton, J. L.; Steimle, B. C.; Schaak, R. E. Tunable Intraparticle Frameworks for Creating Complex Heterostructured Nanoparticle Libraries. *Science.* **2018**, *360* (6388), 513–517. https://doi.org/10.1126/science.aar5597.

(40) Nelson, A.; Fritz, K. E.; Honrao, S.; Hennig, R. G.; Robinson, R. D.; Suntivich, J. Increased Activity in Hydrogen Evolution Electrocatalysis for Partial Anionic Substitution in Cobalt Oxysulfide Nanoparticles. *J. Mater. Chem. A* **2016**, *4* (8), 2842–2848. https://doi.org/10.1039/c5ta08706f.

(41) Fagan, A. M.; Jeffries, W. R.; Knappenberger, K. L.; Schaak, R. E. Synthetic Control of Hot-Electron Thermalization Efficiency in Size-Tunable Au-Pt Hybrid Nanoparticles. *ACS Nano.* **2021**, *15* (1), 1378–1387. https://doi.org/10.1021/acsnano.0c08661.

(42) Sen, R.; Gordon, T. M.; Millheim, S. L.; Smith, J. H.; Gan, X. Y.; Millstone, J. E. Multimetallic Post-Synthetic Modifications of Copper Selenide Nanoparticles. *Nanoscale.* **2023**, 6655–6663. https://doi.org/10.1039/d3nr00441d.

(43) Lyu, Z.; Chen, R.; Mavrikakis, M.; Xia, Y. Physical Transformations of Noble-Metal Nanocrystals upon Thermal Activation. *Acc. Chem. Res.* **2021**, *54* (1), 1–10.

https://doi.org/10.1021/acs.accounts.0c00640.

(44) Chen, Y.; Zhan, X.; Bueno, S. L. A.; Shafei, I. H.; Ashberry, H. M.; Chatterjee, K.; Xu, L.; Tang, Y.; Skrabalak, S. E. Synthesis of Monodisperse High Entropy Alloy Nanocatalysts from Core@shell Nanoparticles. *Nanoscale Horizons.* **2021**, *6* (3), 231–237. https://doi.org/10.1039/d0nh00656d.

(45) Song, Y.; Casale, S.; Miche, A.; Montero, D.; Laberty-Robert, C.; Portehault, D. Converting Silicon Nanoparticles into Nickel Iron Silicide Nanocrystals within Molten Salts for Water Oxidation Electrocatalysis. *J. Mater. Chem. A* **2022**, *10* (3), 1350–1358. https://doi.org/10.1039/d1ta08097k.

(46) Li, C. H.; Nanba, Y.; Asakura, D.; Okubo, M.; Talham, D. R. Li-Ion and Na-Ion Insertion into Size-Controlled Nickel Hexacyanoferrate Nanoparticles. *RSC Adv.* **2014**, *4* (48), 24955–24961. https://doi.org/10.1039/c4ra03296a.

(47) Wang, J. W.; Liu, X. H.; Mao, S. X.; Huang, J. Y. Microstructural Evolution of Tin Nanoparticles during in Situ Sodium Insertion and Extraction. *Nano Lett.* **2012**, *12* (11), 5897–5902. https://doi.org/10.1021/nl303305c.

(48) Gibot, P.; Casas-Cabanas, M.; Laffont, L.; Levasseur, S.; Carlach, P.; Hamelet, S.; Tarascon, J.-M.; Masquelier, C. Room-Temperature Single-Phase Li Insertion/Extraction in Nanoscale LixFePO4. *Nat. Mater.* **2008**, *7* (9), 741–747. https://doi.org/10.1038/nmat2245.

(49) Wu, L.; Bresser, D.; Buchholz, D.; Giffin, G. A.; Castro, C. R.; Ochel, A.; Passerini, S. Unfolding the Mechanism of Sodium Insertion in Anatase TiO2 Nanoparticles. *Adv. Energy Mater.* **2015**, *5* (2), 1–11. https://doi.org/10.1002/aenm.201401142.

(50) Lee, S. H.; Kim, Y. H.; Deshpande, R.; Parilla, P. A.; Whitney, E.; Gillaspie, D. T.; Jones, K. M.; Mahan, A. H.; Zhang, S.; Dillon, A. C. Reversible Lithium-Ion Insertion in Molybdenum Oxide Nanoparticles. *Adv. Mater.* **2008**, *20* (19), 3627–3632. https://doi.org/10.1002/adma.200800999.

(51) Kim, S.; Yin, L.; Bak, S. M.; Fister, T. T.; Park, H.; Parajuli, P.; Gim, J.; Yang, Z.; Klie, R. F.; Zapol, P.; Du, Y.; Lapidus, S. H.; Vaughey, J. T. Investigation of Ca Insertion into α-MoO3 Nanoparticles for High Capacity Ca-Ion Cathodes. *Nano Lett.* **2022**, *22* (6), 2228–2235. https://doi.org/10.1021/acs.nanolett.1c04157.

(52) Yin, Y.; Rioux, R. M.; Erdonmez, C. K.; Hughes, S.; Somorjal, G. A.; Alivisatos, A. P. Formation of Hollow Nanocrystals Through the Nanoscale Kirkendall Effect. *Science.* **2004**, *304* (5671), 711–714. https://doi.org/10.1126/science.1096566.

(53) Ha, D. H.; Moreau, L. M.; Bealing, C. R.; Zhang, H.; Hennig, R. G.; Robinson, R. D. The Structural Evolution and Diffusion during the Chemical Transformation from Cobalt to Cobalt Phosphide Nanoparticles. *J. Mater. Chem.* **2011**, *21* (31), 11498–11510. https://doi.org/10.1039/c1jm10337g.

(54) Carenco, S.; Liu, Z.; Salmeron, M. The Birth of Nickel Phosphide Catalysts: Monitoring Phosphorus Insertion into Nickel. *ChemCatChem.* **2017**, *9* (12), 2318–2323. https://doi.org/10.1002/cctc.201601526.

(55) Sarac, M. F.; Wu, W. C.; Tracy, J. B. Control of Branching in Ni3C1-x Nanoparticles and Their Conversion into Ni12P5 Nanoparticles. *Chem. Mater.* **2014**, *26* (10), 3057–3064. https://doi.org/10.1021/cm4034353.

(56) Carenco, S.; Demange, M.; Shi, J.; Boissière, C.; Sanchez, C.; Le Floch, P.; Mézailles, N. White Phosphorus and Metal Nanoparticles: A Versatile Route to Metal Phosphide Nanoparticles. *Chem. Commun.* **2010**, *46* (30), 5578–5580. https://doi.org/10.1039/c0cc00684j.

(57) Wang, J.; Johnston-Peck, A. C.; Tracy, J. B. Nickel Phosphide Nanoparticles with Hollow, Solid, and Amorphous Structures. *Chem. Mater.* **2009**, *21* (19), 4462–4467. https://doi.org/10.1021/cm901073k.

(58) Carenco, S.; Resa, I.; Le Goff, X.; Le Floch, P.; Mézailles, N. White Phosphorus as Single Source of "P" in the Synthesis of Nickel Phosphide. *Chem. Commun.* **2008**, No. 22, 2568–2570. https://doi.org/10.1039/b802454e.

(59) Carenco, S. Designing Nanoparticles and Nanoalloys with Controlled Surface and Reactivity. *Chem. Rec.* **2018**, *18* (7), 1114–1124. https://doi.org/10.1002/tcr.201700106.

(60) Moreau, L. M.; Ha, D. H.; Zhang, H.; Hovden, R.; Muller, D. A.; Robinson, R. D. Defining Crystalline/Amorphous Phases of Nanoparticles through X-Ray Absorption Spectroscopy and X-Ray Diffraction: The Case of Nickel Phosphide. *Chem. Mater.* **2013**, *25* (12), 2394–2403. https://doi.org/10.1021/cm303490y.

(61) Chunduri, A.; Gupta, S.; Bapat, O.; Bhide, A.; Fernandes, R.; Patel, M. K.; Bambole, V.;

Miotello, A.; Patel, N. A Unique Amorphous Cobalt-Phosphide-Boride Bifunctional Electrocatalyst for Enhanced Alkaline Water-Splitting. *Appl. Catal. B Environ.* **2019**, *259* (August), 118051. https://doi.org/10.1016/j.apcatb.2019.118051.

(62) Masa, J.; Andronescu, C.; Antoni, H.; Sinev, I.; Seisel, S.; Elumeeva, K.; Barwe, S.; Marti-Sanchez, S.; Arbiol, J.; Roldan Cuenya, B.; Muhler, M.; Schuhmann, W. Role of Boron and Phosphorus in Enhanced Electrocatalytic Oxygen Evolution by Nickel Borides and Nickel Phosphides. *ChemElectroChem.* **2019**, *6* (1), 235–240. https://doi.org/10.1002/celc.201800669.

(63) Wang, W.; Liu, P.; Wu, K.; Zhang, K.; Li, L.; Qiao, Z.; Yang, Y. Synthesis of Ni-P-B Amorphous Nanoparticles with Uniform Size as a Potential Hydrodeoxygenation Catalyst. *New J. Chem.* **2015**, *39* (2), 813–816. https://doi.org/10.1039/c4nj01770f.

(64) Huang, C. J.; Xu, H. M.; Shuai, T. Y.; Zhan, Q. N.; Zhang, Z. J.; Li, G. R. A Review of Modulation Strategies for Improving Catalytic Performance of Transition Metal Phosphides for Oxygen Evolution Reaction. *Appl. Catal. B Environ.* **2023**, *325* (December 2022), 122313. https://doi.org/10.1016/j.apcatb.2022.122313.

(65) Akopov, G.; Yeung, M. T.; Kaner, R. B. Rediscovering the Crystal Chemistry of Borides. *Advanced Materials*. **2017**. https://doi.org/10.1002/adma.201604506.

(66) Gupta, S.; Patel, M. K.; Miotello, A.; Patel, N. Metal Boride-Based Catalysts for Electrochemical Water-Splitting: A Review. *Adv. Funct. Mater.* **2020**, *30* (1). https://doi.org/10.1002/adfm.201906481.

(67) Lee, E.; Fokwa, B. P. T. Nonprecious Metal Borides: Emerging Electrocatalysts for Hydrogen Production. *Acc. Chem. Res.* **2022**, *55* (1), 56–64. https://doi.org/10.1021/acs.accounts.1c00543.

(68) Menezes, P. W.; Indra, A.; Das, C.; Walter, C.; Göbel, C.; Gutkin, V.; Schmeißer, D.; Driess, M. Uncovering the Nature of Active Species of Nickel Phosphide Catalysts in High-Performance Electrochemical Overall Water Splitting. *ACS Catal.* **2017**, *7* (1), 103–109. https://doi.org/10.1021/acscatal.6b02666.

(69) Lyu, F.; Bai, Y.; Wang, Q.; Wang, L.; Zhang, X.; Yin, Y. Coordination-Assisted Synthesis of Iron-Incorporated Cobalt Oxide Nanoplates for Enhanced Oxygen Evolution. *Mater. Today Chem.* **2019**, *11*, 112–118. https://doi.org/10.1016/j.mtchem.2018.10.010.

(70) Zhang, H.; Jin, M.; Wang, J.; Li, W.; Camargo, P. H. C.; Kim, M. J.; Yang, D.; Xie, Z.; Xia, Y. Synthesis of Pd-Pt Bimetallic Nanocrystals with a Concave Structure through a Bromide-Induced Galvanic Replacement Reaction. *J. Am. Chem. Soc.* **2011**, *133* (15), 6078–6089. https://doi.org/10.1021/ja201156s.

Chapter 2: Molten salts-based conversion of nickel into nanocrystals of nickel borides

I) Introduction: the chemistry of borides

Boride materials present strong covalent bonds between boron atoms and even between boron and metal atoms[1,2]. Complex charge transfers between boron and metal atoms tend to strengthen bonding. These specificities are responsible for their large fields of interest[3,4] in ceramics[5], hard materials[6], thermoelectrics[7,8] and catalysis[9–11], in particular for electrocatalytic water splitting[12].

One can distinguish metal-rich borides and boron-rich borides, which exhibit different properties. Metal-rich borides encompass isolated boron atoms or short B-B chains[1,13,14]. Reversely, boron-rich borides present concatenation of covalent boron chains in 2D or 3D dimensions. Conventional synthesis routes for borides involve high temperatures, such as arc melting above 2500 °C, and/ or high pressures; which are most often not compatible with the recovery of nanostructures[1,2,15]. In contrast, the synthesis of nanoscale borides is most commonly based on chemical vapor deposition with gaseous boron sources or redox reactions using metal salts, a reducing agent and a boron source[1–3,15–17].

In addition to the composition, tuning the morphology of the nano-objects is an effective way to improve the properties, especially in catalysis[18]. Classical methods such as the use of surface ligands or structuring agents/templates allow the tuning of boride nanostructures[18]. Unfortunately, the removal of the structuring agent can be delicate due to the risk of the contamination, dissolution or structural modification of the nanomaterial. In addition, the surface ligand may affect the properties and be detrimental to catalytic processes.

To overcome these limitations, structural modifications of nanostructures have been developed for several ranges of materials. Especially, the insertion of heteroelements inside pre-formed metal nanostructures has been reported for alkali group metals[19–21], chalcogenides[22–25], carbon[26] and phosphorus[27,28], which were diffused into metal containing nanocrystals.

In this work, we develop a method for the synthesis of size-controlled nickel boride nanoparticles by incorporating boron into nickel (0) nanoparticles synthesized prior to the reaction (**Figure 1**). We perform these reactions on nickel nanoparticles suspended into molten salts, in order to avoid extensive crystal growth and particle coalescence. Molten salts provide media that enable performing such reactions between ~350 and 900 °C, a temperature range required to activate the reaction and to crystallize nickel borides. By combining *in situ* X-ray diffraction and pair distribution function (PDF) analysis of total X-ray scattering patterns, we monitor the reaction mechanism and the amorphous intermediates identified. Revealing the nature of these intermediates paves the way to the understanding of the mechanism of boron

diffusion and the identification of key factors for selective boride crystallization. First insights in this reactivity for borides were performed by Tsou-Hsi Camille Chan Chang[29] during her PhD work. Herein, we focus on the synthesis of Ni_3B and Ni_4B_3 nanocrystals and assess in detail the mechanistic pathway of the reaction. The electrocatalytic properties of these nanomaterials for overall water splitting will be discussed in chapter 3.

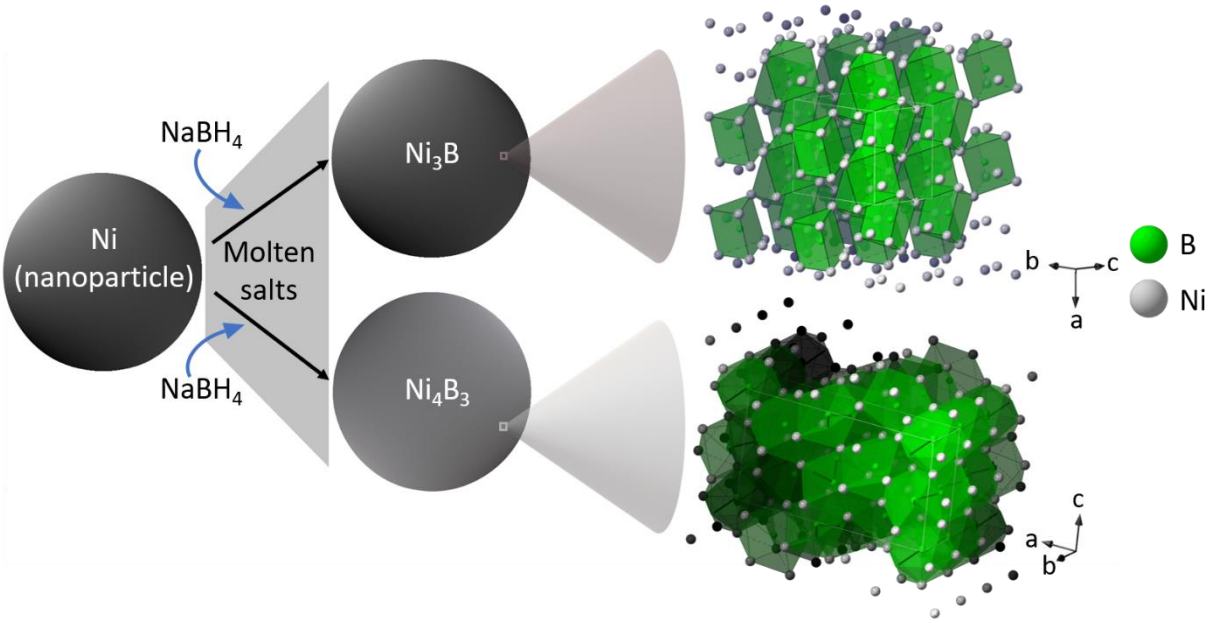

Figure 1. Schematic mechanisms of the syntheses of Ni_3B and Ni_4B_3 nanocrystals, with the corresponding crystal structures.

II) The incorporation of boron into nickel nanoparticles

a) Synthesis of Ni_3B and Ni_4B_3 nanocrystals

The synthesis of boride nanocrystals relies on pre-formed nickel nanoparticles as reagents (**Figure 1**). Nickel borides nanocrystals were prepared from $Ni^{(0)}$ nanoparticles of *ca*. 30-40 nm **(Figure 2A-C**), obtained by colloidal synthesis according to a reported procedure[30] (Supporting information) based on the reaction between $Ni(acac)_2$, oleylamine and trioctylphosphine as a capping agent. A strict compliance of the synthesis temperature is necessary in order to avoid appearance of a nickel phosphide by-product during the synthesis. The $Ni^{(0)}$ nanoparticles are then dispersed into the salt powders that will yield the molten medium, in order to provide optimal dispersion of the particle reagent in the molten salt. $NaBH_4$

is used as boron source with adjusted content. Its thermal decomposition catalyzed by nickel nanoparticles yields elemental boron[31], so that the borohydride can act as efficient source of boron (0) to be incorporated into the nickel nanoparticles. A slight excess of boron source is used to circumvent uncomplete reaction of elemental boron and then obtain pure phases. The reaction is carried out in a LiI:KI eutectic mixture (T_f = 286 °C) at 475 °C for 1.5 h. The molten salts inorganic mixture is used to provide a thermally stable liquid medium over a wide temperature range, with a low viscosity, thus supporting homogeneous reactivity[5,32]. A 70-75 % yield is achieved for Ni_3B and Ni_4B_3 nanocrystals. Transmission electron microscopy (TEM, (**Figure 2**) shows that the size distribution (**Figure 2C, F, I**) is maintained during the transformation from the nickel nanoparticles to the boride nano-objects. Dispersion states and size distributions are also maintained, despite a slight coalescence of the particles (**Figure 2H**). High resolution transmission electron microscopy (HRTEM) images and the corresponding Fast Fourier Transforms (FFTs) are consistent with the respective Ni_3B/Ni_4B_3 crystal structures (**Figure 2E, H**).

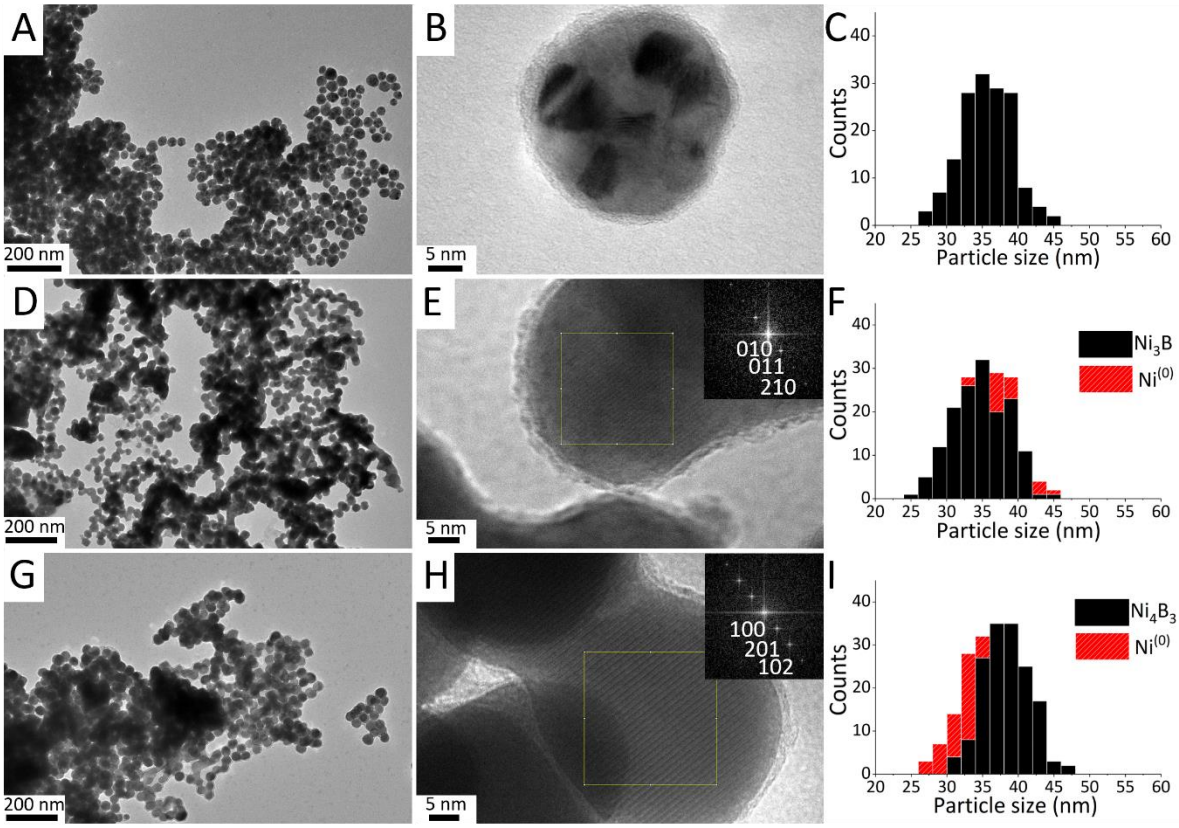

Figure 2. TEM study of (A-C) $Ni^{(0)}$ nanoparticles, (D-F) Ni_3B nanocrystals and (G-I) Ni_4B_3 nanoparticles: (A, D, G) TEM images; (B, E, H) HRTEM images with FFTs of the squared areas, indexed along the corresponding crystal structures of borides; (C, F, I) particle size

distributions. The size distributions of the boride nanocrystals are plotted with the distribution of the initial $Ni^{(0)}$ nanoparticle, for comparison.

Energy Dispersive X-ray Spectroscopy (EDS) indicates a B:Ni ratio of 0.4 and 1, in agreement with the expected values for Ni_3B and Ni_4B_3, respectively. Besides, phosphorus from trioctylphosphine used as a surface ligand for the synthesis of Ni nanoparticles is also detected with a P:Ni ratio of 0.01, although it is lower than the ratio of 0.05 measured on the pristine Ni nanoparticles after washing. This observation highlights partial elimination of phosphorus as volatile species during the synthesis in molten salts, and possibly a concomitant incorporation of phosphorus with boron inside nickel nanoparticles.

Powder X-Ray Diffraction (XRD) and the corresponding Rietveld refinements indicate that by simply adjusting the $NaBH_4$ content, it is possible to achieve two compounds crystallizing respectively into the Ni_3B and Ni_4B_3 (**Figure 3A-B**) crystal structures, with lattice parameters in agreement with the reported values for Ni_3B (a = 5.2421(9) Å, b = 6.630(1) Å, c = 4.4016(8) Å *versus* tabulated values a = 5.22190 Å, b = 6.61710 Å, c = 4.39180 Å) and for Ni_4B_3 (a = 11.984(1) Å, b = 2.9887(3) Å, c = 6.5702(8) Å *versus* tabulated values a =11.9530 Å, b = 2.9810 Å, c = 6.5690 Å). The pair distribution function (PDF, **Figure 3C-D**) obtained by refinement of the total X-ray scattering pattern (**Figure S2-I**) is fully consistent with the reported structures of the borides, and does not indicate any additional amorphous component.

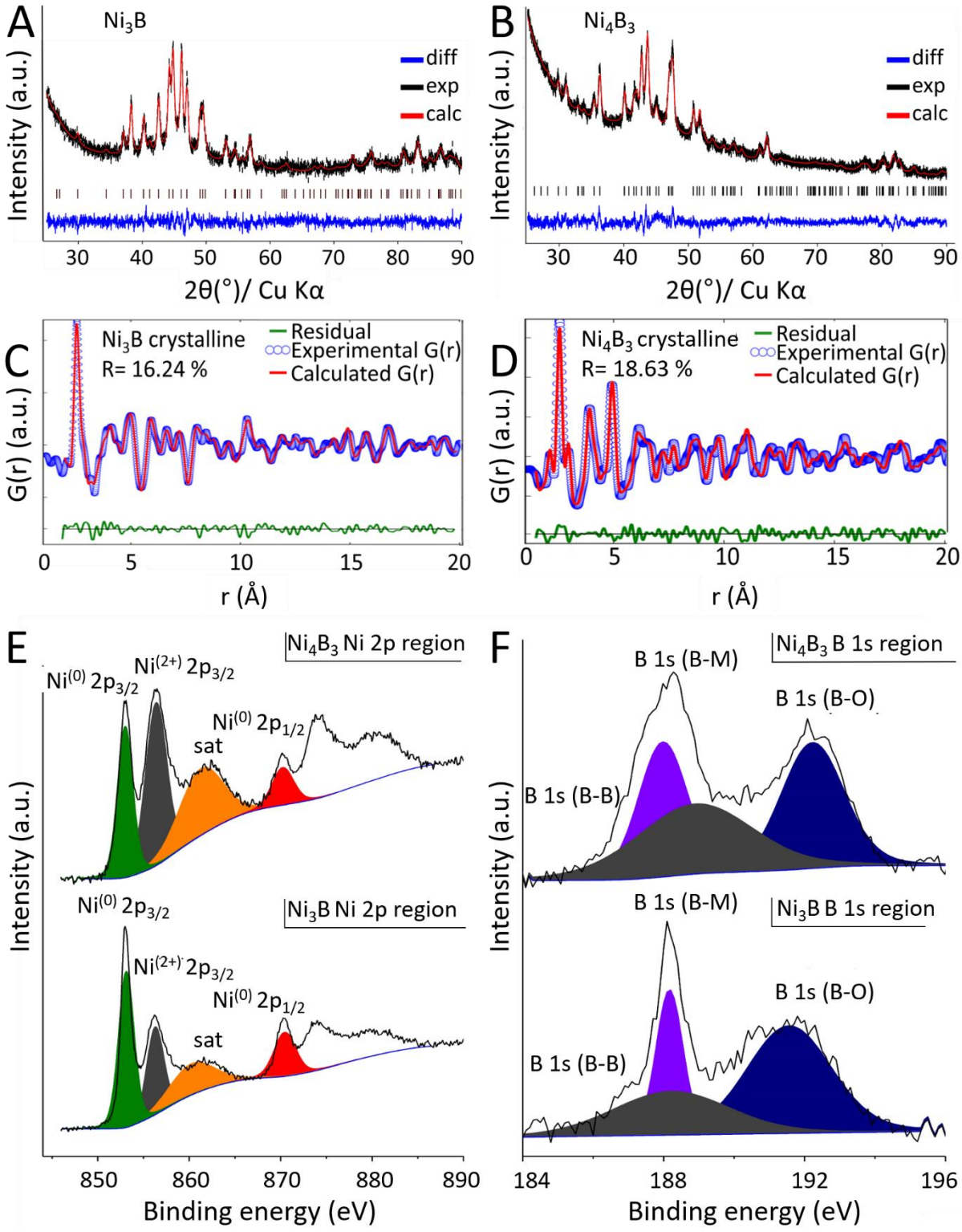

Figure 3. XRD patterns with corresponding Rietveld refinements of (A) Ni_3B and (B) Ni_4B_3 nanocrystals. Pair distribution functions of (C) Ni_3B and (D) Ni_4B_3 nanocrystals fitted along the corresponding crystal structures. XPS of Ni_3B and Ni_4B_3 in (E) Ni 2p (F) B 1s region.

Ni_3B and Ni_4B_3 crystallize in the same space group (*Pnma*, 62) in an orthorhombic structure. Both borides contain covalent nickel-boron bonds (**Figure 1**). In Ni_3B, each boron occupies the center sites of trigonal prisms BNi_6 (B-Ni bond length 2 Å) formed by the nickel atoms without B-B bonding. A seventh Ni neighbor is located outside the trigonal prisms, with a B-Ni bond length of 2.3 Å[3,13]. In the Ni_4B_3 structure, the boron atoms are 9-fold coordinated. Two different types of coordination are observed (**Figure 4**): $B(Ni_7B_2)$ polyhedra with boron bonding to seven nickel atoms (bond lengths of 2-2.2 Å) and to two other boron atoms with shorter bonds (1.9 Å), and $B(Ni_9)$ polyhedra with boron bonding to nine nickel atoms with bonds of 2-2.2 Å and one at 2.5 Å [33]. In this structure, boron forms infinite zig-zag chains of B-B bonds along the ***b*** axis, inducing the formation of a boron-boron covalent bond sublattice[1]. This B-B sublattice tends to reinforce the structure[34].

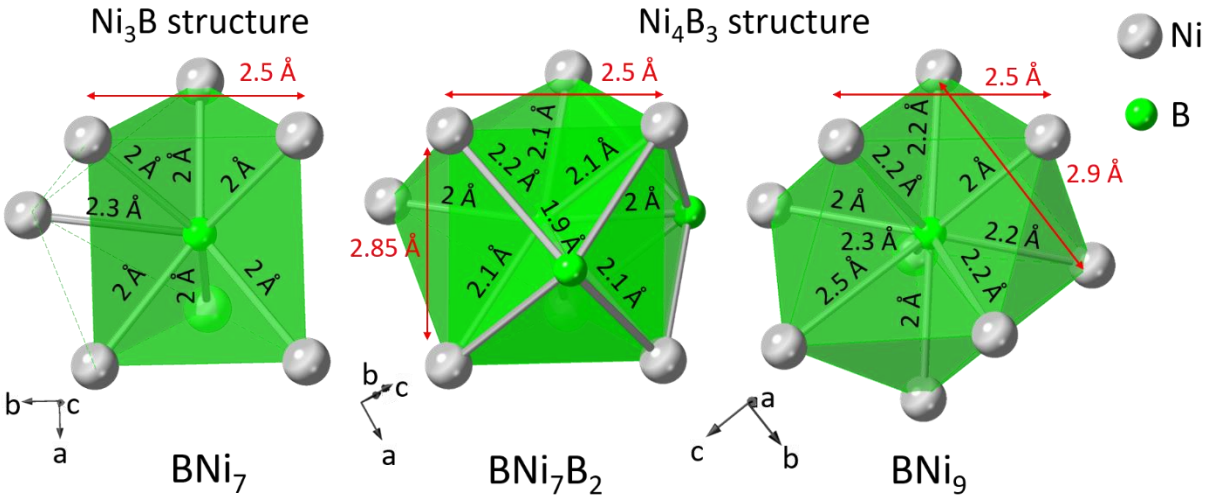

Figure 4. Single boron polyhedra constituting the Ni_3B and Ni_4B_3 crystal structures. The red marks indicate the distances between nickel atoms not directly engaged in a binding.

For both materials, TEM highlights an amorphous shell of 1-2 nm thickness on the surface of the particles (**Figure 2E, H**). We have then performed X-ray photoelectron spectroscopy (XPS, **Figure 3E-F**) to probe the surface states. The Ni 2p region for Ni_3B (**Figure 3E**) is similar to those previously reported[35,36,37], where the peaks at binding energies of 853.1 and 870.5 eV are assigned to nickel atoms of the boride, with a charge state close to elemental nickel. The peak at 856.2 eV corresponds to Ni^{2+} $2p_{3/2}$, which we ascribe to surface oxidation during washing. Note that nickel phosphides would feature a peak at a bonding energy of 853.1 eV in the case of Ni_2P, hence overlapping with the boride signal, so that phosphorus doping cannot be ruled out. The Ni_4B_3 sample shows the same features (**Figure 3E**). The B 1s region shows similar

contributions for both samples (**Figure 3F**), *i.e.* at 187.8, 188.2 and 191.4 eV, attributed to boron within the boride, to elemental boron, and oxidized boron respectively. We ascribe the second contribution to the amorphous layer observed at the surface of the particles by TEM (**Figure 2E, H**) and the third contribution to the partial oxidation of this amorphous boron layer during washing and exposure to air.

b) Investigation of the reaction mechanism by *in situ* X-ray diffraction

In order to investigate the mechanism of the conversion of nickel into nickel boride nanoparticles, we have monitored the reaction *in situ* by synchrotron radiation-based XRD in transmission mode on the ID11 beamline of ESRF synchrotron. We have developed a capillary oven dedicated to this purpose. The setup enables to mimic the argon flow, oxygen-free conditions used in the lab-scale synthesis. A vertical fused silica capillary containing the reaction mixture is prepared in an Ar-filled glovebox and adapted to an airtight capillary holder enabling gas flow through Swagelok® valves. The ensemble is then inserted inside a capillary oven equipped with two resistive heating $Pt_{0.9}Ir_{0.1}$ coils. The argon flow is maintained through the opened top of the capillary in order to evacuate volatile species such as H_2 produced by thermal decomposition of $NaBH_4$. Different positions on the capillary are probed by continuous vertical scan of the capillary in order to assess the homogeneity of the reaction medium.

Figure S2-IIA-B and **C-D** show overlays of the XRD diagrams obtained on one position for the Ni_3B and Ni_4B_3 reaction mixtures, respectively, for a heating ramp of 10 °C min^{-1} followed by a plateau, hence mimicking the lab-scale conditions. The original 55 °C shift of the measured melting point coming from the distance between the thermocouple and the capillary was corrected by using the LiI:KI melting point as reference at 286 °C. **Figures 5** and **S2-III** show focuses on the temperature range where the reaction media are liquid. The diffraction peaks of LiI, KI, NaI and Ni are observed until melting of the reaction media for the Ni_3B and Ni_4B_3 experiments. NaI is formed either by the metathesis reaction of LiI:KI with $NaBH_4$ or by the decomposition of $NaBH_4$ and is molten 12 min after the start of the experiment, i.e. before the salt has completely melt. Above the melting point, a diffuse scattering, signature of the inorganic liquid, is observed at ca. 1.5 $Å^{-1}$. The absence of diffraction peak related to nickel species indicates the formation of an XRD amorphous material from 33 min/330 °C to 43 min/415 °C for Ni_3B (**Figure 5**, **Figure S2-IIA-B**). A similar trend is observed for the Ni_4B_3 synthesis (**Figure S2-IIC-D, Figure S2-III**) with the absence of crystalline phase from

39 min/360 °C to 50 min/470 °C. Further heating to 510 °C followed by a temperature plateau yields the crystallization of Ni_3B and Ni_4B_3 phases, respectively, as sole crystalline phases. The *in situ* total X-ray scattering diagrams recorded for PDF analysis (**Figure S2-IV**) are consistent with the *in situ* data discussed above.

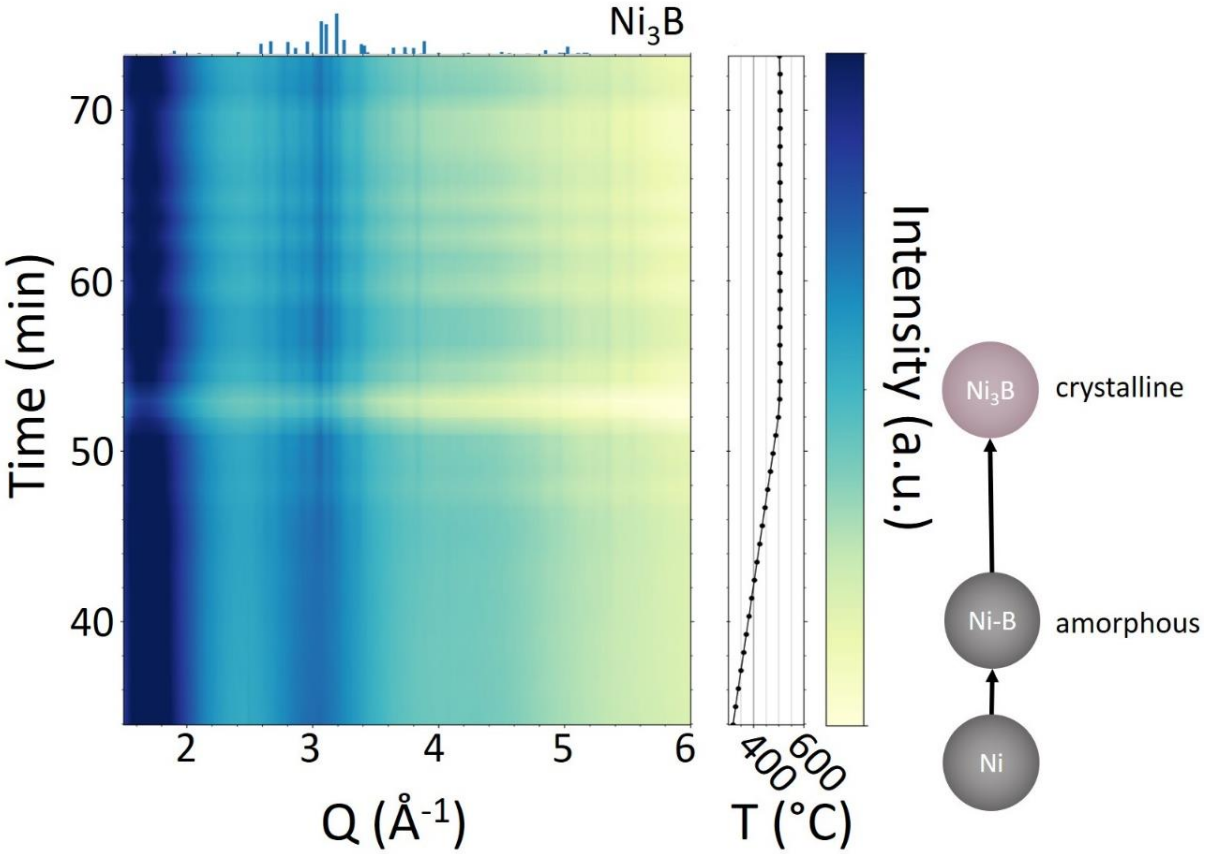

Figure 5. *In situ* XRD diagrams recorded during the synthesis of Ni_3B nanocrystals after melting of the eutectic salt mixture.

As *in situ* XRD suggests that crystallization of Ni_3B and Ni_4B_3 proceeds through amorphous intermediates, we have inquired on the exact nature of these amorphous species. First, we have used the *in situ* XRD results to identify the conditions to form and isolate these intermediates. Amorphous phases could then be retrieved *ex situ* at 390 °C after 1 h of plateau for the Ni_3B synthesis, at 370-390 °C after 1.5 h for the Ni_4B_3 synthesis (**Figure S2-V**). We note that retrieving the Ni_3B amorphous intermediate without any trace of Ni is difficult, probably due to the low content of boron in the corresponding phase, which implies close relative stabilities of both components and also the absence of stiff B-B covalent bonds, hence a relatively loose framework that enables fast restructuration of the Ni-B phase. TEM pictures of the amorphous

intermediates confirm morphologies similar to the initial Ni and final Ni_3B/Ni_4B_3 nanoparticles, (**Figure 6**) further supporting the hypothesis of boron incorporation into the nickel particles as overall reaction pathway. The onset of aggregation between particles is observed but the spherical morphology and diameter are maintained. HRTEM (**Figure 6**) shows no local order, which is consistent with the XRD patterns. The corresponding XPS signals in the Ni 2p region (**Figure S2-VI)** show peaks characteristic of low valence Ni, as in the crystalline borides, thus indicating a similar electronic state of Ni. Likewise, corresponding Ni^{2+} $2p_{3/2}$ contributions are also observed at 856.8 and 857.5 eV for the amorphous intermediates from the Ni_3B and Ni_4B_3 syntheses, probably originating from exposure to air for washing and measurement.

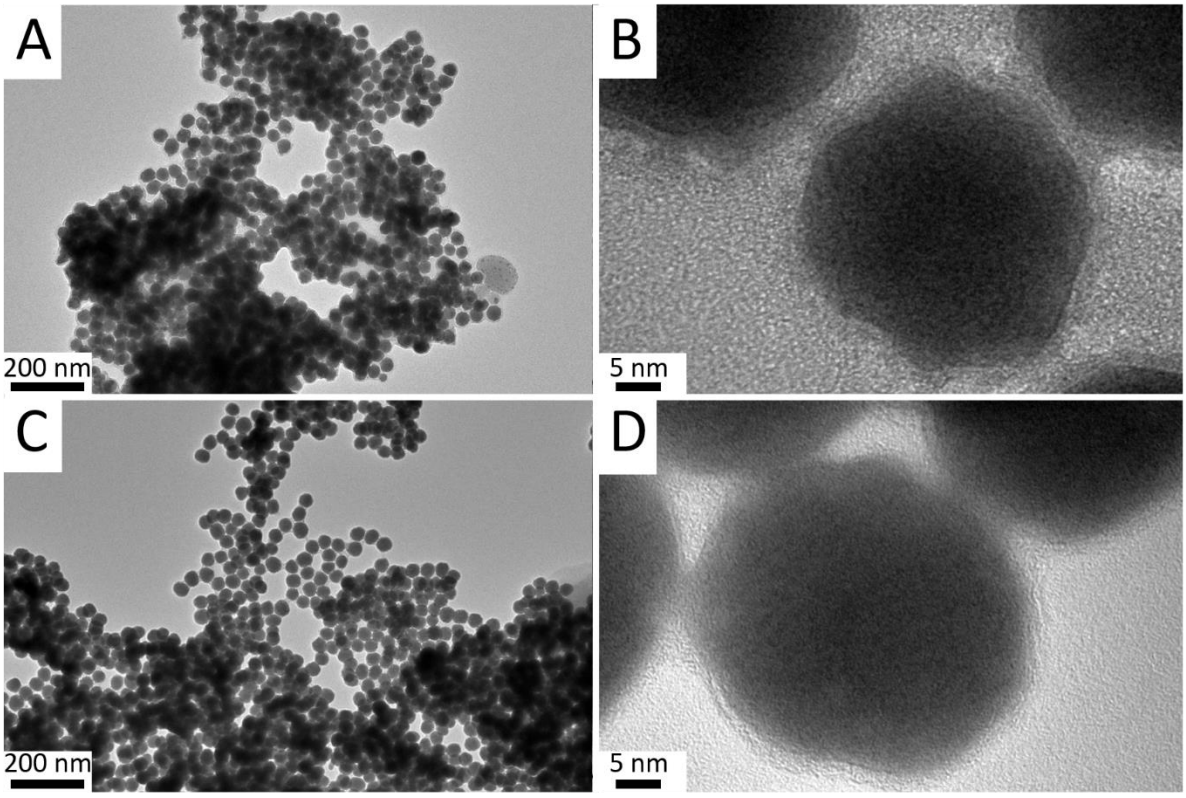

Figure 6. TEM pictures of the amorphous nanoparticles formed during the synthesis of (A, B) Ni_3B and (C, D) Ni_4B_3 nanocrystals. (A, C) Low and (B, D) high magnification images.

The fact that incorporation of boron towards Ni_4B_3 does not involve a crystalline Ni_3B state suggests that the crystallization of both phases occurs through two distinct amorphous states, contrary to what could be expected from the Ostwald rule[38], which would suggest sequential crystallization of borides from boron-poor (Ni_3B) to boron-richer (Ni_4B_3) phases upon continuous incorporation of boron into the initial nickel nanoparticles. We have then used PDF analysis of the *ex situ* total X-ray scattering patterns to study the short-range order in the two

amorphous intermediates. We have first fixed the coherence range of the respective crystalline structures to 10 Å and attempted to fit the PDFs. At first sight, the two amorphous phases display similar PDFs (**Figure 7A**). The PDFs show common features with the respective crystalline phases: two first peaks at 2 and 2.5 Å for Ni_3B (**Figure 3C**), three peaks at 2, 2.5 and 2.95 Å for Ni_4B_3 (**Figure 3D**). Nevertheless, satisfactory fitting could not be achieved from the sole crystal structures of Ni_3B and Ni_4B_3, mostly due to inconsistent relative intensities of these peaks (**Figure S2-VIIA, B**). For the amorphous intermediate to Ni_3B, second components like Ni, $Ni(OH)_2$, B and B_2O_3, did not yield improvement of the fit, but the incorporation of NiO led to a significant enhancement of R_w from 37 to 32 % for a NiO content adjusted to 9 wt.% (**Figure S2-VIIB**). NiO would probably occur from exposure to air and moisture during washing to recover this elusive intermediate, as mentioned above. No NiO could be detected from the PDF of the amorphous intermediate to Ni_4B_3, which is consistent with the higher stability of this intermediate phase compared to the intermediate to Ni_3B, as already observed from XRD (**Figure S2-V**).

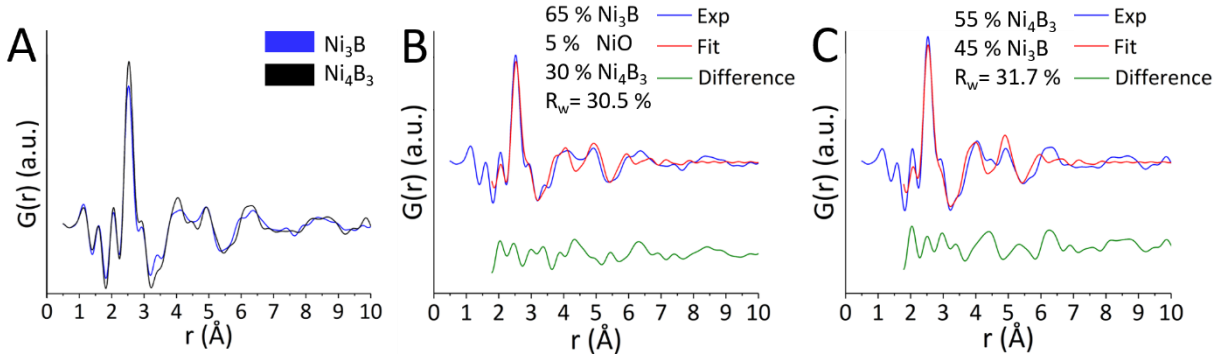

Figure 7. (A) *Ex situ* PDFs of the amorphous intermediates retrieved in the course of the syntheses of Ni_3B and Ni_4B_3. (B) PDF of Ni_3B refined as a mixture of Ni_3B, Ni_4B_3 and NiO crystal structures. (C) PDF of Ni_4B_3 refined as a mixture of Ni_4B_3 and Ni_3B.

To refine the model and since the PDFs of both amorphous intermediates (**Figure 7A**) display similarities with those of the crystalline phases (**Figure 3C, D**), we have treated the PDFs of the amorphous phases as mixtures of Ni_3B and Ni_4B_3. For the amorphous intermediate to Ni_3B, the best refinement gave a R_w of 30.5 % for a sample constituted of 65 wt. % of Ni_3B, 30 wt. % of Ni_4B_3 and 5 wt. % of NiO (**Figure 7B**). As reference, a R_w of 31.9 % is obtained if only a mixture of 60 wt. % of Ni_3B and 40 wt. % Ni_4B_3 is considered (**Figure S2-VIIC**). This fitting figure of merit is satisfactory for an amorphous solid showing a distribution of local

geometries[39]. For the Ni_4B_3 intermediate, the R_w decreased to a satisfactory value of 31.7 % when considering 55 % of Ni_4B_3 mixed with 45 % of Ni_3B (**Figure 7C**).

Considering the amorphous phases using the two different model structures Ni_3B and Ni_4B_3 forces the fit towards relatively ordered systems, especially by maintaining the local coordination polyhedra (**Figure 4**). At scales as short as 10 Å, which corresponds to 1 or 2 unit cells for nickel borides, one can foresee the possibility of fluctuations in the boron coordination spheres. By calculating the PDFs of each single polyhedron (**Figure 4**) isolated in a cubic box of 10x10x10 Å, we confirm that PDF analysis makes it possible to decipher the different polyhedra present in Ni_3B and Ni_4B_3 structures (**Figure 8A**), especially due to different relative intensities of peaks at 2, 2.5 and 2.9 Å. Especially, the 2.9 Å contribution is absent for the Ni_3B polyhedral. In the calculated PDFs of Ni_3B and Ni_4B_3 (**Figure 8B-C**), the two first peaks are identical and can be attributed to the distance between nickel and boron atoms separated by 2 Å and two nickel atoms at 2.5 Å. The peak indicating a distance of 2.9 Å is specific to the two polyhedra of Ni_4B_3 and corresponds to the distance between two nickel atoms. These distances are consistent with those identified on the structural polyhedra (**Figure 4**). Note however that assignment of the contributions of B-B, Ni-B and Ni-Ni distances in the calculated PDFs of Ni_3B and Ni_4B_3 (**Figure 8B-C**) show that the B-B contribution is insignificant while the Ni-Ni peaks contribute for 90 % of the PDF, in agreement with the low *Z* number of boron. The strong contrast limits the propensity of PDF analysis to probe subtle changes in the coordination sphere of boron. These peaks are also observed in the experimental PDFs of the amorphous intermediates, which show similarities with the calculated polyhedra PDFs.

Since the three same peaks with different intensities are also observed in the experimental PDFs of the amorphous states, this confirms that the local order cannot be described by considering assembly of only Ni_3B or only Ni_4B_3 polyhedra. Therefore, a mixture in variable proportions of the three types of polyhedra, regardless of their respective assignation to Ni_3B or Ni_4B_3, is a model that may fit also the experimental PDF of the amorphous phases. However, in a first approximation, because the fitting figures of merit are acceptable, the model relying on a mixture of Ni_3B and Ni_4B_3 structures provides satisfactory results, without discrediting other short-range disorder.

Note also that e*x situ* PDF analysis provides a snapshot of the amorphous intermediates, which differ from each other whether further heat treatment would yield Ni_3B or Ni_4B_3. *In situ* analysis appears essential to confirms the proposed model and observe the evolution towards the crystalline phases. This data treatment is in progress.

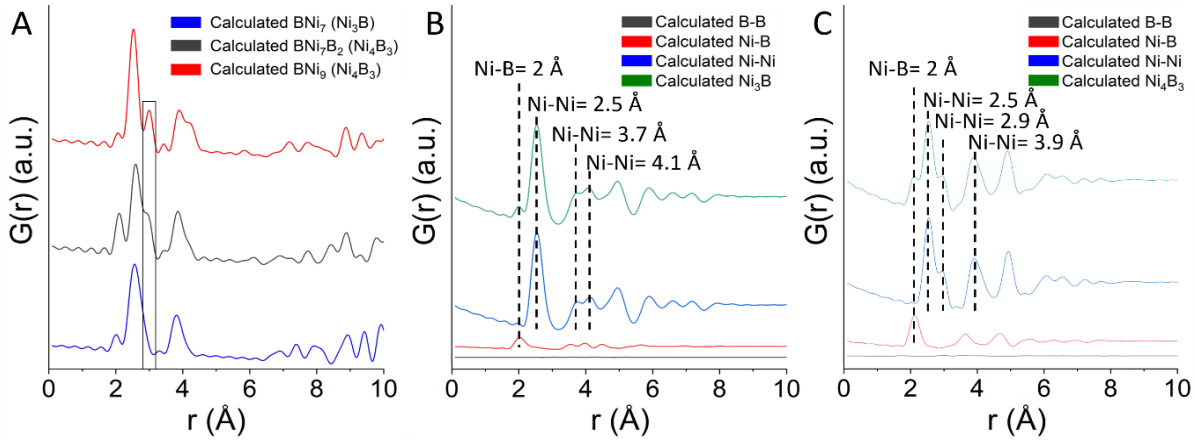

Figure 8. (A) Calculated PDF of the isolated polyhedra consisting of Ni_3B (BNi_7) and Ni_4B_3 (BNi_7B_2, BNi_9). The rectangle highlights the 2.9 Å peak unobserved in the BNi_7 coordination of Ni_3B. Calculated PDF of the (B) Ni_3B and (C) Ni_4B_3 structures in a range of 9 Å and assignment of the contributions of B-B, Ni-B and Ni-Ni distances.

c) Role of aggregation

The amorphous particle intermediates of Ni_3B and Ni_4B_3 observed by TEM (**Figure 6**) show an aggregation state close to that of the initial nickel nanocrystals (**Figure 2**). However, Ni_3B and Ni_4B_3 nanocrystals (**Figure 2**) show crystallinity associated with a more pronounced coalescence in the form of long-range chains. Thus, none of the rare isolated particles (**Figure S2-VIIA**) present any observable local order. The crystalline domains extend along the coalescence interface of the particles (**Figure 2D-H**), while some particles are coalesced without sign of crystallization (**Figure S2-VIIIB**).

From these observations, a mechanism of crystallization can be postulated. The initial nickel nanoparticles incorporate boron to form the amorphous phases. Then, partial coalescence and the onset of aggregation take place. The coalescence of at least two particles seems to trigger crystallization. Since no partial crystalline domains are observed within a particle, the composition of each coalesced particle should correspond to that of the crystalline phase. By maintaining heating, the diffusion of the nanocrystals allows them to react either with other amorphous nanoparticles or with nanocrystals. As both Ni_3B and Ni_4B_3 characteristics are possibly observed at the local range of the amorphous intermediates, the coalescence could then be essential to guide the crystallization toward the pure phase.

III) Solid-state reaction reference

Recently, the mechanochemical synthesis of nickel boride nanocrystals was reported for Ni_3B and Ni_2B [3], through the reduction of a nickel halide by $NaBH_4$ or by reaction between $NaBH_4$ and commercial nickel nanoparticles for 24 h to 72 h of reaction at 400 °C. We have then probed the reactivity of sodium borohydride with nickel nanoparticles without molten salt. The conditions for synthesis of Ni_3B and Ni_4B_3 in molten salts were maintained as well as the washing steps to remove the sodium by-product from the decomposition of $NaBH_4$. In these conditions, partial reactivity is observed and yields a mixture of borides including the targeted phases (**Figure S2-IXA-B**). Moreover, at 475 °C for 1.5 h, all the nickel nanoparticles are not converted. Furthermore, we observe crystallization of Ni_3P from the reaction mixture forming sole Ni_3B in the molten salt. This implies a competition mechanism between the insertion of boron and phosphorus. Phosphorus was introduced as TOP for the synthesis of nickel nanoparticles. This mechanism is discussed more in detail in the Chapter 4. The Ni_3B mixture (**Figure S2-IXC**) yielded extensive aggregation, contrary to the Ni_4B_3 mixture (**Figure S2-IXD**), in agreement with the lack of particles dispersion in the solid mixture. The lower coalescence of the particles in the Ni_4B_3 sample can be attributed to the higher boron content, which increases the Tammann temperature and limits surface atom migration. These data confirm the necessity of using molten salts as reaction media to perform liquid-phase synthesis of boride nanocrystals with narrow distribution and high dispersion state.

Conclusion and perspectives

In summary, we have performed the phase-selective conversion of nickel nanoparticles into morphology-controlled Ni_3B and Ni_4B_3 nickel boride nanocrystals in molten salts. We have addressed the reaction mechanism with synchrotron-based *in situ* X-ray diffraction and pair distribution function analysis. This study enabled us to identify the crystallization pathway, which involves amorphization triggered by incorporation of boron into the metal nanoparticles and directed coalescence to trigger the crystallization. An in-depth study of these intermediates, also isolated, revealed that the amorphous intermediates to Ni_3B and Ni_4B_3 deviate from each other in terms of local order, and can be considered, in a first approximation, as mixtures of Ni_3B and Ni_4B_3 polyhedral building blocks in different ratios.

Extension of the method described in this chapter, for the incorporation of heteroelement into

first row transition metal nanoparticles is discussed in the following chapters. In the case of the nickel borides, studies about the homogeneity at the local state of the intermediates identified would provide better understanding of the reaction pathway.

Annexes

Experimental methods

Reagents. Lithium iodide (99%, Alfa Aesar), potassium iodide (99%, Sigma-Aldrich), anhydrous hexane (95%, Sigma-Aldrich), Nickel (II) acetylacetonate (95%, $Ni(acac)_2$, Strem Chemicals), trioctylphosphine (TOP, 97%, $P(C_8H_{16})_3$, Strem Chemicals), $NaBH_4$ (min 98%, Alfa Aesar) were stored and manipulated as received in an Ar-filled glovebox (H_2O < 0.5 ppm, O_2 < 0.5 ppm). Oleylamine (technical grade 70%, Sigma-Aldrich), tetrahydrofuran (THF, VWR Normapur grade), Acetone (VWR Normapur grade), methanol (VWR Normapur grade), sulfuric acid (98%, Sigma-Aldrich) and ethanol (absolute, VWR Normapur grade) were stored and used under air.

Synthesis of nickel nanoparticles

The synthesis is based on a reported procedure[30] for the obtention of size tunable nickel nanoparticles. First, 20.8 g (25.6 ml, 78mmol) oleylamine is introduced in a 50 ml three-necked round-bottomed flask containing a Teflon-coated stir bar and connected on a Schlenk line *via* a reflux condenser. Oleylamine was degassed under stirring at room temperature by applying 3 cycles of vacuum and N_2 purge and maintain under vacuum for 30 minutes. Afterward, 0.7 mL (1.7 mmol) TOP and then 2 g $Ni(acac)_2$ were added. The mixture was then heated under nitrogen flow with a heating mantle at 212 °C for 2 h with a rapid degassing step over 100 °C to remove the side products. A precise control of the temperature is necessary to avoid phosphidation of nickel and formation of a side product Ni_3P. The suspension was then cooled by just removing the heating mantle. The nanoparticles were washed under nitrogen flow on the Schlenk line. A first washing step was performed by adding a mixture of ≈10 mL THF with ≈30-40 mL acetone, followed by sonication in a sonification batch and reprecipitation of the particles by placing a magnet under the flask to trash the supernatant. Eight other washing steps were performed by adding ≈10 mL of THF, followed by dispersion through sonication, addition of ≈30 mL acetone and finally placing a magnet under the flask to separate the particles from the solvent. After the last washing, the particles were placed in THF without sonication, transferred in a Schlenk tube maintained under N_2 flow and recovered by separation with a magnet of the particles and the dispersion solvent and dried. The particles were then stored in an Ar-filled glovebox.

Synthesis of Ni_3B and Ni_4B_3 nanoparticles

All steps were performed in oxygen-free atmosphere. In a typical reaction, 100 mg of nickel nanoparticles (1.7 mmol) were firstly adapted under vacuum ramp maintained under N_2 flow. The nanoparticles were impregnated by dispersion in 1.6 mL of anhydrous hexane for 30 min and rapid addition of 5 g of salts mixture composed of LiI-KI eutectic mixture (T_f =286 °C). The salt mixture was previously prepared by mixing under inert atmosphere respectively 2.9 g LiI (21.7 mmol) with 2.1 g KI (12.7 mmol) or 6.63 g LiCl (15.6 mmol) with 8.37 g KCl (11.2 mmol) by ball milling for 2 min at 20 Hz. The mixture was then sonicated for 15 min under N_2 and dried under vacuum. Respectively for Ni_3B and Ni_4B_3, 27 mg or 64 mg of $NaBH_4$ was added under inert atmosphere and the mixture was ball-milled for 2 min at 20 Hz. Finally, under inert atmosphere, the powder was placed inside a molybdenum crucible, itself introduced in a closed quartz tube and heated at 475 °C for 1.5 h under Ar flow. After cooling, the powder was dispersed in methanol and washed several times by centrifugation-redispersion. The nanoparticles were finally dried on a vacuum ramp and introduced in an Ar filled glovebox. The reaction yield was 65 % and 71 % for Ni_3B and Ni_4B_3 syntheses, respectively.

Synthesis of Ni_3B and Ni_4B_3 nanoparticles without molten salts

The procedure was similar to the previous case except that all precursors were directly prepared in a glove box and mixed by ball milling.

Supplementary data for chapter 2

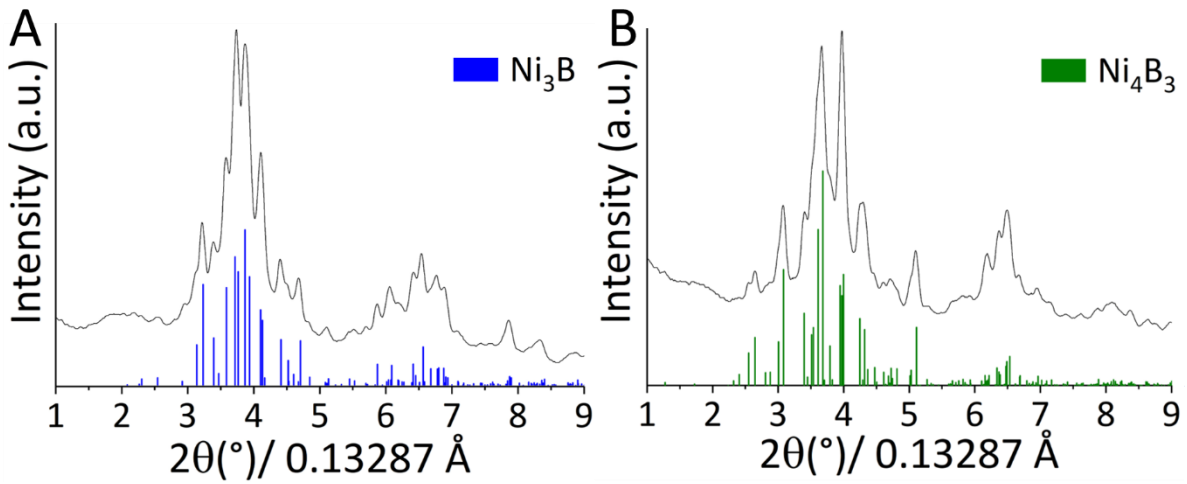

Figure S2-I. Powder XRD diagrams of (A) Ni_3B and (B) Ni_4B_3 nanocrystals acquired in total X-ray scattering configuration by using synchrotron-based radiation, with wavelength 0.13287 Å.

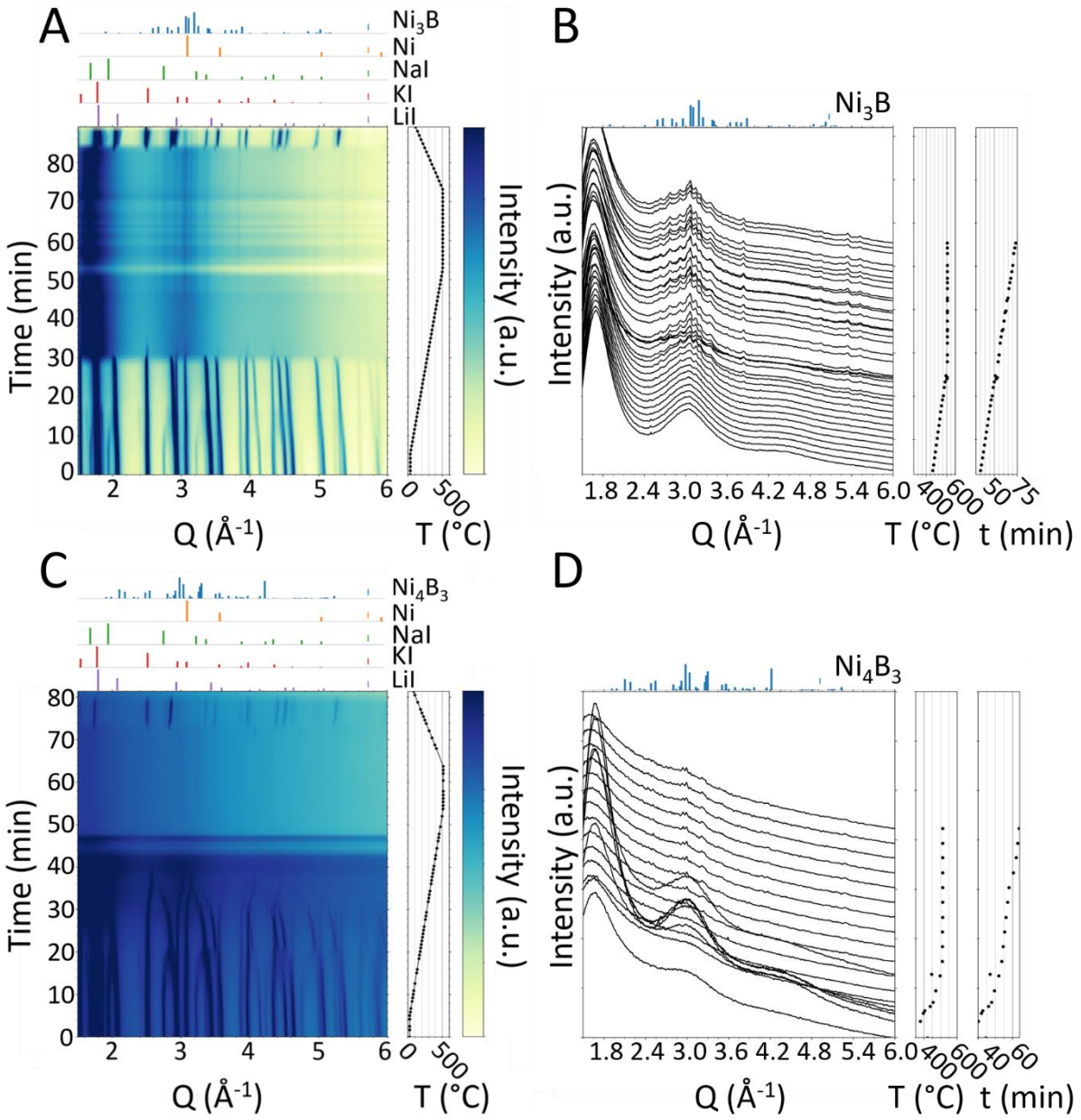

Figure S2-II. *In situ* XRD diagrams recorded during the synthesis of (A, B) Ni_3B and (C, D) Ni_4B_3 nanocrystals.

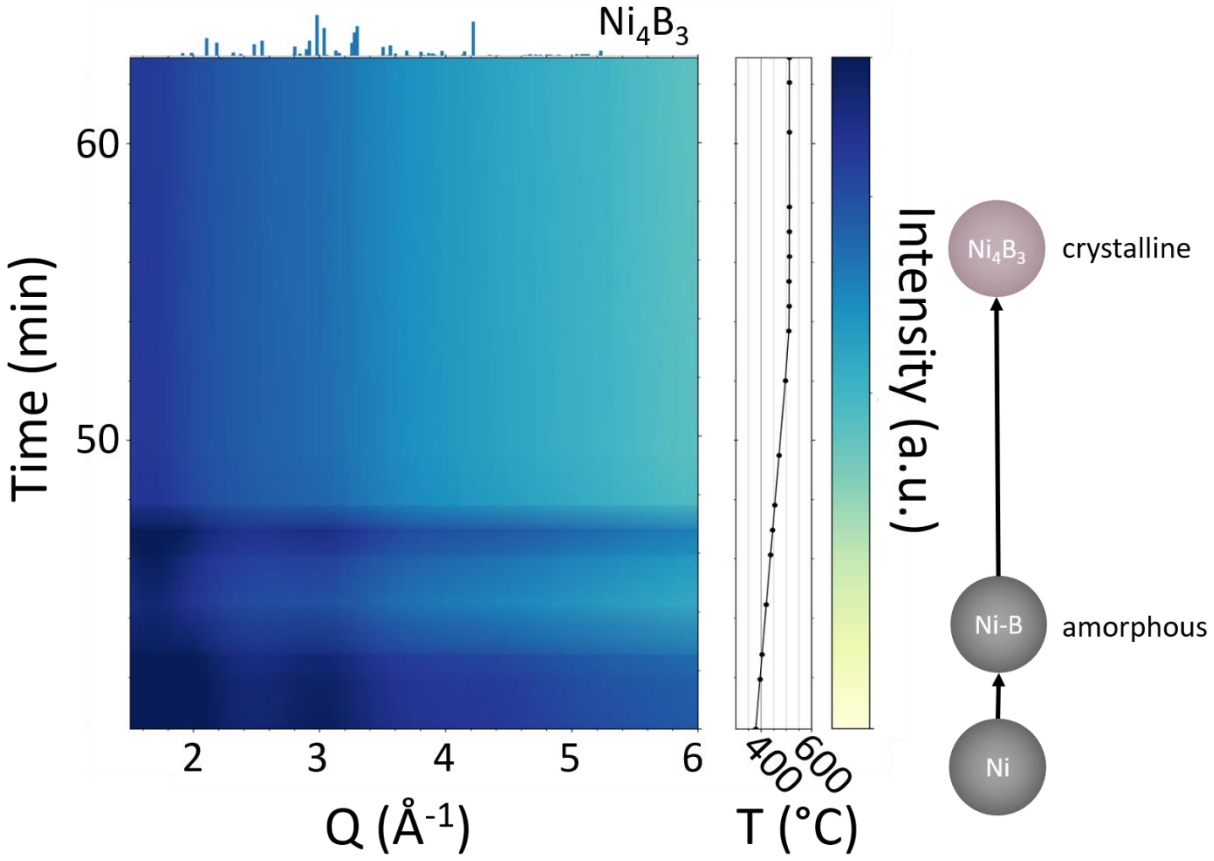

Figure S2-III. *In situ* XRD diagrams recorded during the synthesis of Ni_4B_3 nanocrystals after melting of the eutectic salt mixture.

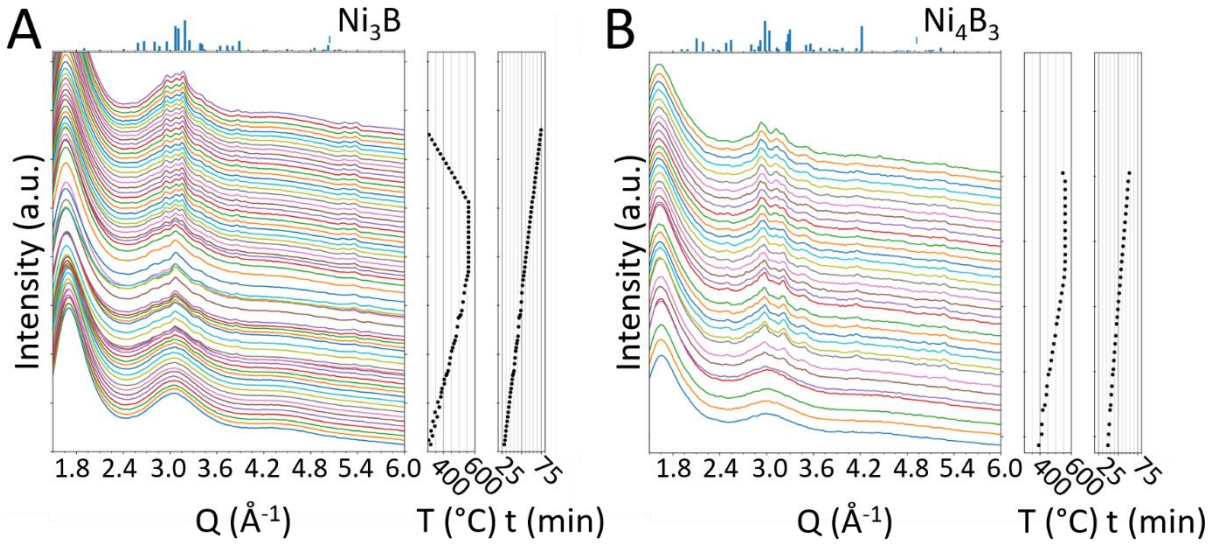

Figure S2-IV. *In situ* powder X-ray diagrams in total X-ray scattering configuration for (A) Ni_3B and (B) Ni_4B_3 mixtures.

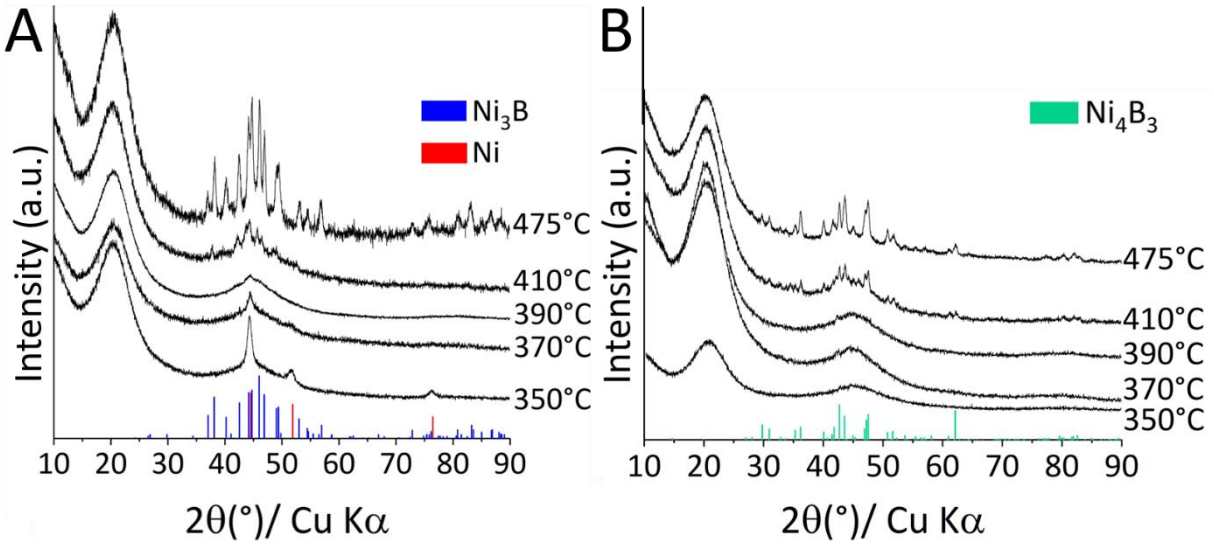

Figure S2-V. *Ex situ* powder XRD patterns of samples retrieved at different temperatures for 1.5 h plateaus from the (A) Ni_3B and (B) Ni_4B_3 reaction mixtures.

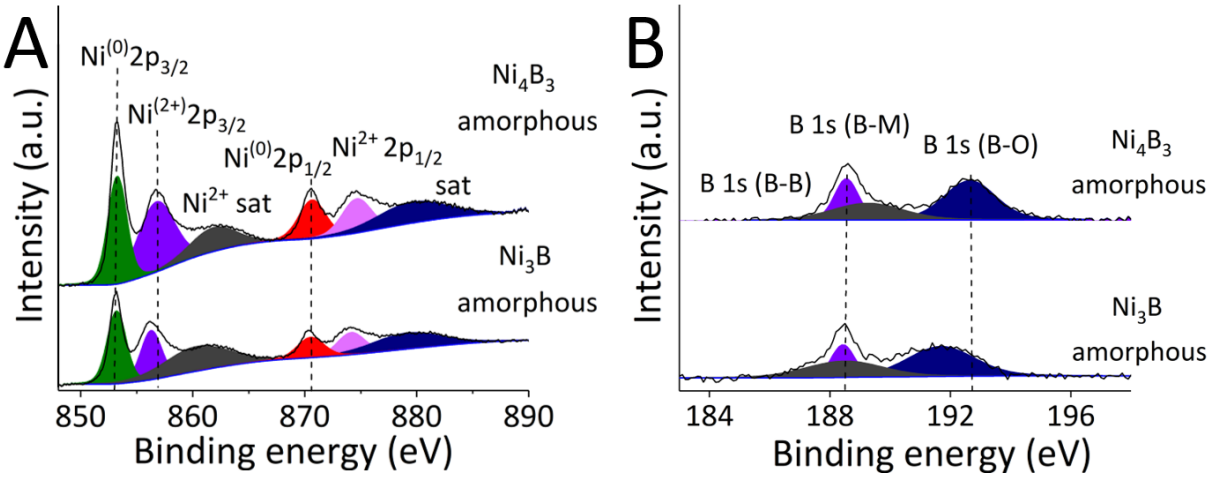

Figure S2-VI. XPS of amorphous Ni_3B and Ni_4B_3 nanoparticles: (A) Ni 2p region, (B) B 1s region.

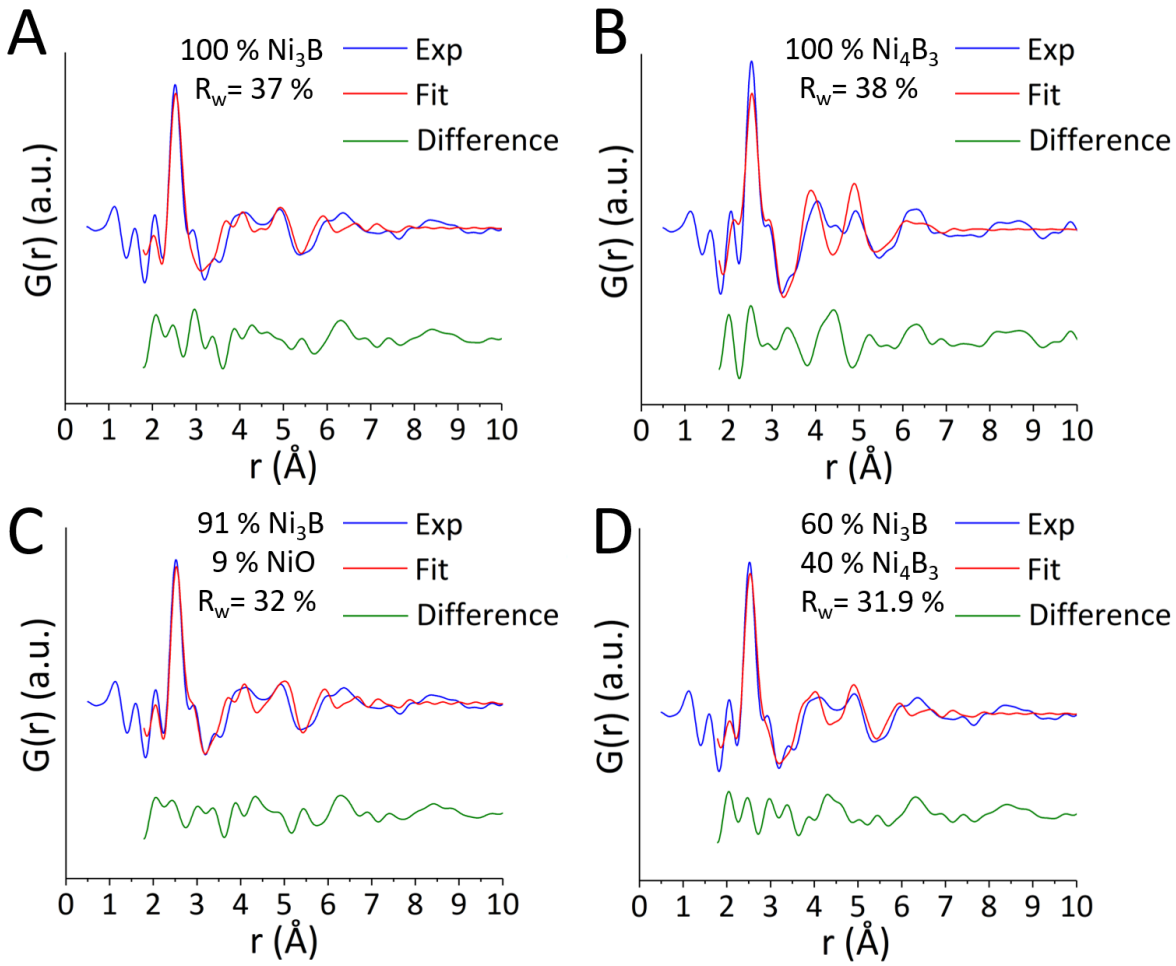

Figure S2-VII. PDFs of the amorphous intermediate to (A) Ni_3B fitted along the crystalline structure of Ni_3B, (B) Ni_4B_3 fitted along the crystalline structure Ni_4B_3. PDF of the amorphous intermediate to Ni_3B fitted along the crystalline structure of (C) Ni_3B mixed with NiO, (D) Ni_3B mixed with Ni_4B_3.

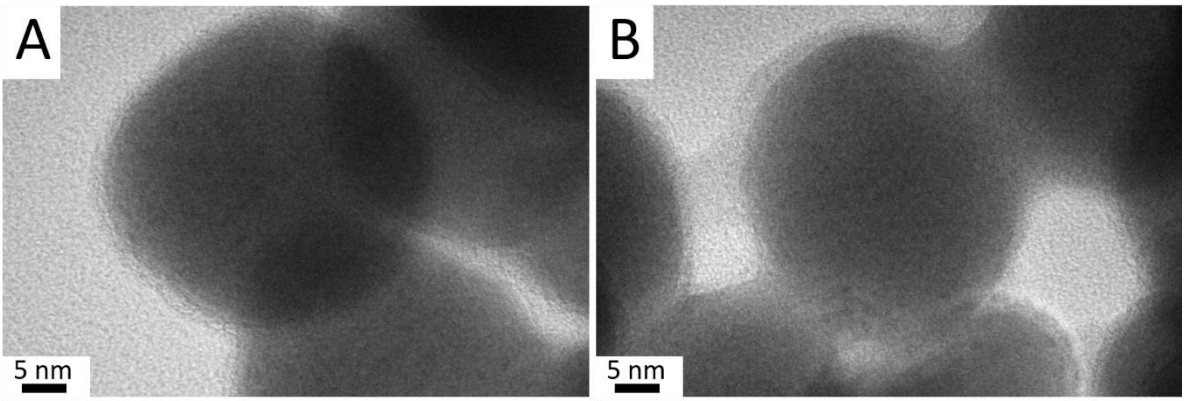

Figure S2-VIII. HRTEM images of Ni_3B nanoparticles obtained by synthesis at 475 °C for 1.5 h: of (A) single amorphous nanoparticle, (B) coalesced amorphous nanoparticles.

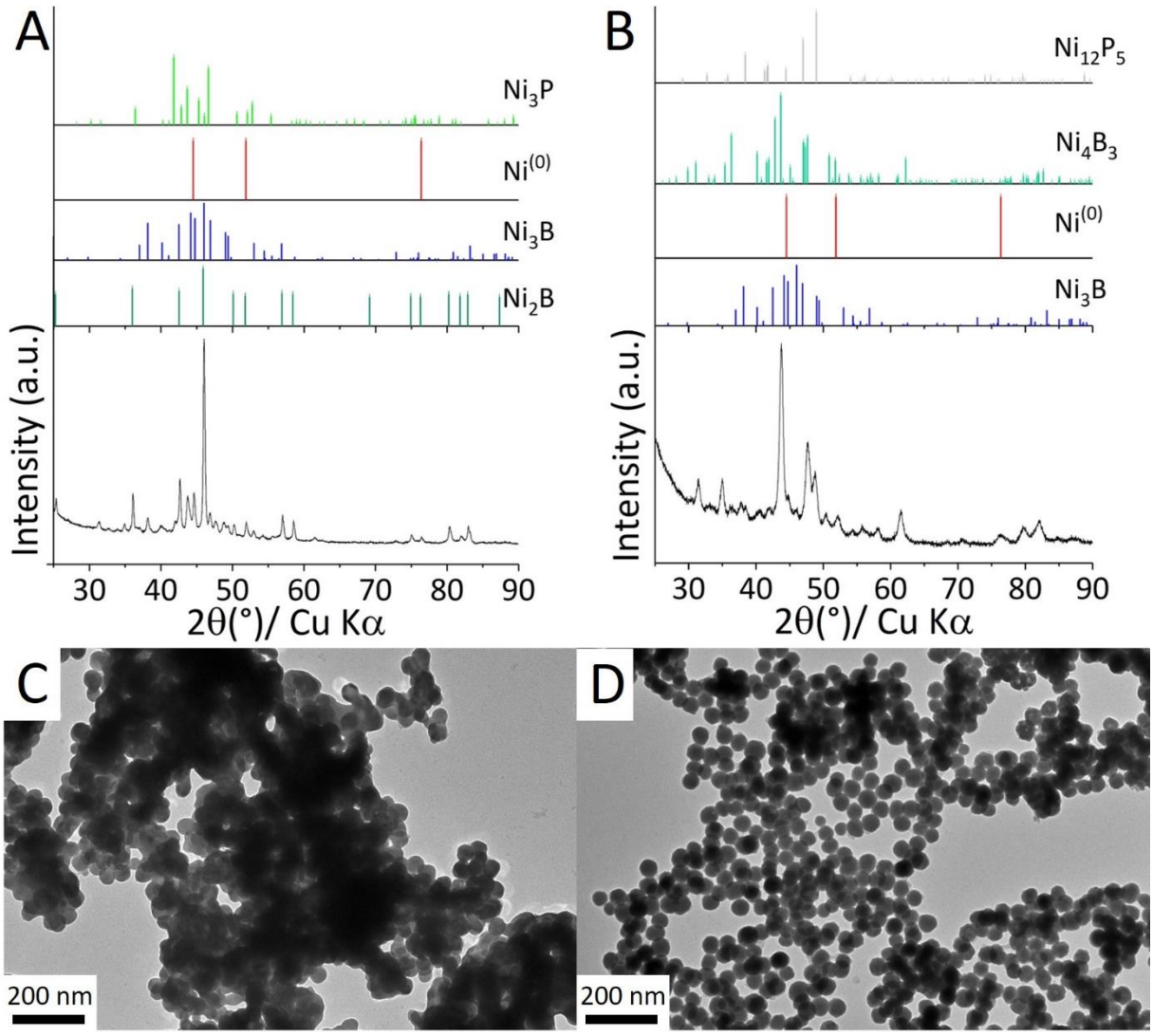

Figure S2-IX. Syntheses of borides nanoparticles without molten salts. XRD pattern and corresponding TEM images of (A, C) Ni_3B mixture, (B, D) Ni_4B_3 mixture.

Impact of modulation of the key parameters on the reactivity

In order to assess the reactivity between nickel nanoparticles and $NaBH_4$ in molten salts, we have investigated three kinds of modifications of the synthetic method. Firstly, we discuss the need for an excess in $NaBH_4$, as the shell of amorphous boron demonstrates that this excess is not incorporated into the nickel nanoparticles. Secondly, as just discussed, the state of aggregation influences the reactivity. Therefore, the role of the impregnation step in maintaining a dispersion of the nanoparticles needs to be investigated. Finally, we address the role of molten salts as a high temperature liquid state medium to enhance the diffusion of boron.

In complement, Camille Chan Chang described in her PhD thesis manuscript[29] other modification of several key parameters. Thus, preliminary studies through of a large screening of the stoichiometries B:Ni, the target temperature range, the nature of the eutectic salt mixture

(LiI:KI (58:42 mass.) or LiCl:KCl (44:56 mass.)) and the size of the initial nickel nanoparticles served as a basis for this study.

a) The need of boron excess

The incorporation of boron is a non-stoichiometric reaction as an excess of boron is required to reach the pure phase. In the case of Ni_3B, instead of Ni:B = 2.3, we considered a ratio Ni:B = 2.6 corresponding to 24.8 mg of $NaBH_4$ (instead of 27 mg for 100 mg of nickel). This tiny modification, despite maintaining an excess to the stoichiometry, induces the incomplete conversion into boride according to the remaining diffraction peaks of nickel (**Figure S2-X**).

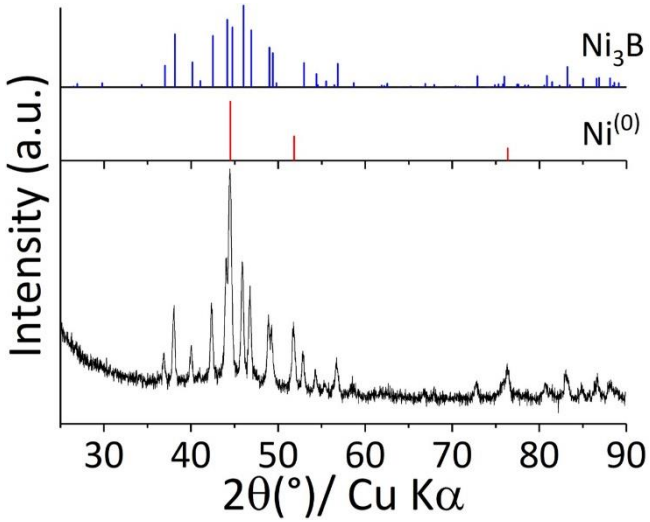

Figure S2-X. Powder XRD pattern of the sample obtained for B: Ni of 2.6 at 475 °C/ 1.5 h in LiI-KI (58:42 mass.).

b) The impregnation step

The impregnation step is performed to enhance the dispersion state and the homogeneity of the reaction. During this step, the nickel particles impregnate the salt grains to prevent their interaction during the evaporation of the solvent. A synthesis carried out without impregnation shows that boron incorporation is maintained (**Figure S2-XIA**), but particle coalescence is more important (**Figure S2-XIB**). In addition, without impregnation inhomogeneous reactivity could lead to an incomplete reaction or a mixture of boride phases.

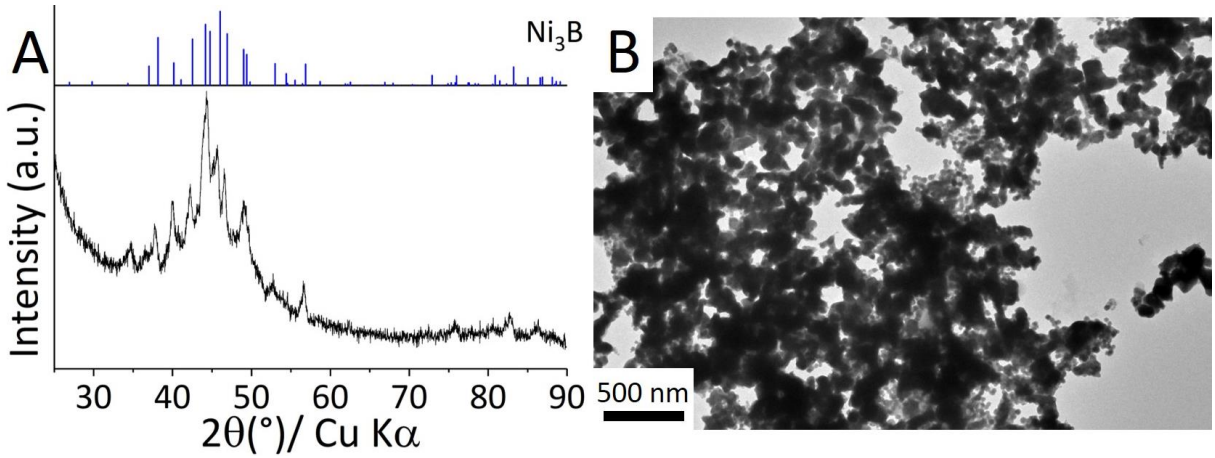

Figure S2-XI. (A) Powder XRD pattern (A) and (B) TEM image of Ni_3B nanoparticles synthetized without impregnation using a hexane dispersion of nickel nanoparticles.

References

(1) Carenco, S.; Portehault, D.; Boissière, C.; Mézailles, N.; Sanchez, C. Nanoscaled Metal Borides and Phosphides: Recent Developments and Perspectives. *Chem. Rev.* **2013**, *113* (10), 7981–8065. https://doi.org/10.1021/cr400020d.

(2) Chen, H.; Zou, X. Intermetallic Borides: Structures, Synthesis and Applications in Electrocatalysis. *Inorg. Chem. Front.* **2020**, *7* (11), 2248–2264. https://doi.org/10.1039/d0qi00146e.

(3) Hong, J.; Mutalik, S.; Miola, M.; Gerlach, D.; Mehrabi K, R.; Ahmadi, M.; Kooi, B. J.; Portale, G.; Rudolf, P.; Pescarmona, P. P.; Protesescu, L. Nickel Boride (NixB) Nanocrystals: From Solid-State Synthesis to Highly Colloidally Stable Inks. *Chem. Mater.* **2023**, *35* (4), 1710–1722. https://doi.org/10.1021/acs.chemmater.2c03478.

(4) Albert, B.; Hillebrecht, H. Boron: Elementary Challenge for Experimenters and Theoreticians. *Angew. Chemie - Int. Ed.* **2009**, *48* (46), 8640–8668. https://doi.org/10.1002/anie.200903246.

(5) Liu, X.; Fechler, N.; Antonietti, M. Salt Melt Synthesis of Ceramics, Semiconductors and Carbon Nanostructures. *Chem. Soc. Rev.* **2013**, *42* (21), 8237–8265. https://doi.org/10.1039/c3cs60159e.

(6) Failamani, F.; Podloucky, R.; Bursik, J.; Rogl, G.; Michor, H.; Müller, H.; Bauer, E.; Giester, G.; Rogl, P. Boron-Phil and Boron-Phob Structure Units in Novel Borides Ni3Zn2B and Ni2ZnB: Experiment and First Principles Calculations. *Dalt. Trans.* **2018**, *47* (10), 3303–3320. https://doi.org/10.1039/c7dt04769j.

(7) Sussardi, A.; Tanaka, T.; Khan, A. U.; Schlapbach, L.; Mori, T. Enhanced Thermoelectric Properties of Samarium Boride. *J. Mater.* **2015**, *1* (3), 196–204. https://doi.org/10.1016/j.jmat.2015.07.007.

(8) Gouget, G.; Bregiroux, D.; Grosjean, R.; Montero, D.; Maier, S.; Gascoin, F.; Sanchez, C.; Portehault, D. Liquid-Phase Synthesis, Sintering, and Transport Properties of Nanoparticle-Based Boron-Rich Composites. *Chem. Mater.* **2021**, *33* (6), 2099–2109. https://doi.org/10.1021/acs.chemmater.0c04762.

(9) Sun, H.; Meng, J.; Jiao, L.; Cheng, F.; Chen, J. A Review of Transition-Metal Boride/Phosphide-Based Materials for Catalytic Hydrogen Generation from Hydrolysis

of Boron-Hydrides. *Inorg. Chem. Front.* **2018**, *5* (4), 760–772. https://doi.org/10.1039/c8qi00044a.

(10) Paksoy, A.; Kurtoğlu-Öztulum, S. F.; Yağcı, M. B.; Balcı-Çağıran, Ö. Low-Cost and Reusable Iron- and Nickel-Based Metal Boride Nanoparticles for Efficient Catalytic Hydrolysis of Sodium Borohydride. *Int. J. Hydrogen Energy* **2022**. https://doi.org/10.1016/j.ijhydene.2022.08.269.

(11) Fu, Y.; Richardson, P.; Li, K.; Yu, H.; Yu, B.; Donne, S.; Kisi, E.; Ma, T. Transition Metal Aluminum Boride as a New Candidate for Ambient-Condition Electrochemical Ammonia Synthesis. *Nano-Micro Lett.* **2020**, *12* (1), 1–13. https://doi.org/10.1007/s40820-020-0400-z.

(12) Gupta, S.; Patel, M. K.; Miotello, A.; Patel, N. Metal Boride-Based Catalysts for Electrochemical Water-Splitting: A Review. *Adv. Funct. Mater.* **2020**, *30* (1). https://doi.org/10.1002/adfm.201906481.

(13) Akopov, G.; Yeung, M. T.; Kaner, R. B. Rediscovering the Crystal Chemistry of Borides. *Adv. Mater.* **2017**, *29* (21). https://doi.org/10.1002/adma.201604506.

(14) Masa, J.; Sinev, I.; Mistry, H.; Ventosa, E.; de la Mata, M.; Arbiol, J.; Muhler, M.; Roldan Cuenya, B.; Schuhmann, W. Ultrathin High Surface Area Nickel Boride (NixB) Nanosheets as Highly Efficient Electrocatalyst for Oxygen Evolution. *Adv. Energy Mater.* **2017**, *7* (17), 1–8. https://doi.org/10.1002/aenm.201700381.

(15) Lee, E.; Fokwa, B. P. T. Nonprecious Metal Borides: Emerging Electrocatalysts for Hydrogen Production. *Acc. Chem. Res.* **2022**, *55* (1), 56–64. https://doi.org/10.1021/acs.accounts.1c00543.

(16) Dinh, K. N.; Liang, Q.; Du, C. F.; Zhao, J.; Tok, A. I. Y.; Mao, H.; Yan, Q. Nanostructured Metallic Transition Metal Carbides, Nitrides, Phosphides, and Borides for Energy Storage and Conversion. *Nano Today.* **2019**, *25*, 99–121. https://doi.org/10.1016/j.nantod.2019.02.008.

(17) Jothi, P. R.; Yubuta, K.; Fokwa, B. P. T. A Simple, General Synthetic Route toward Nanoscale Transition Metal Borides. *Adv. Mater.* **2018**, *30* (14), 2–7. https://doi.org/10.1002/adma.201704181.

(18) Kang, Y.; Tang, Y.; Zhu, L.; Jiang, B.; Xu, X.; Guselnikova, O.; Li, H.; Asahi, T.;

Yamauchi, Y. Porous Nanoarchitectures of Nonprecious Metal Borides: From Controlled Synthesis to Heterogeneous Catalyst Applications. *ACS Catal.* **2022**, 14773–14793. https://doi.org/10.1021/acscatal.2c03480.

(19) Li, C. H.; Nanba, Y.; Asakura, D.; Okubo, M.; Talham, D. R. Li-Ion and Na-Ion Insertion into Size-Controlled Nickel Hexacyanoferrate Nanoparticles. *RSC Adv.* **2014**, *4* (48), 24955–24961. https://doi.org/10.1039/c4ra03296a.

(20) Wang, J. W.; Liu, X. H.; Mao, S. X.; Huang, J. Y. Microstructural Evolution of Tin Nanoparticles during in Situ Sodium Insertion and Extraction. *Nano Lett.* **2012**, *12* (11), 5897–5902. https://doi.org/10.1021/nl303305c.

(21) Gibot, P.; Casas-Cabanas, M.; Laffont, L.; Levasseur, S.; Carlach, P.; Hamelet, S.; Tarascon, J.-M.; Masquelier, C. Room-Temperature Single-Phase Li Insertion/Extraction in Nanoscale LixFePO4. *Nat. Mater.* **2008**, *7* (9), 741–747. https://doi.org/10.1038/nmat2245.

(22) Yin, Y.; Rioux, R. M.; Erdonmez, C. K.; Hughes, S.; Somorjal, G. A.; Alivisatos, A. P. Formation of Hollow Nanocrystals Through the Nanoscale Kirkendall Effect. *Science.* **2004**, *304* (5671), 711–714. https://doi.org/10.1126/science.1096566.

(23) Cabot, A.; Puntes, V. F.; Shevchenko, E.; Yin, Y.; Balcells, L.; Marcus, M. A.; Hughes, S. M.; Alivisatos, A. P. Vacancy Coalescence during Oxidation of Iron Nanoparticles. *J. Am. Chem. Soc.* **2007**, *129* (34), 10358–10360. https://doi.org/10.1021/ja072574a.

(24) Ha, D. H.; Moreau, L. M.; Honrao, S.; Hennig, R. G.; Robinson, R. D. The Oxidation of Cobalt Nanoparticles into Kirkendall-Hollowed CoO and Co3O4: The Diffusion Mechanisms and Atomic Structural Transformations. *J. Phys. Chem. C.* **2013**, *117* (27), 14303–14312. https://doi.org/10.1021/jp402939e.

(25) Chen, J.; Jiang, F.; Yin, Y. Manipulation of Interfacial Diffusion for Controlling Nanoscale Transformation. *Acc. Chem. Res.* **2021**, *54* (5), 1168–1177. https://doi.org/10.1021/acs.accounts.0c00743.

(26) Meffre, A.; Mehdaoui, B.; Kelsen, V.; Fazzini, P. F.; Carrey, J.; Lachaize, S.; Respaud, M.; Chaudret, B. A Simple Chemical Route toward Monodisperse Iron Carbide Nanoparticles Displaying Tunable Magnetic and Unprecedented Hyperthermia Properties. *Nano Lett.* **2012**, *12* (9), 4722–4728. https://doi.org/10.1021/nl302160d.

(27) Anderson, B. D.; Tracy, J. B. Nanoparticle Conversion Chemistry: Kirkendall Effect, Galvanic Exchange, and Anion Exchange. *Nanoscale.* **2014**, *6* (21), 12195–12216. https://doi.org/10.1039/c4nr02025a.

(28) Carenco, S.; Liu, Z.; Salmeron, M. The Birth of Nickel Phosphide Catalysts: Monitoring Phosphorus Insertion into Nickel. *ChemCatChem.* **2017**, *9* (12), 2318–2323. https://doi.org/10.1002/cctc.201601526.

(29) Chan Chang, T.-H.-C. Elaboration de Borures et Phosphures Métalliques : Synthèse de Nanomatériaux En Sels Fondus et Réactivité de Surface. **2017**.

(30) Carenco, S.; Boissière, C.; Nicole, L.; Sanchez, C.; Le Floch, P.; Mézailles, N. Controlled Design of Size-Tunable Monodisperse Nickel Nanoparticles. *Chem. Mater.* **2010**, *22* (4), 1340–1349. https://doi.org/10.1021/cm902007g.

(31) Martelli, P.; Caputo, R.; Remhof, A.; Mauron, P.; Borgschulte, A.; Z̈ttel, A. Stability and Decomposition of NaBH4. *J. Phys. Chem. C* **2010**, *114* (15), 7173–7177. https://doi.org/10.1021/jp909341z.

(32) Portehault, D.; Delacroix, S.; Gouget, G.; Grosjean, R.; Chan-Chang, T. H. C. Beyond the Compositional Threshold of Nanoparticle-Based Materials. *Acc. Chem. Res.* **2018**, *51* (4), 930–939. https://doi.org/10.1021/acs.accounts.7b00429.

(33) Rundqvist, S.; Hauge, S.; Fex, H.; Högberg, B.; Kneip, P.; Palmstierna, H. An X-Ray Investigation of the Nickel-Boron System. The Crystal Structures of Orthorhombic and Monoclinic Ni4B3. *Acta Chemica Scandinavica*. **1959**, pp 1193–1208. https://doi.org/10.3891/acta.chem.scand.13-1193.

(34) Wang, K.; Du, D.; Chang, B.; Hong, Y.; Ju, J.; Sun, S.; Fu, H. Mechanical Properties, Electronic Structures, and Debye Temperature of Ni x B y Compounds Obtained by the First Principles Calculations. *Crystals* **2018**, *8* (12). https://doi.org/10.3390/cryst8120451.

(35) Ma, F.; Wang, S.; Liang, X.; Wang, C.; Tong, F.; Wang, Z.; Wang, P.; Liu, Y.; Dai, Y.; Zheng, Z.; Huang, B. Ni3B as a Highly Efficient and Selective Catalyst for the Electrosynthesis of Hydrogen Peroxide. *Appl. Catal. B Environ.* **2020**, *279* (July). https://doi.org/10.1016/j.apcatb.2020.119371.

(36) Zhou, Y.; Ye, Q.; Shi, X.; Zhang, Q.; Song, Q.; Zhou, C.; Li, D.; Jiang, D. Ni3B as P-

Block Element-Modulated Cocatalyst for Efficient Photocatalytic CO2Reduction. *Inorg. Chem.* **2022**, *61* (43), 17268–17277. https://doi.org/10.1021/acs.inorgchem.2c02850.

(37) Legrand, J.; Taleb, A.; Gota, S.; Guittet, M. J.; Petit, C. Synthesis and XPS Characterization of Nickel Boride Nanoparticles. *Langmuir.* **2002**, *18* (10), 4131–4137. https://doi.org/10.1021/la0117247.

(38) Cardew, P. T. Ostwald Rule of Stages─Myth or Reality? *Cryst. Growth Des.* **2022**. https://doi.org/10.1021/acs.cgd.2c00141.

(39) Bates, S.; Zografi, G.; Engers, D.; Morris, K.; Crowley, K.; Newman, A. Analysis of Amorphous and Nanocrystalline Solids from Their X-Ray Diffraction Patterns. *Pharm. Res.* **2006**, *23* (10), 2333–2349. https://doi.org/10.1007/s11095-006-9086-2.

Chapter 3: Nickel borides as water splitting electrocatalysts

I) Introduction: borides as electrocatalysts for water splitting

a) The water splitting process

Dihydrogen is mainly used for the Haber Bosch process of ammonia synthesis[1,2] and for hydrocracking reactions of petroleum and complex organic molecules[1,3]. A new growing interest in dihydrogen production is correlated to the need to develop efficient energy carriers to address global warming. While numerous fields as transportation, industry or construction require the substitution of fossil fuels, dihydrogen appears among the most promising candidates as energy carrier[4,5,6]. Indeed, H_2 exhibits high calorific value, thermal conductivity, energy density, natural abundance resources. It does not reject harmful products when burnt[7]. Notwithstanding the ecological aspects of dihydrogen development, the main way to synthetize dihydrogen is based on fossil fuels, by hydrocarbon reforming[8]. As a consequence, its use is only marginally beneficial and does not provide strong environmental advantages compared to fossil fuels. Therefore, besides optimizing the processes that use dihydrogen, intensive efforts are required to provide a sustainable way of H_2 production.

The water splitting process is one of the possible solutions, which requires only water and electricity to provide high purity H_2. Commercial electrolyzers show efficiencies of 56-73 %[8,9,10,11]. The process is described by two half-reactions within an electrochemical cell (**Figure 1**). The Oxygen Evolution Reaction (OER) takes place on the anodic side while the Hydrogen Evolution Reaction (HER) occurs on the cathodic side. The corresponding reactions depend on the pH of the medium (Equation 1-6)[9,11]. Equations (1) and (2) occur in acidic media; (3) and (4) in neutral media, (5) and (6) in basic electrolyte.

<u>In acidic medium:</u>

Cathode: $4H^+ + 4e^- \rightarrow 2H_2$ (1) Anode: $2H_2O \rightarrow O_2 + 4H^+ + 4e^-$ (2)

<u>In neutral medium:</u>

Cathode: $4H_2O + 4e^- \rightarrow 2H_2 + 4OH^-$ (3) Anode: $2H_2O \rightarrow O_2 + 4H^+ + 4e^-$ (4)

<u>In basic medium:</u>

Cathode: $4H_2O + 4e^- \rightarrow 2H_2 + 4OH^-$ (5) Anode: $4HO^- \rightarrow O_2 + 2H_2O + 4e^-$ (6)

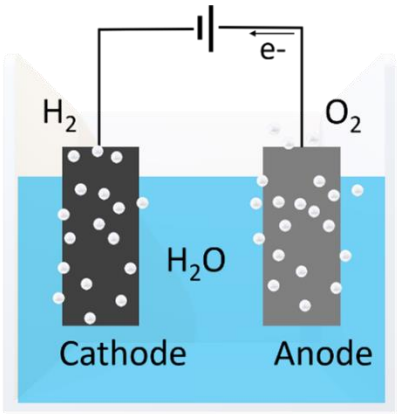

Figure 1: Scheme of an electrochemical water splitting cell.

While the HER reaction can theoretically occur from 0 V/RHE, the OER reaction requires a theoretical voltage of 1.23 V/RHE. This value corresponds to the free energy (ΔG) of the water splitting reaction, 237.2 kJ.mol^{-1} at 25 °C at 1 atm. The HER requires the transfer of two electrons per proton or water molecule for the formation of H_2, while the OER is a four-electron process. Therefore, these reactions, especially OER, suffer from slow kinetics, hence large overpotentials, and then require catalysts[4,7,10,12]. The benchmarks electrocatalysts for HER and OER are based on platinum and iridium/ ruthenium oxides, respectively[11–13]. The scarcity of these materials render them inadequate for large scale applications.

b) HER/OER mechanism

To go further in detail, it is instructive to question the mechanisms of HER and OER.

The water Pourbaix diagram shows that HER is favored in acidic medium. In such conditions, the first step, called the Volmer reaction, is the formation of adsorbed hydrogen intermediate (H_{ads}) on the cathode:

$$H^+ + e^- \rightarrow H_{ads} \qquad (7)$$

Then, the second step of desorption of H_2 can occur along two routes, depending of the coverage of H_{ads}. The Heyrovsky reaction (8) corresponds to an electrochemical desorption of H_2, while the Tafel reaction (9) is a chemical H_2 desorption[9,12]:

$$H^+ + H_{ads} + e^- \rightarrow H_2 \qquad (8)$$

$$H_{ads} + H_{ads} \rightarrow H_2 \quad (9)$$

In an alkaline environment, the HER occurs first by adsorption through the Volmer step (7):

$$H_2O + e^- \rightarrow H_{ads} + OH^- \quad (10)$$

H_2 formation and desorption then follows two possible routes[14,15]. The first one is the Tafel step:

$$H_{ads} + H_{ads} \rightarrow H_2 \quad (11)$$

The second path is the Heyrovsky step:

$$H_2O + e^- + H_{ads} \rightarrow H_2 + OH^- \quad (12)$$

For OER, different mechanisms have been proposed, depending on the medium and the catalyst nature. They involve reaction intermediates such as M-O, M-OH and M-OOH (with M as the metal). The formation of some of these intermediates corresponds to the rate-limiting step. The overall potential to trigger OER is the result of these reactions[9,12,16]. Thermodynamically, the water Pourbaix diagram shows that the OER process is favored in alkaline medium, following equation (6). In these conditions, OER is described by the following reactions[16,17]:

$$M + 4OH^- \rightarrow MOH + 3OH^- + e^- \quad (13)$$

$$MOH + 3OH^- \rightarrow MO + 2OH^- + H_2O_{(l)} + e^- \quad (14)$$

$$MO + 2OH^- + H_2O \rightarrow MOOH + OH^- + H_2O + e^- \quad (15)$$

$$MOOH + OH^- + H_2O \rightarrow M + O_{2(g)} + 2H_2O_{(l)} + e^- \quad (16)$$

The catalytic activity is linked to the Sabatier principle: a catalyst having moderate binding strength towards the intermediates involved in the rate-limiting steps is desirable[9,16]. Different transition metal-based catalysts are reported to compete with platinum-group metals currently used for each half or overall water splitting reactions[11]. Among them, transition metal-based borides focus attention to provide stable and highly active electrocatalysts.

c) The role of boron to enhance the catalytic activity

Some publications and reviews have recently focused on transition metal boride materials as emerging candidates for water splitting [7,9,11,12,16,18,19]. Indeed, compared to other materials such as sulfides, nitrides, selenides, carbides or phosphides also studied for the same application[7,9,18,19], studies on boride materials for water splitting have started more recently [9,12].

Borides present generally ambivalent activities for HER and OER, including high performances and long-term stability[12]. In general, most catalysts are reported at the nanoscale in order to increase the surface-to-volume ratio, hence the number of actives sites per mass unit of catalyst. Thus, the development of synthesis methods towards nanoscaled borides is one of the main targets for water splitting[11,19]. For HER, the role of boron in electrocatalysis has been investigated by density functional theory (DFT) calculations with the case study of the molybdenum boride α-MoB_2 compared to surface layer (110) of elemental Mo and (111) of the benchmark Pt [19]. The Gibbs free energy (ΔG_H) of H adsorption was close to the optimal zero value for B-containing surfaces of the boride, particularly those presenting a graphene-like boron layer like the (001) facets of α-MoB_2, which then behave similarly to the benchmark platinum (111) surface. This value corresponds to the maximum rate of H adsorption and H_2 desorption as described by the Sabatier principle. Such an observation highlights the role of boron in borides to provide the catalytic sites.

It is also clear that the reverse electron transfer mechanism between boron and the metal plays a role in the enhancement of the activity and stability[9]. As seen in Chapter 1, although electron transfer from metal to boron occurs in accordance to the electronegativity scale, partial electron density is given back in the *d* band of the metal, thus significantly downshifting the *d*-band center of the metal compared to the pure metal. This enrichment protects the metal against oxidation, enhances its stability and facilitates the HER[9,19,20].

For OER, the electrocatalytic activity is related to the *in situ* formation at the boride surface of metal oxides/(oxy)hydroxides species that catalyze the reaction[9,12]. Boron atoms or borates in these conditions play a key role to distort the native geometry, thus facilitating the adsorption and the oxidation of water molecules and hydroxyl groups[9,16].

Nickel borides, as other transition metal borides, have been reported to provide stable and highly active ambivalent electrocatalysts for OER and HER[7,9–11,14,18,19,21,22]. While synthesis difficulties limit the active site exposure due to a lack of morphology and size control[11], dispersed nanoparticles could deeply increase the active site densities resulting in high surface area. Achieving crystalline nanomaterials that avoid strong coalescence induced by thermal treatment could then be highly profitable to enhance the electrocatalytic activities. Herein, the well size-controlled nickel boride nanocrystals developed in Chapter 2 are investigated to provide highly active electrocatalyst for overall water splitting.

II) Nickel boride as ambivalent catalyst for overall water splitting reactions

We have investigated the electrocatalytic properties of amorphous and crystalline Ni_3B and Ni_4B_3 nanoparticles for HER in an argon saturated 0.5 M H_2SO_4 electrolyte. For OER, an O_2-saturated 0.1 M KOH electrolyte was used, previously purified from any iron species that could act as an active dopant[23]. Rotating glassy carbon disk electrodes were used as supports, except for chronoamperometry measurements performed on carbon paper substrates (MGL370, Fuelcell store). An ink composed by the nanocatalyst, carbon black, and Nafion® was drop-casted on the carbon electrode to reach a mass loading of 0.25 mg cm^{-2}. The measurements were reproduced at least two times to ensure the reproducibility of the measured activity. **Figure 2** presents the electrocatalytic properties of Ni_3B and Ni_4B_3 crystalline phases and their respective amorphous intermediates during HER (**Figure 2A-C**) and OER (**Figure 2D-E)**.

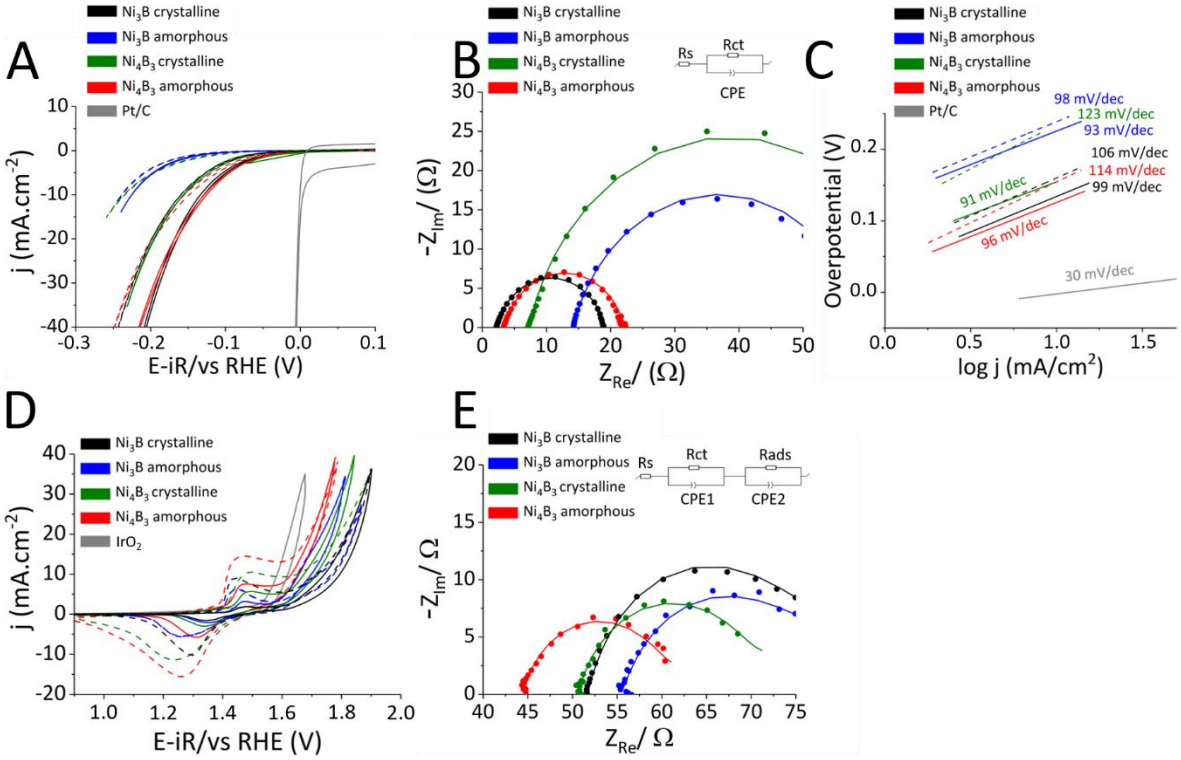

Figure 2. Electrochemical properties of Ni_3B and Ni_4B_3 nanocrystals and of their corresponding amorphous nanoparticle intermediates. HER study in aqueous Ar saturated 0.5 M H_2SO_4 electrolyte: (a) CV curves at the 1st cycle (continuous lines) and 30th cycle (dashed lines), (b) Nyquist plot (dots) and fitting curve (continuous line) recorded at -0.23 V vs RHE after activation by 30 cyclic voltammograms, (C) Tafel slopes before (continuous lines) and after (dashed line) activation. OER study in aqueous O_2-saturated 0.1 M KOH Fe purified electrolyte: (D) CV curves at the 1st cycle (continuous lines) and 30th cycle (dashed lines), (E) Nyquist plot

(dots) and fitting curve (continuous line) recorded at 2.26 V vs RHE. Insets in (B and E) indicate the equivalent circuits used for fitting the EIS data.

Under HER conditions and after stabilization of the electrochemical response through 30 electrochemical cycles (**Figure S3-IA**), cyclic voltammograms (CVs) indicate that the highest activity after 30 cycles is obtained for the Ni_4B_3 amorphous intermediate (0.148 V vs RHE at -10 mA cm^{-2}) and crystalline Ni_3B (0.160 V vs RHE at -10 mA cm^{-2}); followed by crystalline Ni_4B_3 and finally Ni_3B amorphous which exhibit the highest overpotential (**Table S3-I**). Chronopotentiometry measurements performed at -10 mA cm^{-2} on a 1 cm^2 carbon paper electrode (**Figure S3-IIA**) for 8 h, with conservation of the mass loading normalized to the geometrical surface of the substrate, show a different activity ranking with crystalline Ni_4B_3 and Ni_3B as the most active electrocatalysts, while the activity of the amorphous intermediates of Ni_3B and Ni_4B_3 are inferior and overlap from 2 h. A lower stability of the amorphous phases in the HER conditions would explain the degradation of the activity.

Electrochemical impedance spectroscopy (EIS) was used to evaluate charge transfer resistances (R_{ct}) within the material at an electrochemical potential where HER occurs. The values were obtained by fitting the experimental impedance with an equivalent circuit currently used to extract R_{ct} values (**Figure 2B** inset)[24,25]. The lowest R_{ct} values (**Figure 2B**) are measured for amorphous Ni_4B_3 (18.9 Ω) and crystalline Ni_3B (17.0 Ω), which is correlated with their higher HER activity after stabilization of the electrochemical response (**Figure 2A, Figure S3-IA**). Hence, the most active electrocatalysts in HER are the most conductive ones. The Tafel slopes (**Figure 2C**), used to evaluate the HER catalytic reaction kinetics show similar results for all borides studied, with values of about 90 mV dec^{-1} for the first cycle, while the slopes increase to about 100 mV dec^{-1} after 30 cycles, which is in agreement with previously reported values for boride electrocatalysts[9,11]. The rate-determining step (RDS) may be determined by the Tafel slope: the Volmer, Heyrovsky and Tafel steps as RDS yield Tafel slopes of 120, 30 and 40 mV dec^{-1}, respectively[26,27]. These theoretical values however assume extreme H_{ads} coverage, while actual values depend on the surface coverage[28], which explains the discrepancy between theoretical and experimental values. Nonetheless, after 30 cycles of activation, the slope values suggest that the Volmer reaction may be limiting. A comparison of HER electrocatalytic activity in a similar electrolyte for selected borides, carbides and phosphides is presented in **Figure S3-IIIA-B**. The materials discussed herein, especially Ni_3B nanocrystals and

amorphous Ni_4B_3 nanoparticles appear particularly active similarly to state-of-the-art materials exempt of platinum-group metals (PGMs).

To enable a more in depth comparison of the materials, the electrochemically active surface areas (*ECSA*) were determined by measuring the double layer capacitance C_{DL} (**Figure S3-IV, Table S3-II**) and dividing the C_{DL} values by the specific capacitance C_s, assumed at a value of 40 µF cm^{-2}, most commonly used for transition-metal-based electrocatalysts[29,30]. *ECSA* estimations vary from 3.6 cm^2 to 9.8 cm^2 for HER, which indicate relatively similar values, in agreement with close size distributions. The electrocatalytic activities have then been normalized by the *ECSA* values[29,31] (**Figure S3-IIC**). The ranking of activity between the catalysts studied herein is unchanged (**Figure 2A** and **Figure S3-III**).

Interestingly, the difference in activity for HER observed for the amorphous intermediates and their crystalline counterpart cannot be related to a difference in the number of nickel active sites. Indeed, the morphology of the particles is similar between the samples, hence the number of active sites is fixed by the nickel nanoparticles used as reagent. The large R_{ct} value for amorphous Ni_3B indicates that it is probably less stable that crystalline Ni_3B and oxidizes in contact with an aqueous electrolyte, which may explain its poor activity. On the contrary, amorphous Ni_4B_3 shows a low R_{ct}, which suggest higher stability than amorphous Ni_3B, in agreement with the higher B content. The fact that amorphous Ni_4B_3 is more active than crystalline Ni_4B_3 is again related to lower R_{ct}, and may originate from remaining Ni species into the boron-rich shell at the surface of the particles. Crystallization of Ni_4B_3 indeed is accompanied by segregation of Ni_4B_3 and an amorphous boron-rich shell (see chapter 2), which is insulating and then hinders electrocatalysis.

Reversely, under OER conditions (**Figure 2D**), the highest activity after activation is observed for the Ni_4B_3 amorphous intermediate (0.400 V vs RHE at 10 mA cm^{-2}) followed by Ni_4B_3 crystalline (0.421 V vs RHE at 10 mA cm^{-2}), Ni_3B crystalline and Ni_3B amorphous (**Table S3-I**). A reversible anodic wave observed from the first cycle for all samples at *ca.* 1.5 V, corresponding to the Ni^{3+}/Ni^{2+} redox couple, indicating that the material was already partially oxidized to Ni^{2+} species at the open circuit voltage (OCV)[22]. An increase of the redox wave area is observed upon cycling, which correlates with a slight increase of the current density during the first cycles. This suggests that oxidized nickel species engaged in the anodic wave are active surface sites, as previously reported[9,20,22], and that their quantity is increased during the first ~30 cycles. CP measurements were performed on impregnated carbon papers similarly to HER measurements, but at a current density of 10 mA cm^{-2} (**Figure S3-IIB**). The stability of

the overall catalyst is confirmed for 8 h. The noisy curves are attributed to oxygen bubbles temporary stuck on the surface or in the porosity of the electrode.

EIS measurements were performed to investigate the charge transfer resistance (**Figure 2E**). The R_{ct} values (**Table S3-I**) were determined by fitting the experimental Nyquist plot with an equivalent circuit currently used for alkaline OER electrocatalysis[11]. The R_{ct} values follow well the order of activity, ranging from 11.2 Ω for amorphous Ni_4B_3 to 20.5 Ω for amorphous Ni_3B while the R_{ct} of crystalline Ni_3B and crystalline Ni_4B_3 are close, respectively 19.1 and 19.6 Ω. Tafel slopes were not determined due to the overlap of the anodic wave and the OER process, rendering the determination of each contribution challenging.

A comparison of the measured catalytic properties with selected references in 0.1 M KOH (**Figure S3-IIIC-D**) reveals similar OER performances compared to state-of-the-art boride, phosphide and carbides materials. The ECSA values evaluated in a way similar to HER conditions (**Figure S3-IV, Table S3-II**)[29,30] range from 7.4 to 17.4 cm^2 in OER conditions. The *ECSA*-normalized OER activities (**Figure S3-IID)** indicate a ranking of activities similar to the geometrically normalized values.

Post-catalysis surface analysis of the electrocatalyst for HER and OER

XPS analyses were conducted on post-catalysis (PC) electrodes after at least 8 h of chronoamperometry (**Figure S3-V**). After both HER and OER, the contributions of nickel associated to the boride phases (Ni $2p_{3/2}$ at 853.1 eV and Ni $2p_{1/2}$ at 870.5 eV) are not observed. While surface oxidation was expected for OER[11,18], the same observation after HER in acidic conditions is surprising as catalysis occurs in reducing conditions. Indeed, PC analyses after HER indicate contributions of nickel borate species, including a $Ni^{(II)}$ $2p_{3/2}$ peak at 856.7 eV without significant shift between the samples[14,32]. It is likely that oxidation occurred after catalysis during exposure to air while the electrodes were drying. This is supported by long term stability studies of borides under air[11], as well as *in situ* X-ray absorption spectroscopy (XAS) at the Ni K-edge, which show that nickel boride nanocrystals are stable under HER conditions (not shown here, see Madeleine Han's PhD thesis)[33].

The case of OER is different as a reversible oxidation wave $Ni^{2+} \rightarrow Ni^{3+}$ shows that at least part of the boride material is converted to an (oxyhydr)oxide. Previous reports have shown the complete oxidation of Ni into nickel borides into NiO, $Ni(OH)_2$ and NiOOH in OER

conditions[9,22,]. Our team has shown previously by *in situ* XAS that nickel boride nanocrystals only partially oxidize during OER (not shown here, see Madeleine Han's PhD thesis)[33]. XPS does not enable to discriminate the nickel hydroxide and the oxyhydroxide, which show binding energies of 855.6 and 855.7 eV as reference values for the Ni $2p_{3/2}$ peak , respectively[34,35]. Nonetheless, the nature of surface sites differs between the crystalline and amorphous materials. Indeed, all initial nanomaterials exhibit a Ni $2p_{3/2}$ peak at 856.2 eV attributed to surface oxidation upon exposure of the powder to air for XPS analysis, through the formation of $Ni(OH)_2$ or NiOOH in the surface nickel borate[14,32,35]. After OER, the crystalline materials exhibit a shift to lower binding energies, at 854.2 and 854.8 eV for Ni_4B_3 and Ni_3B, respectively. We ascribe this shift to the formation of NiO[34,35]. On the opposite, the amorphous nanoparticles do not exhibit such a shift of the oxo component, which indicates that the materials form (oxy)hydroxides after electrocatalysis and drying. The ordered structure of the crystalline phases compared to their amorphous counterpart may explain the difference of surface state.

III) Attempts to improve the dispersion of nanoelectrocatalysts

a) Reported strategy of activity improvement by roll milling

To enhance the activity of a catalyst materials, a strategy is to optimize the number of active sites per mass unit of catalyst, hence the exposed surface area within the composite electrode film. Some authors have reported an enhancement of the dispersion, hence the mass-normalized activity, by roll milling the ink, which is a simple, economical and environmentally friendly method compared to strategies based on modified syntheses[36–38]. For instance, TaC particles were roll milled for several days with zirconia balls[36]. The resulting material showed a decrease of the particle size, an increase of the exposed surface area, higher activity and long-term stability during OER, with no zirconia contamination even after 14 days of roll milling. Similar beneficial effects of roll milling have been observed on $SrTi_{x-1}Fe_xO_{3-\delta}$ (x= 0.35, 0.5, 0.7, 0.9, and 1.0) particles of average 250 nm[38]. Nonetheless tantalum carbide and iron-substituted strontium titanate perovskites are relatively inert and hard materials. Therefore, these examples may not be representative of more reactive particles, like metal borides. According to these studies, in the following section, we have investigated the possibility to enhance the electrocatalytic activity of metal boride nanoparticles toward HER and OER, by roll milling of the catalytic ink.

b) Influence of roll milling of catalyst inks on their electrocatalytic properties

After their preparation, the inks were roll milled by 2 mm diameter zirconium beads under inert atmosphere (see details in the experimental section). We have screened different durations of roll milling. **Figure 3** shows the experimental setup. A glass flask is flushed with argon before introduction of the ink, to decrease the risk of potential side oxidation reactions with air.

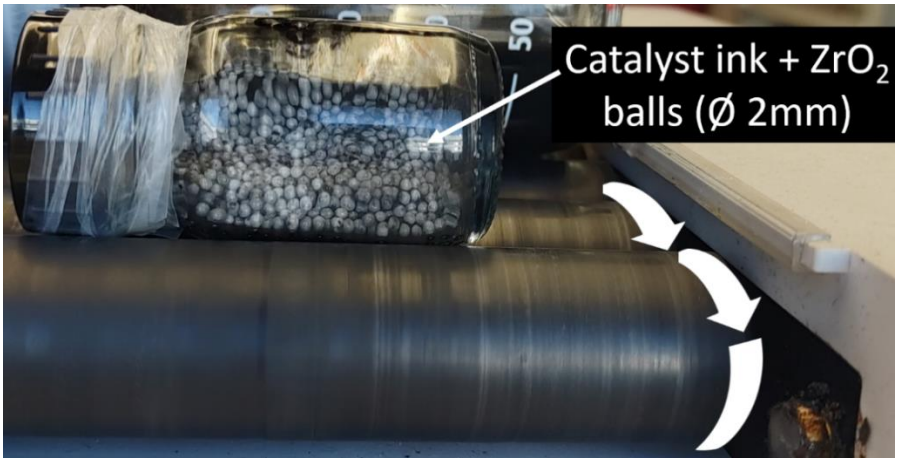

Figure 3. Experimental setup for ink dispersion studies by roll milling with zirconia balls.

We have used Ni_3B crystalline nanoparticles as case of study as these nanoparticles exhibit interesting activities in both OER and HER. We designate as *sonication only* the classical procedure, described in the previous section, without roll milling. 30 CVs were recorded in acidic HER conditions (**Figure 4A**). No significant enhancement of the properties can be observed between the *sonication only* and the *roll milled* samples. We also observe a non-monotonous evolution, as the ink roll milled for 1 h is much less active than the *sonication only* and 3h *roll milled* samples. This shows that besides the absence of enhancement, roll milling also raises issues of reproducibility for HER.

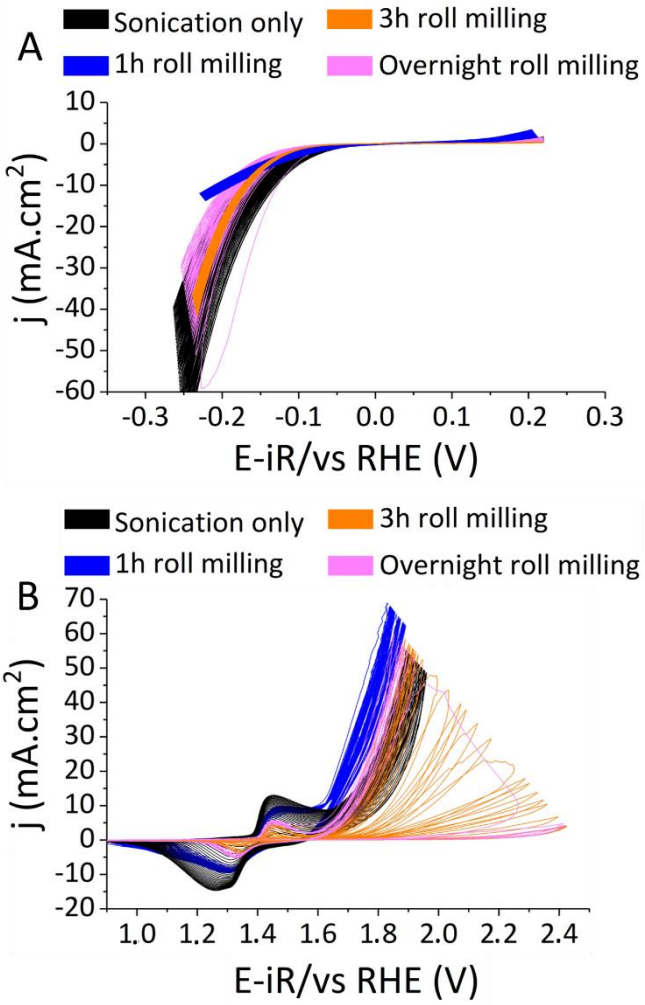

Figure 4. Cyclic voltammetry recorded under (A) HER in 0.5 M H_2SO_4, (B) OER in Fe purified 0.1 M KOH with roll milling under argon for 1h, 3h and overnight in comparison to the case of sonication only.

On the OER side (**Figure 4B**), 1 h roll milling yields an enhancement of electrocatalytic activity compared to a *sonication only* ink. Longer roll milling is detrimental to the activity, as the material shows an important deactivation upon cycling when the ink is roll milled for more than 3 h. We also observed, for HER and OER, partial to complete detachment of the catalyst film when the ink was roll milled, which may coincide with a better dispersion of the nanoparticles. Additional morphological studies would be interesting to observe the state of dispersion of the nanoparticles. However, these measurements indicate that roll milling is overall detrimental to the long-term electrocatalytic activity of nickel boride nanoparticles. Different hypotheses could explain these results. First, enhanced dispersion may favor materials loss (detachment) from the film. Second, and as evidenced by OER measurements, roll milling for several hours

may trigger oxidation of the metal borides, hence yielding poorer materials stability, loss of electrical conductivity of the catalyst films and activity loss.

Conclusion and perspectives

In summary, the electrocatalytic activities of nickel borides derived from the conversion of nickel nanoparticles rival with those reported for state-of-the-art materials, both in HER and OER conditions. For HER, crystalline Ni_4B_3 and crystalline Ni_3B exhibit the highest activity and steady properties for at least 8 h of operation. For OER, crystalline Ni_3B and amorphous Ni_4B_3 yields the higher activities. Contrary to HER, an activation process is observed, which corresponds to the formation of oxy(hydro)xydes species at the surface of the nanoparticles. These observations agree with previous studies[9–12,16,18,19] that presented the stability of the catalyst in HER conditions, while partial oxidation occurred on the surface in OER. Post-catalysis studies showed the complete oxidation of the materials after prolonged exposure to air.

In parallel, we have attempted to improve the dispersion state of the catalytic ink by a roll milling method using inert zirconia balls. While no significant enhancement was observed in HER, this method was detrimental in long-term electrocatalytic activity in OER, and is therefore not recommended for materials sensitive to oxidation before electrochemical measurements.

Annexes

Experimental methods

Reagents. Ni_3B, Ni_4B_3 powders were stored in an Ar-filled glovebox (H_2O < 0.5 ppm, O_2 < 0.5 ppm). Sulfuric acid (98%, Sigma-Aldrich), Ethanol (absolute, VWR Normapur grade), potassium hydroxide flakes (≥85 %, Sigma-Aldrich) were stored and used under air. For polishing, MasterPrep™ 0.05µm (Buehler), MasterMet™ 2 and Supreme Polycrystalline Diamond Suspension (1µm, MetaDi™) polishing suspensions were purchased from Buehler. For ink preparation, the Nafion™ 117 solution (≈5% in a mixture of lower aliphatic alcohols and water, Aldrich), acetylene black powder (≥99.0 %, Carbon black, Super P, Alfa Aesar), nitric acid (68 % normapur, VWR), were used as received. Zirconia balls (Ø 2mm, Zirmil®) and carbon paper (MGL370, Fuelcell store) were used for electrode preparation. For KOH purification, nickel nitrate (98%, Alfa Aesar) was used. Water was purified by a MilliQ® system.

Hydrophilic carbon black preparation

The preparation is reported elsewhere[39]. The acetylene black powder was previously treated in nitric acid, by dispersing 500 mg of acetylene black in a 50 mL of HNO_3 20% aqueous solution at 80 °C overnight under stirring, followed by centrifugation, washing with water and vacuum drying.

Rotating disk electrode preparation

A rotating disk electrode (RDE, Biologic BluRev RRDE/RDE) composed of a glassy carbon disk with a diameter of 5 mm was used for cyclic voltammetry (CV) and electrochemical impedance spectroscopy measurements (EIS). It was manually polished in two times by first using a Supreme Polycrystalline Diamond Suspension on dedicated plates and then by using a 50:50 mass mixture of MasterPrep™: MasterMet™ 2 solutions similarly. The catalyst film was prepared by drop-casting an ink. The ink was prepared by the following procedure: 3.5 mg of catalyst was sonicated at least 20 min. in 480 µL absolute ethanol until homogeneous dispersion of the particle was observed. Then, 3.5 mg of hydrophilized carbon black was added and the mixture was sonicated 20 min. Thereafter, 20 µL of a Nafion solution (5 % in alcohols and water, Sigma-Aldrich) was added and the mixture was sonicated again 20 min. Finally, 7µL of the homogeneously dispersed ink was dropped on the previously polished RDE to obtain a

catalyst loading of 0.25 $mg.cm^{-2}_{electrode}$ and dried under air.

Carbon paper electrode preparation

Carbon paper (CP) sheets were used as substrate for chronopotentiometry (CP) measurements. The electrode was firstly impregnated immersed in absolute ethanol and dried under vacuum on a Schlenk line. A 1 cm^2 square electrode was prepared by drop-casting. The ink suspension is similar to the previous method except for the absence of carbon black. 35.7 µL of ink was drop-casted on one side of the electrode. The electrode was then dried under vacuum on a schlenk line before covering the not catalyst deposed face with Kapton ®.

Measurements of the electrocatalytic properties

A typical three-electrode configuration was used for electrochemical measurements including the working electrode, a reference electrode Ag/AgCl in saturated KCl and a counter electrode, which was a graphite rod for HER studies, a platinum wire for OER studies. The RDE was rotating at 1600 rpm for all measurements. A Teflon-coated stir bar was added to the electrolyte and stirred at 300 rpm to enhance homogeneity of the ionic strength within the electrolyte. All CV and EIS measurements were performed at a scan rate of 20 mV s^{-1}. *ECSA* determination was performed in a low faradic potential range ([0; -0.1] V vs. AgCl/Ag for HER, [0; 0.3] V vs. Ag/AgCl for OER) at scan rates of 20, 10, 5, 2.5 mV s^{-1}. The C_{DL} values were obtained by considering the linear slope of the measured current plotted as a function of the scan rate for a selected potential in the recorded CVs. All CV measurements were corrected from the ohmic drop iR. The resistance value (R), was evaluated by recording impedance spectroscopy at 0 V vs the open circuit voltage (OCV) and is given when the imaginary part of the impedance is equal to 0 Ω in the Nyquist plot. In HER conditions, average R values of 8 Ω are observed, respectively 46 Ω in OER. The measured potentials were converted to the Reversible Hydrogen Electrode following the Nernst equation to correct for the pH value: $E_{RHE} = E_{WE} + 0.197 + 0.0591 \times pH$.

HER measurements were performed in a 0.5 M H_2SO_4 aqueous electrolyte at measured pH 0.38. Before measurement, the electrolyte was saturated by argon bubbling for at least 20 minutes.

HER measurements were performed in a 0.1M KOH aqueous electrolyte with pH = 13. The hydroxide solution was beforehand purified in order to remove Fe impurities present in commercial solid KOH[23]. To do so, 2 g of $Ni(NO_3)_2$ was centrifugated 2 times (26000 rpm, 10

min) with *ca.* 20 mL KOH 1 M and 2 mL water, followed by 3 times centrifugation with *ca.* 20 mL of water and 2 mL KOH. The $Ni(OH)_2$ powder obtained was put into 50 mL of as-prepared 1 M KOH aqueous solution. 450 mL of water was then added to obtain a 0.1 M KOH solution. The suspension was sonicated 3 min. and then rested for at least 3h. $Ni(OH)_2$ was finally removed by centrifugation.

Preparation of roll milled inks

The preparation of the inks followed the procedure described above for RDE studies except that a glass vial of 50 mL previously degassed and maintained under argon was used. A gentle flush with argon was operated between each introduction steps for the ink preparation. Then, around 20 g of ZrO_2 balls (2 mm diameter) was added, the vial was again gently flushed with argon for 1 min. to evacuate air and to avoid the evaporation of ethanol. The mixture was sonicated 20 min and placed under rotation on a roll mill (60 rpm rotation speed). Finally, the roll milled inks were drop-casted as described above.

Supplementary data for chapter 3

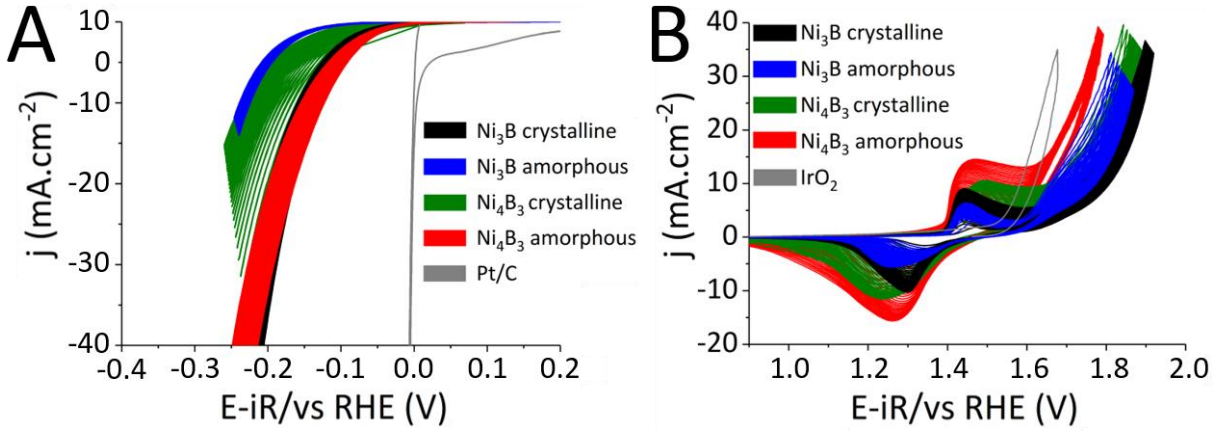

Figure S3-I. Cyclic voltammetry recorded with boride catalysts for 30 cycles until stabilization of the electrochemical response, under (A) HER conditions in Ar-saturated 0.5 M H_2SO_4, (B) OER in Fe purified O_2-saturated 0.1 M KOH. For comparison, The Pt/C and IrO_2 benchmark curves corresponding to the first CV cycle are also plotted.

Table S3-I. Comparison of the overpotential at 10 mA cm^{-2} for HER, OER, charge transfer R_{ct} values for HER and OER after 30 CV cycles of Ni_3B and Ni_4B_3 crystalline and amorphous nanoparticles.

Sample	$\lvert\eta\rvert$ at 10mA cm^{-2} HER	$\lvert\eta\rvert$ at 10mA cm^{-2} OER	R_{ct} HER	R_{ct} OER
Ni_3B crystalline	0.160 V vs RHE	0.482 V vs RHE	17.0 Ω	19.1 Ω
Ni_3B amorphous	0.238 V vs RHE	0.496 V vs RHE	45.6 Ω	20.5 Ω
Ni_4B_3 crystalline	0.235 V vs RHE	0.421 V vs RHE	62.9 Ω	19.6 Ω
Ni_4B_3 amorphous	0.148 V vs RHE	0.400 V vs RHE	18.9 Ω	11.2 Ω

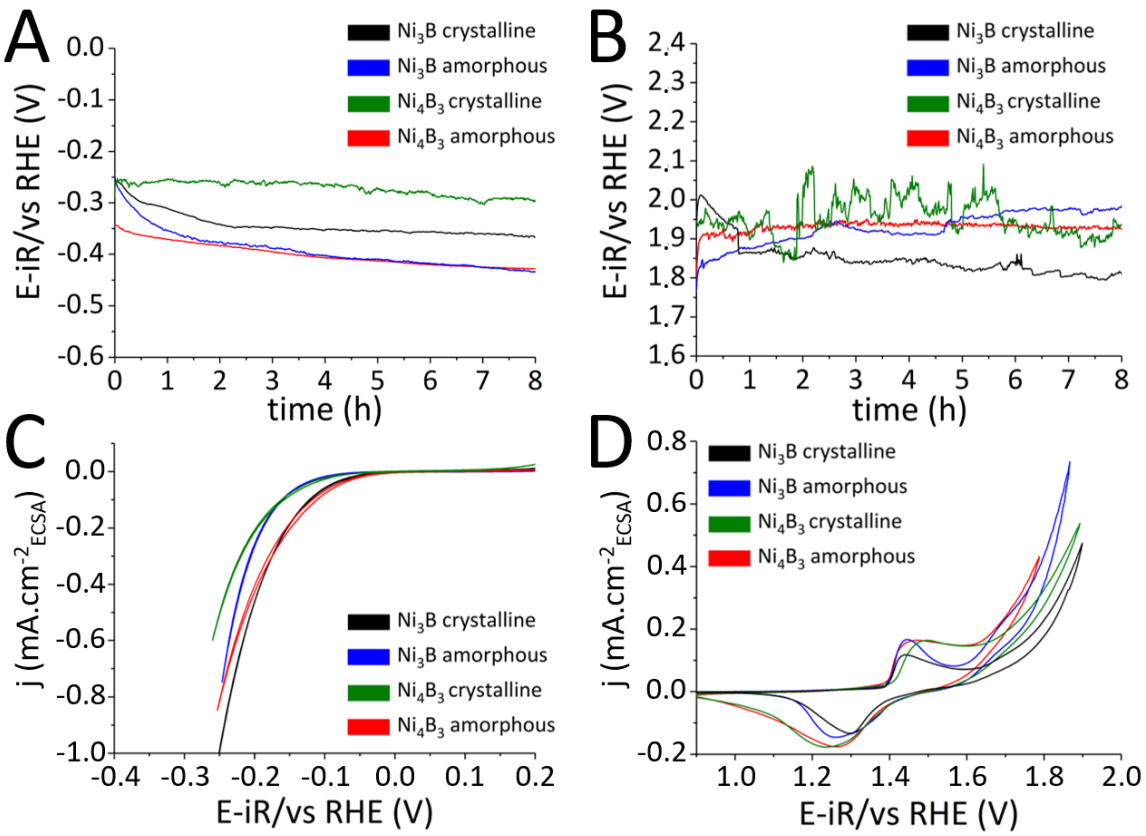

Figure S3-II. Chrono potentiometry (CP) for 8 h recorded at a current density of |10| mA.cm^2 on a 1 cm^2 carbon paper working electrode during (A) HER, (B) OER. Surface area normalized CV curves at the 30th cycle during (C) HER, (D) OER.

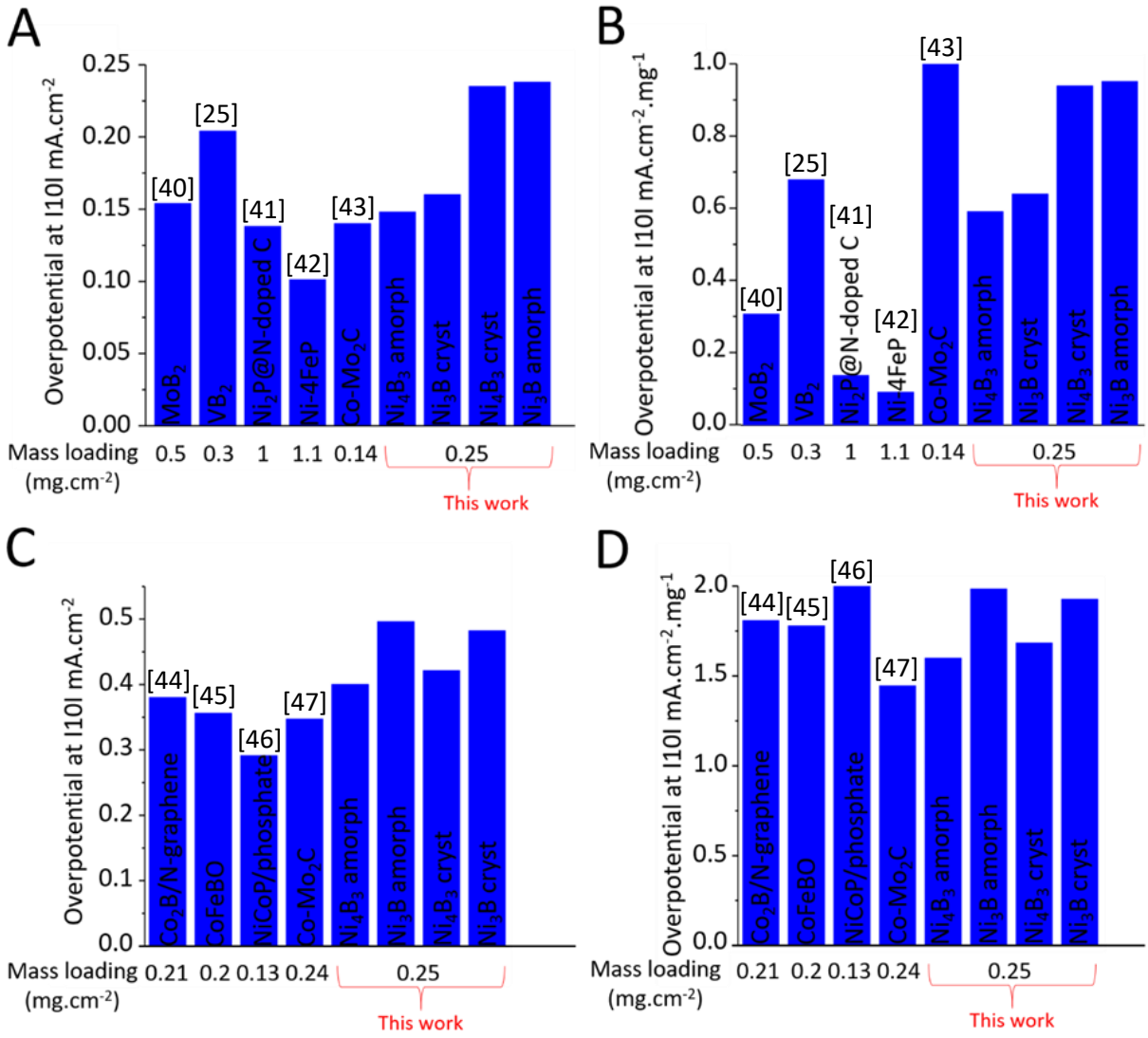

Figure S3-III. Overpotentials and mass normalized overpotentials measured at |10| mA cm^{-2} in (A-B) HER and (C-D) OER conditions, for selected transition metal borides, phosphides and carbides from the literature and from the present work. Data reported for (A-B) HER and (C-D) OER correspond to 0.5 M H_2SO_4 and 0.1 M KOH electrolytes, respectively.

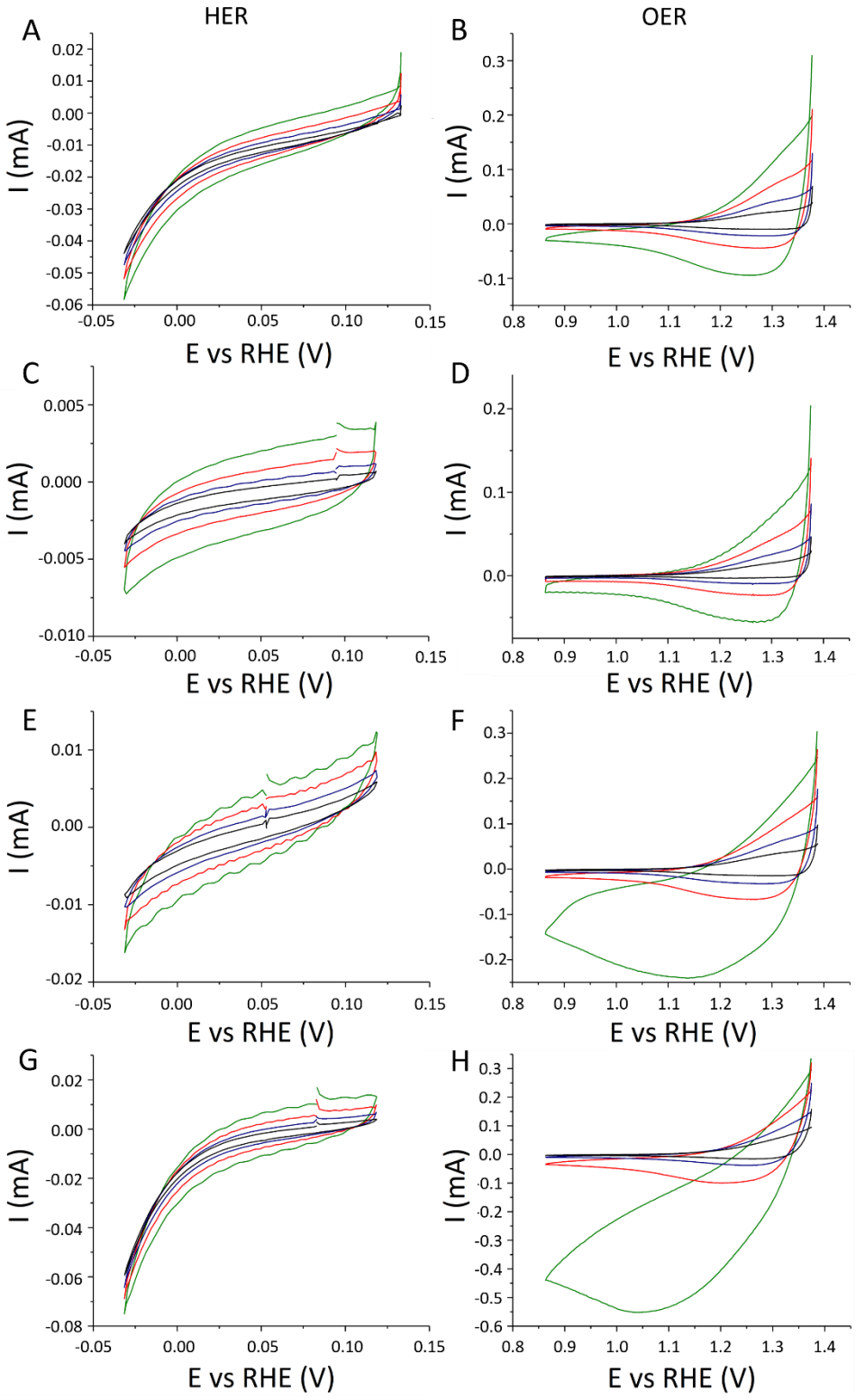

Figure S3-IV. Cyclic voltammetry curves recorded at scan rates of 2.5, 5, 10, 20 mV s^{-1} in a low faradic region in HER and OER to estimate the double layer capacitance (C_{DL}). (A, B) Ni_3B crystalline, (C, D) Ni_3B amorphous, (E, F) Ni_4B_3 crystalline, (G, H) Ni_4B_3 amorphous.

Table S3-II. Double layer capacitance C_{DL} values evaluated from the data displayed in **Figure S3-IV** from catalyst inks deposited on a rotating disk electrode in conditions of HER and OER. *ECSA* values are obtained by division of C_{DL} values by C_s= 40 µF cm^{-2}.

Sample	C_{DL} measured in HER (µF)	C_{DL} measured in OER (µF)	*ECSA* in HER (cm^2)	*ECSA* in OER (cm^2)
Ni_3B crystalline	350	605	8.7	15.1
Ni_3B amorphous	123	295	3.1	7.4
Ni_4B_3 crystalline	200	504	5.0	12.6
Ni_4B_3 amorphous	393	697	9.8	17.4

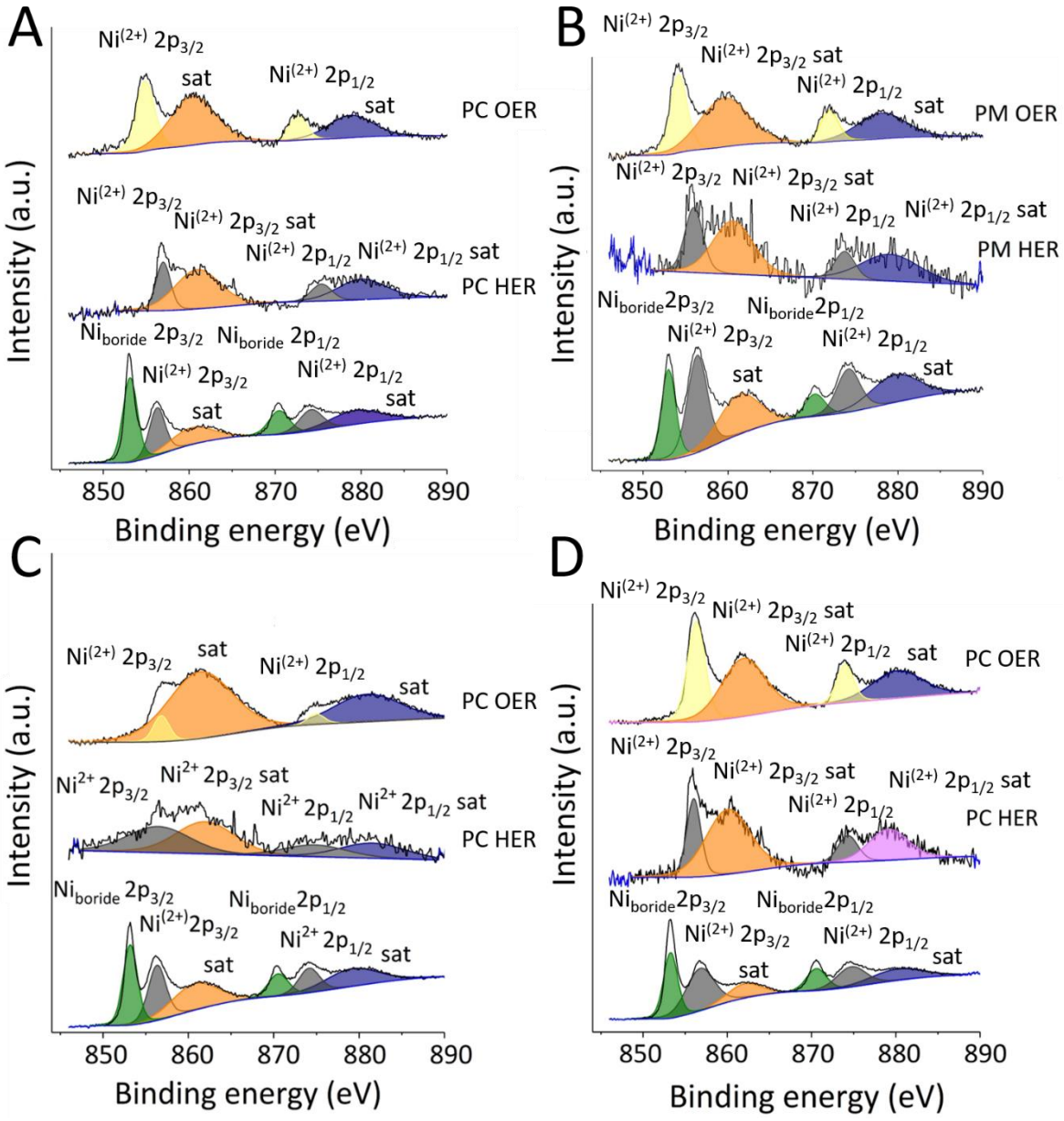

Figure S3-V. XPS spectra of electrodes and post-catalysis (PC) after chronopotentiometry at |10| $mA.cm^{-2}$ under HER and OER conditions for 8 h, compared to the pristine nanoparticles: (A) crystalline Ni_3B, (B) crystalline Ni_4B_3, (C) amorphous Ni_3B and (D) amorphous Ni_4B_3.

References

(1) Ramachandran, R.; Menon, R. K. An Overview of Industrial Uses of Hydrogen. *Int. J. Hydrogen Energy* **1998**, *23* (7), 593–598. https://doi.org/10.1016/s0360-3199(97)00112-2.

(2) Kyriakou, V.; Garagounis, I.; Vourros, A.; Vasileiou, E.; Stoukides, M. An Electrochemical Haber-Bosch Process. *Joule* **2020**, *4* (1), 142–158. https://doi.org/10.1016/j.joule.2019.10.006.

(3) Félix, G.; Quitian, A.; Rodríguez, E.; Ancheyta, J.; Trejo, F. Methods to Calculate Hydrogen Consumption during Hydrocracking Experiments in Batch Reactors. *Energy and Fuels* **2017**, *31* (11), 11690–11697. https://doi.org/10.1021/acs.energyfuels.7b01878.

(4) Gong, Y.; Yao, J.; Wang, P.; Li, Z.; Zhou, H.; Xu, C. Perspective of Hydrogen Energy and Recent Progress in Electrocatalytic Water Splitting. *Chinese J. Chem. Eng.* **2022**, *43*, 282–296. https://doi.org/10.1016/j.cjche.2022.02.010.

(5) Fan, L.; Tu, Z.; Chan, S. H. Recent Development of Hydrogen and Fuel Cell Technologies: A Review. *Energy Reports* **2021**, *7*, 8421–8446. https://doi.org/10.1016/j.egyr.2021.08.003.

(6) Liu, W.; Zuo, H.; Wang, J.; Xue, Q.; Ren, B.; Yang, F. The Production and Application of Hydrogen in Steel Industry. *Int. J. Hydrogen Energy* **2021**, *46* (17), 10548–10569. https://doi.org/10.1016/j.ijhydene.2020.12.123.

(7) Sun, L.; Luo, Q.; Dai, Z.; Ma, F. Material Libraries for Electrocatalytic Overall Water Splitting. *Coord. Chem. Rev.* **2021**, *444*, 214049. https://doi.org/10.1016/j.ccr.2021.214049.

(8) Holladay, J. D.; Hu, J.; King, D. L.; Wang, Y. An Overview of Hydrogen Production Technologies. *Catal. Today* **2009**, *139* (4), 244–260. https://doi.org/10.1016/j.cattod.2008.08.039.

(9) Gupta, S.; Patel, M. K.; Miotello, A.; Patel, N. Metal Boride-Based Catalysts for Electrochemical Water-Splitting: A Review. *Adv. Funct. Mater.* **2020**, *30* (1). https://doi.org/10.1002/adfm.201906481.

(10) Lao, J.; Li, D.; Jiang, C.; Luo, R.; Peng, H.; Qi, R.; Lin, H.; Huang, R.; Waterhouse, G. I. N.; Luo, C. Efficient Overall Water Splitting Using Nickel Boride-Based Electrocatalysts. *Int. J. Hydrogen Energy* **2020**, *45* (53), 28616–28625. https://doi.org/10.1016/j.ijhydene.2020.07.171.

(11) Chen, Z.; Duan, X.; Wei, W.; Wang, S.; Zhang, Z.; Ni, B. J. Boride-Based Electrocatalysts: Emerging Candidates for Water Splitting. *Nano Res.* **2020**, *13* (2), 293–314. https://doi.org/10.1007/s12274-020-2618-y.

(12) Jiang, Y.; Lu, Y. Designing Transition-Metal-Boride-Based Electrocatalysts for Applications in Electrochemical Water Splitting. *Nanoscale* **2020**, *12* (17), 9327–9351. https://doi.org/10.1039/d0nr01279c.

(13) Yan, Y.; Xia, B. Y.; Zhao, B.; Wang, X. A Review on Noble-Metal-Free Bifunctional Heterogeneous Catalysts for Overall Electrochemical Water Splitting. *J. Mater. Chem. A* **2016**, *4* (45), 17587–17603. https://doi.org/10.1039/C6TA08075H.

(14) Song, F.; Zhang, T.; Qian, Y.; Shaw, J.; Chen, S.; Chen, G.; Sun, Y.; Rao, Y. Multifunctional Electrocatalysts of Nickel Boride Nanoparticles for Superior Hydrogen Oxidation and Water Splitting. *Mater. Today Energy* **2021**, *22*, 100846. https://doi.org/10.1016/j.mtener.2021.100846.

(15) Zhu, J.; Hu, L.; Zhao, P.; Lee, L. Y. S.; Wong, K. Y. Recent Advances in Electrocatalytic Hydrogen Evolution Using Nanoparticles. *Chem. Rev.* **2020**, *120* (2), 851–918. https://doi.org/10.1021/acs.chemrev.9b00248.

(16) Cui, L.; Zhang, W.; Zheng, R.; Liu, J. Electrocatalysts Based on Transition Metal Borides and Borates for the Oxygen Evolution Reaction. *Chem. - A Eur. J.* **2020**, *26* (51), 11661–11672. https://doi.org/10.1002/chem.202000880.

(17) Huang, C. J.; Xu, H. M.; Shuai, T. Y.; Zhan, Q. N.; Zhang, Z. J.; Li, G. R. A Review of Modulation Strategies for Improving Catalytic Performance of Transition Metal Phosphides for Oxygen Evolution Reaction. *Appl. Catal. B Environ.* **2023**, *325* (December 2022), 122313. https://doi.org/10.1016/j.apcatb.2022.122313.

(18) Masa, J.; Piontek, S.; Wilde, P.; Antoni, H.; Eckhard, T.; Chen, Y. T.; Muhler, M.; Apfel, U. P.; Schuhmann, W. Ni-Metalloid (B, Si, P, As, and Te) Alloys as Water Oxidation Electrocatalysts. *Adv. Energy Mater.* **2019**, *9* (26), 1–8. https://doi.org/10.1002/aenm.201900796.

(19) Lee, E.; Fokwa, B. P. T. Nonprecious Metal Borides: Emerging Electrocatalysts for Hydrogen Production. *Acc. Chem. Res.* **2022**, *55* (1), 56–64. https://doi.org/10.1021/acs.accounts.1c00543.

(20) Carenco, S.; Portehault, D.; Boissière, C.; Mézailles, N.; Sanchez, C. Nanoscaled Metal Borides and Phosphides: Recent Developments and Perspectives. *Chem. Rev.* **2013**, *113* (10), 7981–8065. https://doi.org/10.1021/cr400020d.

(21) Jiang, W. J.; Niu, S.; Tang, T.; Zhang, Q. H.; Liu, X. Z.; Zhang, Y.; Chen, Y. Y.; Li, J. H.; Gu, L.; Wan, L. J.; Hu, J. S. Crystallinity-Modulated Electrocatalytic Activity of a Nickel(II) Borate Thin Layer on Ni3B for Efficient Water Oxidation. *Angew. Chemie - Int. Ed.* **2017**, *56* (23), 6572–6577. https://doi.org/10.1002/anie.201703183.

(22) Masa, J.; Sinev, I.; Mistry, H.; Ventosa, E.; de la Mata, M.; Arbiol, J.; Muhler, M.; Roldan Cuenya, B.; Schuhmann, W. Ultrathin High Surface Area Nickel Boride (NixB) Nanosheets as Highly Efficient Electrocatalyst for Oxygen Evolution. *Adv. Energy Mater.* **2017**, *7* (17), 1–8. https://doi.org/10.1002/aenm.201700381.

(23) Trotochaud, L.; Young, S. L.; Ranney, J. K.; Boettcher, S. W. Nickel-Iron Oxyhydroxide Oxygen-Evolution Electrocatalysts: The Role of Intentional and Incidental Iron Incorporation. *J. Am. Chem. Soc.* **2014**, *136* (18), 6744–6753. https://doi.org/10.1021/ja502379c.

(24) Fu, Y.; Richardson, P.; Li, K.; Yu, H.; Yu, B.; Donne, S.; Kisi, E.; Ma, T. Transition Metal Aluminum Boride as a New Candidate for Ambient-Condition Electrochemical Ammonia Synthesis. *Nano-Micro Lett.* **2020**, *12* (1), 1–13. https://doi.org/10.1007/s40820-020-0400-z.

(25) Lee, E.; Park, H.; Joo, H.; Fokwa, B. P. T. Unexpected Correlation Between Boron Chain Condensation and Hydrogen Evolution Reaction (HER) Activity in Highly Active Vanadium Borides: Enabling Predictions. *Angew. Chemie - Int. Ed.* **2020**, *59* (29), 11774–11778. https://doi.org/10.1002/anie.202000154.

(26) Park, H.; Lee, E.; Lei, M.; Joo, H.; Coh, S.; Fokwa, B. P. T. Canonic-Like HER Activity of Cr1–XMoxB2 Solid Solution: Overpowering Pt/C at High Current Density. *Adv. Mater.* **2020**, *32* (28), 2–7. https://doi.org/10.1002/adma.202000855.

(27) Park, H.; Encinas, A.; Scheifers, J. P.; Zhang, Y.; Fokwa, B. P. T. Boron-Dependency of Molybdenum Boride Electrocatalysts for the Hydrogen Evolution Reaction. *Angew.*

Chemie - Int. Ed. **2017**, *56* (20), 5575–5578. https://doi.org/10.1002/anie.201611756.

(28) Shinagawa, T.; Garcia-Esparza, A. T.; Takanabe, K. Insight on Tafel Slopes from a Microkinetic Analysis of Aqueous Electrocatalysis for Energy Conversion. *Sci. Rep.* **2015**, *5* (August), 1–21. https://doi.org/10.1038/srep13801.

(29) Wei, C.; Sun, S.; Mandler, D.; Wang, X.; Qiao, S. Z.; Xu, Z. J. Approaches for Measuring the Surface Areas of Metal Oxide Electrocatalysts for Determining Their Intrinsic Electrocatalytic Activity. *Chem. Soc. Rev.* **2019**, *48* (9), 2518–2534. https://doi.org/10.1039/c8cs00848e.

(30) Connor, P.; Schuch, J.; Kaiser, B.; Jaegermann, W. The Determination of Electrochemical Active Surface Area and Specific Capacity Revisited for the System MnOx as an Oxygen Evolution Catalyst. *Zeitschrift fur Phys. Chemie* **2020**, *234* (5), 979–994. https://doi.org/10.1515/zpch-2019-1514.

(31) Ren, H.; Pan, Y.; Sorrell, C. C.; Du, H. Assessment of Electrocatalytic Activity through the Lens of Three Surface Area Normalization Techniques. *J. Mater. Chem. A* **2020**, *8* (6), 3154–3159. https://doi.org/10.1039/c9ta13170a.

(32) Zhang, Q.; Zhao, J.; Wu, Y.; Li, J.; Jin, H.; Zhao, S.; Chai, L.; Wang, Y.; Lei, Y.; Wang, S. Rapid and Controllable Synthesis of Nanocrystallized Nickel-Cobalt Boride Electrode Materials via a Mircoimpinging Stream Reaction for High Performance Supercapacitors. *Small* **2020**, *16* (39). https://doi.org/10.1002/smll.202003342.

(33) Han, M. New Nanoparticles for Electrocatalysis Applied to Energy Conversion : Synthesis and Operando X-Ray Absorption Analysis, **2022**.

(34) Biesinger, M. C.; Payne, B. P.; Grosvenor, A. P.; Lau, L. W. M.; Gerson, A. R.; Smart, R. S. C. Resolving Surface Chemical States in XPS Analysis of First Row Transition Metals, Oxides and Hydroxides: Cr, Mn, Fe, Co and Ni. *Appl. Surf. Sci.* **2011**, *257* (7), 2717–2730. https://doi.org/10.1016/j.apsusc.2010.10.051.

(35) National Institute of Standards and Technology. NIST X-ray Photoelectron Spectroscopy Database,NIST Standard Reference Database Number 20. https://doi.org/10.18434/T4T88K.

(36) Rezaei, N.; Mutambanengwe, R. L.; Peppley, B. A. Study of Electrochemical Stability and Physical Characteristics of Ball Milled Tantalum Carbide as a Support for Oxygen

Evolution Reaction Electrocatalysts. *Ceram. Int.* **2021**, *47* (11), 15464–15470. https://doi.org/10.1016/j.ceramint.2021.02.112.

(37) Orfanidi, A.; Rheinländer, P. J.; Schulte, N.; Gasteiger, H. A. Ink Solvent Dependence of the Ionomer Distribution in the Catalyst Layer of a PEMFC. *J. Electrochem. Soc.* **2018**, *165* (14), F1254–F1263. https://doi.org/10.1149/2.1251814jes.

(38) Lankauf, K.; Mroziński, A.; Błaszczak, P.; Górnicka, K.; Ignaczak, J.; Łapiński, M.; Karczewski, J.; Cempura, G.; Jasiński, P.; Molin, S. The Effect of Fe on Chemical Stability and Oxygen Evolution Performance of High Surface Area SrTix-1FexO3-δ Mixed Ionic-Electronic Conductors in Alkaline Media. *Int. J. Hydrogen Energy* **2021**, *46* (56), 28575–28590. https://doi.org/10.1016/j.ijhydene.2021.06.088.

(39) Azor, A.; Ruiz-Gonzalez, M. L.; Gonell, F.; Laberty-Robert, C.; Parras, M.; Sanchez, C.; Portehault, D.; González-Calbet, J. M. Nickel-Doped Sodium Cobaltite 2D Nanomaterials: Synthesis and Electrocatalytic Properties. *Chem. Mater.* **2018**, *30* (15), 4986–4994. https://doi.org/10.1021/acs.chemmater.8b01146.

(40) Jothi, P. R.; Zhang, Y.; Scheifers, J. P.; Park, H.; Fokwa, B. P. T. Molybdenum Diboride Nanoparticles as a Highly Efficient Electrocatalyst for the Hydrogen Evolution Reaction. *Sustain. Energy Fuels* **2017**, *1* (9), 1928–1934. https://doi.org/10.1039/C7SE00397H.

(41) Pu, Z.; Zhang, C.; Amiinu, I. S.; Li, W.; Wu, L.; Mu, S. General Strategy for the Synthesis of Transition-Metal Phosphide/N-Doped Carbon Frameworks for Hydrogen and Oxygen Evolution. *ACS Appl. Mater. Interfaces* **2017**, *9* (19), 16187–16193. https://doi.org/10.1021/acsami.7b02069.

(42) Kwong, W. L.; Lee, C. C.; Messinger, J. Scalable Two-Step Synthesis of Nickel-Iron Phosphide Electrodes for Stable and Efficient Electrocatalytic Hydrogen Evolution. *J. Phys. Chem. C* **2017**, *121* (1), 284–292. https://doi.org/10.1021/acs.jpcc.6b09050.

(43) Lin, H.; Liu, N.; Shi, Z.; Guo, Y.; Tang, Y.; Gao, Q. Cobalt-Doping in Molybdenum-Carbide Nanowires Toward Efficient Electrocatalytic Hydrogen Evolution. *Adv. Funct. Mater.* **2016**, *26* (31), 5590–5598. https://doi.org/10.1002/adfm.201600915.

(44) Masa, J.; Weide, P.; Peeters, D.; Sinev, I.; Xia, W.; Sun, Z.; Somsen, C.; Muhler, M.; Schuhmann, W. Amorphous Cobalt Boride (Co 2 B) as a Highly Efficient Nonprecious Catalyst for Electrochemical Water Splitting: Oxygen and Hydrogen Evolution. *Adv. Energy Mater.* **2016**, *6* (6), 1–10. https://doi.org/10.1002/aenm.201502313.

(45) Liu, G.; He, D.; Yao, R.; Zhao, Y.; Wang, M.; Li, N.; Li, J. Amorphous CoFeBO Nanoparticles as Highly Active Electrocatalysts for Efficient Water Oxidation Reaction. *Int. J. Hydrogen Energy* **2018**, *43* (12), 6138–6149. https://doi.org/10.1016/j.ijhydene.2018.01.191.

(46) He, L.; Gong, L.; Gao, M.; Yang, C. W.; Sheng, G. P. In Situ Formation of NiCoP@phosphate Nanocages as an Efficient Bifunctional Electrocatalyst for Overall Water Splitting. *Electrochim. Acta* **2020**, *337*, 135799. https://doi.org/10.1016/j.electacta.2020.135799.

(47) Kim, M. J.; Kim, S.; Song, D. H.; Oh, S. K.; Chang, K. J.; Cho, E. A. Promotion of Electrochemical Oxygen Evolution Reaction by Chemical Coupling of Cobalt to Molybdenum Carbide. *Appl. Catal. B Environ.* **2018**, *227* (October 2017), 340–348. https://doi.org/10.1016/j.apcatb.2018.01.051.

Chapter 4: Synthesis and identification of key parameters for the synthesis of nickel borophosphides

I) Introduction: The challenge of crystalline nickel borophosphide nanomaterials

As discussed in the general introduction, ternary metal borophosphides could exhibit deep modification of the properties compared to the binary boride/phosphide counterparts. We have discussed in the previous chapter how boron impacts the electronic state of nickel into nickel borides. Incorporation of phosphorus should bring increased ionicity, hence modified charge states on the metal atoms. This can favor catalytic properties, as previously demonstrated for hydrogenation catalysis[1]. Because hydrogenation catalysis involves hydrogen adsorption, one can speculate that similar enhancement could occur in electrocatalysis of the hydrogen evolution reaction[2]. To date, ternary metal borophosphides (M-B-P) are only scarcely reported, both at the bulk scale and at the nanoscale, and most of them are amorphous[3,4]. More specifically, if we consider first-row transition metals, only a few ternary compositions have been reported according to the PDF-4+ database[5]. Compared to amorphous solids, targeting crystalline phases could provide better stability, making them more suitable in catalysis conditions. Specific synthesis conditions are required to stabilize ternary phases as the combination of a metal with two p-block elements can easily lead to phase depletion to more thermodynamically stable products. In addition, the composition has to be carefully selected with respect to the reported and possible structures to avoid any by-products.

Only two crystalline nickel borophosphides are known, $Ni_2B_{0.6}P_{0.4}$ and $Ni_3P_{0.7}B_{0.3}$, reported by Mickhalenko[6]. They are isostructural to their corresponding nickel phosphide phases, respectively Ni_2P and Ni_3P, by incorporating random substitution of P by B. Their syntheses were achieved under harsh conditions by a solid-state reaction of elemental powders at 1000 °C for 70 h with further homogenization at 800 °C for 250 h. These results suggest the possibility to target new ternary compositions, at least by modifying the substitution rate. To improve the reactivity, nanoscale reagents and the corresponding shorter diffusion length involved during chemical reactions could provide more homogeneous products, at a lower temperature and for a shorter dwell time compared to bulk reagents. In addition, inorganic molten salt media allow liquid phase reactions at 300-1000°C under conditions milder than the reported solid-state reaction, thus conditions prone to maintain the nanoscale of the initial objects and to yield metastable solids and nanomaterials.

Throughout this chapter, different strategies are developed to target amorphous/crystalline borophosphide compositions using nickel as a case of study and to understand the reactions mechanisms (**Figure 1**). In more details, we develop along this chapter four molten salts-based

strategies, based respectively on hetero-element insertion in nanoparticles for three of them and on a one-pot approach from a nickel (II) precursor.

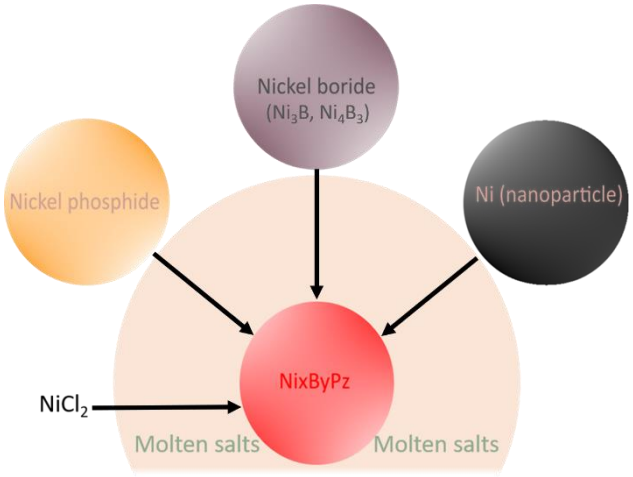

Figure 1. Strategies to achieve nanoscale ternary nickel borophosphide phases in molten salts.

II) The one-pot approach from $Ni^{(0)}$ nanoparticles

This synthesis pathway is inspired by that described in the Chapter 2 for the formation of morphology-controlled boride nanoparticles. Spherical nickel nanoparticles with a size of about 30 nm were dispersed in a eutectic mixture LiI:KI (58:42 mass.) or LiCl:KCl (44:56 mass.) by impregnation (details in the Experimental methods section). Then, $NaBH_4$ as the source of boron (0) and trioctylphosphine (TOP) or red phosphorus as phosphorus sources were added and mixed with the impregnated powder by grinding. We note that incorporation of $NaBH_4$ in the solvent used for evaporation (eg. hexane) results in its partial degradation, so that the two-step process impregnation-mixture grinding of B and P sources is preferred (see Methods for details).

The reaction mixture was then heat treated under argon flow, washed with methanol after cooling down, and then dried under vacuum. In order to obtain pure phases before searching for new compounds and solid solutions, we use Ni/B/P atomic ratios 3/0.6/0.7 and 2/1/0.4, close to the two ternary phases reported, $Ni_3P_{0.7}B_{0.3}$ and $Ni_2B_{0.6}P_{0.4}$, respectively. These reagents ratios correspond to slight excess of $NaBH_4$, as the study of nickel boride synthesis in chapter 2 showed that the borohydride does not react to form the boride quantitatively, but instead a slight proportion yields a boron-rich amorphous layer on the surface of the particles.

a) Red phosphorus as P source

The first studies were conducted at 475 °C with a plateau of 1.5 h (**Figure 2A-B**), similar to the conditions used for the conversion of nickel to nickel borides. The phosphorus source is red phosphorus, which has already been used as non-toxic phosphorus source for the synthesis of nickel phosphide nanoparticles[7]. $NaBH_4$ is used as the source of boron (0) by thermal decomposition at a temperature similar to the melting temperature of the salt (see chapter 2). For both reagent ratios, we observe the formation of phase mixtures composed by unreacted nickel (0) and phosphides Ni_3P and Ni_2P, as predominant phases. These phases possibly coexist with the borophosphides targeted. For the composition Ni:B:P = 3:0.6:0.7 at., $Ni_{12}P_5$ is also detected. For the composition the richest in boron (Ni:B:P = 2:1:0.4 at.), in addition to Ni_5P_2, the boride Ni_3B is also detected. TEM images (**Figure 2C-D**) show a diversity of objects, partial aggregation and an amorphous layer, which is assumed to be composed of amorphous boron partially oxidized during the washing steps (see chapter 2)[8].

As some nickel(0) did not react, we conclude from these results that the reaction is not complete, contrary to what was observed with nickel boride syntheses (Chapter 2) with similar Ni:heteroelement initial ratio. Therefore, the incorporation of phosphorus seems to hinder the conversion of Ni(0) nanoparticles. Nonetheless, red phosphorus exhibits significant reactivity, as some phosphides are detected. On another side, the composition also plays a role in the phase selection, as indicated by the crystallization of Ni_3B only for a B-rich initial ratio.

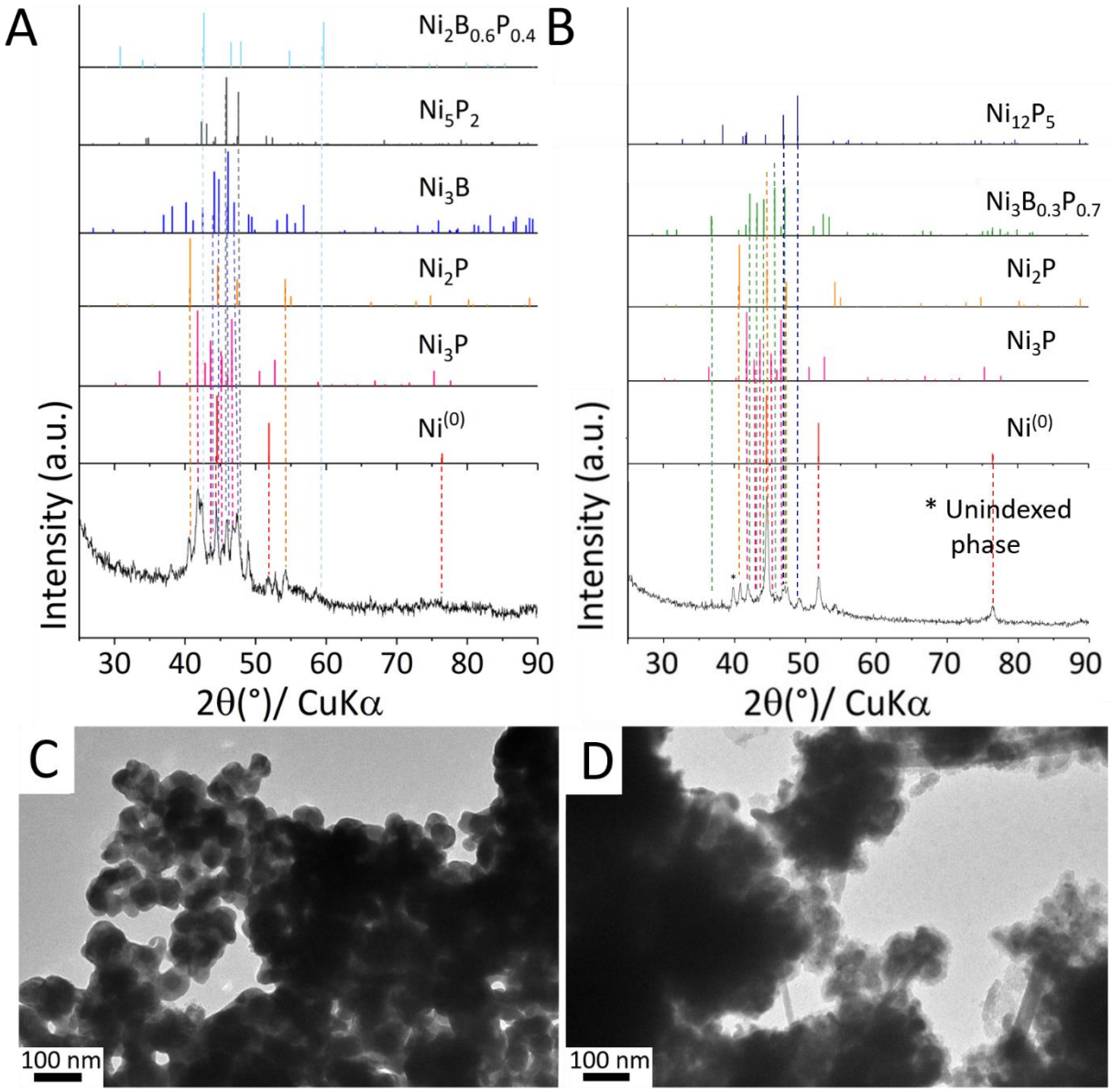

Figure 2. Powder XRD patterns of the samples prepared in the LiI:KI eutectic mixture at 475 °C for 1.5 h with initial Ni:B:P ratios (A) 2:1:0.4 and (B) 3:0.6:0.7. Corresponding TEM pictures in (C) and (D), respectively.

b) Trioctylphosphine as source of P

We have studied the possibility to replace red phosphorus by less reactive trioctylphosphine (TOP), also often used as phosphorus source for the synthesis of phosphide nanoparticles[9,10,11]. Again, we observe a predominance of unreacted nickel(0) and of nickel phosphides, although with lower phase diversity (**Figure S4-I**).

c) Partial conclusion: competitive reactivity of nickel nanoparticles versus B and P sources

In summary, when starting from Ni(0) nanoparticles to trigger the one-pot incorporation of B and P, whether red phosphorus or trioctylphosphine is used, we observe a vast majority of phosphide phases compared to borides, despite a P initial content close to or smaller than the B initial content. This suggests that the incorporation of phosphorus is favored over boron. A second general observation is the uncomplete reaction of initial elemental nickel, which was not observed for the corresponding nickel boride synthesis with similar B:heteroelement ratio (**Chapter 2**). This indicates that the presence of phosphorus sources hinders the reactivity of the boron source. This could be explained by a side reaction between the borohydride and the phosphorus source, for instance through the formation of boron phosphide. Additional studies were performed at 500 °C with different Ni:TOP:$NaBH_4$ ratios by maintaining an initial ratio Ni:(B+P) = 1:1 at., but with a slight boron excess. The stoichiometries were fixed as Ni:TOP:$NaBH_4$ of 1:0.25:0.75; 1:0.5:0.5 and 1:0.75:0.25. In all cases, a mixture of boride and phosphide phases with the predominance of nickel (0) was observed even for the richest composition in boron (Ni:TOP:$NaBH_4$ of 1:0.25:1). However, for this latter, Ni_3B and Ni_2B were observed with Ni_3P, while the phosphorus-rich composition (Ni:TOP:$NaBH_4$ of 1:0.75: 0.4) showed a predominance of phosphides over borides.

We then discard the simultaneous introduction of B and P sources as a suitable reaction pathway. More efficient pathways should enable retaining the reactivity of the boron source and bypassing the reactivity gradient between B and P sources, the latter being more reactive. For these reasons, a substitute method is to incorporate the heteroelement from pure phase boride or phosphide nanoparticles synthesized as first step.

III) Heteroelement (B/P) insertion in nickel boride or phosphide nanoparticles

a) Boron insertion into nickel phosphide nanoparticles

We use Ni_2P and Ni_3P nanoparticles as precursors, synthesized by adapting reported procedures[12,13]. The Ni_2P sample comprises a secondary $Ni_{12}P_5$ phase (**Figure 3A-a**), in agreement with the reported procedure[12]. The Ni_3P sample contains a significant fraction of unreacted $Ni^{(0)}$ **(Figure 3B-e)**, due to an incomplete etching[13]. TEM shows that Ni_2P (**Figure S4-II A-B**) is obtained as a monodisperse sample of nanoparticles with a size

distribution centered on ~11 nm. The Ni_3P sample on the opposite presents a large aggregation of anisotropic objects (**Figure S4-IIC**). Nevertheless, these particles are used to get a first insight on the reactivity of Ni_3P with sodium borohydride.

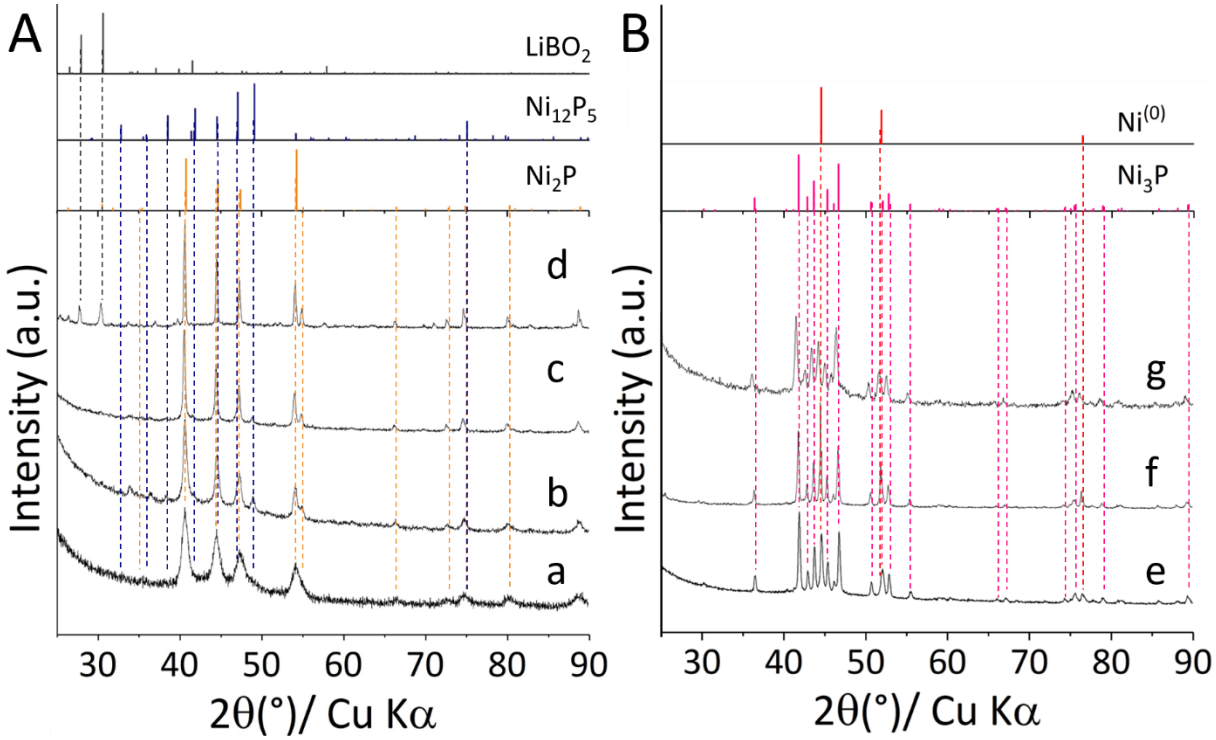

Figure 3. Powder XRD patterns of the products obtained by reacting (A) Ni_2P nanoparticles and (B) Ni_3P with $NaBH_4$ in a molten LiI:KI eutectic mixture syntheses: (a) initial Ni_2P nanoparticles with minor amounts of $Ni_{12}P_5$, Ni_2P:$NaBH_4$ atomic ratios of (b) 1:0.4 at 500 °C/1.5 h, (c) 1:1 at 500 °C/1.5 h, (d) 1:1 at 800 °C/1.5 h; (e) initial Ni_3P nanoparticles, Ni_3P:$NaBH_4$ atomic ratios of (f) 1:0.4 at 600 °C/3 h, (g) 1:1 at 600 °C/3 h.

The reaction of Ni_2P and Ni_3P samples with $NaBH_4$ in molten LiI:KI eutectic mixtures with reagents ratios similar to the reported ternary phases (**Figure 3A-b, 3B-f**), and to those used in the one-pot approach discussed in the previous section, yielded only a narrowing of the diffraction peaks of the initial nanoparticles, hence further crystallization of the phosphides but no significant incorporation of boron. We have then increased the boron source content (**Figure 3A-c, 3B-g**) and the reaction temperature to 800 °C (**Figure 3A-d**), in order to trigger boron incorporation. We observe the same behavior: crystal growth of the phosphides and no crystallization of boron-containing phases, except the formation of $LiBO_2$, which could arise from oxidation during washing of a lithium boride formed by reaction between the borohydride and the molten salt. The overall outline is a strong stability of the formed phosphide phases in

the conditions studied. This also confirms the strong tendency to crystallization of phosphides during the one-pot process studied in the previous section. The reverse approach, namely phosphorus diffusion into nickel boride nanoparticles, was then investigated, with an attempt to first lock boron atoms into the solid, before reaction with phosphorus sources.

b) Phosphorus insertion into nickel boride nanoparticles

We use the nickel boride Ni_3B nanoparticles obtained from the syntheses described in Chapter 2, for their narrow size distribution and for the expected higher reactivity of Ni_3B versus Ni_4B_3, due to lower covalence. These particles are reacted with red phosphorus in the eutectic mixture LiI:KI. **Figure 4** and **Figure S4-III** present synchrotron-based *in situ* XRD patterns (incident beam energy of ca. 90 keV) acquired during heating at 10 °C min^{-1} up to 750 °C with a 10 min plateau. A progressive intensity decrease of the Ni_3B diffraction peaks from 416 °C is correlated with crystallization of Ni_2P, Ni_3P and/or isostructural $Ni_2P_{0.6}B_{0.4}$ and $Ni_3P_{0.7}B_{0.3}$, respectively, or with similar compositions $Ni_2P_{1-x}B_x$ and $Ni_3P_{1-x}B_x$. Some Ni_3B peaks remain after this conversion. The distinction between Ni_3P/Ni_2P and the isostructural borophosphides is challenging due to the expected small shifts of the diffraction peaks. However, a better fit is observed for Ni_3P and Ni_2P.

Increasing the temperature above 582 °C leads to a narrowing of the phosphide XRD peaks, indicating enhanced crystallization, and to crystallization of NiP from about 650 °C.

The fact that some Ni_3B remains suggests that temperatures above 750 °C or dwell times longer than the 10 min investigated *in situ* might be necessary for complete conversion of the boride. In order to avoid crystallization of NiP detected *in situ* above 650 °C, we have favored long dwell times by maintain relatively low temperatures. We have thus investigated two temperature profiles: 630 °C for 1.5 h and 450 °C for 3h. Reagents ratios were chosen close to the targeted compositions (Ni:B:P = 2:0.4:0.6 and 3:0.7:0.3 at.) with initial atomic Ni:B:P ratios equivalent to those investigated in the previous sections (Ni_3B:P = 1:0.7) and Ni_4B_3:P = 1:0.94 corresponding to Ni:B:P = 3:1:0.7 and 3:2.25:0.7, respectively, in comparison to Ni:B:P = 3:0.6:0.7 in the previous section). We have also investigated unreported ternary phase compositions by substituting P by B through the use of a phosphorus default compared to the reported ternary phases with compositions of Ni_3B:P = [1:0.3- 1:0.6] and Ni_4B_3:P = 1:0.7 (**Figure S4-IV**, **Figure S4-V**, **Table S4-I**).

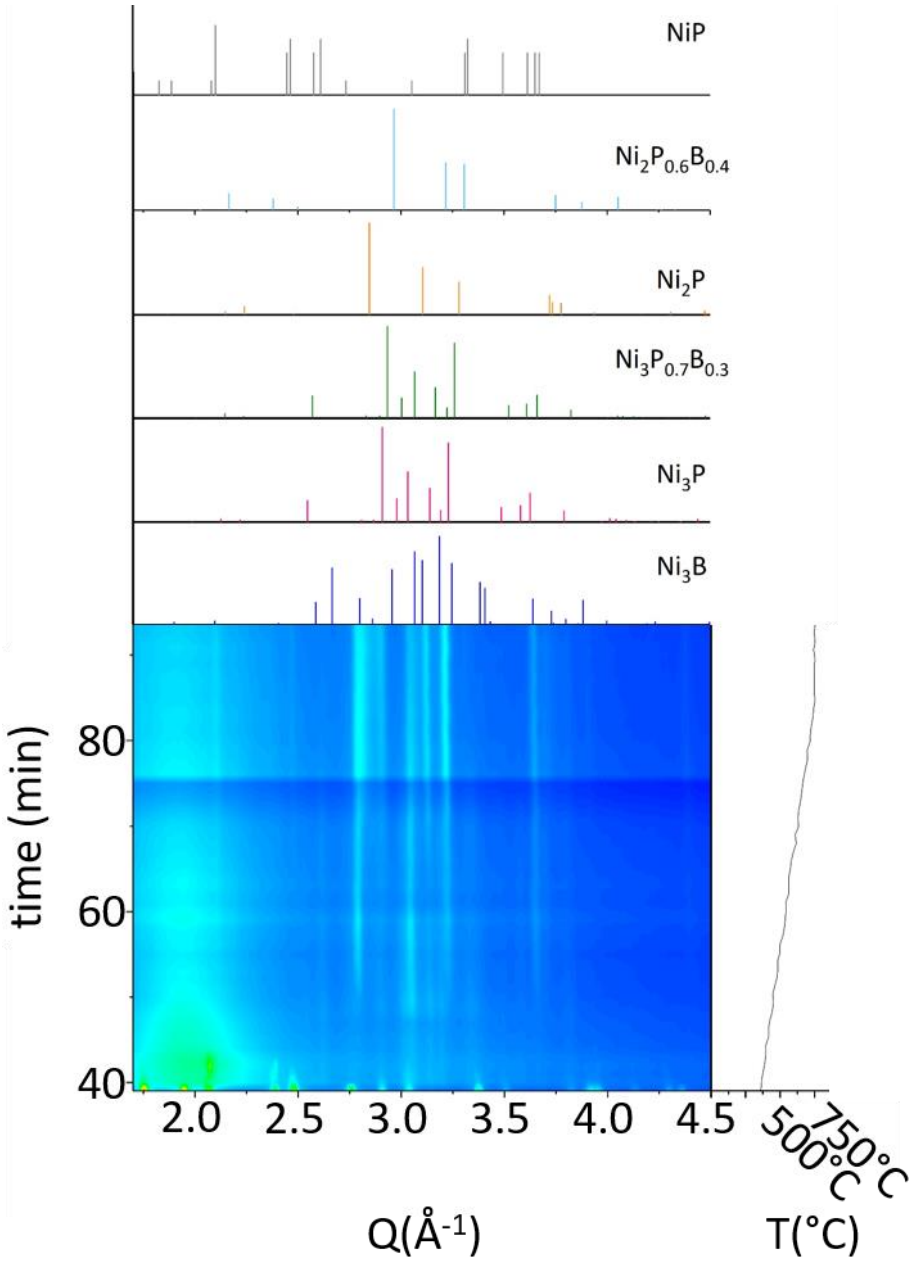

Figure 4. Synchrotron *in situ* XRD diagrams recorded during heating of a reaction mixture containing Ni_3B nanoparticles and red phosphorus in proportions $Ni_3B:P_{red}$ = 1:0.7 at. in the molten eutectic mixture LiI:KI.

In all conditions studied, XRD indicates conversion of the borides into phosphides (Ni_3P, Ni_2P, $Ni_{12}P_5$, Ni_5P_4, Ni_5P_2) and possible some ternary phases ($Ni_2B_{0.6}P_{0.4}$, $Ni_3P_{0.7}B_{0.3}$) and/or unreacted boride nanoparticles (Ni_3B, Ni_4B_3). As expected, no NiP phase was observed, in agreement with the lower reaction temperatures compared to *in situ* XRD. For reaction mixtures starting from Ni_3B, for an initial P content lower than the ratio in reported $Ni_3P_{0.7}B_{0.3}$, formation of nickel (0) is observed, which suggests removal of boron from the initial boride. TEM pictures

(**Figure S4-VI**) are in good agreement with XRD, showing a variety of morphologies from anisotropic nanoparticles to micrometer-sized particles and nanowires.

Despite the non-achievement of crystallization of a pure ternary phase, several trends can be highlighted. First, in Ni_3B-P_{red} mixtures at 630 °C for 1.5 h, an increase of the initial phosphorus content in the initial mixture from Ni_3B:P_{red} = 1:0.3 to 1:0.4 at. (**Figure S4-IV**, **Table S4-I**) results in the complete disappearance of the Ni_3B diffraction peaks, which were maintained for the lowest P content, mixed with Ni_3P and $Ni_{12}P_5$. In parallel, (re)formation of nickel (0) is observed for ratios Ni_3B:P_{red} = 1:0.4, 1:0.5 and 1:0.6 (**Figure S4-IV, Table S4-I**). For Ni_3B:P_{red} = 1:0.7, a mixture of phosphides and borophosphides is obtained. The phosphides could originate from the Ni(0) species detected at intermediate ratios 1:0.4 to 1:0.6. The "dealloying" of Ni_3B does not occur during the annealing of Ni_3B at similar temperatures[14–16]. Therefore, "dealloying" is linked to the reactivity of the Ni_3B particles in P_{red}-containing reaction mixture. Two origins can be proposed. First, reactivity with phosphorus could trigger boron dealloying, either by phase segregation in the course of phosphide formation or by formation of boron phosphide as a poorly structured material not detectable by XRD. Second, the partially oxidized surface of the Ni_3B nanoparticles formed during their washing could trigger dealloying by formation of highly stable boron oxide. This latter behavior has already been observed for cobalt boride nanoparticles during their activation for CO_2 methanation catalysis,[8] so that we consider this hypothesis as the most probable. This suggests that using pristine Ni_3B nanoparticles, before washing, could circumvent the issue of boron loss by dealloying, and could at the same time avoid the formation of phosphides, possibly issued from nickel (0).

Although conversion into phosphides and ternary phases is also identified when using Ni_4B_3 as precursor instead of Ni_3B (**Figure S4-V**, **Table S4-I)**, we do not observe diffraction peaks of elemental nickel, but Ni-rich borides like Ni_2B and Ni_3B are detected, which indicates "dealloying" similar to Ni_3B. This boron segregation leads to a wide diversity of phosphides for initial reaction mixtures rich in red phosphorus.

For limiting such boron segregation, we have attempted reactions at lower temperature, 450 °C, focused on Ni_3B (**Figure S4-IV, Table S4-I**). We observe similar trends, with the predominance of phosphide phases and borophosphides.

Overall, the conversion of nanoparticles did not enable to reach the objective of borophosphide synthesis. However, we could identify important trends that will be used for the design of suitable reaction pathways. First, phosphides are thermodynamically favored compared to

borides, when their formations are in competition (reactions of B and P sources with Ni(0) nanoparticles, or reaction of B source with nickel phosphides). That is the reason why locking boron atoms in crystal structures of nickel borides seems the most adapted approach, as it should enable to maintain reactions under kinetic control by avoiding boron segregation out of the metal compound. The suitability of this path is partially confirmed by the identification of borophosphide phases in the final product mixtures. However, we observe the concomitant formation of many phosphides, which could be traced back to the detection of intermediate Ni(0) or borides richer in nickel than the precursors. These species result from boron "dealloying". This behavior shows that boron is not fully locked in the boride structures. This is surprising as it does not correspond to the known stability of nickel borides[14]. We tentatively ascribe the "dealloying" to the presence of oxo species at the surface of the boride nanoparticles after the washing step following their synthesis, which act as boron scavengers to form highly stable boron oxide during the heat treatment of the borophosphide synthesis. A future research track could then be to react the boride particles before their washing, for instance by hot injection of the phosphorus source after formation of the boride nanoparticles, or by recovery of the boride particles trapped in the solidified salt, before washing.

IV) The one-pot approach from a metal salt

The approaches discussed above as well as in chapter 2 are based on the diffusion of heteroelements inside solid nanostructures. The results obtained show that these reactions are relatively slow and require thermal activation to trigger crystallization, above 450 °C. Using faster reactions may be a way to level the reactivities of B and P sources, hence to ensure that both elements get associated with nickel, by avoiding the faster incorporation of phosphorus, observed in the previous section. To do so, while the previous approaches did not involve redox processes of the nickel atoms (nickel was already in the elemental state at the beginning of the process), we have sought to trigger redox reactivity of nickel. Indeed, usual synthesis of boride[17,18,16] and phosphide[7,1] nanostructures consist in the reduction of metal salts to metal (0) by a reducing agent in the presence of phosphorus or boron source. In the case of borides, the reducing agent, borohydride, serves also as the source of elemental boron. Phosphorus sources commonly used are more diversified[19]. In the case of borides, such redox reactions, when used in molten salts, occur at the melting point of the salts in only few minutes[20]. They are then much faster than the approaches starting from elemental Ni nanoparticles. They also do not involve elemental metal intermediates, but instead form readily amorphous borides. As the involvement

of Ni(0) reagents or intermediates has been discussed above to favor the formation of phosphides, then the redox reactions may bring highly suited methods, both for their rate and for the absence of Ni(0) species in the course of the reactions.

a) Rietveld refinement on ternary Ni-B-P/ Ni_3P nanoparticles

We have investigated the formation of the two reported ternary phases of composition $Ni_xP_{1-y}B_y$, with x = 2 or 3. We have used mixtures of $NiCl_2$, $NaBH_4$ and P_{red} as precursors in the molten eutectic mixture LiCl:KCl (44:56 mass.), as this medium is more compatible for potential synchrotron-based *in situ* X-ray studies when a strong absorbance of the beam may be expected (incident beam energy of 18 keV). The initial P:Ni molar ratio is in accordance with the targeted ternary phase (0.7:3 and 0.4:2, respectively). The B:Ni molar ratio is fixed at 2:1 in agreement with equation (1). The overall reaction corresponds to the sum of equations (1) and (2):

$$x\ NiCl_2 + 2x\ NaBH_4 \rightarrow x\ Ni^{(0)} + 4x\ H_{2(g)} + 2x\ B^{(0)} + 2x\ NaCl \quad (1)$$

$$x\ Ni^{(0)} + (1-y)\ P_{red}^{(0)} + y\ B^{(0)} \rightarrow Ni_xP_{1-y}B_y \quad (2)$$

with x = 2 and y = 0.6, or x = 3 and y = 0.3.

Note that equation (1) is written as a tool to evaluate the amount of required reduced reagent to form the boride, it does describe the formation of actual $Ni^{(0)}$ intermediates. This ensure that the $Ni^{(II)}$ precursor is reduced to $Ni^{(0)}$; thus providing a large excess of boron with respect to the targeted stoichiometry. This unreacted boron excess is expected to form an amorphous shell on the surface of the nanoparticles, which may act as a growth restriction medium and as a passivation layer against oxidation, as reported for metal borides[16,20].

A mixture $NiCl_2$:$NaBH_4$:P_{red} = 3:6:0.7 at., aiming at the composition $Ni_3P_{0.7}B_{0.3}$, was reacted in molten LiCl:KCl at 600 °C with a plateau of 3 h. The associated powder XRD pattern (**Figure 5A**) presented the crystallization of $Ni_2B_{0.6}P_{0.4}$ and Ni_3P. This is confirmed by Rietveld refinement of the pattern by considering only Ni_3P (**Figure 5B**), only $Ni_2B_{0.6}P_{0.4}$ (**Figure 5C**) and a mixture of both (**Figure 5D**). The Ni_3P phase is not sufficient to account for all diffraction peaks. The best fit is obtained by considering $Ni_2B_{0.6}P_{0.4}$ together with Ni_3P. The corresponding cell parameters are in agreement with the reported ones for $Ni_2B_{0.6}P_{0.4}$ (space group *P-62m* (189), *a*=*b*= 5.820(2) Å, *c*= 3.139(3) Å *vs.* *a*=*b*= 5.803 Å, *c*= 3.100 Å as reference) and for Ni_3P (space group *I-4* (82), *a*=*b*= 9.007(1) Å, *c*= 4.374(1) Å *vs.* *a*=*b*= 8.9499 Å, *c*= 4.385 Å). Note that $Ni_2B_{0.6}P_{0.4}$ is isostructural with Ni_2P, but that the cell parameters are sufficiently different

to discriminate both phases by XRD (**Figure 5A**). Thus, the crystallization of the phosphide phase can be related to the excess of phosphorus introduced into the mixture (P:Ni = 0.7 at.) compared to the observed stoichiometry of the actually obtained ternary phase (P:Ni = 0.2 at.).

The crystallite sizes for $Ni_2B_{0.6}P_{0.4}$ and for Ni_3P are 22 and 12 nm, respectively. The weight fraction $Ni_2B_{0.6}P_{0.4}$:Ni_3P is 0.54:0.46. We note that the refinement with the two phases considers a quasi-equal contribution of the ternary and the Ni_3P phase with a strong difference of the crystallite size. According to TEM images (**Figure 5E-F**), the sample is polydisperse, made of aggregated particles with diameters ranging from 4 to 22 nm (**Figure 5G**), in agreement with the crystallite sizes. HRTEM and the corresponding FFT (**Figure 5F**) present the identification of a crystal plane belonging to $Ni_2B_{0.6}P_{0.4}$.

Finally, as expected, an amorphous matrix surrounding the particles is observed and ascribed to amorphous boron, according to previous reports on nickel borides[16].

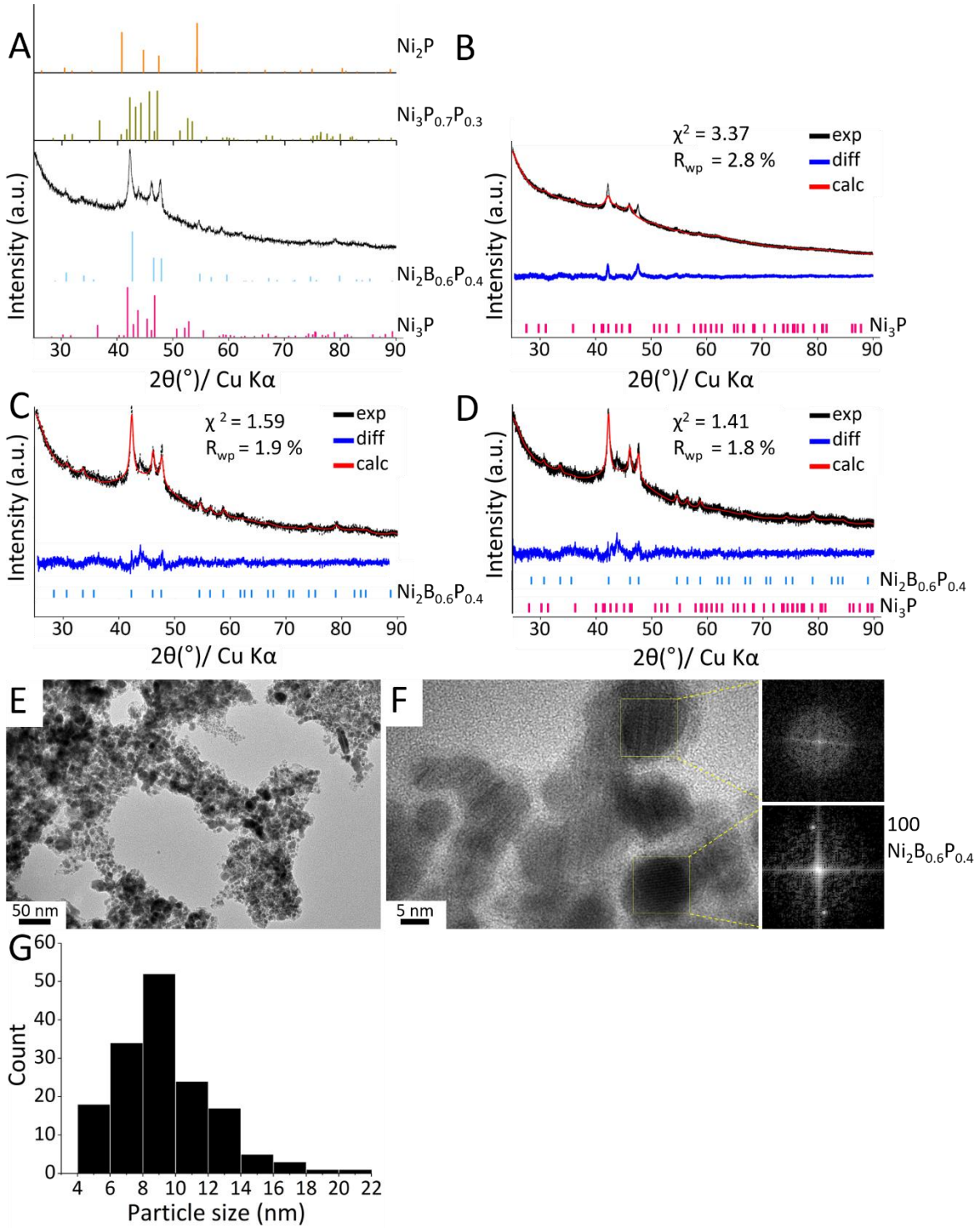

Figure 5. (A) Powder XRD pattern and corresponding Rietveld refinements performed by implementation of (B) Ni_3P, (C) $Ni_2B_{0.6}P_{0.4}$, (D) both Ni_3P and $Ni_2B_{0.6}P_{0.4}$. (E, F) TEM pictures including Fast Fourier Transform on selected particles, (G) Diagram of size distribution.

b) Screening of the optimal conditions for Ni-P-B ternary phases

To avoid the formation of Ni_3P and favor the formation of ternary phases, we have screened the stoichiometry, temperature and dwell time as experimental parameters. All syntheses were performed in the molten eutectic mixture LiCl:KCl with the precursors concentration fixed at 2 mmol of $NiCl_2$ per g of salts (**Figure S4-VIIA**). The results are summarized in **Figure 6A**. Increasing the dwell time and/or the temperature yields a secondary phase Ni_4B_3 in addition to the phases already observed in the previous section. If the temperature is decreased (450 °C/6 h), an amorphous phase attested by a broad diffraction peak appears in addition to the borophosphide, Ni_3P and nickel (0). The crystallization of Ni_4B_3 is not observed in this case.

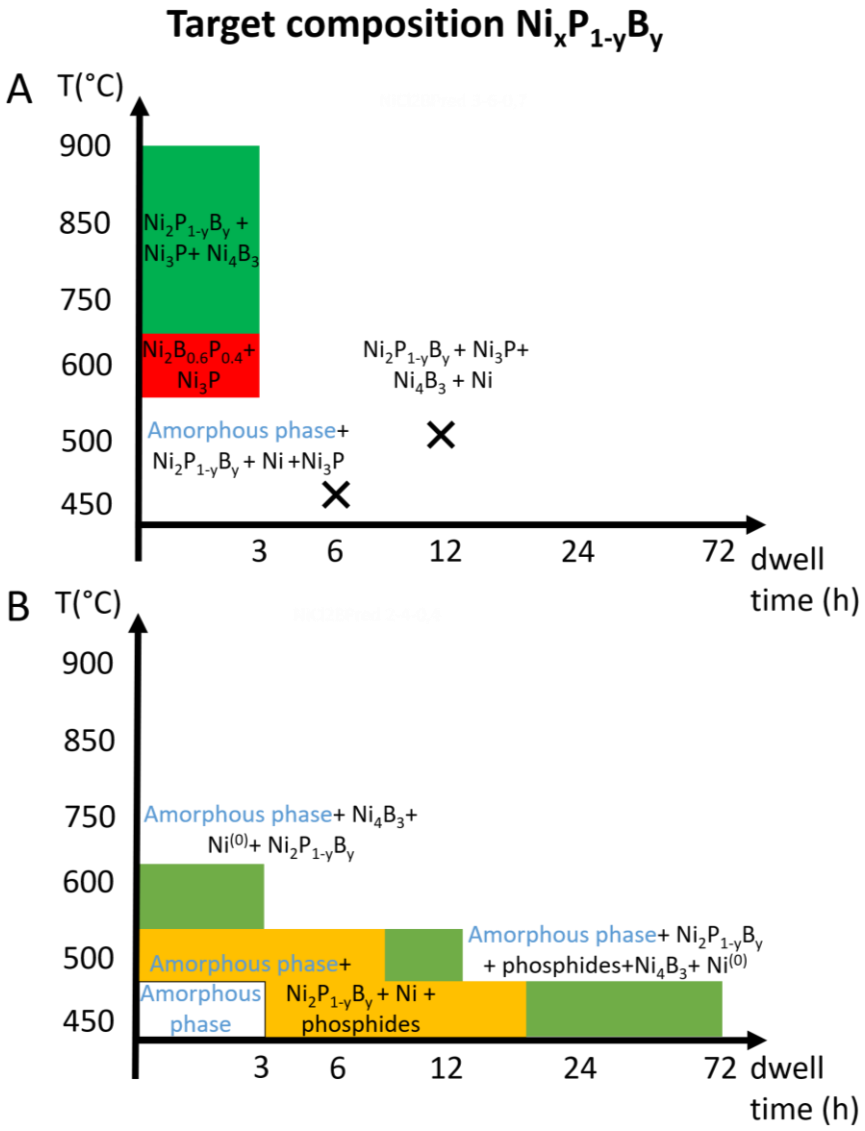

Figure 6. Screening of experimental conditions (dwell time, temperature *T*) performed to target reported Ni-B-P ternary phases using Ni:B:P ratios of (A) 3:6:0.7, (B) 2:4:0.4. The red area corresponds to the conditions of the Rietveld refinement described above, the green areas

correspond to a mixture of ternary $Ni_2P_yB_{1-y}$, phosphide(s) and Ni_4B_3. the orange area corresponds to a mixture of amorphous, ternary and phosphide phases.

We then adapted the initial reagents ratio to the ternary phase $Ni_2B_{0.6}P_{0.4}$ by applying a ratio P:Ni = 0.2 and maintaining the ratio B: Ni fixed by the reduction of $Ni^{(II)}$ to $Ni^{(0)}$ (**Figure 6B**, **Figure S4-VIIB**). Using the same synthesis conditions as in the previous section (red area in **Figure 6A:** 600 °C/3 h), an amorphous phase is detected together with a ternary phase $Ni_2B_yP_{1-y}$, nickel (0) and Ni_4B_3. Phosphides, including Ni_3P, are not detected. Lowering the temperature (450-500°C) by increasing the dwell time (3-72 h) leads first to an amorphous phase, then to a mixture of a ternary phase $Ni_2B_yP_{1-y}$ with nickel (0) and phosphides, and finally to the addition of Ni_4B_3 in this mixture, from 24 h at 450 °C. Although no condition could be found to reach pure $Ni_2B_yP_{1-y}$, several trends are distinguished:

- Despite the crystallization of Ni_3P isostructural with the borophosphide $Ni_3P_{0.7}B_{0.3}$ and Ni:B:P ratios compatible with the formation of this borophosphide, we did not observe such a ternary phase. Only the borophosphide $Ni_2P_{1-y}B_y$ isostructural to Ni_2P is observed. This suggests that $Ni_3P_{1-y}B_y$ is much less stable.
- Lowering the phosphorus content in the reagents ratio (from **Figure 6A** to **Figure 6B**) limits the crystallization of phosphides (Ni_3P is not observed anymore), but it is accompanied by a larger presence of nickel (0), which suggests that phosphides, and at least Ni_3P, may originate from a side reaction of phosphorus species with Ni(0). The same hypothesis was drawn from the study presented in the previous sections of this chapter.
- A large excess of boron results in the crystallization of Ni_4B_3 at long dwell time and/or high temperature. Again, in agreement with the other synthesis methods studied above, the phosphide crystallization precedes that of borides. However, by modifying the stoichiometry, the reactivity can be tuned, so that in most conditions the ternary phase is observed, although always mixed with phosphides, borides and even nickel (0).
- Low temperatures and/or short dwell times yield an XRD amorphous solid, with no feature of crystallized species for the stoichiometry Ni:B:P 2:4:0.4 (**Figure 6B** and **Figure S4-VIIB**).

We have then focused on the latter product. XRD shows that the solid is amorphous (**Figure 7A)**. TEM (**Figure 7B-C**) indicates partially aggregated particles of size ≈ 5-14 nm.

They are embedded into a poorly contrasted layer, ascribed to amorphous boron according to previous reports[16]. Among the particles that do not show any feature of local order according to HRTEM (**Figure 7C**) and the corresponding Fast Fourier Transform (FFT, **Figure 7D)**, several particles exhibit lattice fringes (**Figure 7C** and **7E**) indexed along the Ni_3P structure.

Energy Filtered TEM (EFTEM, **Figure 7F-H**) shows that the amorphous layer comprises boron but is exempt of Ni, as hypothesized above. EFTEM also shows that the Ni distribution in the particles is homogeneous. The B-K filtered image seems to indicate inhomogeneous distribution of boron, especially with some domains richer in boron within the same nanoparticles. STEM-EDX (**Figure 7I, J**) reveals the presence of phosphorus homogenously distributed at the scale of the sample. An analysis performed on selected particles (**Figure S4-VIII**) reveals two equivalent populations of particles depending on the P:Ni atomic ratio: 0.15 and 0.67 to 0.95. Overall, the sample seems heterogeneous at the nanoscale, even within a single particle. This may explain the further crystallization into a variety of phases. If such local heterogeneities may be at the origin of interesting properties in catalysis and in magnetism[21], they are particularly difficult to address in amorphous nano-objects, so that we did not pursue in this research direction.

Finally, another amorphous intermediate was detected for the Ni:B:P ratio 3:6:0.7 (**Figure 6A, Figure S4 VIIA**) at short dwell time (1-3 h) and 450 °C. It has not yet been studied, but we note that tuning the composition of an XRD amorphous ternary solid may provide new tracks to adjust properties, especially in water splitting electrocatalysis[4,1,22,].

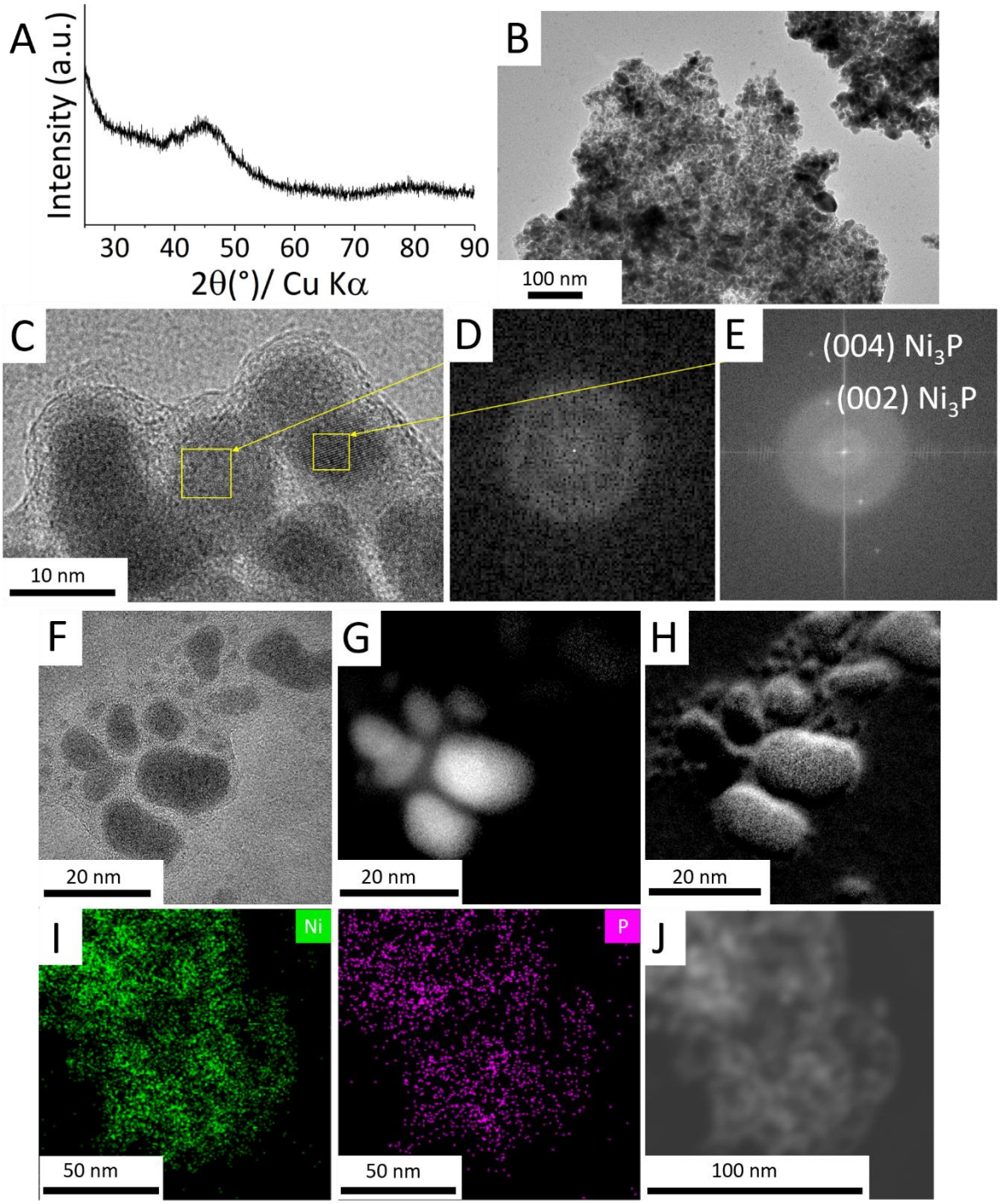

Figure 7. Nickel borophosphide obtained by reacting $NiCl_2$, $NaBH_4$ and P_{red} (2:4:0.4 at. ratio) at 450 °C/3 h in the molten eutectic mixture LiCl:KCl. (A) Powder XRD pattern, (B) TEM and (C) HRTEM images with (D-E) corresponding FFTs. (F) TEM and corresponding EFTEM images at the (G) Ni-L and (H) B-K edges. (I) STEM-EDX chemical maps of Ni and P with (J) the corresponding TEM image.

c) NaH as reducing agent

Equation (1) does not allow to adjust the B:Ni ratio, as the borohydride content in the initial reaction mixture is fixed by the required amount of reducing agent to bring Ni species to the elemental state. We have then incorporated NaH as an additional reducing agent, in order to adjust independently the boron content, according to equation (3):

$$x\ NiCl_2 + 2x\ NaH + x\ NaBH_4 = x\ Ni^{(0)} + 3x\ H_{2(g)} + x\ B^{(0)} + x\ Na_{(s)} + 2x\ NaCl \quad (3)$$

$NaBH_4$ and P_{red} were conserved as boron and phosphorus sources, respectively, and introduced in stoichiometric proportions. Using 600 °C/3 h as the reference conditions studied above (**Figure 6A**), the powder XRD pattern for the initial Ni:B:P ratio 3:0.39:0.7 (**Figure S4-IXb**) presented a highly crystalline Ni_3P phase mixed with $Ni^{(0)}$ and Ni_3B as minor phases. Modification of the stoichiometry towards phosphorus-rich (**Figure S4-VIXa**) and reversely boron-rich (**Figure S4-IXc)** compositions led to a predominance of Ni_3P in all cases. A secondary ternary phase $Ni_2B_{0.6}P_{0.4}$ may be indexed as a by-product of the boron-rich synthesis. TEM for the Ni:B:P = 3:0.39:0.7 sample (**Figure S4-IXd**) indicates anisotropic particles of hundreds nanometer size, in accordance with the highly resolved XRD pattern. No further evolution of the phosphide into a ternary phase was expected with respect to the attempts to incorporate boron into the phosphide nanoparticles discussed in the previous sections. Studies at higher temperatures/ longer dwell times confirmed the predominance of highly crystalline phosphide phases.

NaH is a strong reducing agent. Even at ambient temperature, the reduction of $Ni^{(II)}$ to $Ni^{(0)}$ occurs by mechanochemistry during mixing by ball milling. From the clues observed for the reactivity of nickel with boron and phosphorus; P should react rapidly with elemental nickel even before thermal decomposition of $NaBH_4$. This would explain the high crystallinity of the phosphide phase Ni_3P in parallel with the larger particles observed. The nature of the phosphide phase is related to the composition introduced, as Ni_3P is one of the most commonly reported metal-rich phosphide phases. Residual nickel (0) observed in all conditions studied (even at higher synthesis temperatures) could be related to the phosphorus content, in default *versus* the stoichiometry of Ni_3P.

Conclusion and perspectives

In this chapter, we have studied different ways to achieve nickel borophosphide phases. By focusing on boron-substituted Ni_2P and Ni_3P phases, which have been already reported from conventional solid-state chemistry, we have shown that the substituted Ni_2P structure is much easier to achieve than the Ni_3P one in mild reaction conditions ensured by molten salts syntheses.

We have been able to rank the relative stabilities of nickel phosphide and boride phases, showing that once phosphides are formed, they do not evolve further in the presence of a boron source, in the conditions of molten salts synthesis, hence at relatively low temperatures compared to conventional solid-state syntheses of borophosphides. This stability ranking goes along with the relatives reactivities of a boron source (borohydride) and a phosphorus source (red phosphorus) *versus* elemental nickel, as the latter readily reacts with the P source to form a phosphide. An excess of boron tends to limit to a certain extent the crystallization of phosphides, which shows competitive incorporation of B and P into Ni(0). Nonetheless, these considerations indicate that Ni(0) and nickel phosphide reagents or intermediates must be avoided to make possible the recovery of borophosphides at mild temperatures. For this reason, the most promising approaches are the use of nickel boride nanoparticles as reagents, or the use of a redox reaction involving Ni(II) precursors, to associate simultaneously B and P with Ni(0).

The strategy based on boride precursors showed reluctant crystallization of phosphides, and possible crystallization of borophosphide phases. The fact that Ni(0) is detected in some conditions relates to a “dealloying” of the borides. We hypothesize that this behavior may originate from (hydro)oxo species formed at the surface of the boride nanoparticles during their washing. These species may scavenge boron atoms from the boride. The resulting Ni(0) is then engaged into phosphide formation, in the main path identified above. Hence, future work on this research track will require bypassing the oxidizing boride recovery conditions, which could be performed either by harsh drying of the borides after washing, or by avoiding washing, for instance by hot injection of the phosphorus precursor in the reaction mixture once the nickel boride nanoparticles are formed. It would also be possible to wash the boride nanoparticles in contact with phosphine ligands, which could passivate the borides during washing and act as P source in a second step.

The strategy based on the one-pot fast redox reactivity of a Ni(II) salt showed partial success, as a ternary phase $Ni_2B_yP_{1-y}$ could be identified, although always mixed with other phases, especially Ni(0) and Ni_3P, which suggests that B and P are not homogeneously incorporated into the amorphous reaction intermediate. This heterogeneity of the amorphous intermediate was confirmed by TEM, thus showing that the redox reaction at play is not fast enough to avoid B and P segregation. Future tracks on this research line may involve triggering faster reactions, for example by using high heating ramps, with microwave or induction heating. As a perspective, variation of the stoichiometries of the constituents could lead to adjustable nanoscale amorphous ternary phases, either homogenous or with local heterogeneities. These solids may be of particular interest for water splitting electrocatalysis, and their precise compositional adjustment could deeply modify their properties.

Annexes

Experimental methods

Reagents. Nickel (II) acetylacetonate ($Ni(acac)_2$, 95%, Strem Chemicals), nickel (II) chloride ($NiCl_2$, 99%, Alfa Aesar), trioctylphosphine (TOP, 97%, $P(C_8H_{16})_3$, Strem Chemicals), sodium borohydride ($NaBH_4$, min 98%, Alfa Aesar), red phosphorus (P_{red}, 97%, Merck), sodium hydride (NaH, 90%, Sigma-Aldrich), sodium hypophosphite (NaH_2PO_2, 98%, Sigma-Aldrich), anhydrous hexane (95%, Sigma-Aldrich), lithium iodide (99%, Alfa Aesar), potassium iodide (99%, Sigma-Aldrich), lithium chloride (99.9% Alfa Aesar), potassium chloride (99.9% Sigma-Aldrich) were stored and manipulated as received in an Ar-filled glovebox (H_2O < 0.5 ppm, O_2 < 0.5 ppm). Oleylamine (98 %, SAFC), dioctylether (99%, Aldrich), Ammonia solution (28-30%, Merck), Hydrochloric acid (37 %, Carlo Erba), nickel (II) chloride hexahydrate (97 %, Acros), Sodium acetate (NaAc, Sigma-Aldrich) Potassium hydroxide flakes (≥85 %, Sigma-Aldrich) were stored and used in air. Acetone (VWR Normapur grade), tetrahydrofuran (THF, VWR Normapur grade), methanol (VWR Normapur grade) were used for washing. All water used is purified by the Milli Q® system.

Nickel phosphide synthesis procedures

a) Synthesis method of Ni_2P nanoparticles[12]

10 ml of dioctylether (33.2 mmol) and 9.35 g of oleylamine 98 % (34.9 mmol) were introduced in a schlenk tube degassed under vacuum ramp for 30 minutes with manual mixing. Meanwhile, 0.585g of $Ni(acac)_2$ (2 mmol) were introduced in a schlenk tube in a glovebox and the tube was placed under argon on a vacuum ramp. The degassed solvent mixture as then introduced with a syringe in the schlenk containing the nickel precursor and finally 5 mL of TOP (11.2 mmol) were added to the mixture with a syringe. The schlenk tube was adapted on a vertical oven under argon flow and heated at 350 °C/2 h. After cooling, the product was washed once by adding a mixture of ≈ 10-20 mL THF and ≈ 40 mL acetone to the reaction medium and centrifugation. Nine other washing cycles were performed by first adding ≈ 10-20 mL THF, dispersing by sonication and then adding ≈ 40 mL acetone to reprecipitate the particles during centrifugation. The particles were then dried under vacuum ramp and stored in a glovebox. Around 167 mg (1.12 mmol) of powder was obtained, corresponding to a yield of 56 % related to pure Ni_2P.

b) Synthesis of porous hollow Ni_3P nanosphere[13]

100 mL of deionized water introduced into a three-necked flask was degassed three times on a N_2/ vacuum ramp and maintained under nitrogen atmosphere. 2.9 g (35.3 mmol) sodium acetate (NaAc), 5g (21.0 mmol) $NiCl_2.6H_2O$ and 24.4 g (0.23 mol) NaH_2PO_2 were added and the pH was adjusted to 8 by adding around 3 mL KOH 10M. The pH value was checked with a pH indicator paper. The solution was heated at 90 °C for 1 h under nitrogen atmosphere. After cooling, the black precipitate was decanted for 1 h to eliminate the solvent. A mixture of ammonia solution (25-28 wt. %) was used to disperse the particles and deionized water was used to reprecipitate these particles by centrifugation. Five cycles of washing were done before drying under vacuum of the particles dispersed in the ammonia solution. The obtained amorphous nanoparticles were then introduced in a molybdenum crucible in a glovebox and annealed at 500 °C for 1 h under argon flow to form the $Ni@Ni_3P$ nanoparticles. Then, under stirring, the particles were etched for 24 h under nitrogen flow with HCl 37% aq. previously degassed three times on a vacuum ramp. The resulting particles were finally washed similarly to the previous step and dried under vacuum to obtain the porous hollow nanospheres.

Ternary nickel-boron-phosphorus synthesis procedure

a) Molten salts-based reaction of nickel (0) with $NaBH_4$ and red phosphorus (P_{red})/ trioctylphosphine (TOP)

100 mg of nickel nanoparticles (1.70 mmol) were weighted in a glovebox, introduced in a Schlenk tube and degassed three times N_2/vacuum ramp. The tube was then maintained under nitrogen atmosphere. 1.6 mL of anhydrous hexane previously prepared in glove box is quickly added under N_2 flow and the mixture was sonicated for at least 20 minutes. 5 g of LiI:KI (58:42 mass.), P_{red}/ TOP and $NaBH_4$ prepared in a glove box were quickly added to the impregnation mixture. A quick purge under vacuum was performed after addition of the reagents. The mixture was then sonicated for 10-15 minutes before placing the tube under vacuum to remove the hexane. The powder as then placed in a molybdenum crucible in a quartz tube inside a glovebox. A vertical oven maintained under argon was used for the heating step with a ramp of 10°C/min and the product was naturally cooled down. 10 cycles of washing with methanol by dispersion-reprecipitation by centrifugation (41415 g/ 21 000 rpm) were performed to separate the salt from the product. The final product was dried under vacuum on a schlenk line and kept in a glove box.

b) Molten salts-based reaction of $NaBH_4$ with Ni_xP particles

100 mg of Ni_2P (0.67 mmol), respectively Ni_3P (0.48 mmol), were weighted in a glovebox, introduced in a Schlenk tube and degassed three times on a N_2/vacuum ramp. The tube was then maintained under nitrogen atmosphere. 1.6 mL of anhydrous hexane previously prepared in the glovebox was quickly added under N_2 flow and the mixture was sonicated for at least 20 minutes. 5g of LiI:KI (58:42 mass.) prepared in a glovebox was quickly added to the mixture and the Schlenk tube was rapidly degassed and (re)flushed with N_2 to remove all potential oxygen entrance. The tube was then placed under vacuum to remove the solvent.

The recovered black powder was weighted in a glovebox. An adjusted amount of $NaBH_4$ was added and the reagents were introduced in a milling jar. Ball milling was performed for 2 min at 20 Hz. After re-introduction in the glovebox, the powder was placed in a molybdenum crucible inside a quartz tube and adapted on a tubular oven under argon flow. The targeted heating conditions were adapted according to a calibration curve. The tube was then naturally cooled after the synthesis. The product was extracted by dissolution of the salt in methanol. 10 cycles of washing with methanol by dispersion-reprecipitation by centrifugation (41415 g/ 21 000 rpm) were performed to separate the salt from the product. The final product was dried under vacuum on a schlenk line and kept in a glove box.

c) Molten salts-based reaction of red phosphorus with Ni_xB_y particles

40 mg of Ni_3B (0.21 mmol)/ Ni_4B_3 (0.15 mmol) nanoparticles were weighted in a glovebox with LiI:KI (58:42 mass., 0.4 mmol Ni_xB_y per g of salts) and red phosphorus in a ball milling jar. Ball milling was performed for 2 min at 20 Hz. Then, the recovered powder was placed in a molybdenum crucible in a quartz tube and adapted on a tubular oven under Ar flow. The synthesis temperature was adjusted according to a calibration curve. The tube was then naturally cooled to room temperature. Thereafter, 10 cycles of washing by dispersion-reprecipitation by centrifugation with methanol were performed. Finally, the product was dried under vacuum on a Schlenk line and stored in a glove box.

d) Ternary phase synthesis from $NiCl_2$, $NaBH_4$, red phosphorus (and NaH) in the molten eutectic mixture LiCl:KCl

50 mg of $NiCl_2$ (0.39 mmol) as starting material was weighted with the corresponding $NaBH_4$ and red phosphorus amounts inside a glovebox. For the case studies with NaH, an atomic ratio NaH:Ni = 5:1 was fixed. The reagents were placed in a ball milling jar and mixed for 2 min at

20 Hz before re-introduction in the glove box. The mixed powder was introduced in a carbon crucible inside a quartz tube for the mixtures without NaH and molybdenum crucible for the syntheses with NaH. Using NaH with a carbon crucible leads to breakage of the crucible supposedly due to the insertion of $Na_{(s)}$ inside glassy carbon. The quartz tube was then adapted on a tubular oven under argon for the synthesis. After natural cooling down, 10 cycles of washing by methanol similarly to the other methods were performed before drying the final product on a vacuum ramp.

Supplementary data for chapter 4

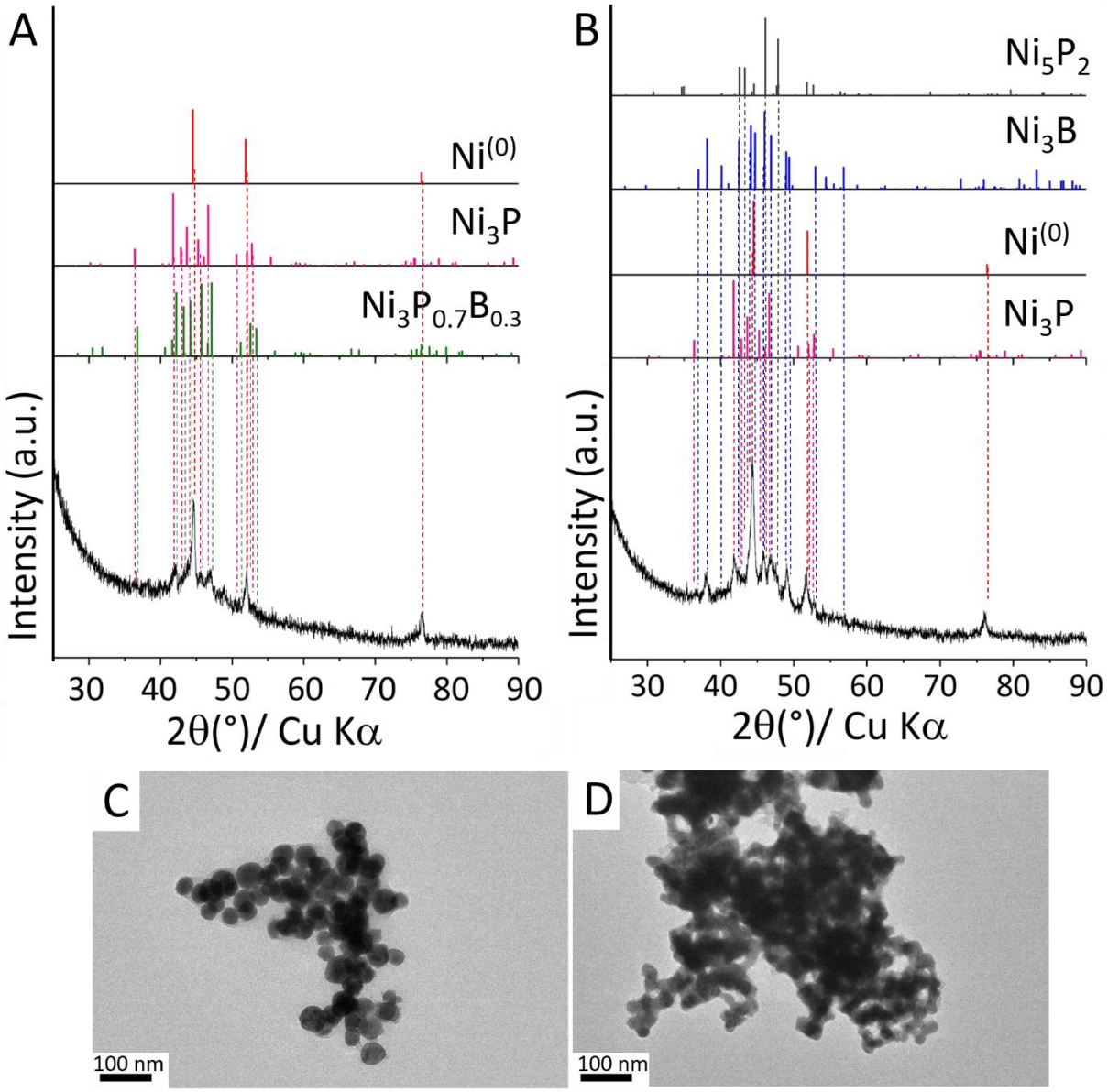

Figure S4-I. Powder XRD patterns of sample prepared in the LiI:KI eutectic mixture at 475 °C for 1.5 h with initial Ni:B:TOP ratios (A) 2:1:0.4 and (B) 3:0.6:0.7. Corresponding TEM pictures in (C) and (D), respectively.

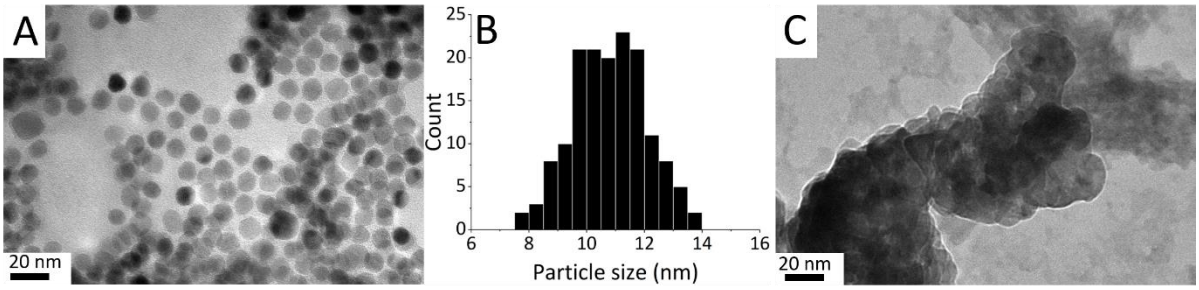

Figure S4-II. TEM image of (A) Ni_2P nanoparticles with (B) corresponding size distribution. (C) TEM image of a Ni_3P sample.

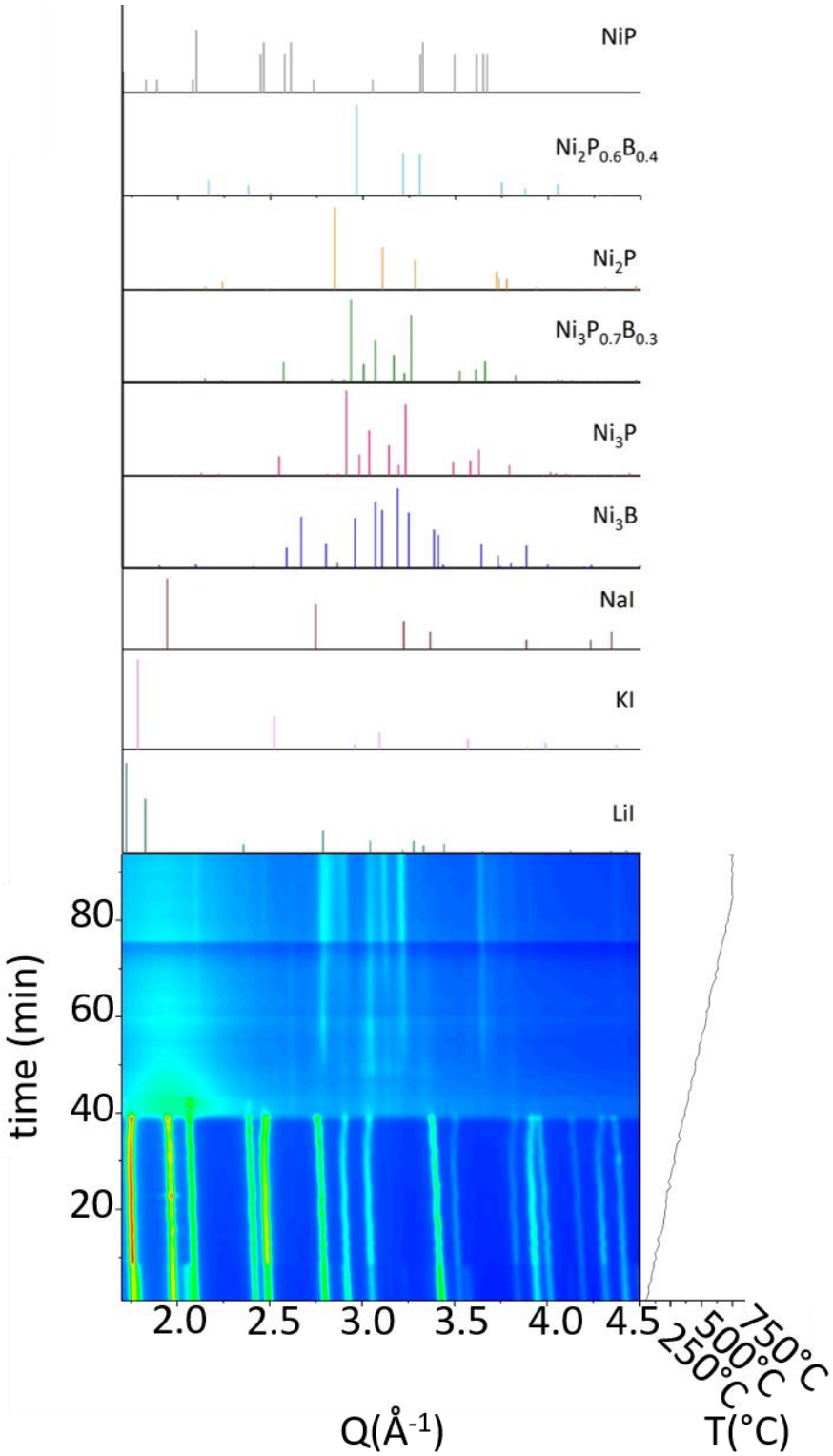

Figure S4-III. *In situ* XRD diagrams recorded during the reaction of Ni_3B with red phosphorus with the ratio $Ni_3B:P_{red}$ = 1:0.7 at. in the eutectic mixture LiI:KI.

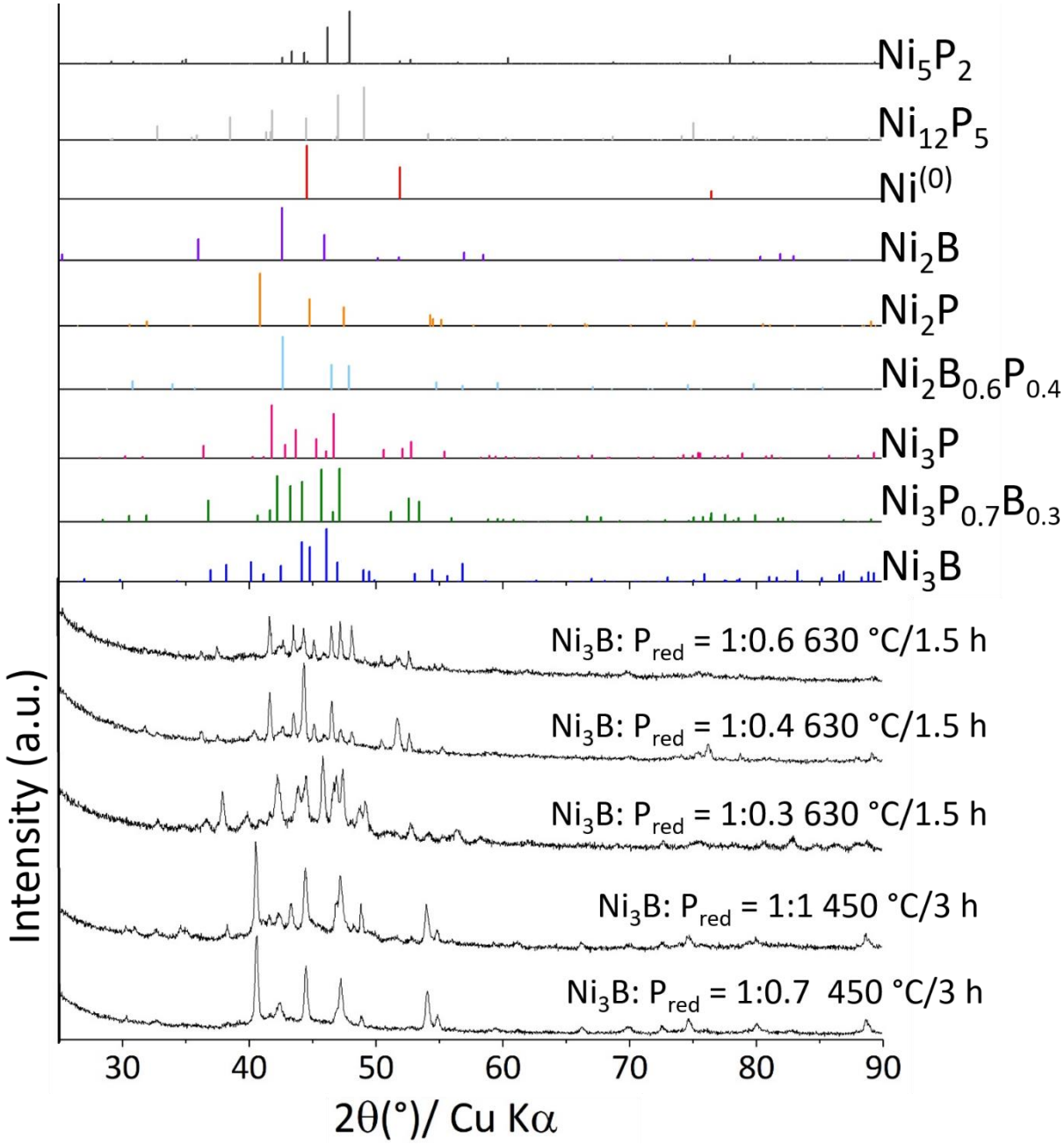

Figure S4-IV. Powder XRD patterns of the products obtained from the reaction of red phosphorus with Ni_3B nanoparticles in the molten eutectic mixture LiI:KI. and (B) nanoparticles.

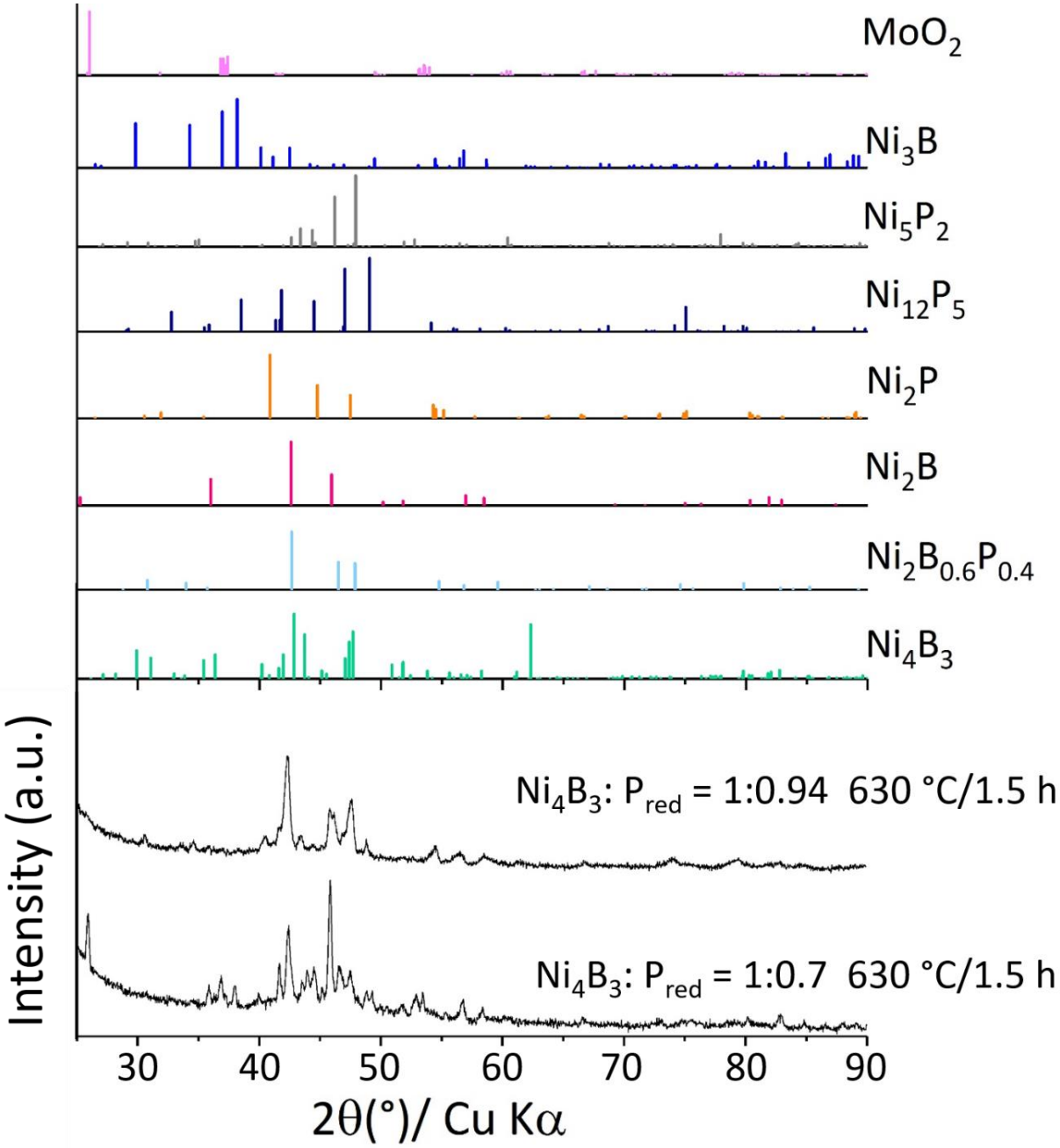

Figure S4-V. Powder XRD patterns of the products obtained from the reaction of red phosphorus with Ni_4B_3 nanoparticles in the molten eutectic mixture LiI:KI.

Table S4-I. Phases indexation of the XRD diagrams shown in **Figure S4-IV** and **Figure S4-V**.

Synthesis conditions	Phases observed
Ni_3B:P (1:0.7) 450 °C/ 3h	Ni_2P, $Ni_{12}P_5$, $Ni_3P_{0.7}B_{0.3}$
Ni_3B:P (1:1) 450 °C/ 3h	Ni_2P, Ni_3P, $Ni_{12}P_5$, $Ni_3P_{0.7}B_{0.3}$
Ni_3B:P (1:0.3) 630 °C/ 1.5 h	Ni_3B, Ni_3P, Ni_5P_2
Ni_3B:P (1:0.4) 630 °C/ 1.5 h	Ni_3P, Ni, Ni_5P_4, $Ni_2B_{0.6}P_{0.4}$
Ni_3B:P (1:0.6) 630 °C/ 1.5 h	$Ni_3P_{0.7}B_{0.3}$, Ni, Ni_3P, $Ni_2B_{0.6}P_{0.4}$, $Ni_3P_{0.7}B_{0.3}$
Ni_4B_3:P (1:0.7) 630 °C/ 1.5 h	Ni_4B_3, $Ni_{12}P_5$, Ni_2B, Ni_3B, MoO_2
Ni_4B_3:P (1:0.94) 630 °C/1.5 h	$Ni_2B_{0.6}P_{0.4}$, Ni_2P, Ni_5P_2

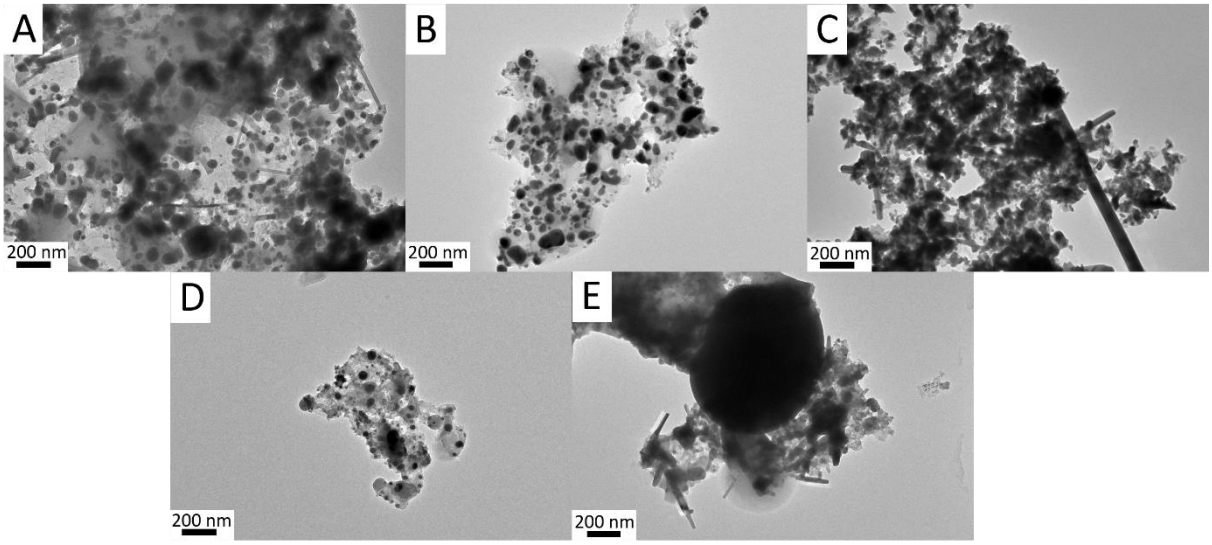

Figure S4-VI. TEM pictures of the products of reactions between nickel borides and red phosphorus into the molten eutectic mixture LiI:KI, from (A-C) Ni_3B and (D-E) Ni_4B_3. Reaction conditions from Ni_3B are (A) $Ni_3B:P_{red}$ = 1:0.4 at 630 °C for 1.5 h, (B) $Ni_3B:P_{red}$ = 1:0.6 at 630 °C for 1.5 h, (C) $Ni_3B:P_{red}$ = 1:1 at 450 °C for 3 h. Reaction conditions from Ni_4B_3 are (D) $Ni_4B_3:P_{red}$ = 1:0.5 at 630 °C for 1.5 h, (E) $Ni_4B_3:P_{red}$ = 1:0.94 at 630 °C for 1.5 h.

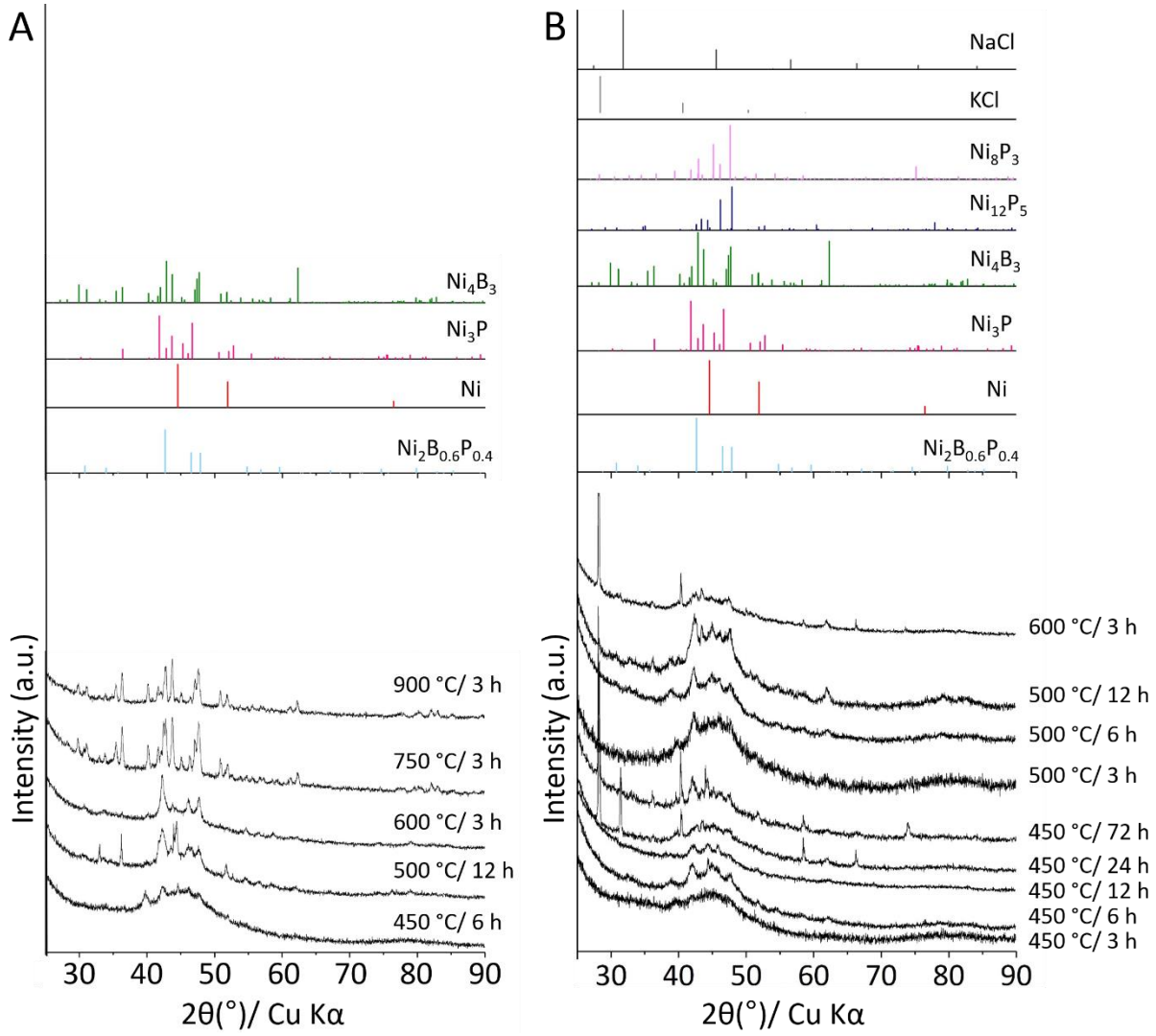

Figure S4-VII. Powder XRD patterns of the powders obtained from the reaction of $NiCl_2$, $NaBH_4$ and P_{red} in the molten eutectic mixture LiCl:KCl performed to target reported Ni-B-P ternary phases using Ni:B:P atomic ratio of (A) 3:6:0.7 and (B) 2:4:0.4. Some KCl and NaCl remains in some powder due to inefficient washing.

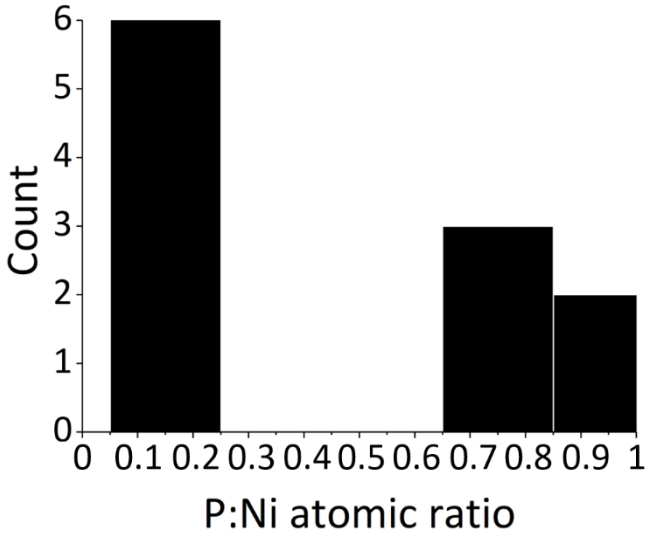

Figure S4-VIII. P:Ni atomic ratio distribution observed by STEM-EDX on 11 single particles from the sample obtained by the reaction of $NiCl_2$, $NaBH_4$ and P_{red} (2:4:0.4 at. ratio) at 600 °C for 3h in the molten eutectic mixture LiCl:KCl.

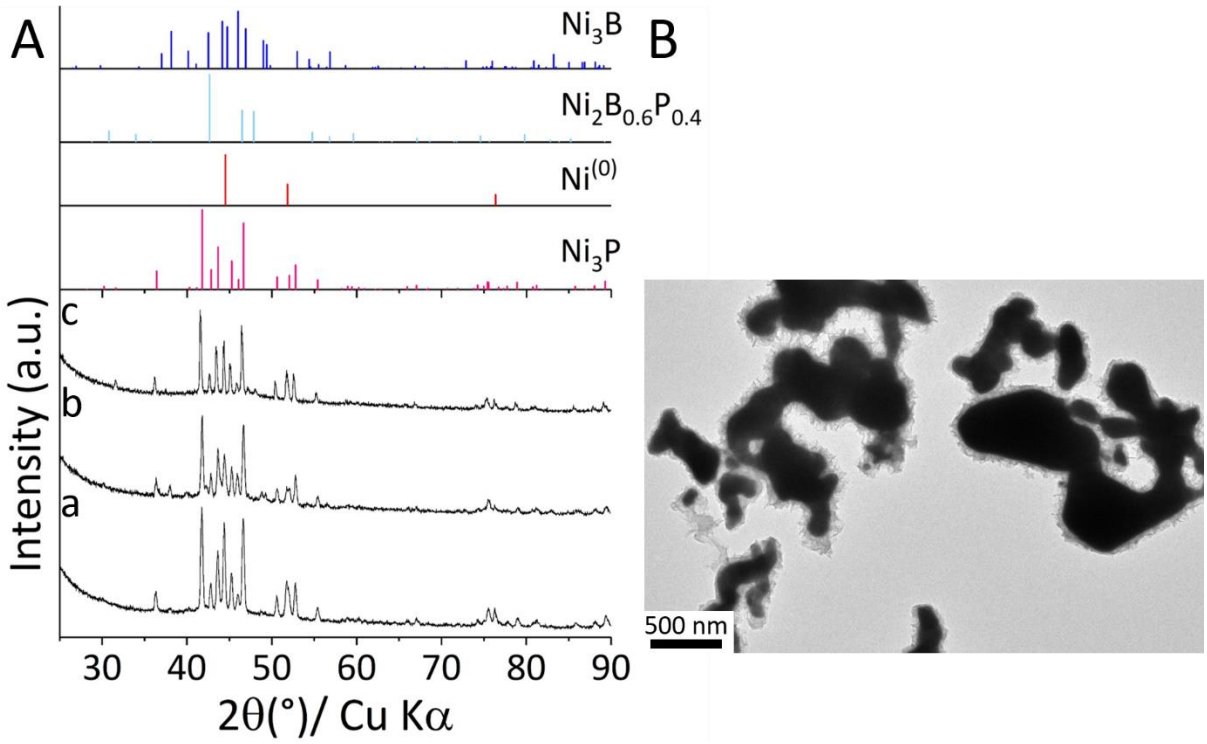

Figure S4-IX. (a-c) XRD diagrams of the powders obtained by reacting $NiCl_2$, $NaBH_4$ and P_{red} with a large excess of NaH in the molten eutectic mixture LiCl:KCl. With initial reagents ratios Ni:B:P (a) 3:0.25:0.75, (b) 3:0.39:0.7, (c) 3:0.75:0.25 at 600 °C/3 h. (d) TEM image of powder obtained with the ratio 3:0.39:0.7

References

(1) Carenco, S.; Portehault, D.; Boissière, C.; Mézailles, N.; Sanchez, C. Nanoscaled Metal Borides and Phosphides: Recent Developments and Perspectives. *Chem. Rev.* **2013**, *113* (10), 7981–8065. https://doi.org/10.1021/cr400020d.

(2) Ling, C.; Zhang, Y.; Li, Q.; Bai, X.; Shi, L.; Wang, J. New Mechanism for N2 Reduction: The Essential Role of Surface Hydrogenation. *J. Am. Chem. Soc.* **2019**, *141* (45), 18264–18270. https://doi.org/10.1021/jacs.9b09232.

(3) Sun, H.; Meng, J.; Jiao, L.; Cheng, F.; Chen, J. A Review of Transition-Metal Boride/Phosphide-Based Materials for Catalytic Hydrogen Generation from Hydrolysis of Boron-Hydrides. *Inorg. Chem. Front.* **2018**, *5* (4), 760–772. https://doi.org/10.1039/c8qi00044a.

(4) Liu, X.; Wu, J.; Guo, X. Ternary Boron-, Phosphorus- and Oxygen-Doped Amorphous Nickel Nanoalloys for Enhanced Activity towards the Oxygen Evolution Reaction. *Electrochem. commun.* **2020**, *111*, 106649. https://doi.org/10.1016/j.elecom.2019.106649.

(5) International Centre for Diffraction Data. PDF 4+ Database https://www.icdd.com/pdfsearch/ (accessed Jul 11, 2023).

(6) Mikhalenko S.I., Chernogorenko V.B., Kuz`ma Yu.B., Muchnik S.V., L. Y. V. Phase Equilibria in the Ni-B-P System. *Inorg. Mater. (Engl. Transl.); (United States)* **1984**, *20*, 1507.

(7) Deng, Y.; Zhou, Y.; Yao, Y.; Wang, J. Facile Synthesis of Nanosized Nickel Phosphides with Controllable Phase and Morphology. *New J. Chem.* **2013**, *37* (12), 4083–4088. https://doi.org/10.1039/c3nj00665d.

(8) Gouget, G.; Debecker, D. P.; Kim, A.; Olivieri, G.; Gallet, J. J.; Bournel, F.; Thomas, C.; Ersen, O.; Moldovan, S.; Sanchez, C.; Carenco, S.; Portehault, D. In Situ Solid-Gas Reactivity of Nanoscaled Metal Borides from Molten Salt Synthesis. *Inorg. Chem.* **2017**, *56* (15), 9225–9234. https://doi.org/10.1021/acs.inorgchem.7b01279.

(9) Wang, J.; Johnston-Peck, A. C.; Tracy, J. B. Nickel Phosphide Nanoparticles with Hollow, Solid, and Amorphous Structures. *Chem. Mater.* **2009**, *21* (19), 4462–4467. https://doi.org/10.1021/cm901073k.

(10) García-Muelas, R.; Li, Q.; López, N. Initial Stages in the Formation of Nickel Phosphides. *J. Phys. Chem. B* **2018**, *122* (2), 672–678. https://doi.org/10.1021/acs.jpcb.7b06020.

(11) Henkes, A. E.; Vasquez, Y.; Schaak, R. E. Converting Metals into Phosphides: A General Strategy for the Synthesis of Metal Phosphide Nanocrystals. *J. Am. Chem. Soc.* **2007**, *129* (7), 1896–1897. https://doi.org/10.1021/ja068502l.

(12) Moreau, L. M.; Ha, D. H.; Zhang, H.; Hovden, R.; Muller, D. A.; Robinson, R. D. Defining Crystalline/Amorphous Phases of Nanoparticles through X-Ray Absorption Spectroscopy and X-Ray Diffraction: The Case of Nickel Phosphide. *Chem. Mater.* **2013**, *25* (12), 2394–2403. https://doi.org/10.1021/cm303490y.

(13) Jin, L.; Xia, H.; Huang, Z.; Lv, C.; Wang, J.; Humphrey, M. G.; Zhang, C. Phase Separation Synthesis of Trinickel Monophosphide Porous Hollow Nanospheres for Efficient Hydrogen Evolution. *J. Mater. Chem. A* **2016**, *4* (28), 10925–10932. https://doi.org/10.1039/c6ta03028a.

(14) Kayser, G. F.; Kayser, F. X. Ni3B: Powder Diffraction Pattern and Lattice Parameters. *J. Alloys Compd.* **1996**, *233* (1–2), 74–79. https://doi.org/10.1016/0925-8388(96)80037-5.

(15) Shahbazi, M.; Cathey, H.; Danilova, N.; Mackinnon, I. D. R. Single Step Process for Crystalline Ni-B Compounds. *Materials (Basel).* **2018**, *10* (7). https://doi.org/10.3390/ma11071259.

(16) Gouget, G.; Beaunier, P.; Portehault, D.; Sanchez, C. New Route toward Nanosized Crystalline Metal Borides with Tuneable Stoichiometry and Variable Morphologies. *Faraday Discuss.* **2016**, *191*, 511–525. https://doi.org/10.1039/c6fd00053c.

(17) Hong, J.; Mutalik, S.; Miola, M.; Gerlach, D.; K, R. M.; Ahmadi, M.; Kooi, B. J.; Portale, G.; Rudolf, P.; Pescarmona, P. P.; Protesescu, L. Nickel Boride (NixB) Nanocrystals: From Solid-State Synthesis to Highly Colloidally Stable Inks. **2023**. https://doi.org/10.1021/acs.chemmater.2c03478.

(18) Jothi, P. R.; Yubuta, K.; Fokwa, B. P. T. A Simple, General Synthetic Route toward Nanoscale Transition Metal Borides. *Adv. Mater.* **2018**, *30* (14). https://doi.org/10.1002/adma.201704181.

(19) Pu, Z.; Liu, T.; Amiinu, I. S.; Cheng, R.; Wang, P.; Zhang, C.; Ji, P.; Hu, W.; Liu, J.; Mu, S. Transition-Metal Phosphides: Activity Origin, Energy-Related Electrocatalysis Applications, and Synthetic Strategies. *Adv. Funct. Mater.* **2020**, *30* (45), 1–23. https://doi.org/10.1002/adfm.202004009.

(20) Portehault, D.; Devi, S.; Beaunier, P.; Gervais, C.; Giordano, C.; Sanchez, C.; Antonietti, M. A General Solution Route toward Metal Boride Nanocrystals. *Angew. Chemie - Int. Ed.* **2011**, *50* (14), 3262–3265. https://doi.org/10.1002/anie.201006810.

(21) Song, Y.; Isabel, G.; Ghoridi, A.; Igoa, F.; Janisch, D.; Sassoye, C.; Dupuis, V.; Hrabovsky, D.; Ruiz-gonz, M. L.; Gonz, M.; Casale, S.; Zitolo, A.; Lassalle-kaiser, B.; Laberty-robert, C.; Portehault, D. Heterostructured Cobalt Silicide Nanocrystals: Synthesis in Molten Salts, Ferromagnetism, and Electrocatalysis. *J. Am. Chem. Soc.* **2023**. https://doi.org/10.1021/jacs.3c01110.

(22) Masa, J.; Andronescu, C.; Antoni, H.; Sinev, I.; Seisel, S.; Elumeeva, K.; Barwe, S.; Marti-Sanchez, S.; Arbiol, J.; Roldan Cuenya, B.; Muhler, M.; Schuhmann, W. Role of Boron and Phosphorus in Enhanced Electrocatalytic Oxygen Evolution by Nickel Borides and Nickel Phosphides. *ChemElectroChem* **2019**, *6* (1), 235–240. https://doi.org/10.1002/celc.201800669.

Chapter 5: Conversion of core-shell metal nanoparticles as a path towards bimetallic borides

I) Introduction: bimetallic nickel cobalt borides structures: a way to improve the properties

Bimetallic borides comprising first row transition metals are of particular interest to design electrocatalysts for water splitting. Indeed, single metal borides are efficient electrocatalysts for for both half-reactions of water splitting: the hydrogen evolution reaction (HER) and the oxygen evolution reaction (OER)[1–10]. Nickel borides are highly active catalysts for acidic HER (Chapter 3). They are also pre-catalysts for alkaline OER (Chapter 3), like cobalt borides[9,11]. While bimetallic cobalt and iron borides have demonstrated the ability to operate as bifunctional electrocatalysts[12,13] with higher performances than monometallic CoB and FeB, bimetallic nickel and cobalt borides also provide highly active electrocatalyst materials for water splitting, even better than the monometallic borides[6,14–22].

As discussed in chapter 3 and in the literature[6,10,14,23–25], the active sites are different for HER and OER driven on metal boride catalysts. While acidic HER active sites seem to relate to the pristine borides[15,22], in alkaline OER conditions the boride surface undergoes oxidation and formation of OER active oxyhydroxides, especially CoOOH and NiOOH[7,18,26,27]. DFT calculations on bulk Ni-Co_2B showed that the formation of the Ni and Co oxyhydroxides involves a lower energy barrier than for monometallic Co_2B, due to a regulation of the electronic structure on the Co-Co bridge-sites and Co site as active sites during OER. This fast surface transformation overall results readily in an electrocatalytic active material[19]. The resulting bimetallic oxyhydroxide exhibits higher OER electrocatalytic activity compared to their monometallic Ni and Co counterparts[28].

While bimetallic nickel cobalt borides are attractive materials as HER electrocatalysts and OER pre-catalysts, few previous works have attempted the synthesis of such ternary Co-Ni-B compounds. Preparation methods for bulk and nanoscale Co-Ni-B materials are generally based on the co-reduction of metal precursors either by a chemical reducing agent in aqueous solutions or by electrodeposition on a support[15–18,21,22,29–34]. Solid-state boronization of a CoNi foam has also been attempted [19]. The resulting products are usually amorphous and yield upon annealing mixtures of phases including borides and single metals, thus indicating local inhomogeneities[15–17,19,22,29–34]. Avoiding phase segregation in nickel cobalt borides to form a bimetallic structure is therefore challenging.

Successful approaches in this direction have been developed for metal-rich borides. Through a series of arc melting and subsequent undercooling, metastable Co-Ni-B alloys have been

obtained at the bulk scale[35]. The resulting alloys have a composition of $(Co_{1-x}Ni_x)_{79.3}B_{20.7}$ (x = 0, 0.25, 0.5, 0.75, 1). At large undercoolings, these alloys form $M_{23}B_6$ (M = Co or/and Ni) metastable phases. For solids richer in boron, homogeneous nanoscale borides $(Co_{1-x}Ni_x)_2B$ (x ϵ [0.1-0.2]) have been prepared by co-reduction of Co^{II} and Ni^{II} precursors using $NaBH_4$ in an aqueous solution[18], followed by annealing at 500 °C. A solid solution between Co_2B and Ni_2B was obtained, in agreement with their Au_2Cu-type structures. For compositions richer in nickel (x ϵ]0.2-0.5]), the Ni_3B by-product was obtained. The material was polydisperse in morphology, forming a nanoscale porous rod-like structure, with OER electrocatalytic performances enhanced for $x \leq 0.2$ compared to Co_2B obtained by a similar method.

Other nickel cobalt boride compositions should be within reach given structural similarities (**Figure 1**). Indeed, while Co_2B and Ni_2B crystallize both in the Au_2Cu-type structure (S.G. *I4/mcm*), Co_3B and Ni_3B crystallize in the same cementite structure (S.G. *Pnma*) [11,36], while CoB and NiB crystallize respectively in the β-FeB and CrB structures, which are closely related, as we have recently discussed[37–39]. Therefore, solid solutions $(Co_{1-\delta}Ni_\delta)_xB$ (x = 1, 2, 3), different than those reported for Co_2B and Ni_2B[18,40] may be reasonably within reach.

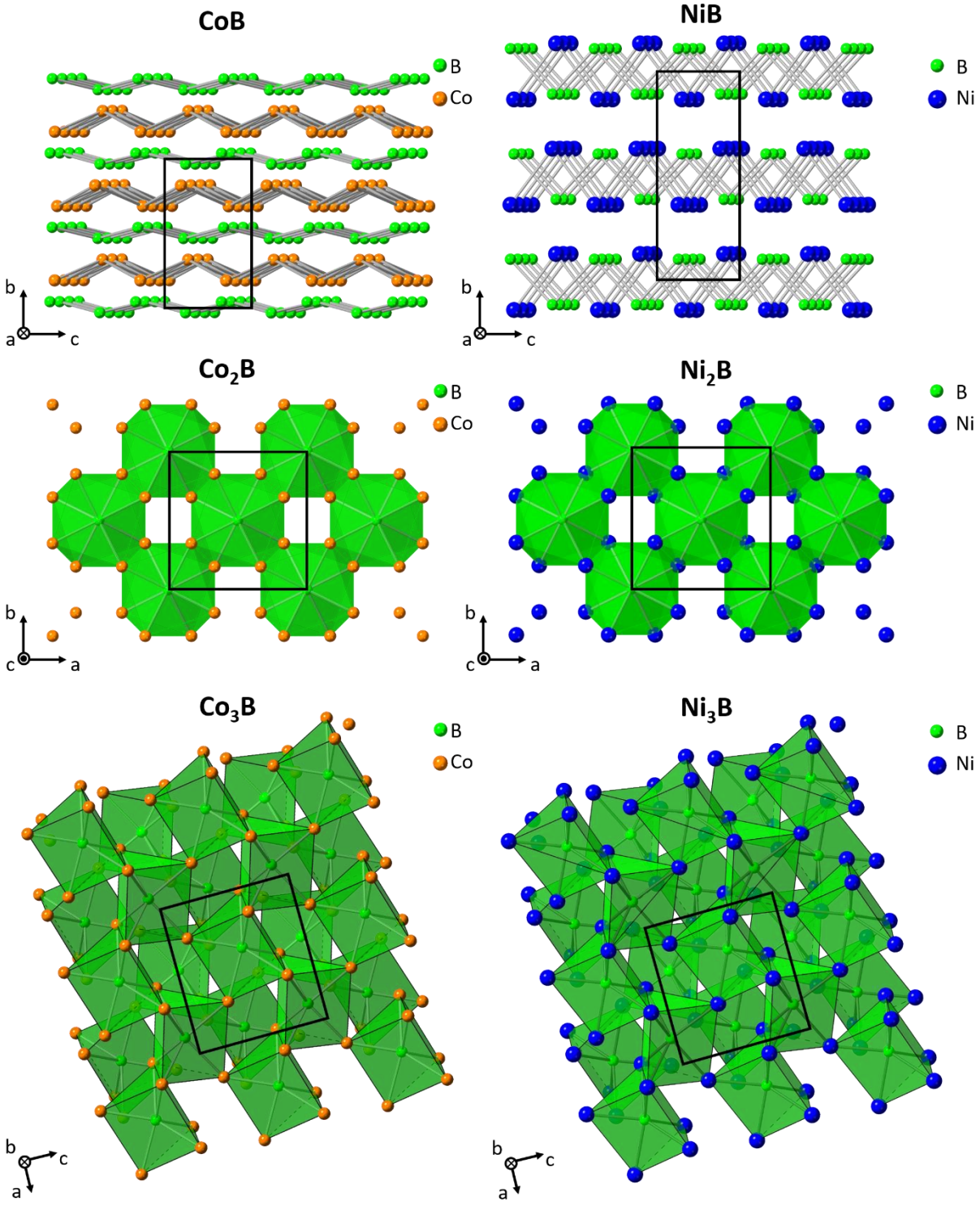

Figure 1. Schemes of the crystal structures of Co_xB and NixB, for x= 1, 2 and 3.

Attempts to use molten salts syntheses in order to react both metals with boron into a liquid to ensure homogeneous reactivity of Ni and Co have been unsuccessful. Indeed, reducing nickel

and cobalt chlorides with $NaBH_4$ in a eutectic molten salt mixture LiCl:KCl at 850-900 °C [41] yielded only mixtures of monometallic borides with particles exhibiting diameters from 50 to 100 nm.

Overall, the absence of multimetallic compounds beyond the M_2B composition may relate to the synthesis procedures usually employed. Most syntheses involve the reduction of Co^{2+}/Ni^{2+} species, with different redox potentials, especially in molten chloride salts[42], which drives the separate precipitation of nickel and cobalt (Ni^{2+} is a stronger oxidant than Co^{2+}). Therefore, reaching a homogeneous phase containing both Ni and Co would request bypassing this first oxidation step.

Along this chapter, we extend the methodology developed for boron incorporation into nickel nanoparticles, described in chapter 2, to design bimetallic borides. To do so, we use nickel-cobalt alloy nanoparticles, formed by *in situ* transformation of pre-synthesized core-shell nanoparticles. We then discuss how to achieve the controlled incorporation of boron and ultimately original homogeneous nickel, cobalt and boron crystalline nano-objects.

II) New route to homogeneous nickel cobalt boride

Carenco *et al*. have designed[43] and studied the evolution of triocylphosphine (TOP)-capped Ni-Co core-shell nanoparticles when heated under vacuum, by using *in situ* TEM and XPS.[44] They have shown (**Figure 2**)[44] that after the reduction of surface oxide species by the carbonaceous moieties of the TOP ligands (from 120 to 550 °C) and the desorption of resulting organic species, the nanoparticles were exempt of oxide and carbide species above 440 °C. The particles also encountered internal restructuration above 440 °C by interdiffusion of Co and Ni atoms and formation of a homogeneous nickel cobalt alloy at 600 °C. This temperature range is easily accessible in molten salts. Therefore, the initial Ni-Co core-shell nanoparticles are ideal candidates to form in molten salts homogeneous Ni-Co alloy nano-objects, which boron could incorporate by subsequent reaction, through a one-pot synthesis in molten salts. By using this approach, one can bypass the steps of Ni and Co reduction during reaction with the boron source, and then avoid segregation of the two metals, thus setting an ideal stage to crystallize a ternary nickel cobalt boride.

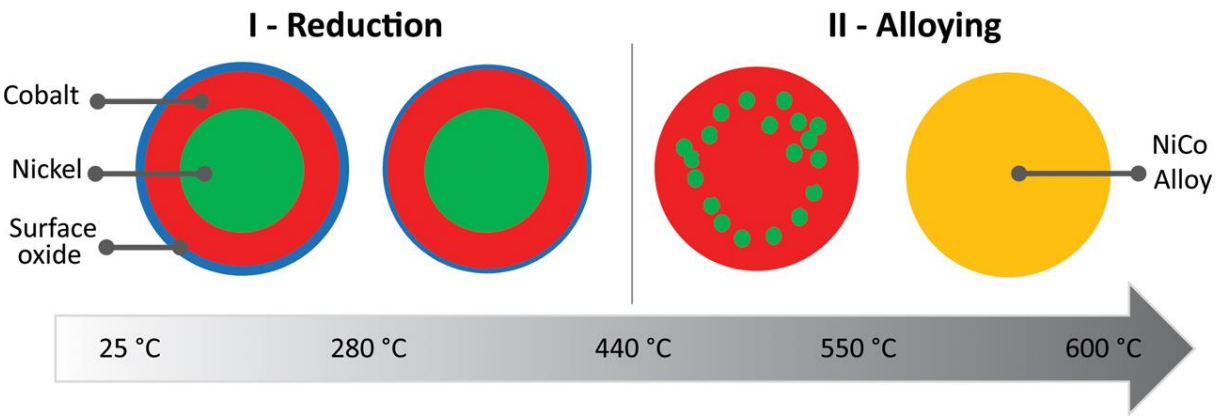

Figure 2. Evolution of the Ni-Co core-shell nanoparticles during heating under vacuum. Reproduced from [44].

a) Synthesis of Ni-Co core-shell nanoparticles

The synthesis of nickel-cobalt nanoparticles is adapted from a colloidal synthesis reported by Carenco *et al.*[43]. This method enables to avoid oxygen-containing surface ligands, which may have in turn reacted with the oxophilic boron precursor during the boride synthesis. The method is based on a simple adaptation of the nickel nanoparticles synthesis procedure (Chapter 2). The first step consists in the formation of nickel nanoparticles, with a higher ratio of TOP ligand compared to the synthesis of sole Ni nanoparticles (see Chapter 2). Then, the temperature is lowered to avoid further homogeneous nucleation, and $Co_2(CO)_8$ is added to the reaction mixture, which is further heated to trigger heterogeneous nucleation and the formation of a Co shells on Ni cores.

SEM-EDS (**Table S5-I**) shows a Co:Ni atomic ratio of 1:1 and some remaining phosphorus, with a ratio P:(Ni+Co) close to 20 at. %. TEM shows that the sample is monodisperse, with the formation of nano-spheres of about 13 nm (**Figure 3A-C**). High magnification TEM (**Figure 3B**) does not show any feature of a crystalline order, in agreement with XRD (**Figure 3D**). We clearly distinguish on the HRTEM image (**Figure 3B**) a 2-3 nm-thick shell. No crystalline phosphide was detected by XRD.

XPS analysis in the Co/Ni $3p_{3/2}$ region (**Figure 3E**) confirms the presence of both nickel (0) and cobalt (0) contributions. Partial oxidation during the washing step is observed, with a peak attributed to oxide species for both metals, which suggests that the shell observed by TEM is a Ni and Co (hydr)oxide. XPS also detects some phosphorus species from the TOP ligands, as observed in the P 2p region (**Figure 2F**). Three contributions are observed with binding

energies of 129.7 eV, 130.5 eV and 133 eV; assigned to P-Co, P-Ni and P-O species, respectively[45–47].

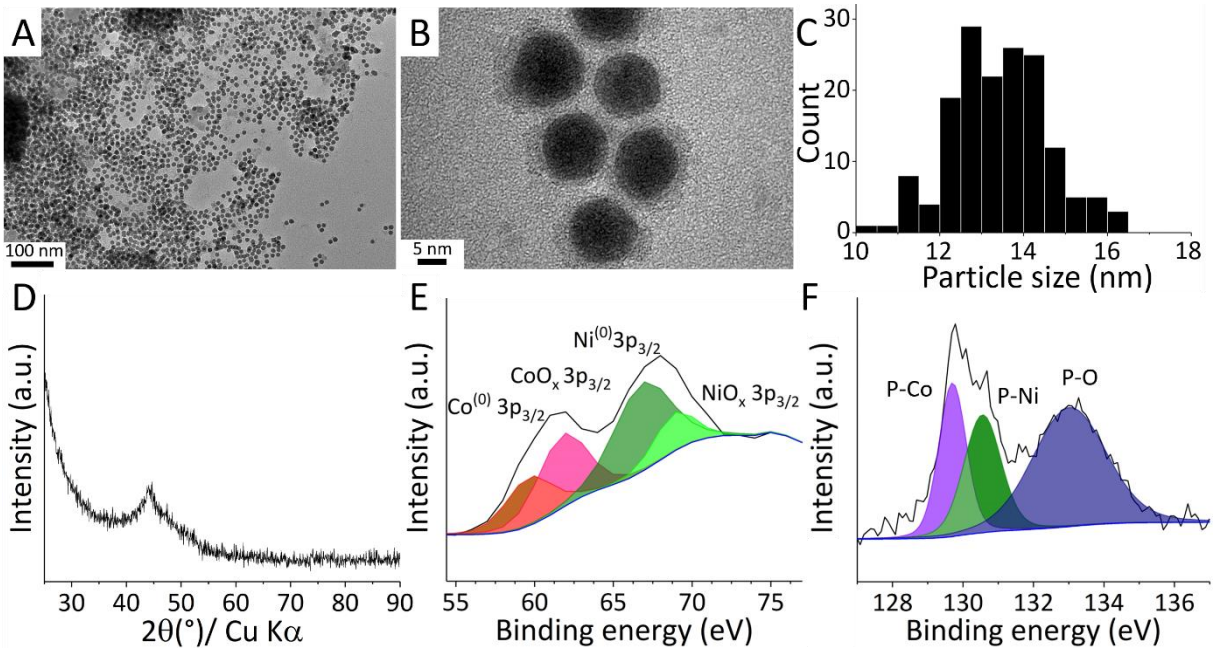

Figure 3. Ni-Co core-shell nanoparticles. (A) TEM image, (B) high magnification TEM image showing no local order and (C) size distribution of the particles, (D) powder XRD pattern, (E) XPS in the Co/Ni $3p_{3/2}$ region, (F) XPS in the P 2p region.

b) Aiming at Ni-Co-B compositions

As discussed before, the formation of bimetallic nickel-cobalt boride crystalline nanomaterials without segregation into cobalt borides and nickel borides remains unexplored for several compositions. Better control of the reactivity is expected by incorporating boron into the Ni-Co nanoparticles in molten salt conditions.

A first insight into the reactivity of Ni-Co core-shell nanoparticles with borohydride in molten salts has been given by Camille Chan Chang[48]. A unique synthesis was described by using a B:(Ni-Co) ratio of 4:1 at. at 450 °C/1.5 h in the eutectic mixture LiI:KI (58:42 mass.). SEM-EDS analysis confirmed the incorporation of boron and the preservation of the Co:Ni ratio with some residual phosphorus, but XRD indicated a segregation of Co and Ni, since diffraction peaks could be unambiguously assigned to the separate CoB and NiB structures.

To target specific conditions of interest, we use MatLearn,[49] a machine learning-based tool to map the minimal formation energies along a binary or ternary phase diagram, trained on the Materials Project database[50]. Regions of potentially low formation energies in the Ni-Co-B system are shown in the calculated phase diagram **Figure 4**. Although no crystalline nickel cobalt boride compound has been reported according to structure databases (PDF-4+, ICSD), the prediction algorithm highlights an area of possible existence of bimetallic borides on the $(Co_{1-x}Ni_x)B$ line and at proximity, especially for x ranging from $x = 0$ (CoB) to 0.5 ($CoNiB_2$). Conversely, the Ni-rich domain seems less favorable to provide stable compounds, in agreement with the homogeneous compositions of $(Co_{1-x}Ni_x)_2B$ reported[18,40], and the higher formation energy of CoB (-69.52 ±6.0 kJ mol^{-1}) compared to NiB (-40.2 ±3.77 kJ mol^{-1}). However, this comparison does not fit for Ni_2B (-67.66 kJ mol^{-1}) compared to Co_2B and (-58.1 kJ mol^{-1}) meaning that other factors such as kinetic, surface ligands or structural preferences drive the resulting bimetallic phase[51]. Although MatLearn does not take into consideration any structural features, it is interesting to note that both CoB and NiB (**Figure 1**) crystallize in the orthorhombic system (S.G. *Pbmn* (62) and *Cmcm* (63) for CoB and NiB, respectively). The two structures are relatively close, as they contain as main structural motifs 1D zig-zag covalent boron chains. Therefore, one can expect the possibility to design Ni-substituted CoB, although no corresponding compound has been reported. Along this chapter, we investigate the synthesis of a bimetallic $Co_{1-x}Ni_xB$ compound by reacting Ni-Co core-shell nanoparticles with sodium borohydride in molten salts.

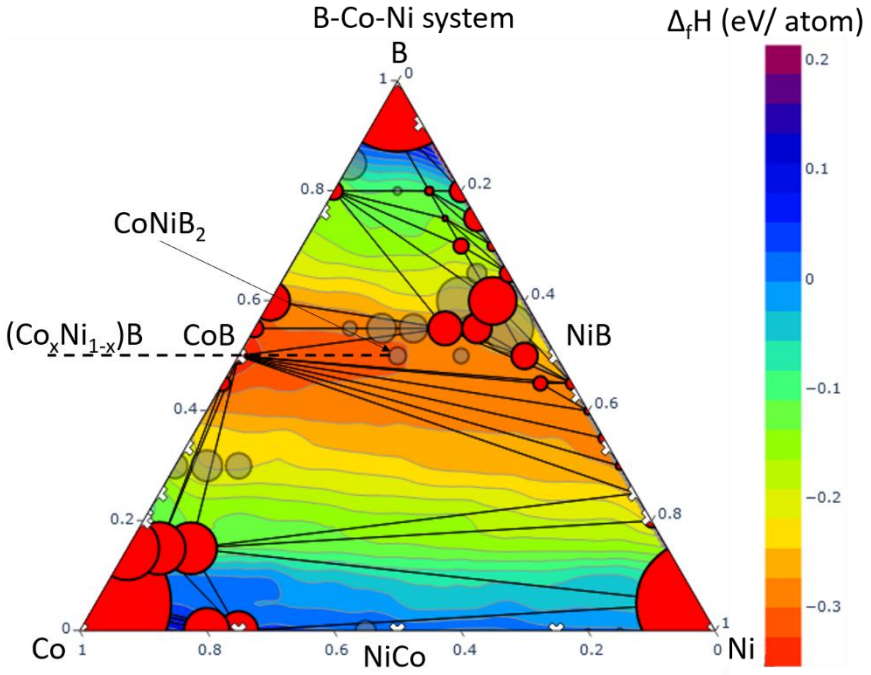

Figure 4. Predicted formation energy diagram of Ni-Co-B according to Matlearn[49]. White crosses indicate reported compositions in the training database. Red areas show the low formation energy zones. Red circles indicate predicted compositions on the convex hull, grey circles indicate compositions slightly above the convex hull, hence potentially metastable. The dotted line represents the targeted compositions.

III) Key parameters of structural evolution

a) Effect of the boron-to-metal content

A reagent ratio metal:B = 1:1.3 at., where the metal amount accounts for nickel and cobalt, was first assessed for a synthesis at 600 °C for 3 h. We use a 30 % excess of boron compared to the targeted content, as we observed in chapter 2 that the borohydride reaction is not quantitative and that boron excess was required to form XRD-pure nickel borides. The heating conditions are chosen based on the reactivity discussed later in this chapter. Both eutectic salt mixtures LiI:KI (58:42 mass.) and LiCl:KCl (44:56 mass.) have been studied. As shown in **Figure S5-I**, the nature of the salt has no impact on the crystallinity and morphologies at 600 °C. The powder XRD patterns indicate the crystallization of a CoB structure along with some Ni_2P. SEM-EDS indicates a composition P:(Ni+Co) of 20 at. %. The presence of phosphorus is in line with the detection of Ni_2P by XRD, which arises from incorporation of phosphorus by decomposition

of the TOP ligands from the colloidal synthesis. Nevertheless, the morphology of the initial nanoparticles is retained according to TEM (**Figure S5-IB-C**), despite partial coalescence.

We then increased the metal:boron ratio to 1:2.6 to provide a large excess of boron and then counteract crystallization of the phosphide phase. With the same temperature profile, we again observed similar results with both molten salt mixtures (not shown). We then preferentially used LiI:KI (58:42 mass.) as solvent, because its lower melting point may favor reactions at lower temperature, hence enhance crystallization while avoiding extensive particle coalescence.

b) Structural evolution with the dwell time

We fixed the synthesis conditions to 600 °C for a metal:B ratio of 1:2.6 at., by varying the dwell time from 0.5 to 3 h. In contrast to the metal:B ratio of 1:1.3 at., no crystallized phosphide could be detected by XRD. Interestingly, the XRD patterns and corresponding Rietveld refinement indicate structural evolutions by increasing the temperature plateau. At 0.5 h (**Figure 5A**), the reflections of CoB and NiB can be identified, along with $Ni_{0.5}Co_{0.5}$ as minor phase.

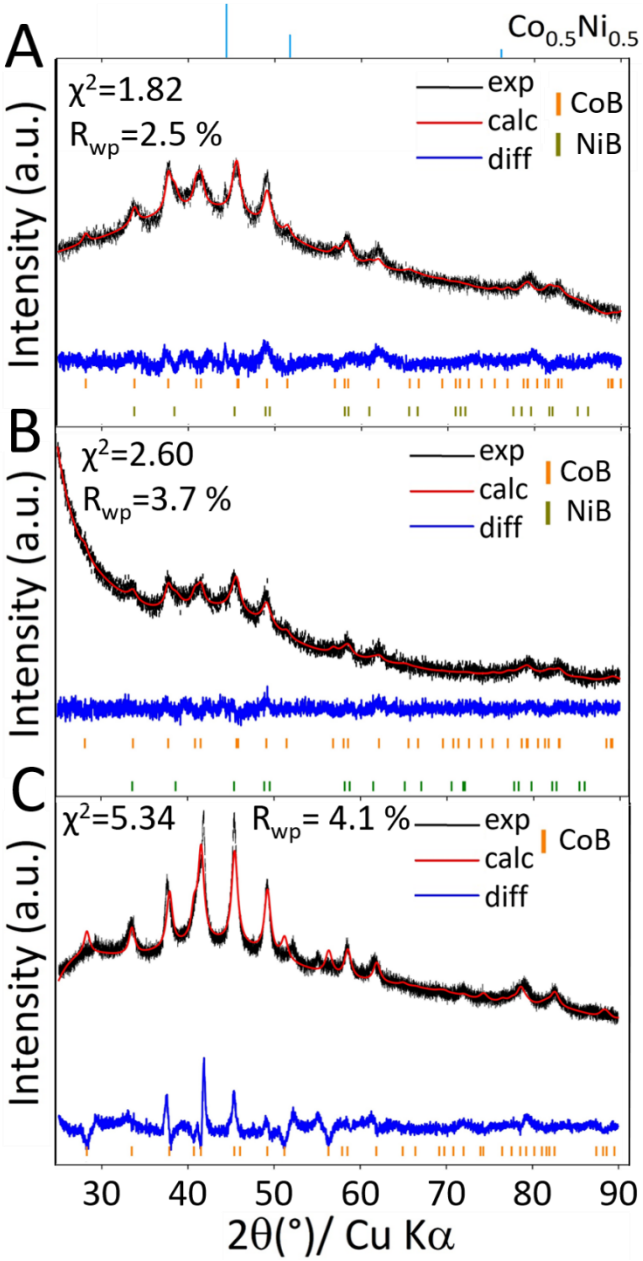

Figure 5. Rietveld refinements of the XRD pattern of powders obtained by reacting Ni-Co nanoparticles with $NaBH_4$ for metal:B = 1:2.6 at. in LiI:KI at 600 °C for (A) 0.5, (B) 1.5, and (C) 3 h. The phase indexed $Co_{0.5}Ni_{0.5}$ in (A) was not accounted for in the refinement, as adding this third phase led to misinterpretation due to a large number of variables involved in the fit.

Rietveld refinement by omitting $Ni_{0.5}Co_{0.5}$ suggests a mixture of CoB and NiB at 59 and 41 wt. %, respectively. However, the corresponding cell parameters (**Table S5-II**) present distortions compared to the reported structures. In comparison, the refinement performed by implementing only CoB (**Figure S5-IIA**) is not satisfactory. The morphology and composition

of the particles were investigated by TEM, EFTEM and STEM-EDS. For a plateau of only 0.5 h, the morphologies and sizes are maintained (**Figure 6A-B**). An amorphous matrix is also observed around all particles. HRTEM and the corresponding FFTs highlight polycrystalline domains of CoB and NiB. The lattice fringes identified on 9 particles indicate 8 particles attributed with the CoB structure and only one for NiB. However, STEM-EDS performed on single particles (**Table S5-III**) show a bimetallic composition Ni:Co = 1:1 at. Energy-Filtered TEM (EFTEM) at the Co/Ni-L and B-K edges was used to assess the location of the metal atoms and of boron. Because the Co-L and Ni-L edge energies are close, they cannot be discriminated by EFTEM with the apparatus used. We observe co-location of the metal atoms and boron into the core and the matrix. The uniform repartition of cobalt and nickel tend to demonstrate the evolution of the Ni-Co core-shell structure into a bimetallic boride. The amorphous matrix is expected to be composed of boron, borate and oxy/hydroxides of nickel and cobalt formed during the washing step, as detailed in chapter 2.

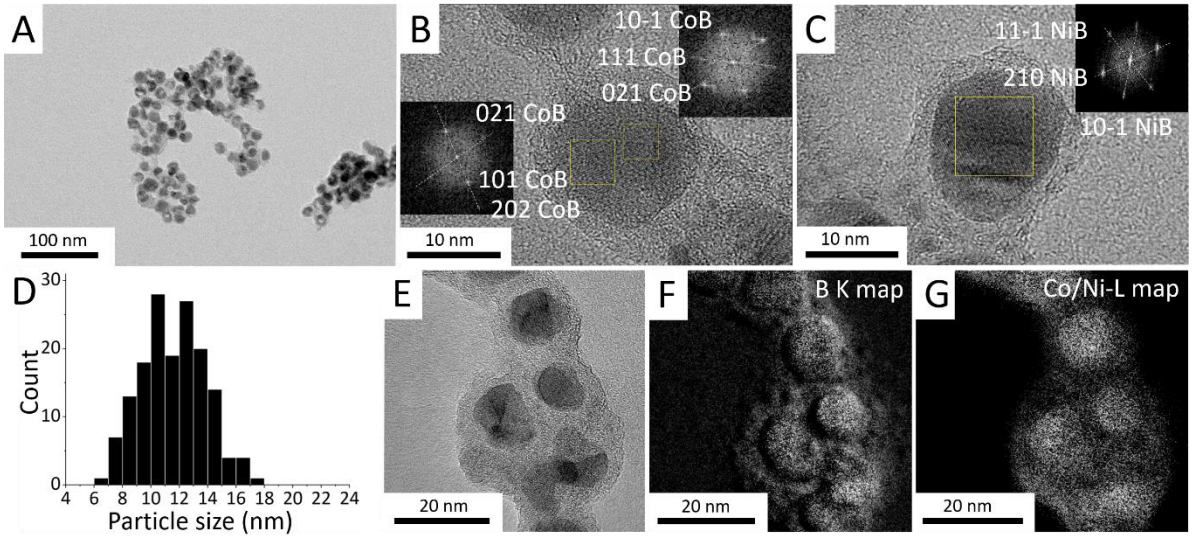

Figure 6. Morphology and composition study of bimetallic boride nanoparticles obtained by reacting Ni-Co nanoparticles with $NaBH_4$ (metal:B = 1:2.6 at.) at 600 °C for 0.5 h in molten LiI:KI. (A) TEM and (B, C) HRTEM images with corresponding FFTs. (D) Corresponding size distribution. (E) TEM and corresponding EFTEM images at the (F) B-K and (G) Co/Ni-L edges.

By increasing the dwell time to 1.5 h, the XRD pattern and the corresponding Rietveld refinement (**Figure 5B**) show a structure similar to the one observed for the 0.5 h sample. However, no $Ni_{0.5}Co_{0.5}$ phase is detected anymore, suggesting full conversion of the pristine particles to borides. The weight fractions for CoB and NiB are 55.8 and 44.2, respectively. Again, it was necessary to implement both CoB and NiB in the refinement to obtain satisfying results (**Figure S5-IIB, C**). A TEM image and the corresponding size distribution (**Figure S5-III**) confirm morphologies similar to the pristine nanoparticles. The composition and crystallinity assessed by STEM-EDS (**Table S5-III**) are also similar to the sample obtained at 0.5 h. HRTEM and corresponding FFTs performed on 16 particles were related for 11 particles to the CoB structure, one for the NiB structure while lattice fringes associated to both structures were observed inside four nanoparticles.

Increasing the dwell time to 3 h yields a dramatic modification of the powder XRD pattern (**Figure 5C**). According to the Rietveld refinement, no peak can be attributed to NiB. The assignment of the diffraction peaks to CoB reflections cannot account for the shift of several peaks. Rietveld refinement was performed by considering only CoB, allowing large shifts of CoB cell parameters (**Figure 5C**). The results were inconclusive.

A collaboration with Gwenaelle Rousse (Sorbonne Université-Collège de France, UMR 8260, group « Chimie du solide et énergie ») allowed a deeper structural refinement. We could confirm that no NiB or other reported cobalt boride structure fits with the diagram. A structural transition from orthorhombic to monoclinic CoB was also considered, but was also inconclusive. The best refinement was obtained by maintaining the *Pnma* structure of CoB and allowing morphological anisotropy and microstrain features (**Figure 7A**). The corresponding structural model (**Figure 7B**) accounts for mixed occupancies Ni/Co on the single metal sites, which would be consistent with the conservation of the Ni:Co atomic ratio 1:1 observed by STEM-EDS in the resulting particles. The corresponding *a* and *b* cell parameters are identical to those reported for CoB (a = 5.243 Å, b = 3.037 Å) but the *c* parameter exhibits a slight elongation with c = 3.950 Å compared to pristine CoB (c = 3.948 Å).

Note that CoB and NiB crystallize in the β-FeB and CrB structures, respectively[37,38]. These two structures, because of their similarities, are known to coexist in single samples. Especially, in the case of FeB, we have recently demonstrated that α-FeB is a statistical intergrowth of β-FeB and CrB-type domains[39]. Hence, it would be interesting to consider a second structural model, by refining the experimental pattern of the sample obtained after 1.5 h as a stochastic assembly of β-FeB and CrB-type structural layers stacked along the $[010]_{CoB}$ direction, as for α-FeB. Such

an in-depth work cannot be achieved by common Rietveld refinement and will require further work in the near future, for example by implementing FAULT refinement[52,53].

A model of crystallite morphology was obtained by refinement of anisotropic parameters. It suggests elongated crystallites along the *c* axis of the CoB structure, corresponding to the 1D boron chains, with an average size of 22 x 5 nm (**Figure 7C**). This observation would be consistent with an intergrowth of layers stacked along the $[010]_{CoB}$ direction, hence elongated along the *a* and *c* axes.

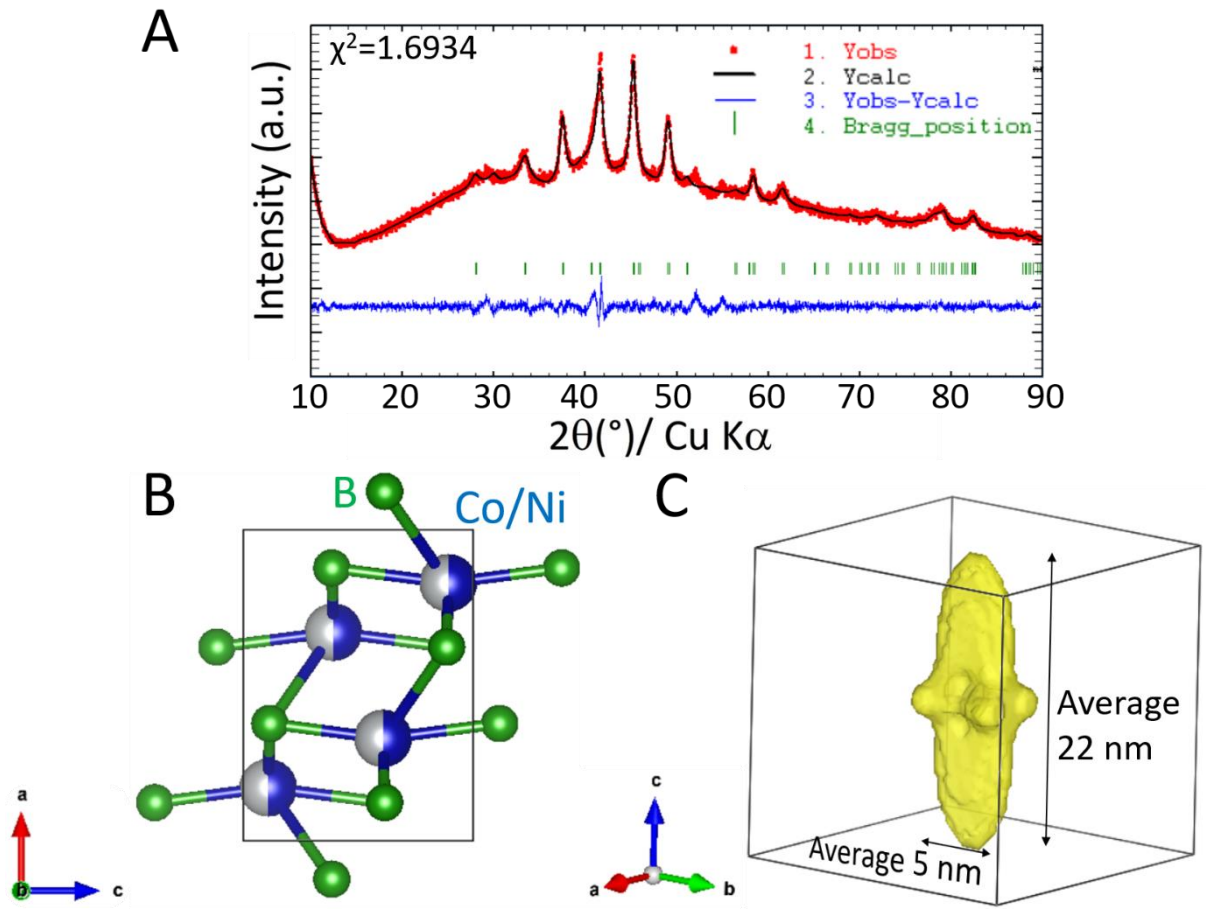

Figure 7. (A) Powder XRD pattern and corresponding Rietveld refinement of Ni-Co-B (M:B = 1:2.6 at.) in LiI:KI (58:42 mass.) at 600 °C for 3 h. The refinement is performed by maintaining the CoB space group and the atomic positions. (B) corresponding crystal structure and (C) model of particle morphology.

TEM images (**Figure 8A-C**) show indeed some anisotropy resulting from the coalescence of the particles (**Figure 8C**). The overall particle size distribution remains similar to the initial Ni-Co nanoparticles (**Figure 8D**). FFT performed on 8 particles indicated only lattice fringes of

the CoB structure. EFTEM (**Figure 8E-G**) and STEM-EDS elemental mapping (**Figure 8H-I**) confirm the homogeneous distribution of Co, Ni and B. Remaining phosphorus is also homogeneously distributed, with a P:(Ni+Co) ratio of 0.2 at. %. No nickel/cobalt phosphide could be accounted for the changes observed on the XRD pattern. This observation may indicate that phosphorus remains on the surface of the particles and/or is incorporated into the CoB-like structure.

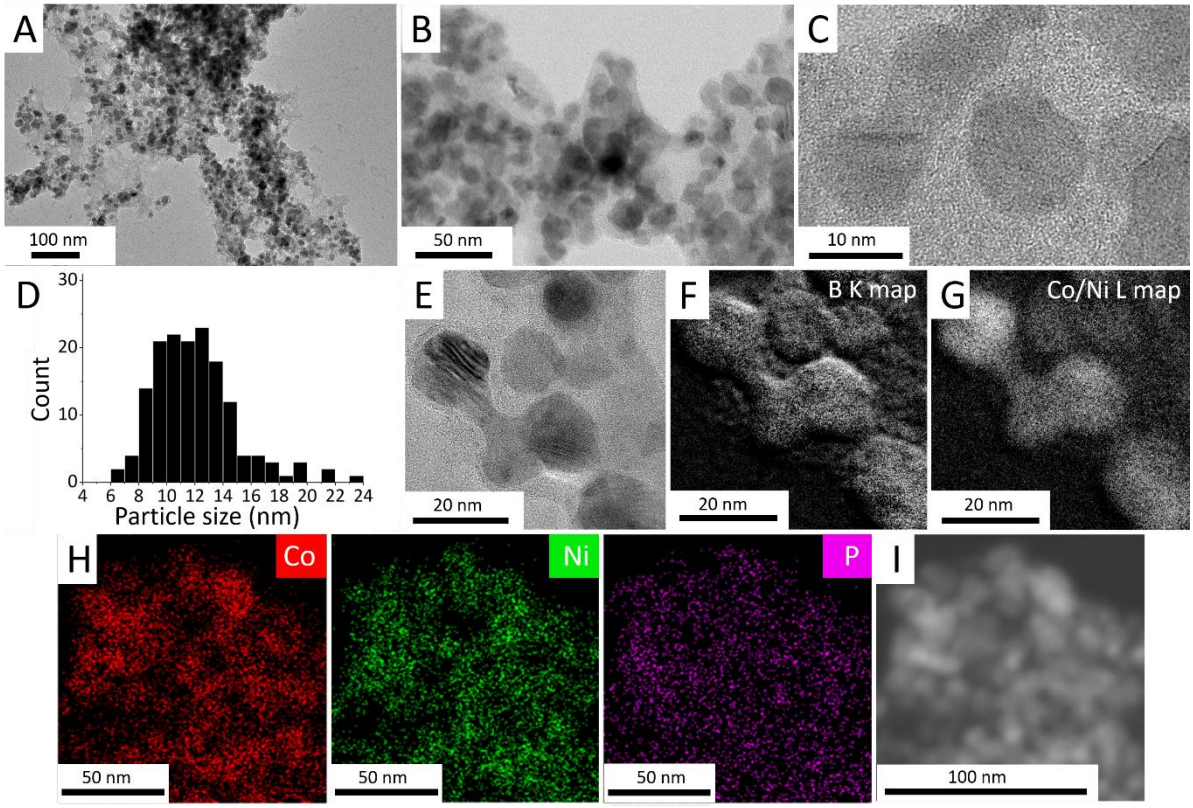

Figure 8. Transmission electron microscopy study of Ni-Co-B nanoparticles obtained by obtained by reacting Ni-Co nanoparticles with $NaBH_4$ (metal:B = 1:2.6 at.) at 600 °C for 1.5 h in molten LiI:KI. (A-C) TEM and HRTEM images and (D) corresponding size distribution. (E) TEM and corresponding EFTEM images at the (F) B-K and (G) Co-L edge. (H) STEM-EDS chemical maps of Co, Ni and P with (I) the corresponding TEM image.

XPS shows in the Co, Ni 3p region (**Figure 9A**) the same contributions of low valence Ni and Co species in the boride, compared to the pristine Ni-Co particles, with no obvious shift of the binding energies. Most drastic changes are observed in the B 1s region for the borides synthetized at 1.5 and 3 h (**Figure 9B**). While the oxidized boron peak at 192.3 eV is unchanged, the boride and elemental boron components exhibit a binding energy increasing

from 188.6 to 189.3 eV when the heat treatment is increased from 1.5 to 3 h. This positive shift confirms a structural modification of the core of the nanoparticles. In comparison, similar contributions were observed in the nickel borides Ni_3B and Ni_4B_3 (chapter 2) at 191.4 eV for oxidized boron, 187.8 eV for elemental boron atoms and 188.2 eV for the boride; thus confirming a positive shift of all contributions in the bimetallic boride.

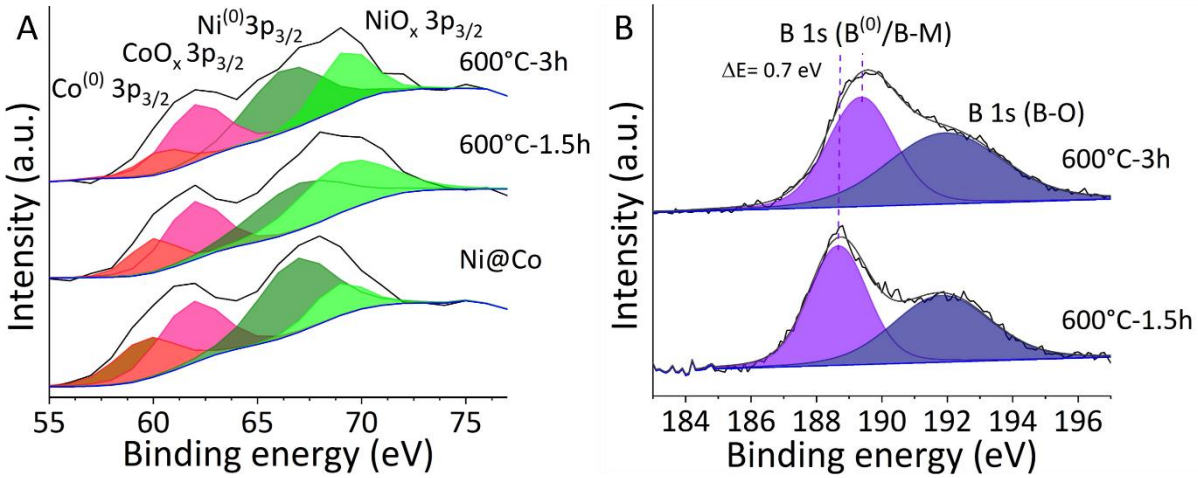

Figure 9. XPS spectra of Ni-Co nanoparticles and the products of their reaction with $NaBH_4$ in molten LiI:KI for a metal:B ratio of 1:2.6 at. at 600 °C for 1.5 and 3 h: (A) Ni, Co 3p region and (B) B 1s region.

c) Temperature effect on structural evolutions

In order to understand the crystallization mechanism, we have performed *in situ* X-ray diffraction on the DIFFABS beamline at the synchrotron SOLEIL (**Figure 9**) in transmission mode through the reaction mixture placed into a 1 mm diameter fused silica capillary, which was heated thanks to a resistive capillary oven designed in our team.

A first study under conditions similar to those used *ex situ* (concentration of 2 mmol of Ni-Co nanoparticles per gram of LiCl:KCl (44:56 mass.), ramp rate of 10 °C min^{-1}) was performed up to 800 °C for a dwell time of 1.5 h (**Figure 10A**). Before melting of the salt at around 350 °C, the diffractograms were dominated by the intense diffraction peaks of LiCl and KCl. Before the melting point, we observe the progressive formation of NaCl, which shortly dissolves after melting of the eutectic mixture, with rapid increase of its cell parameters, around 25 and 35 min after the beginning of the experiment. Sodium is supplied by either metathesis of $NaBH_4$ with

LiCl and/or KCl, or by the decomposition of $NaBH_4$. From around 440 °C, crystallization of both NiB and CoB occur approximately at the same time.

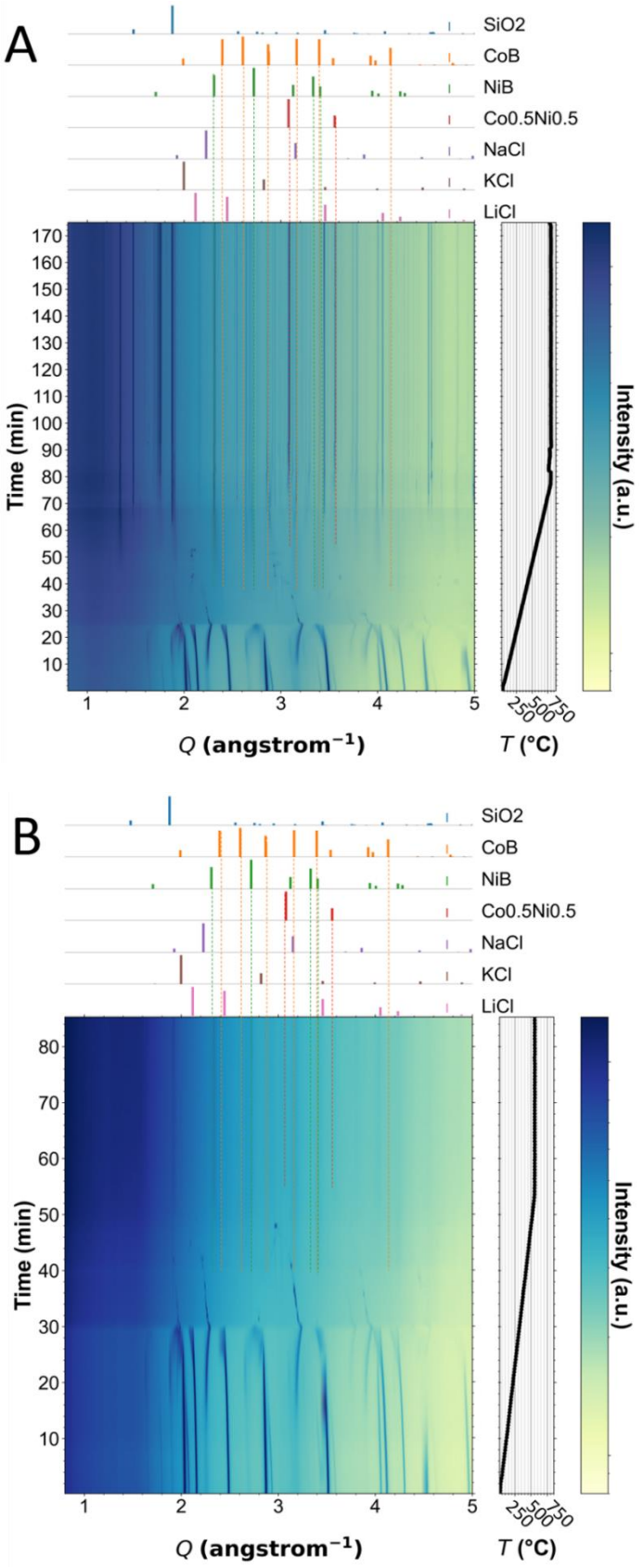

Figure 10. Synchrotron radiation *in situ* XRD diagrams recorded during the reaction of Ni-Co nanoparticles with $NaBH_4$ (Metal:B = 1:2.6 at.) in LiCl:KCl (44/56 mass.): (A) Ramping up to 800 °C, (B) ramping up to 555 °C.

Subsequently, from around 555 °C the diffraction peaks of the CoNi alloy appear, at 3.10 and 3.58 $Å^{-1}$, in agreement with the reported thermal behavior of the core-shell nanoparticles[44]. Slightly above this temperature, crystallization of silica from the capillary wall occurs. This crystallization event occurs usually above 800 °C. It is possible that boron in the reaction medium lowers the crystallization onset temperature. Indeed, not all diffraction peaks could be indexed, which might indicate the formation of borosilicate phases, with a complex structural diversity. We have then performed a second experiment by limiting the plateau temperature at 555 °C (**Figure 10B**). The crystallization sequence is the same as in the initial reaction, with the salt melting around 350 °C and then crystallization of NiB and CoB from 440 °C. The CoNi alloy then appears on the plateau at 55 min after the beginning of the experiment. No other phase is identified along the plateau except again crystalline SiO_2, but the diffraction peaks of $Co_{0.5}Ni_{0.5}$ are still visible at the end of the dwell time.

The overall sequence observed *in situ* is consistent with the *ex situ* studies at 600 °C. As a first step, the core-shell nanoparticles incorporate boron and crystallize into NiB and CoB structures while progressively forming a NiCo alloy. A short dwell time, as in the case of 600 °C for 0.5 h did not allow a complete conversion of the alloy into the boride. Finally compared to the stoichiometry metal:B of 1:1.3 at., no phosphide crystallization was observed.

We note that the crystallization of the monometallic borides starts before the formation of the alloy. This suggests that once formed, the monometallic borides can undergo restructuration into the bimetallic boride, probably within a single nanoparticle. Besides, this observation suggests the possibly to design multi-compartment, if not core-shell, nanoparticles containing NiB and CoB domains. We have then addressed the reactivity at lower temperature, by using a longer dwell time (6 h) at a relatively low temperature of 450 °C was explored in *ex situ* conditions. These conditions may favor a kinetic control of the reaction, able to lead to a different reactivity. Surprisingly, the resulting XRD diagram (**Figure S5-IV**) indicates an amorphous powder. By referring to *in situ* XRD, the target temperature is above the crystallization temperature of CoB and NiB but below the onset of the $Co_{0.5}Ni_{0.5}$ alloy crystallization, we then assume that the amorphous material retrieved *ex situ* corresponds to an intermediate stage, stabilized at this temperature, during the incorporation of boron towards the crystallization of NiB and CoB. Chemical mapping at the nanoscale would be of high interest to observe the local organization of Co, Ni and B in this intermediate amorphous material. More studies will be needed in the near future to address the internal structuration of nanoparticles with multiple NiB and CoB domains.

IV) Bimetallic Nickel cobalt boride as water splitting catalyst

The nickel-cobalt boride nanoparticles reported in the litterature[18] presented an enhancement of the catalytic activity toward OER for the bimetallic boride $(Co_{1-x}Ni_x)_2B$ with $(x \leq 0.2)$ compared to Co_2B.

The nanocrystals described herein could present different properties due to the CoB-like structure and to the elemental composition Co:Ni of 1:1. We investigated the catalytic activity towards OER of these nanocrystals obtained for initial metal:B ratio of 1:2.6 at. at 600 °C for 3 h. The cyclic voltammograms (**Figure 11A**) were recorded during OER on a rotative disk electrode in an Fe-free 0.1 M KOH electrolyte, in the same conditions than the studies on nickel borides, including a mass loading of 0.25 mg cm^{-2}. An overpotential of 0.41 V vs RHE was needed to reach 10 mA cm^{-2}, while a value of 0.40 V vs RHE was required for Ni_4B_3 amorphous nanoparticles (see chapter 3). Nevertheless, the activity at higher current densities was enhanced compared to the best nickel boride catalyst (chapter 3) and close to the benchmark IrO_2. Detachment of the catalyst from the electrode after 4 CVs was observed. A Tafel slope (**Figure 11B**) of 109 mV dec^{-1} close to the benchmark IrO_2 at 96 mV dec^{-1} was determined. A C_{DL} value of 543 µF was determined by recording CVs in a non-faradic region at various scan rate [2.5-40] mV s^{-1}. By considering a specific capacitance (C_s) commonly used[54] of 40 µF cm^{-2}, the electrochemical surface active area (ECSA) is 13.6 cm^2. These data are only preliminary and suggest that adjusting the electrode processing may enhance the stability and the performances of the electrode.

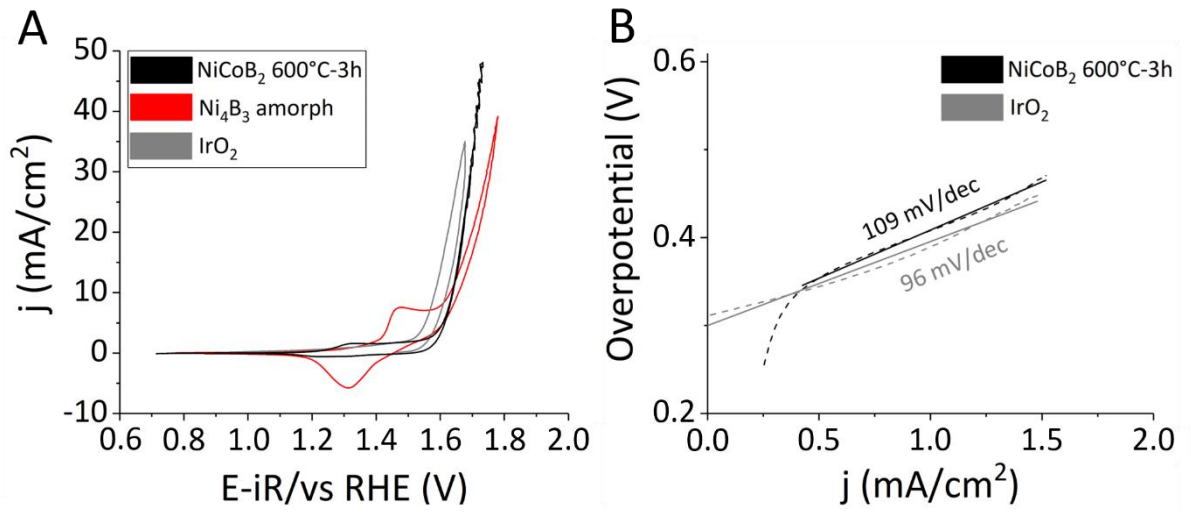

Figure 11. Electrochemical properties of nanocrystals obtained with metal:B ratio = 1:2.6 at. after 600 °C for 3 h. OER study in aqueous O_2-saturated 0.1 M KOH Fe-free electrolyte: (A) CV curves at the 1st cycle compared to Ni_4B_3 amorphous nanoparticles and IrO_2, (B) Tafel slope compared to IrO_2.

Conclusion and perspectives

Along this chapter, we have developed bimetallic nickel-cobalt boride crystalline nanoparticles by designing a pathway, which bypasses redox reactivity of metal cations, a probable origin of phase segregation in the previous attempts. We have demonstrated that the crystallization mechanism passes through crystallization into NiB and CoB structures in the molten salt, as a first step, before the formation of a $Ni_{0.5}Co_{0.5}$ nanoalloy, and then the formation of a bimetallic nickel cobalt boride, whose structure is related to the CoB, β-FeB-type structure. We observed in all cases a homogeneous composition in nickel, cobalt and boron suggesting a random substitution of Co in metallic sites by Ni. First electrochemical characterizations toward OER are promising and need deeper studies.

To go further, a first point is to carry out a deeper investigation of the CoB-derived structure. We observed that a low boron content triggered the crystallization of the phosphide, so at least an optimization of the Ni:Co ratio in the core-shell precursor needs to be studied. This would affect the final bimetallic boride structure to then optimize the (catalytic) properties. In parallel, targeting amorphous nanoparticles with tunable composition could also be of great interest, particularly in catalysis. Amorphous nickel, cobalt, boron phases[32,33,55,56] and phase mixtures[41] presented an enhancement of catalytic activity compared to monometallic borides. This makes the study of the properties and activity towards water splitting catalysis of the amorphous as well as crystalline bimetallic boride nanoparticles of high interest.

Annexes

Experimental methods

Reagents. Nickel (II) acetylacetonate (95%, $Ni(acac)_2$, Strem Chemicals), trioctylphosphine (TOP, 97%, $P(C_8H_{16})_3$, Strem Chemicals), dicobalt octacarbonyl ($Co(CO)_8$, 95%, Strem Chemicals), sodium borohydride ($NaBH_4$, min 98%, Alfa Aesar), anhydrous hexane (95%, Sigma-Aldrich), lithium iodide (99%, Alfa Aesar), potassium iodide (99%, Sigma-Aldrich), lithium chloride (99.9% Alfa Aesar), potassium chloride (99.9% Sigma-Aldrich) were stored and manipulated as received in an Ar-filled glovebox (H_2O < 0.5 ppm, O_2 < 0.5 ppm). Oleylamine (98 %, SAFC) was stored and used in air. Acetone (VWR Normapur grade), tetrahydrofuran (THF, VWR Normapur grade), methanol (VWR Normapur grade) were used for washing.

a) Synthesis of the core-shell nickel-cobalt core-shell nanoparticles

The synthesis was adapted from a reported procedure[43]. 27 mL (21.95 g, 82 mmol) of oleylamine 98 % and a Teflon-coated stirring bar were put in a 50 mL three necked round-bottomed flask connected to a reflux condenser and a Schlenk line. Then, with a heating mantle, oleylamine was heated at 50 °C and degassed three times by cycles of vacuum maintained 2 minutes and nitrogen flow to remove dissolved oxygen. Afterward, 958 mg (3.73 mmol) of $Ni(acac)_2$ and 5 mL (4.15 g, 11.2 mmol) of TOP previously prepared in a glove box were added. The mixture was again subjected to three cycles of vacuum/nitrogen for degassing. Thereafter, the mixture was heated to 220 °C with a brief degassing over 100 °C to evacuate potential water dissolved. After 2 h, the temperature was decreased to the ambient. 638 mg (1.86 mmol) of $Co_2(CO)_8$ prepared in a glove box was added to the mixture. Three degassing cycles were then done. Then, the temperature was raised again to 120 °C for 20 min and finally to 180 °C for 1 h. After cooling down to room temperature, ~ 5 mL of THF and ~ 25 mL of acetone were added before transferring of the nanoparticles into centrifuge tubes for separation. Seven cycles of centrifugation-redispersion were performed by using a THF/acetone mixture. After disposal of the supernatant on the last cycle, the particles were introduced in a Schlenk tube connected to a Schlenk line and dried under vacuum. The product was then stored in an Ar-filled glovebox.

b) Synthesis of nickel cobalt boride nanoparticles

50 mg (0.42 mmol) of Ni-Co nanoparticles prepared in a glovebox were introduced into a Schlenk tube and connected to on a Schlenk line. Under nitrogen flow, 1 mL of anhydrous hexane is added with a syringe and the particles were dispersed for 30 min by sonification. Thereafter, 0.2125 g (2 mmol of Ni-Co per g of salts) of LiI:KI (58:42 mass.) or LiCl:KCl (44:56 mass.) are added to the mixture and the Schlenk tube was quickly degassed and flushed with nitrogen. The mixture was then sonicated for additional 15 min and dried under vacuum. 0.0209 g (0.55 mmol) for metal:$NaBH_4$ of (1:1.3) resp. 0.0413 g (1.092 mmol) for (1:2.6) of $NaBH_4$ was added to impregnated mixture. The powder was ball-milled for 2 min at 20 Hz before being introduced into a carbon crucible, which itself was introduced into a quartz tube closed for the transfer from the glovebox to the Schlenk line under Ar flow. A tubular oven was used for heating at 10 °C min^{-1}. After natural cooling, the product was washed by methanol with ten cycles of dispersion/ condensation by centrifugation at 21 000 rpm. Finally, the washed particles were introduced in a Schlenk tube connected to a Schlenk line for vacuum drying. The final powder was weighted and stored in a glovebox.

For the mixtures studied on a synchrotron beamline, the preparation was similar but the final mixture of reagents was introduced in a quartz capillary (1 mm-diameter) in a glovebox and adapted on a capillary oven maintained under argon. The synchrotron beamline DIFFABS at SOLEIL Synchrotron facility operated the *in situ* XRD studies in transmission mode. The signal was recorded by a circular 2D detector covering 140° detection [57].

c) Preparation of the electrochemical setup for OER measurements

The preparation was similar to the procedure described in chapter 3 including the preparation of carbon black. The CV were recorded on a rotative disk electrode on which the catalytic ink was deposed by drop casting to form a film with a mass loading of 0.25 $mg.cm^{-2}_{electrode}$, then dried under air. The ink was prepared by sonication at least 20 minutes of 3.5 mg of catalyst in 480 µL absolute ethanol until reaching a homogeneous dispersion. Then, 3.5 mg of carbon black was added and the mixture was sonicated similarly. 20 µL Nafion solution (5 % in alcohols and water, Sigma-Aldrich) was added subsequently and the mixture was re-sonicated. Finally, 7µL of the homogeneously dispersed ink was dropped on the previously polished RDE.

Supplementary data for chapter 5

Table S5-I. Elemental compositions from most significant contributions according to SEM-EDS. The oxygen values are not taken into account due the oxidation of the material under air during sample preparation for SEM.

Zone 1	at. %	Zone 2	at. %	Zone 3	at. %
P K	18.73	P K	19.16	P K	20.25
Co K	44.29	Co K	44.82	Co K	41.75
Ni K	34.2	Ni K	35.13	Ni K	37.6

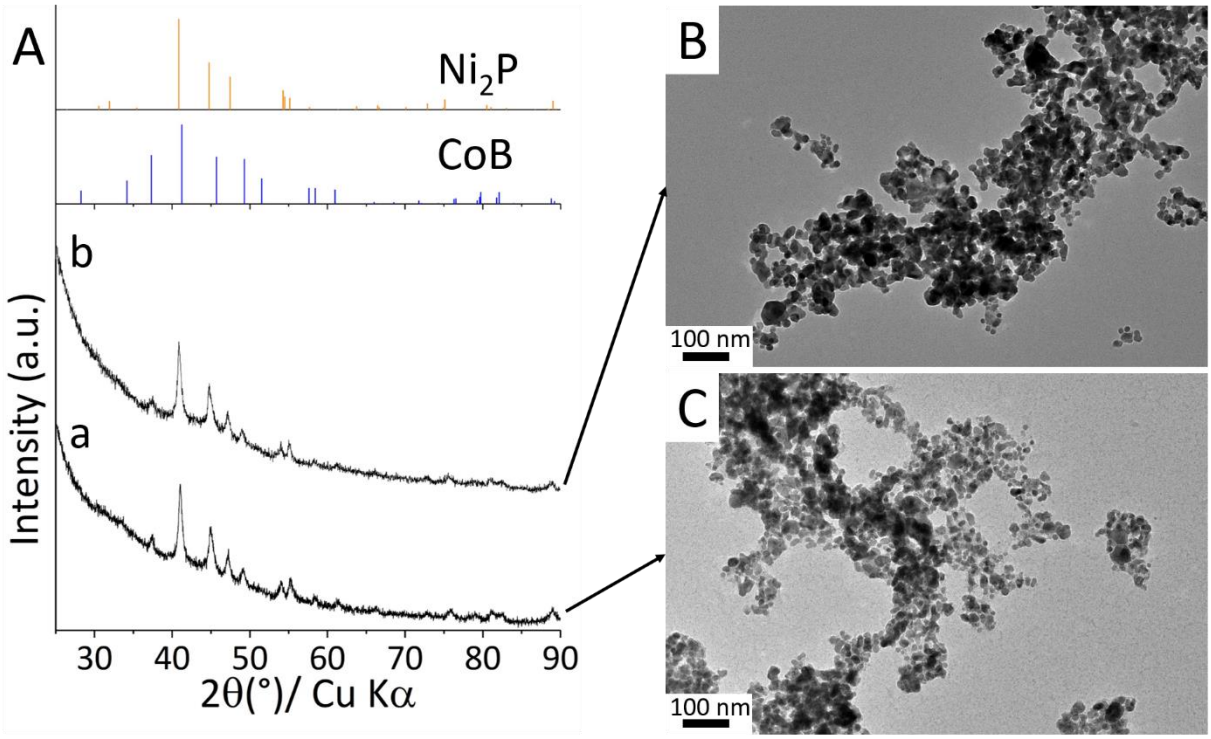

Figure S5-I. (A) Powder XRD patterns and (B, C) corresponding TEM images of nanoparticles obtained with the reagent ratio Metal:B = 1:1.3 at 600 °C for 3 h in molten (a) LiI:KI (58:42 mass.), (b) LiCl:KCl (44:56 mass.).

Table S5-II. Cell parameters according to Rietveld refinement of the XRD patterns of the powders obtained by reacting Ni-Co nanoparticles with $NaBH_4$ (Metal:B = 1:2.6 at.) at 600 °C for 0.5 and 1.5 h by considering CoB and NiB as constituents. *The cell parameters used as reference obtained from the PDF-4+ database, with card numbers 04-003-2122 and 00-006-0567 for CoB and NiB, respectively.

cell parameters	CoB Ref*	CoB (600°C/ 30min)	CoB (600°C/ 1h30)	NiB Ref*	NiB (600°C/ 30min)	NiB (600°C/ 1h30)
a (Å)	3.948	3.966	3.962	2.929	2.851	2.866
b (Å)	5.243	5.319	5.329	7.392	7.387	7.370
c (Å)	3.037	2.997	2.989	2.961	3.043	3.018

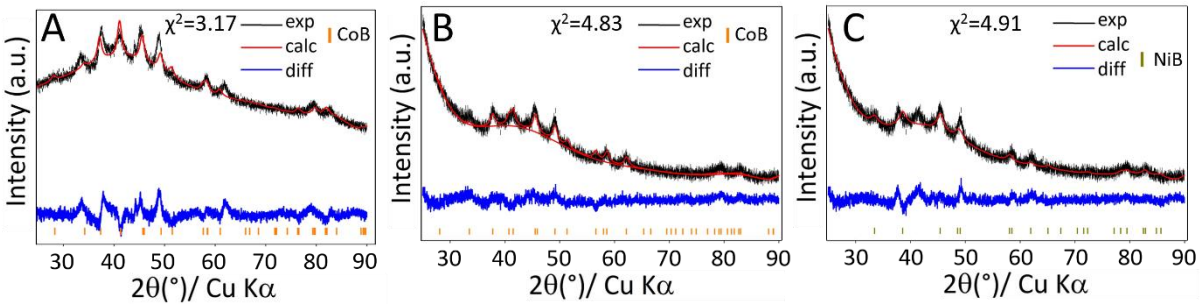

Figure S5-II. Powder XRD patterns and corresponding Rietveld refinements for the samples obtained by reacting Ni-Co nanoparticles with $NaBH_4$ (metal:B = 1:2.6 at.) at 600 °C for (A) 0.5 h by considering only CoB as constituent; for 1.5 h by considering (B) only CoB and (C) only NiB as references.

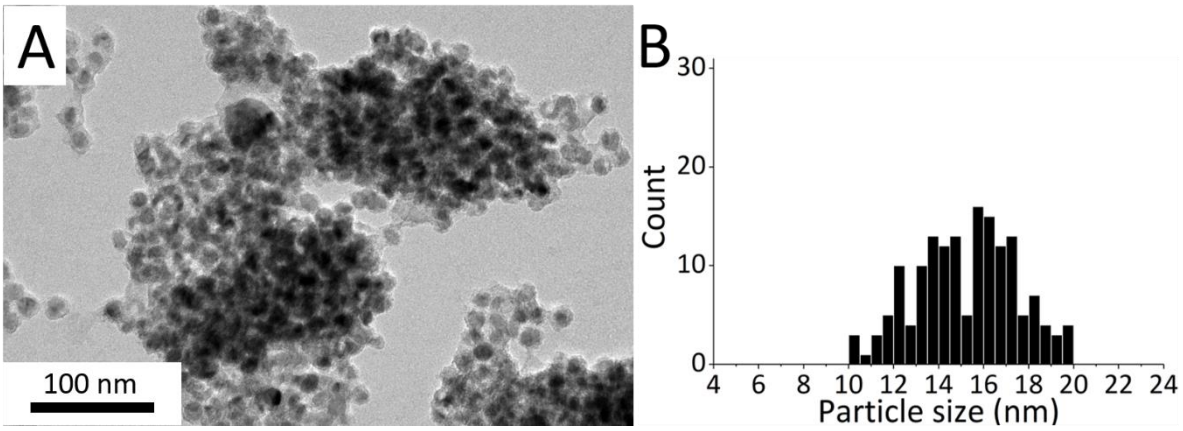

Figure S5-III. TEM image and the corresponding size distribution of the sample obtained by reacting Ni-Co nanoparticles with $NaBH_4$ (metal:B = 1:2.6 at.) at 600 °C for 1.5 h in LiI:KI.

Table S5-III. Elemental metal fractions according to STEM-EDS performed on individual particles obtained by reacting Ni-Co nanoparticles with $NaBH_4$ (metal:B = 1:2.6 at.) at 600 °C for 0.5, 1.5 and 3 h.

0.5 h	Zone 1	Zone 2	Zone 3	1.5 h	Zone 1	Zone 2	Zone 3	3 h	Zone 1	Zone 2	Zone 3
Co at. %	48.85	57.78	48.45	Co at. %	52.25	44.92	44.46	Co at. %	57.29	50.00	40.82
Ni at. %	51.15	42.22	51.55	Ni at. %	47.76	55.08	55.54	Ni at. %	42.71	50.00	59.18

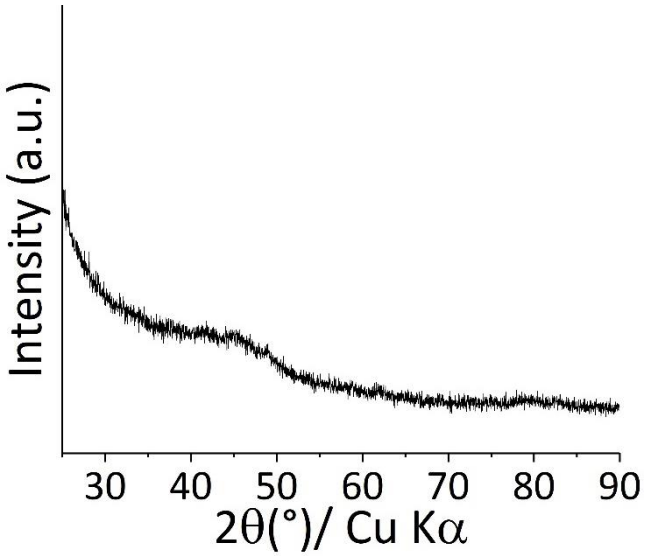

Figure S5-IV. XRD pattern of the powder obtained by reacting Ni-Co nanoparticles with $NaBH_4$ (metal:B = 1:2.6 at.) at 450 °C for 6 h in LiI/KI.

References

(1) Xu, X.; Deng, Y.; Gu, M.; Sun, B.; Liang, Z.; Xue, Y.; Guo, Y.; Tian, J.; Cui, H. Large-Scale Synthesis of Porous Nickel Boride for Robust Hydrogen Evolution Reaction Electrocatalyst. *Applied Surface Science*. **2019**, pp 591–595. https://doi.org/10.1016/j.apsusc.2018.11.127.

(2) Masa, J.; Sinev, I.; Mistry, H.; Ventosa, E.; de la Mata, M.; Arbiol, J.; Muhler, M.; Roldan Cuenya, B.; Schuhmann, W. Ultrathin High Surface Area Nickel Boride (NixB) Nanosheets as Highly Efficient Electrocatalyst for Oxygen Evolution. *Adv. Energy Mater.* **2017**, *7* (17). https://doi.org/10.1002/aenm.201700381.

(3) Jiang, W. J.; Niu, S.; Tang, T.; Zhang, Q. H.; Liu, X. Z.; Zhang, Y.; Chen, Y. Y.; Li, J. H.; Gu, L.; Wan, L. J.; Hu, J. S. Crystallinity-Modulated Electrocatalytic Activity of a Nickel(II) Borate Thin Layer on Ni3B for Efficient Water Oxidation. *Angew. Chemie - Int. Ed.* **2017**, *56* (23), 6572–6577. https://doi.org/10.1002/anie.201703183.

(4) Masa, J.; Weide, P.; Peeters, D.; Sinev, I.; Xia, W.; Sun, Z.; Somsen, C.; Muhler, M.; Schuhmann, W. Amorphous Cobalt Boride (Co 2 B) as a Highly Efficient Nonprecious Catalyst for Electrochemical Water Splitting: Oxygen and Hydrogen Evolution. *Adv. Energy Mater.* **2016**, *6* (6), 1–10. https://doi.org/10.1002/aenm.201502313.

(5) Wang, L.; Li, J.; Zhao, X.; Hao, W.; Ma, X.; Li, S.; Guo, Y. Surface-Activated Amorphous Iron Borides (Fe x B) as Efficient Electrocatalysts for Oxygen Evolution Reaction. *Adv. Mater. Interfaces* **2019**, *6* (6), 1–6. https://doi.org/10.1002/admi.201801690.

(6) Gupta, S.; Patel, M. K.; Miotello, A.; Patel, N. Metal Boride-Based Catalysts for Electrochemical Water-Splitting: A Review. *Adv. Funct. Mater.* **2020**, *30* (1). https://doi.org/10.1002/adfm.201906481.

(7) Masa, J.; Schuhmann, W. The Role of Non-Metallic and Metalloid Elements on the Electrocatalytic Activity of Cobalt and Nickel Catalysts for the Oxygen Evolution Reaction. *ChemCatChem* **2019**, *11* (24), 5842–5854. https://doi.org/10.1002/cctc.201901151.

(8) Masa, J.; Andronescu, C.; Antoni, H.; Sinev, I.; Seisel, S.; Elumeeva, K.; Barwe, S.; Marti-Sanchez, S.; Arbiol, J.; Roldan Cuenya, B.; Muhler, M.; Schuhmann, W. Role of

Boron and Phosphorus in Enhanced Electrocatalytic Oxygen Evolution by Nickel Borides and Nickel Phosphides. *ChemElectroChem* **2019**, *6* (1), 235–240. https://doi.org/10.1002/celc.201800669.

(9) Chen, Z.; Kang, Q.; Cao, G.; Xu, N.; Dai, H.; Wang, P. Study of Cobalt Boride-Derived Electrocatalysts for Overall Water Splitting. *Int. J. Hydrogen Energy* **2018**, *43* (12), 6076–6087. https://doi.org/10.1016/j.ijhydene.2018.01.161.

(10) Lao, J.; Li, D.; Jiang, C.; Luo, R.; Peng, H.; Qi, R.; Lin, H.; Huang, R.; Waterhouse, G. I. N.; Luo, C. Efficient Overall Water Splitting Using Nickel Boride-Based Electrocatalysts. *Int. J. Hydrogen Energy* **2020**, *45* (53), 28616–28625. https://doi.org/10.1016/j.ijhydene.2020.07.171.

(11) Zieschang, A. M.; Bocarsly, J. D.; Schuch, J.; Reichel, C. V.; Kaiser, B.; Jaegermann, W.; Seshadri, R.; Albert, B. Magnetic and Electrocatalytic Properties of Nanoscale Cobalt Boride, Co3B. *Inorg. Chem.* **2019**, *58* (24), 16609–16617. https://doi.org/10.1021/acs.inorgchem.9b02617.

(12) Qiang, C.; Zhang, L.; He, H.; Liu, Y.; Zhao, Y.; Sheng, T.; Liu, S.; Wu, X.; Fang, Z. Efficient Electrocatalytic Water Splitting by Bimetallic Cobalt Iron Boride Nanoparticles with Controlled Electronic Structure. *J. Colloid Interface Sci.* **2021**, *604*, 650–659. https://doi.org/10.1016/j.jcis.2021.07.024.

(13) Klemenz, S.; Schuch, J.; Hawel, S.; Zieschang, A. M.; Kaiser, B.; Jaegermann, W.; Albert, B. Synthesis of a Highly Efficient Oxygen-Evolution Electrocatalyst by Incorporation of Iron into Nanoscale Cobalt Borides. *ChemSusChem* **2018**, *11* (18), 3150–3156. https://doi.org/10.1002/cssc.201801547.

(14) Masa, J.; Piontek, S.; Wilde, P.; Antoni, H.; Eckhard, T.; Chen, Y. T.; Muhler, M.; Apfel, U. P.; Schuhmann, W. Ni-Metalloid (B, Si, P, As, and Te) Alloys as Water Oxidation Electrocatalysts. *Adv. Energy Mater.* **2019**, *9* (26), 1–8. https://doi.org/10.1002/aenm.201900796.

(15) Li, Y.; Huang, B.; Sun, Y.; Luo, M.; Yang, Y.; Qin, Y.; Wang, L.; Li, C.; Lv, F.; Zhang, W.; Guo, S. Multimetal Borides Nanochains as Efficient Electrocatalysts for Overall Water Splitting. *Small* **2019**, *15* (1), 1–8. https://doi.org/10.1002/smll.201804212.

(16) Zhang, J.; Li, X.; Liu, Y.; Zeng, Z.; Cheng, X.; Wang, Y.; Tu, W.; Pan, M. Bi-Metallic Boride Electrocatalysts with Enhanced Activity for the Oxygen Evolution Reaction.

Nanoscale **2018**, *10* (25), 11997–12002. https://doi.org/10.1039/c8nr02198h.

(17) Sun, J.; Zhang, W.; Wang, S.; Ren, Y.; Liu, Q.; Sun, Y.; Tang, L.; Guo, J.; Zhang, X. Ni-Co-B Nanosheets Coupled with Reduced Graphene Oxide towards Enhanced Electrochemical Oxygen Evolution. *J. Alloys Compd.* **2019**, *776*, 511–518. https://doi.org/10.1016/j.jallcom.2018.10.296.

(18) Schuch, J.; Klemenz, S.; Schuldt, P.; Zieschang, A. M.; Dolique, S.; Connor, P.; Kaiser, B.; Kramm, U. I.; Albert, B.; Jaegermann, W. Efficient Oxygen Evolution Electrocatalyst by Incorporation of Nickel into Nanoscale Dicobalt Boride. *ChemCatChem* **2021**, *13* (7), 1772–1780. https://doi.org/10.1002/cctc.202002030.

(19) Yuan, H.; Wei, S.; Tang, B.; Ma, Z.; Li, J.; Kundu, M.; Wang, X. Self-Supported 3 D Ultrathin Cobalt–Nickel–Boron Nanoflakes as an Efficient Electrocatalyst for the Oxygen Evolution Reaction. *ChemSusChem* **2020**, *13* (14), 3662–3670. https://doi.org/10.1002/cssc.202000784.

(20) Kim, B.; Das, G.; Kim, J.; Yoon, H. H.; Lee, D. H. Ni-Co-B Nanoparticle Decorated Carbon Felt by Electroless Plating as a Bi-Functional Catalyst for Urea Electrolysis. *J. Colloid Interface Sci.* **2021**, *601*, 317–325. https://doi.org/10.1016/j.jcis.2021.05.078.

(21) Ma, M.; Qu, F.; Ji, X.; Liu, D.; Hao, S.; Du, G.; Asiri, A. M.; Yao, Y.; Chen, L.; Sun, X. Bimetallic Nickel-Substituted Cobalt-Borate Nanowire Array: An Earth-Abundant Water Oxidation Electrocatalyst with Superior Activity and Durability at Near Neutral PH. *Small* **2017**, *13* (25). https://doi.org/10.1002/smll.201700394.

(22) Xu, N.; Cao, G.; Chen, Z.; Kang, Q.; Dai, H.; Wang, P. Cobalt Nickel Boride as an Active Electrocatalyst for Water Splitting. *J. Mater. Chem. A* **2017**, *5* (24), 12379–12384. https://doi.org/10.1039/c7ta02644g.

(23) Jiang, Y.; Lu, Y. Designing Transition-Metal-Boride-Based Electrocatalysts for Applications in Electrochemical Water Splitting. *Nanoscale* **2020**, *12* (17), 9327–9351. https://doi.org/10.1039/d0nr01279c.

(24) Cui, L.; Zhang, W.; Zheng, R.; Liu, J. Electrocatalysts Based on Transition Metal Borides and Borates for the Oxygen Evolution Reaction. *Chem. - A Eur. J.* **2020**, *26* (51), 11661–11672. https://doi.org/10.1002/chem.202000880.

(25) Lee, E.; Fokwa, B. P. T. Nonprecious Metal Borides: Emerging Electrocatalysts for

Hydrogen Production. *Acc. Chem. Res.* **2022**, *55* (1), 56–64. https://doi.org/10.1021/acs.accounts.1c00543.

(26) Zhang, Q.; Zhao, J.; Wu, Y.; Li, J.; Jin, H.; Zhao, S.; Chai, L.; Wang, Y.; Lei, Y.; Wang, S. Rapid and Controllable Synthesis of Nanocrystallized Nickel-Cobalt Boride Electrode Materials via a Mircoimpinging Stream Reaction for High Performance Supercapacitors. *Small* **2020**, *16* (39). https://doi.org/10.1002/smll.202003342.

(27) Xu, N.; Cao, G.; Chen, Z.; Kang, Q.; Dai, H.; Wang, P. Cobalt Nickel Boride as an Active Electrocatalyst for Water Splitting. *J. Mater. Chem. A* **2017**, *5* (24), 12379–12384. https://doi.org/10.1039/c7ta02644g.

(28) Bajdich, M.; García-Mota, M.; Vojvodic, A.; Nørskov, J. K.; Bell, A. T. Theoretical Investigation of the Activity of Cobalt Oxides for the Electrochemical Oxidation of Water. *J. Am. Chem. Soc.* **2013**, *135* (36), 13521–13530. https://doi.org/10.1021/ja405997s.

(29) Braun, M.; Chatwani, M.; Kumar, P.; Hao, Y.; Sanjuán, I.; Apostoleri, A. A.; Brix, A. C.; Morales, D. M.; Hagemann, U.; Heidelmann, M.; Masa, J.; Schuhmann, W.; Andronescu, C. Cobalt Nickel Boride as Electrocatalyst for the Oxidation of Alcohols in Alkaline Media. *JPhys Energy* **2023**, *5* (2). https://doi.org/10.1088/2515-7655/acbb2a.

(30) Qian, Y.; Wu, Y.; Gu, F.; Zhou, Z.; Huang, Z.; Tang, X.; Pan, S.; Zhang, S.; Chen, S.; Zhang, Q.; Chen, Y.; Wang, S. Controllable and Scale-Up Synthesis of Nickel-Cobalt Boride@Borate/RGO Nanoflakes via Reactive Impingement Mixing: A High-Performance Supercapacitor Electrode and Electrocatalyst. *Front. Chem.* **2022**, *10* (April), 1–14. https://doi.org/10.3389/fchem.2022.874675.

(31) Wang, S.; He, P.; Xie, Z.; Jia, L.; He, M.; Zhang, X.; Dong, F.; Liu, H.; Zhang, Y.; Li, C. Tunable Nanocotton-like Amorphous Ternary Ni-Co-B: A Highly Efficient Catalyst for Enhanced Oxygen Evolution Reaction. *Electrochim. Acta* **2019**, *296*, 644–652. https://doi.org/10.1016/j.electacta.2018.11.099.

(32) Ingersoll, J. C.; Mani, N.; Thenmozhiyal, J. C.; Muthaiah, A. Catalytic Hydrolysis of Sodium Borohydride by a Novel Nickel-Cobalt-Boride Catalyst. *J. Power Sources* **2007**, *173* (1), 450–457. https://doi.org/10.1016/j.jpowsour.2007.04.040.

(33) Li, L.; Liu, P.; Zhou, Y.; Duan, H.; Long, M.; Chen, D. Mechanical Properties and Electronic Structures of Borides in Ni-Co-B Alloy System. *Mater. Lett.* **2022**, *309*

(October 2021). https://doi.org/10.1016/j.matlet.2021.131312.

(34) Duan, Y. e.; Li, S.; Tan, Q.; Chen, Y.; Zou, K.; Dai, X.; Bayati, M.; Xu, B. B.; Dala, L.; Liu, T. X. Cobalt Nickel Boride Nanocomposite as High-Performance Anode Catalyst for Direct Borohydride Fuel Cell. *Int. J. Hydrogen Energy* **2021**, *46* (29), 15471–15481. https://doi.org/10.1016/j.ijhydene.2021.02.064.

(35) Liu, L. J.; Li, J. F. Effect of Co/Ni Atomic Ratio on the Metastable Phase Formation in Co-Ni-B Alloys. *J. Alloys Compd.* **2022**, *899*, 1–8. https://doi.org/10.1016/j.jallcom.2021.163375.

(36) Kayser, G. F.; Kayser, F. X. Ni3B: Powder Diffraction Pattern and Lattice Parameters. *J. Alloys Compd.* **1996**, *233* (1–2), 74–79. https://doi.org/10.1016/0925-8388(96)80037-5.

(37) Liu, Y.; Zhang, C.; Xu, B.; Yang, G.; Jiang, X.; Zhang, S.; Wang, Y.; Zhang, R.; Yin, H. Experimental Investigation and Thermodynamic Modeling of the Mo–Co–B Ternary System. *Calphad Comput. Coupling Phase Diagrams Thermochem.* **2021**, *75* (January), 102354. https://doi.org/10.1016/j.calphad.2021.102354.

(38) Rundqvist, S.; Hauge, S.; Fex, H.; Högberg, B.; Kneip, P.; Palmstierna, H. An X-Ray Investigation of the Nickel-Boron System. The Crystal Structures of Orthorhombic and Monoclinic Ni4B3. *Acta Chemica Scandinavica*. **1959**, pp 1193–1208. https://doi.org/10.3891/acta.chem.scand.13-1193.

(39) Igoa Saldaña, F.; Defoy, E.; Janisch, D.; Rousse, G.; Autran, P. O.; Ghoridi, A.; Séné, A.; Baron, M.; Suescun, L.; Le Godec, Y.; Portehault, D. Revealing the Elusive Structure and Reactivity of Iron Boride α-FeB. *Inorg. Chem.* **2022**. https://doi.org/10.1021/acs.inorgchem.2c03709.

(40) Ma, X.; Zhao, K.; Sun, Y.; Wang, Y.; Yan, F.; Zhang, X.; Chen, Y. Direct Observation of Chemical Origins in Crystalline (Ni: XCo1- x)2B Oxygen Evolution Electrocatalysts. *Catal. Sci. Technol.* **2020**, *10* (7), 2165–2172. https://doi.org/10.1039/d0cy00099j.

(41) Paksoy, A.; Kurtoğlu, S. F.; Dizaji, A. K.; Altıntaş, Z.; Khoshsima, S.; Uzun, A.; Balcı, Ö. Nanocrystalline Cobalt–Nickel–Boron (Metal Boride) Catalysts for Efficient Hydrogen Production from the Hydrolysis of Sodium Borohydride. *Int. J. Hydrogen Energy* **2021**, *46* (11), 7974–7988. https://doi.org/10.1016/j.ijhydene.2020.12.017.

(42) Li, Y.; Shao, H.; Lin, Z.; Lu, J.; Liu, L.; Duployer, B.; Persson, P. O. Å.; Eklund, P.; Hultman, L.; Li, M.; Chen, K.; Zha, X. H.; Du, S.; Rozier, P.; Chai, Z.; Raymundo-Piñero, E.; Taberna, P. L.; Simon, P.; Huang, Q. A General Lewis Acidic Etching Route for Preparing MXenes with Enhanced Electrochemical Performance in Non-Aqueous Electrolyte. *Nat. Mater.* **2020**, *19* (8), 894–899. https://doi.org/10.1038/s41563-020-0657-0.

(43) Palazzolo, A.; Poucin, C.; Freitas, A. P.; Ropp, A.; Bouillet, C.; Ersen, O.; Carenco, S. The Delicate Balance of Phase Speciation in Bimetallic Nickel Cobalt Nanoparticles. *Nanoscale* **2022**. https://doi.org/10.1039/d2nr00917j.

(44) Bonifacio, C. S.; Carenco, S.; Wu, C. H.; House, S. D.; Bluhm, H.; Yang, J. C. Thermal Stability of Core-Shell Nanoparticles: A Combined in Situ Study by XPS and TEM. *Chem. Mater.* **2015**, *27* (20), 6960–6968. https://doi.org/10.1021/acs.chemmater.5b01862.

(45) Yang, S.; Chen, G.; Ricciardulli, A. G.; Zhang, P.; Zhang, Z.; Shi, H.; Ma, J.; Zhang, J.; Blom, P. W. M.; Feng, X. Topochemical Synthesis of Two-Dimensional Transition-Metal Phosphides Using Phosphorene Templates. *Angew. Chemie - Int. Ed.* **2020**, *59* (1), 465–470. https://doi.org/10.1002/anie.201911428.

(46) Chung, Y. H.; Gupta, K.; Jang, J. H.; Park, H. S.; Jang, I.; Jang, J. H.; Lee, Y. K.; Lee, S. C.; Yoo, S. J. Rationalization of Electrocatalysis of Nickel Phosphide Nanowires for Efficient Hydrogen Production. *Nano Energy* **2016**, *26*, 496–503. https://doi.org/10.1016/j.nanoen.2016.06.002.

(47) Carenco, S.; Liu, Z.; Salmeron, M. The Birth of Nickel Phosphide Catalysts: Monitoring Phosphorus Insertion into Nickel. *ChemCatChem* **2017**, *9* (12), 2318–2323. https://doi.org/10.1002/cctc.201601526.

(48) Chan Chang, T.-H.-C. Elaboration de Borures et Phosphures Métalliques : Synthèse de Nanomatériaux En Sels Fondus et Réactivité de Surface. **2017**.

(49) Peterson, G. G. C.; Brgoch, J. Materials Discovery through Machine Learning Formation Energy. *JPhys Energy* **2021**, *3* (2). https://doi.org/10.1088/2515-7655/abe425.

(50) Jain, A.; Ong, S. P.; Hautier, G.; Chen, W.; Richards, W. D.; Dacek, S.; Cholia, S.; Gunter, D.; Skinner, D.; Ceder, G.; Persson, K. A. Commentary: The Materials Project: A Materials Genome Approach to Accelerating Materials Innovation. *APL Mater.* **2013**,

1 (1). https://doi.org/10.1063/1.4812323.

(51) Sato, S.; Kleppa, O. J. Enthalpies of Formation of Borides of Iron, Cobalt, and Nickel by Solution Calorimetry in Liquid Copper. *Metall. Trans. B* **1982**, *13* (2), 251–257. https://doi.org/10.1007/BF02664582.

(52) Casas-Cabanas, M.; Rodríguez-Carvajal, J.; Palacín, M. R. FAULTS, a New Program for Refinement of Powder Diffraction Patterns from Layered Structures. *Zeitschrift fur Krist. Suppl.* **2006**, *1* (23), 243–248. https://doi.org/10.1524/zksu.2006.suppl_23.243.

(53) Casas-Cabanas, M.; Reynaud, M.; Rikarte, J.; Horbach, P.; Rodríguez-Carvajal, J. FAULTS: A Program for Refinement of Structures with Extended Defects. *J. Appl. Crystallogr.* **2016**, *49* (6), 2259–2269. https://doi.org/10.1107/S1600576716014473.

(54) Connor, P.; Schuch, J.; Kaiser, B.; Jaegermann, W. The Determination of Electrochemical Active Surface Area and Specific Capacity Revisited for the System MnOx as an Oxygen Evolution Catalyst. *Zeitschrift fur Phys. Chemie* **2020**, *234* (5), 979–994. https://doi.org/10.1515/zpch-2019-1514.

(55) Gupta, S.; Patel, N.; Fernandes, R.; Kadrekar, R.; Dashora, A.; Yadav, A. K.; Bhattacharyya, D.; Jha, S. N.; Miotello, A.; Kothari, D. C. Co-Ni-B Nanocatalyst for Efficient Hydrogen Evolution Reaction in Wide PH Range. *Appl. Catal. B Environ.* **2016**, *192*, 126–133. https://doi.org/10.1016/j.apcatb.2016.03.032.

(56) Sheng, M.; Wu, Q.; Wang, Y.; Liao, F.; Zhou, Q.; Hou, J.; Weng, W. Network-like Porous Co-Ni-B Grown on Carbon Cloth as Efficient and Stable Catalytic Electrodes for Hydrogen Evolution. *Electrochem. commun.* **2018**, *93* (May), 104–108. https://doi.org/10.1016/j.elecom.2018.06.017.

(57) Desjardins, K.; Mocuta, C.; Dawiec, A.; Réguer, S.; Joly, P.; Dubuisson, J. M.; Alves, F.; Noureddine, A.; Bompard, F.; Thiaudière, D. The CirPAD, a Circular 1.4 M Hybrid Pixel Detector Dedicated to X-Ray Diffraction Measurements at Synchrotron SOLEIL. *J. Synchrotron Radiat.* **2022**, *29*, 180–193. https://doi.org/10.1107/S1600577521012492.

Chapter 6: The delicate conversion of iron into iron borides at the nanoscale

I) Introduction: Targeting iron borides as nanoscale materials

a) The interest of iron borides

Iron boride-based materials have a wide variety of potential application fields, from magnetism and magnetothermal properties for cancer treatment by hyperthermia or boron neutron capture therapy[1,2], to hard materials[3], catalysis including water splitting[4,5] and high capacity anodes for Li-ion batteries[6]. For some applications, especially catalysis and biomedical treatments, designing nanoscale iron borides is of utmost importance to optimize the properties. Besides few scarce compounds like Fe_9B or FeB_{49}, the phases the most reported and studied as nanoscale objects are Fe_2B and FeB with its α and β modifications[7–9]. β-FeB and α-FeB are respectively the high and low temperature forms of iron boride[8]. All the synthesis methods developed to reach these phases require high temperature treatments to trigger the crystallization, in the 600-1500 °C temperature range[1,7–12].

b) Methods to reach nanoscaled iron borides

Several approaches have been developed to reach nanoscale iron boride. Spherical β-FeB nanoparticles of 20 nm diameter were obtained by using arc-melting at 1000 °C followed by long time ball milling in hexane with oleic acid as a surfactant[2]. α-FeB was obtained by reduction of iron chloride with a borohydride into organic solvents. The resulting amorphous nanoparticles were annealed at different temperatures. From 450 to 1050 °C α-FeB nanoparticles were obtained, while treatment at 1500 °C yielded β-FeB[1,7]. Jothi *et al.*[9] developed a general pathway towards metal borides including α-FeB, by the reduction of $FeCl_2$ by liquid tin in the presence of elemental boron at 800 °C for 8 h. The process relies on the fact that tin does not form any boride. However, it lacks control over particle size and dispersion state. Some approaches have also been developed by using molten salts. FeB and Fe_2B were reported from the reaction of elemental iron and boron at 1000 °C in a NaCl-KCl mixture[11]. In our group, we previously reported the synthesis of FeB, among other borides, by reduction of iron(II) chloride by a borohydride at 900 °C in a eutectic salt mixture LiCl:KCl (44:56 mass.)[12]. More recently, we have adapted the procedure for the synthesis of pure α- or β-FeB at 600 and 1100 °C respectively. In addition to FeB, another boride phase, Fe_2B, has been currently reported as nanostructures. Fe_2B was synthesized by a mechanochemical method at ambient temperature using Fe_2O_3, amorphous B and Mg powders. Acid etching with HCl was then performed to remove the by-product MgO and to obtain XRD pure Fe_2B phase with average particle sizes of 38 nm[5]. The high energy ball milling setup allowed to avoid an annealing

treatment to trigger the crystallization. However, this method yielded a large size distribution from *ca.* 30 to 150 nm. Another method for the synthesis of XRD pure phases Fe_2B and FeB is based on the reaction between elemental Fe and amorphous B powder in a NaCl/KCl molten salt mixture at 1000 °C[11]. In these conditions, nanoplatelets of 20-40 nm in thickness were obtained for Fe_2B while FeB was formed as nanorods of 30-40 nm diameter and 100-150 nm length. Interestingly, the authors proposed that FeB crystallization occurred through the formation of Fe_2B first, which then reacted with additional boron to form FeB.

Overall, the syntheses described above suffer from poor control of the particle size, morphology and dispersion state. Enhancing this control is crucial to adjust magnetic and to improve the catalytic properties. Along this chapter, we study the incorporation of boron into Fe nanoparticles, by capitalizing on the reaction pathways discussed in the previous chapters. We use molten salts conditions for two reasons. Firstly, molten salts allow to obtain crystalline materials in a single step, unlike most of the other approaches that require post-annealing. Secondly, this medium demonstrated a large decrease in reaction temperatures compared to other approaches, particularly those from elemental precursors. In parallel with the study of the reaction mechanism, we discuss the role of surface ligands at the surface of the iron nanoparticles on their reactivity.

II) The role of surface ligands during the conversion of iron to iron boride

a) Core-shell iron-iron oxide nanoparticles and their tentative conversion into boride

We use a reported procedure[13] to form spherical body-centered cubic (bcc)-Fe nanoparticles of 10 nm (**Figure S6-IA-B**). As reported, the nanoparticles are amorphous according to XRD (**Figure S6-IC**). The reaction proceeds through a one-pot process at 180 °C by decomposition of $Fe(CO)_5$ in octadecene in the presence of oleylamine as solvent and surfactant, respectively. After washing, the particles showed an iron core surrounded by a shell composed of Fe_3O_4, which originates from passivation in contact with air. SEM-EDS detects only Fe and oxygen as significant species.

We then investigated the conversion of these Fe-Fe_3O_4 nanoparticles by reaction with a borohydride within the molten eutectic salt mixture LiCl:KCl (44:56 mass.). The Fe:B reagents ratio was adjusted to target α-FeB and Fe_2B. These compositions were targeted as both structures can crystallize from 600 °C according to the litterature[8,14]. Secondly, the formation

energy profile calculated as a function of the Fe:B compositions with the machine learning tool Matlearn[15] suggests a unique minimum for the composition Fe:B 1:1 (**Figure S6-II**). The phase Fe_2B is at a slighter higher formation energy.

As in the previous chapters, we have used an excess of borohydride (Fe:B = 1:1.3 at. and 2:1.3 at. to target FeB and Fe_2B, respectively). In order to improve the dispersion state of the nanoparticles and their reactivity, the nanoparticles were first dispersed in the eutectic salt mixture by using an initial dispersion of the nanoparticles in hexane. After drying under vacuum, $NaBH_4$ as boron (0) source was added into the impregnated mixture. The reaction was then performed at 600 °C for 3 h, followed by natural cooling. For both compositions studied, XRD and TEM (**Figure S6-III**) indicate an amorphous material. The morphology and core-shell structure of the initial particles is retained (**Figure S6-IIIC**). SEM-EDS (**Table S6-I**) indicated only boron and iron as significant contribution if oxygen is discarded. Note that this technique is not suitable for the determination of the carbon content. The large excess of boron compared to iron is observed for both stoichiometries and confirms the retention of boron in the product. Variabilities in the Fe:B values indicate inhomogeneities in the samples.

A synchrotron study at the DIFFABS beamline of synchrotron SOLEIL was performed for the stoichiometry Fe:B = 1:1.3 in conditions similar to those used at the lab-scale (**Figure S6-IV**). NaCl is also detected with the crystallized salt mixture, which is attributed to metathesis between $NaBH_4$ and the alkali chlorides. Beyond the melting point, no diffraction peak is observed until 69 min (T_{meas}= 580 °C). It corresponds to the crystallization of Fe_2O_3, also observed after cooling. An unidentified intermediate phase is also observable between 69 and 85 min (T_{meas}= 738 °C). None of the reported iron borides, borates, carbides, oxides or hydroxides can fit with this intermediate phase. We also notice that the crystallization of the Fe_2O_3 was unexpected according to the literature[13], which indicates an oxygen-poorer layer of Fe_3O_4 on the iron nanoparticles. Still during the heating ramp, bcc-Fe crystallizes from 85 min (T_{meas}= 738 °C) and is maintained during the plateau. The crystallization of SiO_2 from the capillary occurs at the same temperature. No additional species were identified during the plateau at 800 °C for 1 h. These data suggest a poor reactivity of the nanoparticles in the reaction conditions, which can be explained by two origins: (1) the oxide passivation layer may hinder diffusion of boron by scavenging boron atoms in the form of boron oxide or hydroxide; (2) some carbides may have formed during the synthesis of the iron nanoparticles. These stable phases may hinder the reactivity of iron cores. Iron carbide formation has been reported[16] from iron pentacarbonyl at 150 °C under 3 bars of H_2 or Ar gas. However, even at ambient pressure,

the thermal decomposition of $Fe(CO)_5$ in presence of long-chains ligands presented degraded magnetic properties attributed to the formation of side products containing carbon or oxygen[17]. Under argon, a core-shell structure was obtained with iron remaining in the core and a crystalline shell made of iron carbides. As the reaction in molten salts is performed at 600 °C, one can hypothesize that carbide formation could occur, even at room pressure. Further investigation would be needed to characterize and understand the composition of the resulting particles and to decipher the two hypotheses.

b) Synthesis of crystalline Fe nanoparticles as precursors for boride synthesis

To enhance reactivity, we have sought to use iron nanoparticles exempt of ligands that could trigger side-reactions. To do so, we have used core-shell bcc-Fe-iron oxide nanoparticles[18] formed by a modification of the previous procedure in presence of hexadecylammonium chloride and oleic acid from a reported procedure[18] and in collaboration with the authors: Dr. Lise-Marie Lacroix and Melik Maksem at Laboratoire de Physique et Chimie des Nano-Objets, Toulouse. As reported, the ammonium chloride facilitates the formation of the crystalline structure by slowing down the decomposition of $Fe(CO)_5$. Contrary to the initial procedure described in the previous section, XRD (**Figure 1A**) shows the diffraction peaks attributed to bcc-Fe. No diffraction peak belonging to any iron oxide is observed. The Fe nanoparticles are spherical with a diameter of ~13 nm according to TEM (**Figure 1B-D**), in agreement with the reported procedure[18]. An amorphous shell of 2-3 nm is observed on the surface of the particles (**Figure 1C**), which is consistent with passivation upon exposure to air for TEM observation.

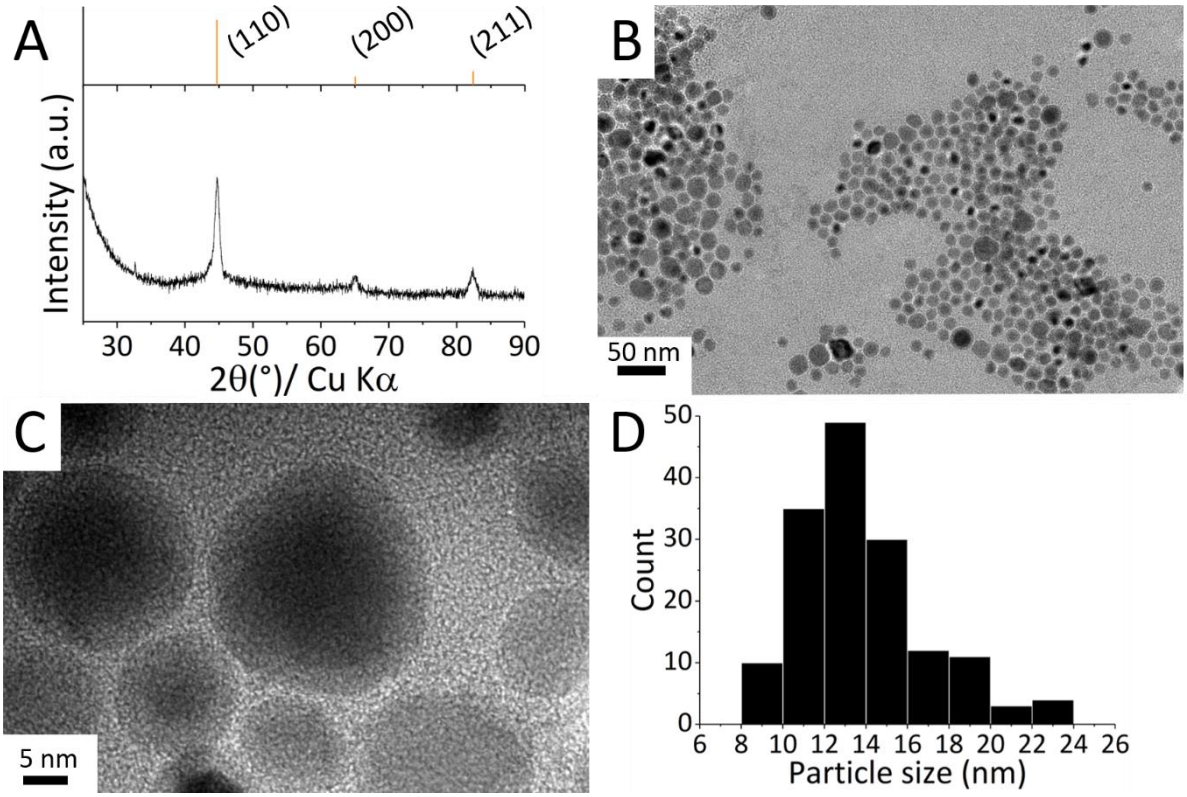

Figure 1. Crystalline bcc-Fe nanoparticles synthesized by adapting the method reported by L.-M. Lacroix *et al.*[18]. (A) Powder XRD pattern indexed along the bcc-Fe. (B) TEM and (C) HRTEM images showing spherical nanoparticles, with (D) the corresponding size distribution (D).

c) Synthesis of iron boride from Fe nanoparticles

We have targeted α-FeB from the iron nanoparticles obtained with the HDA-derived protocol. The reaction was performed at 600 °C and 700 °C for 3 h. For both temperatures, the powder XRD patterns indicate crystallization of α-FeB (**Figure 2A**). Two minor and narrow peaks in the 600 °C pattern remain unidentified. They may correspond to a sub-product formed with the components of the salt. α-FeB can be described as an intergrowth of nanodomains between β-FeB and CrB structural types. Further refinement should help to elucidate the fraction and size of both structure types[8]. The size distribution of the initial Fe nanoparticles is overall maintained although with a slight growth (**Figure 2B-G**), from initially 13 nm to 14 and 17 nm for the α-FeB nanoparticles obtained at 600 and 700 °C, respectively. Thus, we achieve a size and morphology control superior to previous reports on iron boride[1,7–12]. We note that other

diameters should be within reach by adjusting the synthesis parameters of the initial Fe nanoparticles.

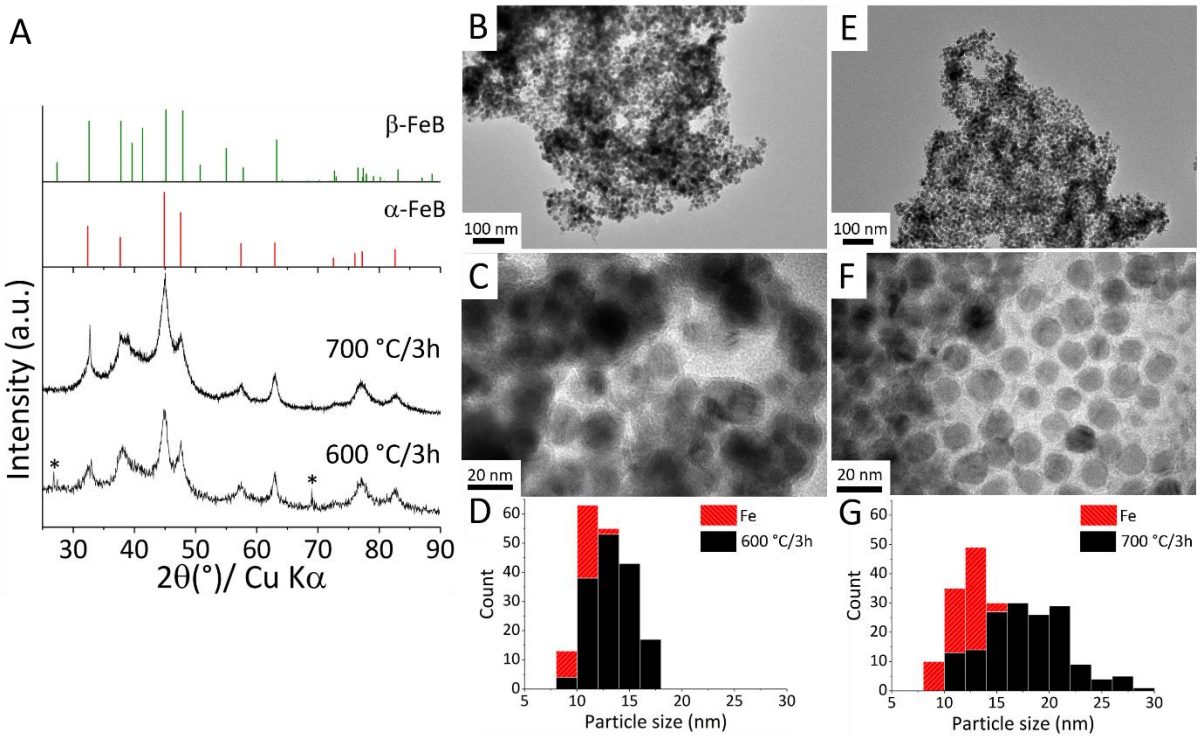

Figure 2. (A) Powder XRD patterns, (B, C, E, F) TEM images and (D, G) corresponding size distributions for the products obtained by reacting HDA-derived Fe nanoparticles with $NaBH_4$ (initial Fe:B atomic ratio 1:1.3) in the molten eutectic mixture LiCl:KCl. The products were obtained by reaction at (B-D) 600 and 700 °C (E-G). *: unindexed peaks.

d) Study of the reaction mechanism by *In situ* X-ray diffraction

Similarly to the previous study, we have investigated *in situ* the reaction pathway towards iron boride, by synchrotron radiation-based XRD in transmission mode at the DIFFABS beamline of synchrotron SOLEIL (**Figure 3**). The reaction medium was inserted into a 1 mm diameter fused silica capillary placed into a custom-made capillary oven dedicated to reactions in molten salts. The conditions are identical to those studied *ex situ*. The salt mixture melts at around 350 °C, as expected. Below this temperature, only the diffraction peaks of LiCl, KCl, NaCl and bcc-Fe are observed. NaCl is only present in a short range between 150 and 350 °C. It is presumably formed by metathesis between $NaBH_4$ and LiCl and/or KCl. Beyond the melting point, the absence of diffraction peaks indicates X-ray amorphous species between 350 and 450 °C. Crystallization of α-FeB occurs from ~450 °C. At 74 min (15 min on the 600 °C

plateau), new intense diffraction peaks appear, which are attributed to the crystallization of silica from the silica capillary in agreement with a reference experiment on a capillary filled with a salt mixture. The slight increase of temperature from 600 to 700 °C triggered the crystallization of FeO(OH) and Fe_2O_3 at 170 min in addition to the already formed α-FeB. We assume that their crystallization is due to the oxygen contained in the silica capillary walls in combination with the oxide shell initially present on the surface of iron nanoparticles.

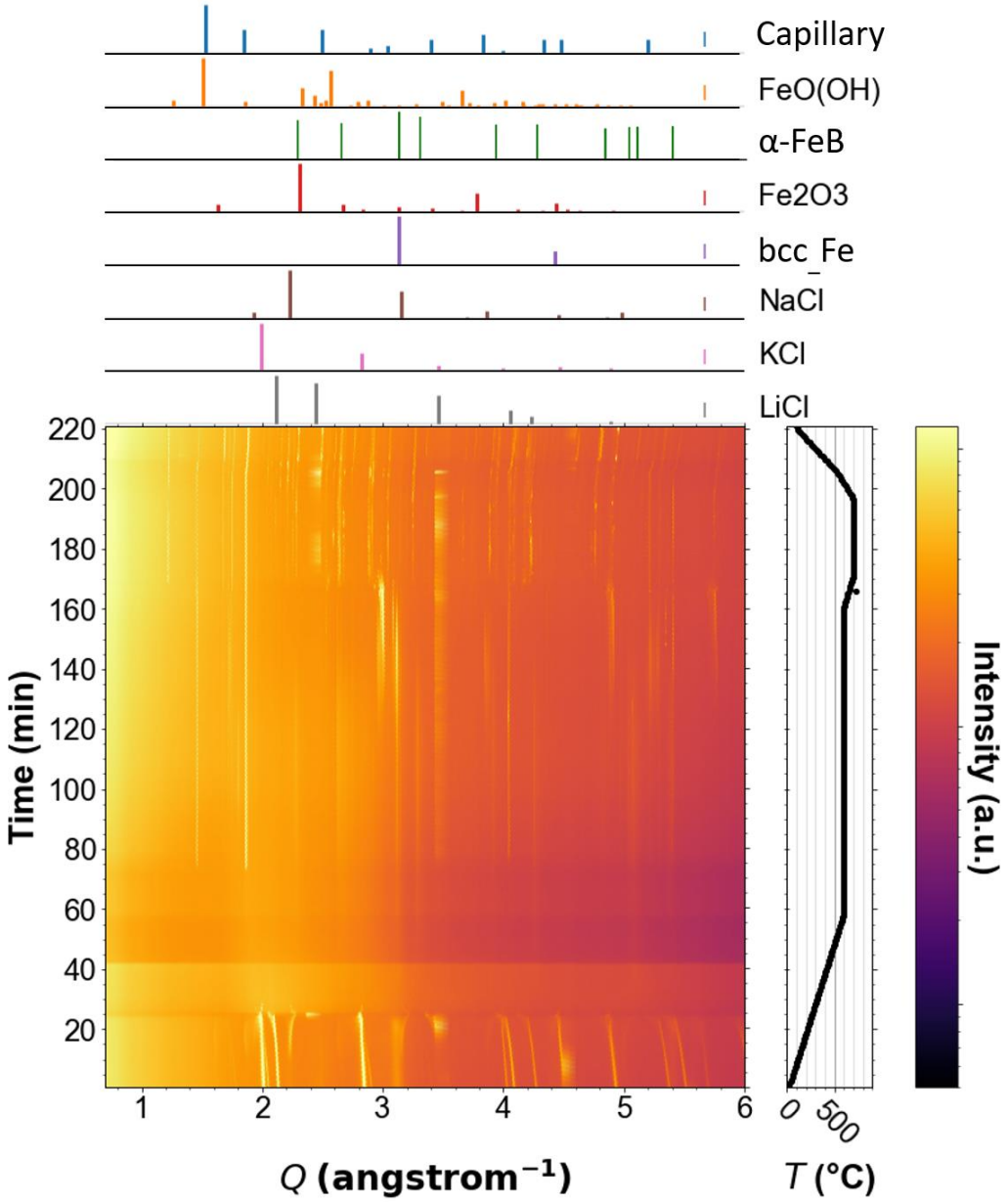

Figure 3. Synchrotron radiation-based *in situ* XRD diagrams recorded during the reaction of bcc-Fe nanoparticles with $NaBH_4$ (initial Fe:B = 1:1.3 at.) in the eutectic mixture LiCl:KCl.

e) Assessment of stability under air

Unexpectedly, the first TEM study, carried out by dispersion in methanol and drying in air for several hours, showed dramatic changes in morphology (**Figure S6-VA-D**). The particles were highly aggregated and embedded in an amorphous matrix. Partial to complete leaching of the particles was also observed. Furthermore, the sample obtained at 700 °C also showed empty shell particles (**Figure S6-VB**), but with a size similar to their homogeneous counterparts (**Figure S6-VA**). Although further investigation of the local composition would be necessary, we suppose that the iron boride nanoparticles form boron-doped iron oxide/hydroxide or borate species. The empty nanoshells observed at 700 °C could correspond to a better crystallization of the shell than at 600°C, leading to a leaching of the core while maintaining the shell. An increase in stability under air may be achievable by additional treatments, as annealing, incorporation into a support, or addition of a surface ligand.

III) Targeting Fe_2B

In parallel with the initial Fe:B 1:1.3 at. ratio for targeting the FeB composition, we have studied the initial Fe:B ratio 2:1.3 at., aiming for Fe_2B. Despite the decrease in boron content, the XRD pattern (**Figure S6-VI**) is similar to those obtained with the initial ratio Fe:B = 1:1.3. The KCl peaks correspond to residues of the salt mixture not sufficiently washed. This observation is however in accordance with the calculated formation energies of iron borides (**Figure S6-II**), which indicate that FeB is the most stable iron boride. As no diffraction peak can be attributed to iron (0), this suggests the formation of amorphous nanoparticles. A higher temperature would then be needed to engage all iron atoms into the boride and then form Fe_2B.

Conclusion and perspectives

In this chapter, we have successfully synthetized α-FeB nanoparticles by incorporating boron atoms into pre-formed iron nanoparticles. This conversion of nanoparticles is isomorphic, in the sense that the initial particle size is maintained. Although the nanocrystals did not present any morphological evolution up 700 °C in molten salts, they undergo a rapid degradation of the structure and the morphology under air, probably by an oxidation process. Our attempts to form

Fe_2B nanocrystals with the same approach were unsuccessful and the system evolves towards α-FeB, the most stable iron boride if Fe and B are not totally associated.

We postulate that a higher temperature would force both elements to react quantitatively and yield Fe_2B. A forthcoming study using *in situ* XRD may also allow to identify the conditions of Fe_2B crystallization. As other perspectives, the stability under air should be enhanced, possibly by post-treatment of the particles surface, and electrocatalytic properties for water splitting should be addressed in the near future.

Annexes

Experimental methods

Reagents. Iron pentacarbonyl ($Fe(CO)_5$,99.99 %,Acros) , sodium borohydride ($NaBH_4$, min 98%, Alfa Aesar), anhydrous hexane (95 %, Sigma-Aldrich), lithium chloride (99.9 % Alfa Aesar), potassium chloride (99.9 % Sigma-Aldrich) were stored and manipulated as received in an Ar-filled glovebox ($H_2O < 0.5$ ppm, $O_2 < 0.5$ ppm). Oleylamine (98 %, SAFC), oleylamine (technical grade 70 %, Sigma Aldrich), 1-octadecene (technical grade 90 %, Sigma Aldrich), hexadecylamine (HDA, 90 %, Sigma Aldrich), HCl solution of 1.0 M in diethylether (Merck), Hexane (VWR Normapur grade), oleic acid (90 %, Sigma Aldrich) were stored and used in air. Acetone (VWR Normapur grade), methanol (VWR Normapur grade) were used for washing.

a) Synthesis of the iron nanoparticles adapted from Peng et al. procedure [13]

16.3 g (60.8 mmol) of oleylamine 98 % and 0.3 g (1.1 mmol) of 1-octadecene were introduced in a 100 mL three-necked round bottom flask and adapted on a Schlenk line with a condenser. The mixture was degassed at 120°C for 30 min under vacuum and then put under N_2. The mixture was then heated up to 180°C. 0.7 mL (5 mmol) of $Fe(CO)_5$ were quickly added with a syringe and the mixture was maintained at 20 min at the same temperature under stirring. Finally, the suspension was cooled down to ambient temperature. The washing steps were performed under N_2. For the first washing, a mixture of ≈ 5 mL of hexane and ≈ 20 mL of acetone was added to the suspension. The flask was placed in a sonication bath while maintaining the N_2 flow. Thereafter, a magnet was used to separate the solvent from the nanoparticles. Four other washing cycles were performed by first using ≈ 5 mL of hexane to disperse the nanoparticles by sonication and then ≈ 20-30 mL of acetone to destabilize the suspension and alloying separation with a magnet. After the final washing, ≈20 mL of acetone was added, the particles were transferred in a tube maintained under N_2 and dried by removing the supernatant. Finally, the tube was transferred in a glove box. Around 0.15 g of product was obtained.

b) Synthesis of the iron nanoparticles adapted from Lacroix et al. procedure[18]

In a three-necked round bottom flask, a mixture of 20 mL (62 mmol) of 1-octadecene, 0.3 mL (1 mmol) of oleylamine 70 % and 0.278 g (1 mmol) of HDA·HCl were stirred while degassed three times by alternating vacuum and N_2 flow at ambient temperature. Then, the solution was

heated to 120 °C under nitrogen with a heating mantle and maintained 30 minutes under vacuum. Subsequently, the flask was flushed by N_2 and heated to 180 °C. 0.7 mL (5 mmol) of $Fe(CO)_5$ was then quickly added with a syringe and the medium was maintained 30 min at this temperature under nitrogen. The temperature was then reduced to 160 °C, 0.3 mL of oleic acid was added and mixture stirred for 30 min at. Finally, the medium was cooled down to room temperature. The washing steps were performed similarly to the previous procedure.

Preparation of HDA·HCl.

A 100 mL single-necked round bottom flask closed with a cap was filled with 100 mL of hexane under stirring and cooled by an ice bath for at least 20 min. 2.44 g (10 mmol) of hexadecylamine (HDA) and then 12 mL of a HCl solution (1.0 M in diethylether) were added successively. A white precipitate formed. The reaction medium was warmed up by removing the ice bath and stirred for 2 h. The precipitate was washed three times by centrifugation with hexane. Finally, the product was dried under a fume hood to remove hexane.

c) Synthesis of iron borides nanoparticles

In a Schlenk tube, 50 mg (0.89 mmol) of Fe nanoparticles were impregnated in 0.447 g of LiCl:KCl salt mixture (44:56 mass.) by adding the salt to a dispersion of these particles into 0.5 mL of anhydrous hexane (2 mmol of Fe per gram of eutectic salt) on a Schlenk line. Thereafter, respectively 0.0440 g (1.16 mmol) for FeB or 0.0220 g (0.58 mmol) for Fe_2B of $NaBH_4$ was added after correction with the experimental mass recovered after impregnation. The mixture was ball milled for 2 min at 20 Hz and re-introduced in a glove box. The powder was placed in a carbon crucible, itself inserted in a closed quartz tube. The synthesis was performed in a calibrated tubular oven under Ar flow. After cooling down to ambient temperature, washing was performed by 10 cycles of dispersion-reprecipitation in methanol by centrifugation. Finally, the product was dried in a Schlenk tube under vacuum on a Schlenk line.

d) Preparation of carbon deposited Cu grids for TEM

- Grids preparation under air conditions. The nanoparticles were dispersed by sonication in the solvent used for washing (hexane for the iron nanoparticles, methanol for iron boride nanoparticles) and a single droplet was drop-casted on the carbon-coated copper grid. The grid was then dried under air.

- Grids preparation in air-free conditions. The carbon-coated copper grid was brought in an argon-filled glovebox. Some sample powder was deposited on the grid. The grid was then transferred in an Eppendorf tube sealed with parafilm, in order to maintain the sample and the grid under inert atmosphere until TEM analysis.

e) *In situ* synchrotron powder XRD studies

The studies were operated at the DIFFABS beamline at the Soleil synchrotron. A capillary oven designed by our team including a quartz capillary of Ø 1 mm served as support for the reaction medium. The conditions are identical to those studied *ex situ* including a concentration of 2 mmol of Fe nanoparticles per gram of LiCl/KCl (44/56 mass.) and a ramp step of 10°C min^{-1}. For the first study, a plateau of 1h at 800 °C was applied. A temperature shift was observed on the diagram as the melting of the eutectic salt LiCl:KCl (44:56 mass.) was observed from 46 min at a temperature of 286 °C instead of 350 °C. The ramp was then recalibrated by using the melting point as reference. For the second study, a temperature of 600 °C was maintained for 100 min to observe the crystallization. Subsequently, a second dwell time of 20 minutes at 700 °C completed the mechanistic study.

Supplementary data for chapter 6

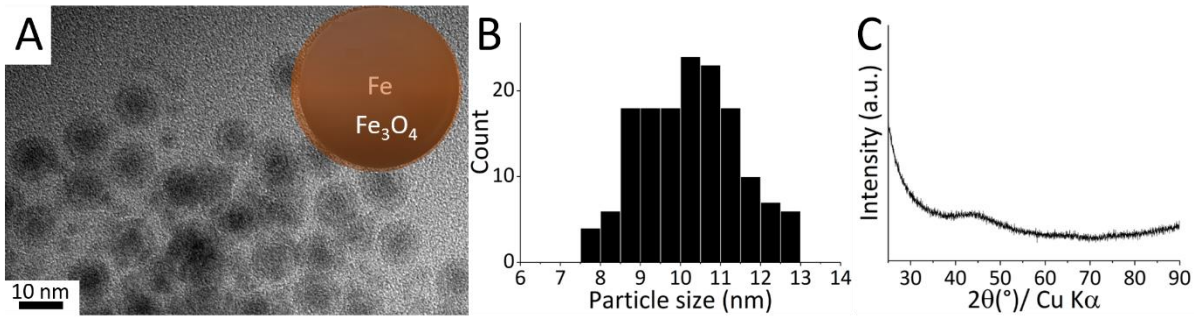

Figure S6-I. Fe nanoparticles synthesized by colloidal chemistry[13] using $Fe(CO)_8$ as precursor. (A) TEM image and the corresponding scheme of the core-shell Fe-Fe_3O_4 structure, corresponding (B) size distribution and (C) powder XRD pattern.

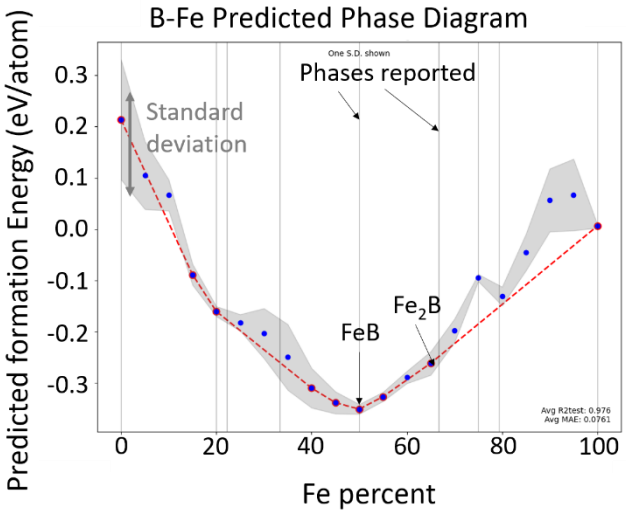

Figure S6-II. Predicted phase diagram at 0 K of Fe-B from the machine learning tool Matlearn[15]. The red dotted line corresponds to the convex hull. The blue point are phases predicted and the continuous vertical lines correspond to the phases reported.

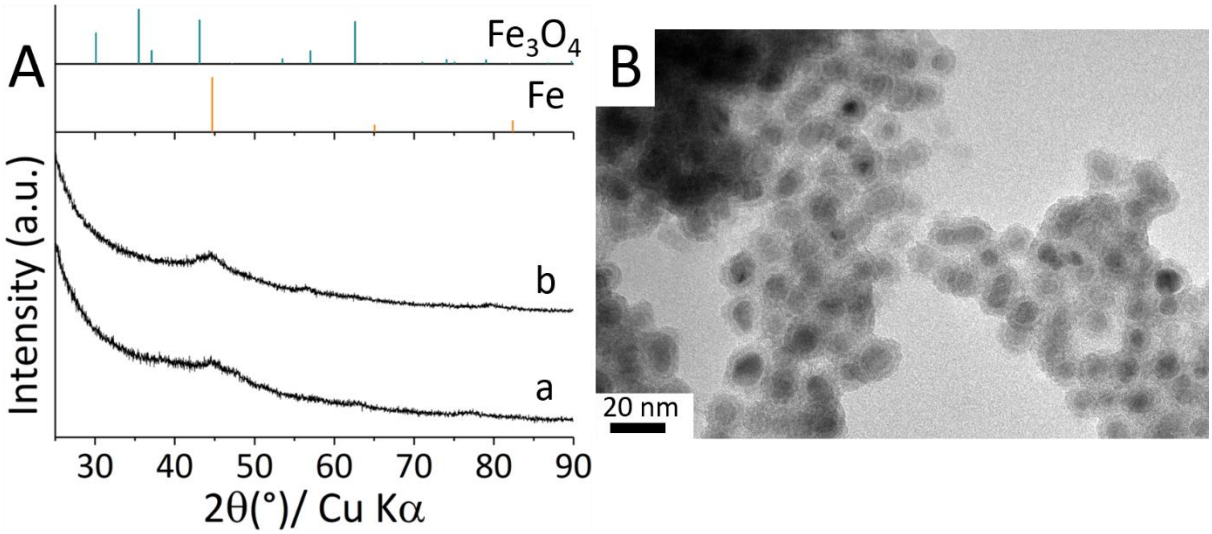

Figure S6-III. (A) Powder XRD patterns of the powders obtained from the reaction of Fe-Fe_3O_4 nanoparticles with $NaBH_4$ in the molten eutectic mixture LiCl:KCl at 600 °C for 3 h with initial Fe:B atomic ratios (a) 1:1.3 and (b) 2:1.3. (B) TEM image of the sample obtained with Fe:B = 2:1.3.

Table S6-I. Elemental composition from most significant contributions of Fe:B compositions according to SEM-EDS. The oxygen values are not taken into account due the oxidation of the material under air during sample preparation for SEM.

Fe:B 1:1.3	Zone 1	Zone 2	Zone 3	Fe:B 2:1.3	Zone 1	Zone 2	Zone 3
B_{atom} %	63.3	64.8	48.0	B_{atom} %	72.7	80.3	56.8
Fe_{atom} %	35.7	33.7	49.8	Fe_{atom} %	24.7	16.8	42.5
$B:Fe_{atom\ \%}$	1.8	1.9	1	$B:Fe_{atom\ \%}$	2.9	4.8	1.3

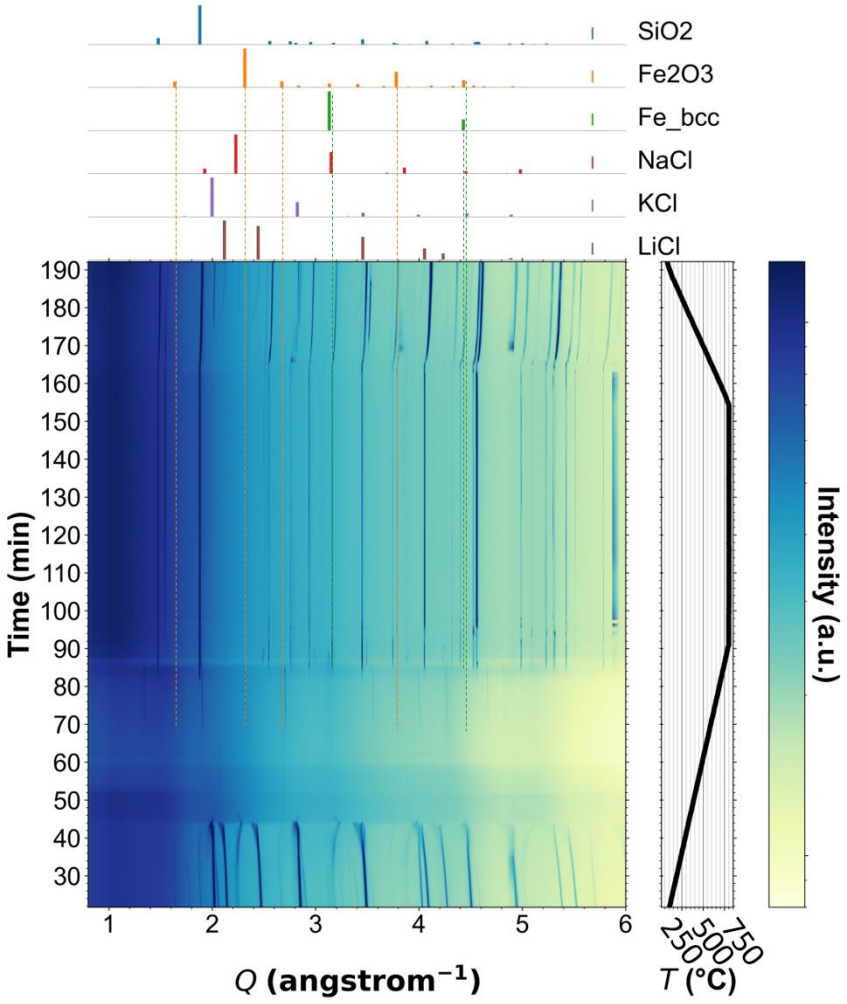

Figure S6-IV. Synchrotron radiation-based *in situ* XRD diagrams recorded during the reaction of bcc-Fe nanoparticles from the Peng et al. procedure[13] with $NaBH_4$ (initial Fe:B = 1:1.3 at.) in the eutectic mixture LiCl:KCl. The heating ramp was recalibrated based on the heating point of the salt mixture.

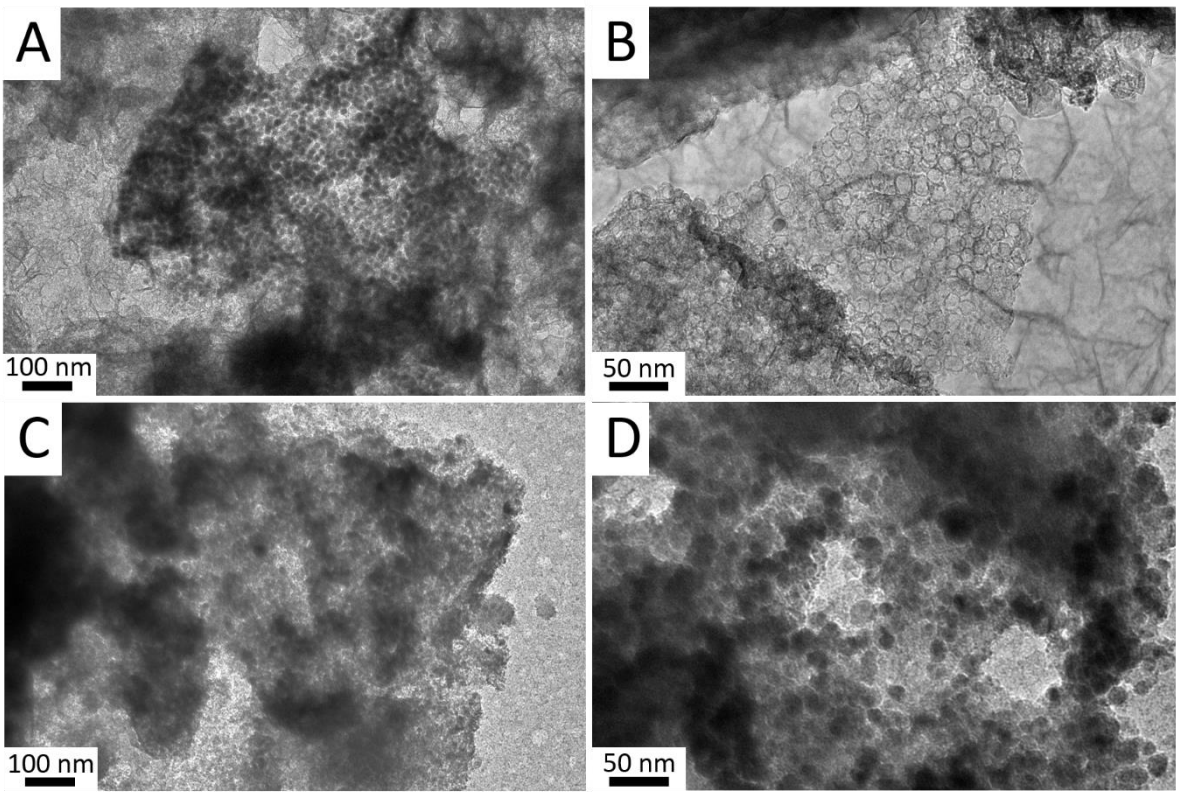

Figure S6-V. TEM images of α-FeB nanoparticles synthetized at (A, B) 600 °C for 3 h, (C, D) 700 °C for 3 h by dispersion of the nanoparticles into methanol before deposition on a TEM carbon-coated copper grid and drying under air.

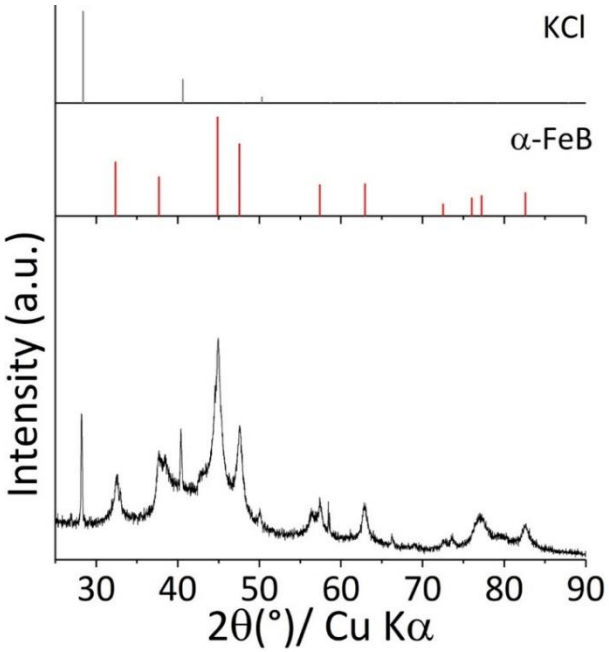

Figure S6-VI. Powder XRD pattern of the particles synthetized with Fe:B = 2:1.3 at. ratio at 700 °C for 3 h in molten LiCl:KCl.

References

(1) Rades, S.; Kraemer, S.; Seshadri, R.; Albert, B. Size and Crystallinity Dependence of Magnetism in Nanoscale Iron Boride, α-FeB. *Chem. Mater.* **2014**, *26* (4), 1549–1552. https://doi.org/10.1021/cm403167a.

(2) Hamayun, M. A.; Abramchuk, M.; Alnasir, H.; Khan, M.; Pak, C.; Lenhert, S.; Ghazanfari, L.; Shatruk, M.; Manzoor, S. Magnetic and Magnetothermal Studies of Iron Boride (FeB) Nanoparticles. *J. Magn. Magn. Mater.* **2018**, *451*, 407–413. https://doi.org/10.1016/j.jmmm.2017.11.088.

(3) Ozdemir, O.; Usta, M.; Bindal, C.; Ucisik, A. H. Hard Iron Boride (Fe2B) on 99.97 Wt% Pure Iron. *Vacuum* **2006**, *80* (11–12), 1391–1395. https://doi.org/10.1016/j.vacuum.2006.01.022.

(4) Qiang, C.; Zhang, L.; He, H.; Liu, Y.; Zhao, Y.; Sheng, T.; Liu, S.; Wu, X.; Fang, Z. Efficient Electrocatalytic Water Splitting by Bimetallic Cobalt Iron Boride Nanoparticles with Controlled Electronic Structure. *J. Colloid Interface Sci.* **2021**, *604*, 650–659. https://doi.org/10.1016/j.jcis.2021.07.024.

(5) Rezaei, F.; Akarsu, C.; Khakzad, F.; Mertdinç, S.; Ağaoğulları, D.; Ölmez-Hancı, T. Fe2B Magnetic Nanoparticles: Photocatalytic Activity towards Degradation of Bisphenol A. *Ceram. Int.* **2022**, *48* (22), 33660–33669. https://doi.org/10.1016/j.ceramint.2022.07.312.

(6) Yu, X.; Licht, S. High Capacity Alkaline Super-Iron Boride Battery. *Electrochim. Acta* **2007**, *52* (28), 8138–8143. https://doi.org/10.1016/j.electacta.2007.07.022.

(7) Rades, S.; Kornowski, A.; Weller, H.; Albert, B. Wet-Chemical Synthesis of Nanoscale Iron Boride, XAFS Analysis and Crystallisation to α-FeB. *ChemPhysChem* **2011**, *12* (9), 1756–1760. https://doi.org/10.1002/cphc.201001072.

(8) Igoa Saldaña, F.; Defoy, E.; Janisch, D.; Rousse, G.; Autran, P. O.; Ghoridi, A.; Séné, A.; Baron, M.; Suescun, L.; Le Godec, Y.; Portehault, D. Revealing the Elusive Structure and Reactivity of Iron Boride α-FeB. *Inorg. Chem.* **2022**. https://doi.org/10.1021/acs.inorgchem.2c03709.

(9) Jothi, P. R.; Yubuta, K.; Fokwa, B. P. T. A Simple, General Synthetic Route toward Nanoscale Transition Metal Borides. *Adv. Mater.* **2018**, *30* (14), 2–7.

https://doi.org/10.1002/adma.201704181.

(10) Barinov, V. A.; Dorofeev, G. A.; Ovechkin, L. V.; Elsukov, E. P.; Ermakov, A. E. Structure and Magnetic Properties of the A-FeB Phase Obtained by Mechanical Working. *Phys. Status Solidi* **1991**, *123* (2), 527–534. https://doi.org/10.1002/pssa.2211230217.

(11) Wei, Y.; Liu, Z.; Ran, S.; Xia, A.; Yi, T. F.; Ji, Y. Synthesis and Properties of Fe-B Powders by Molten Salt Method. *J. Mater. Res.* **2017**, *32* (4), 883–889. https://doi.org/10.1557/jmr.2017.38.

(12) Portehault, D.; Devi, S.; Beaunier, P.; Gervais, C.; Giordano, C.; Sanchez, C.; Antonietti, M. A General Solution Route toward Metal Boride Nanocrystals. *Angew. Chemie - Int. Ed.* **2011**, *50* (14), 3262–3265. https://doi.org/10.1002/anie.201006810.

(13) Peng, S.; Wang, C.; Xie, J.; Sun, S. Synthesis and Stabilization of Monodisperse Fe Nanoparticles. *J. Am. Chem. Soc.* **2006**, *128* (33), 10676–10677. https://doi.org/10.1021/ja063969h.

(14) Li, H.; Wen, P.; Li, Q.; Dun, C.; Xing, J.; Lu, C.; Adhikari, S.; Jiang, L.; Carroll, D. L.; Geyer, S. M. Earth-Abundant Iron Diboride (FeB2) Nanoparticles as Highly Active Bifunctional Electrocatalysts for Overall Water Splitting. *Adv. Energy Mater.* **2017**, *7* (17). https://doi.org/10.1002/aenm.201700513.

(15) Peterson, G. G. C.; Brgoch, J. Materials Discovery through Machine Learning Formation Energy. *JPhys Energy* **2021**, *3* (2). https://doi.org/10.1088/2515-7655/abe425.

(16) Meffre, A.; Mehdaoui, B.; Kelsen, V.; Fazzini, P. F.; Carrey, J.; Lachaize, S.; Respaud, M.; Chaudret, B. A Simple Chemical Route toward Monodisperse Iron Carbide Nanoparticles Displaying Tunable Magnetic and Unprecedented Hyperthermia Properties. *Nano Lett.* **2012**, *12* (9), 4722–4728. https://doi.org/10.1021/nl302160d.

(17) Lacroix, L. M.; Meffre, A.; Gatel, C.; Fazzini, P. F.; Lachaize, S.; Respaud, M.; Chaudret, B. Nanoparticle Ripening : A Versatile Approach for the Size and Shape Control of Metallic Iron Nanoparticles. *Chempluschem* **2019**, *84* (3), 302–306. https://doi.org/10.1002/cplu.201800665.

(18) Lacroix, L. M.; Frey Huls, N.; Ho, D.; Sun, X.; Cheng, K.; Sun, S. Stable Single-Crystalline Body Centered Cubic Fe Nanoparticles. *Nano Lett.* **2011**, *11* (4), 1641–1645.

https://doi.org/10.1021/nl200110t.

General conclusion and perspectives

Along this thesis, we have designed new nanoparticles and nanostructures of metal and p-block elements (boron and phosphorus), by mastering the reactivity of metal nanoparticles into molten salts. This approach consisted in the incorporation of p-block elements (B and P) into metal containing nanoparticles. It has enabled to reach an unprecedented control of the morphology of boride and borophosphide nanoparticles, which is essential to tune their properties, especially as electrocatalysts for water splitting half-reactions. Already reported for a range of nanomaterials, including phosphides, this approach had never been reported for borides, which show similarities with phosphides in terms of bonding, crystal and electronic structures, but with a higher degree of covalence that precluded reactivity in usual solvents. Therefore, we have performed the conversion of nanoparticles dispersed into molten alkali halide salts as liquid reaction media stable over a wide temperature range (≈ 300-1000 °C) to thermally activate reactions within homogeneous media, hence avoiding important particle coalescence and aggregation.

A first breakthrough of this PhD work is the successful synthesis of Ni_3B and Ni_4B_3 nanocrystals with superior size control compared to previously reported synthesis pathways. We have shown that the initial metal nanoparticles are converted by insertion of boron and retention of the particle size. *In situ* studies have provided invaluable insights into the reaction mechanisms, by enabling to identify amorphous intermediates, which show that the incorporation of boron, hence of strong covalent bonds, brings disorder into the metal nanoparticles before complete recrystallization. We have highlighted the crucial role of particle aggregation in the recrystallization process, as the amorphous intermediates seem to be stabilized within single nanoparticles. This apparently non-classical crystallization mechanism will require further demonstration, especially by using *in situ* transmission electron microscopy, coupled to PDF analysis of *in situ* X-ray scattering experiments to track structural changes into the amorphous precursors. We have then shown that the resulting nanocrystals behave as efficient catalysts for the acidic hydrogen evolution reaction and pre-catalysts for the alkaline water oxidation reaction, rivaling state-of-the-art platinum-group-metal-free materials.

The second breakthrough is the extension of the concept of nanoparticles conversion in molten salts to two systems: iron boride and nickel cobalt boride nanocrystals. With the former case,

we have highlighted the importance of the surface states of the initial metal nanoparticles in driving the reaction pathway. In the latter case, we have demonstrated the possibility to convert multimetallic nanoparticles into multimetallic boride nanocrystals. Although the initial core-shell structure of the Ni-Co nanoparticles could not be retained during the conversion, we have shown that the use of pre-made metal nanoparticles enables to bypass redox processes that usually lead to metal segregation during attempts to form multimetallic borides. As a consequence, a new bimetallic boride could be obtained, probably crystallizing as a distorted CoB-type structure. As a perspective, we note that like CoB and NiB, the structures of Co_3B and Ni_3B are identical, which hint at the possibility to design new solid solution bimetallic borides. These bimetallic compositions are promising for water splitting electrocatalysis.

Our attempts to design nickel borophosphides, only scarcely reported, did not reach satisfying results, leading in most cases to a segregation between borides and phosphides, whether the precursors were nickel, boride, or phosphide nanoparticles, or nickel salts. This has however made it possible to highlight a scale of reactivity and stability, showing that in molten salts, phosphides form before borides and are more stable. We have again highlighted the presumably important role of the surface of the initial nanoparticles, also mentioned in the previous paragraph, which might act as a boron scavenger when oxidized, hence destabilizing the boride and borophosphide phases. Consequently, future work will focus on using as precursors nickel boride nanoparticles exempt of any oxidized species. By using more conventional redox reactions, we could however obtain nanoparticles of an amorphous nickel borophosphide, which hints at the possibility to retrieve a range of amorphous phases with tuned compositions.

As mentioned above, a take home message of the PhD work is the importance of the surface chemistry of nanoparticles to be used as reagents within molten salts. While this is a trivial remark for conventional colloidal synthesis in usual solvents, this aspect of nanoparticle chemistry has never been considered for syntheses in molten salts, although we show that the high temperatures used trigger reactions that are not addressed in usual solvents. Therefore, we have engaged in a preliminary work presented as appendix in the next pages, to explore a route for synthesizing metal nanoparticles without organic surface ligands, which are sources of potential side reactions. To do so, we again developed colloidal synthesis in molten salts, by forcing “explosive” nucleation events through the use of fast induction heating and quenching. Although the process will require further enhancement, initial results in the case-study of nickel nanoparticles are highly promising.

Finally, we anticipate that the process developed in this work, namely nanoparticles reactivity and conversion into molten salts will pave the way to a large diversity of compounds achievable for the first time at the nanoscale, and to new families of nanoparticles combining metals and p-block elements, thus reaching a wide range of potential application fields.

Appendix

Induction-assisted molten salts synthesis of nickel nanoparticles

The previous chapters have highlighted how surface ligands and surface composition can impact the reactivity of metal nanoparticles with boron and phosphorus sources. Especially, capping agents often have a detrimental effect on this reactivity, as observed in chapter 2 and chapter 6. Therefore, having a straight forward access to ligand-free metal nanoparticles and nanostructures would unlock new opportunities for nanoparticle synthesis. More generally, it would also open new ways to address the catalytic properties of metal nanostructures.

In this appendix, we take the case study of nickel nanoparticles to investigate a simple method to produce ligand-free metal nanoparticles in molten salts. To achieve this goal, we develop induction heating in order to trigger extensive nucleation in molten salts, followed by quenching of the medium to avoid grain growth and large particle coalescence.

I) Innovative strategies to reach ligand-free metallic nanoparticles

Ligands at the surface of metal nanoparticles can strongly modify their morphology, dispersion state, chemical reactivity, catalytic and plasmonic properties, among others[1]. These organic species are classically used in colloidal syntheses within organic solvents. When organic ligands are detrimental to electrical transport or electrocatalytic properties, for instance, they must be replaced or etched[2],or metal nanostructures must be designed from the beginning without organic ligands.

Nevertheless, new strategies using molten salts are emerging. Stable dispersions of nanocrystals were observed in molten salts for various nanocrystals including quantum dots, oxides (Fe_3O_4) or metals (Pt, Pd)[3]. The nature of the molten salts strongly influences the dispersion as stable colloids were formed only if the chemical affinity with the nanocrystals is sufficient. In more details, the stabilization in molten salts is explained by the formation of ion layers at the solid-liquid interface[3]. The resulting shell formed around the nanocrystals creates charge density oscillations in the molten medium, next to the nanoparticle surface. The interaction between nanocrystals is then dependent on the compacity of these alternating layers, which act as barriers against particle aggregation [3]. In these studies from D. Talapin's group, the nanoparticles were produced by colloidal chemistry in organic solvents, before their

redispersion in molten salts. Synthesis of ligand-free transition metal oxides nanoparticles was also reported by a Lux-Flood reaction in molten salts $LiNO_3$-KNO_3 and $LiNO_3$−$NaNO_3$−KNO_3−$Ca(NO_3)_2$ [4], where lithium oxide was used as a base to deliver oxygen anion to react with metal cations at around 150 °C. However, this method is not suitable for metallic nanoparticles.

II) Synthesis of nickel nanoparticles in molten salts

a) Experimental conditions

To limit nickel particles growth and aggregation, we use diluted conditions compared to the approaches developed in the previous chapters, with a concentration of 0.11 mmol of $Ni^{(II)}$ salt per gram of eutectic molten salts LiI:KI (58:42 mass.), which corresponds to a concentration of 0.33 mol L^{-1}, compared to 6.06 mol L^{-1} generally used in the previous chapters. The choice of alkali halide salts is motivated by the previous observation of colloidal stability in such media for diverse nanocrystals (InP, FePt, Quantum dots)[3]. The other interests in this salt mixture reside first in its relatively low melting point (T_m= 286 °C) essential to perform reactions at temperatures as low as possible and avoid coalescence, second in the possibility to wash these salts with a non-aqueous solvent, methanol. Indeed, if successful, the synthesis yields metal nanostructures embedded into salts that must be washed. Transition metal nanostructures would oxidize in contact to water, so that other solvents are necessary to wash out the salts. Sodium hydride (NaH) is used as reducing agent in excess, to provide rapid nucleation. The reaction mixtures were prepared under inert atmosphere as well as the reactions. In order to trigger extensive nucleation and avoid growth and/or coalescence, we heat the reaction vessel by induction heating, which is made possible by using a molybdenum crucible as susceptor. We measure heating ramps of *ca.* 73 °C s^{-1}. We investigated particularly the induction heating conditions and the role of the nickel ion precursor ($NiCl_2$, NiI_2).

b) $NiCl_2$ as precursor

Preliminary results were obtained in collaboration with Dr. Yang Song from our group by using a tubular oven for heating at 350 °C for 40 min. TEM pictures presented Ni particles partially coalesced and the XRD pattern showed only the diffractions peaks of the nickel. In order to trigger extensive nucleation and avoid growth and/or coalescence, we heat the reaction vessel by induction heating, which is made possible by using a molybdenum crucible as susceptor. Induction heating (**Figure 1**) provides an ultrafast heating ramp up to 600 °C (or even higher) in less than 12 seconds, where the temperature is measured with a pyrometer accounting for the

permissivity of molybdenum. As the oven has negligible thermal inertia, it also cools much faster than a tubular oven, which enables to quench reactions and avoid restructuration or diffusion phenomena.

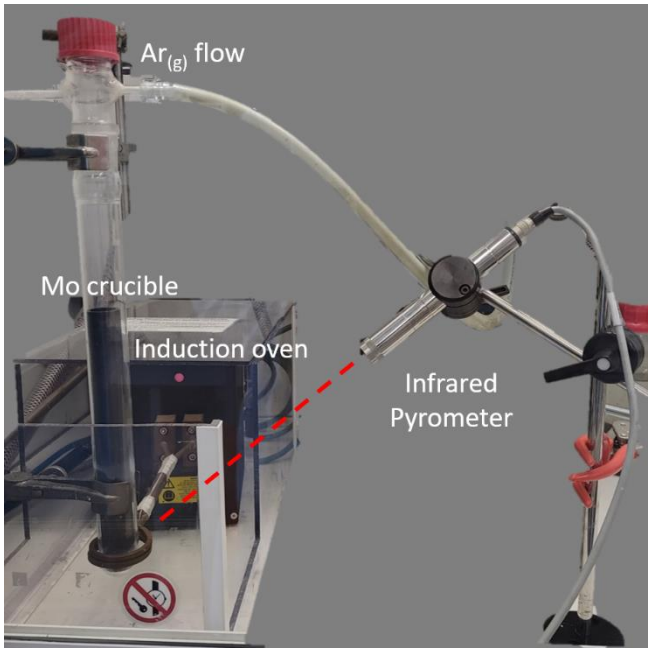

Figure 1: Experimental setup for induction heating. The temperature is measured by infrared pyrometry.

Different reaction temperatures and dwell times have been studied. At 325 °C for 5 min. (**Figure 2A**), slightly above the melting point of the eutectic salt mixture (T_m = 286 °C), XRD indicates a poorly crystalline powder with low signal-to-noise diffractions peaks of nickel (0) and some remaining nickel chloride. TEM (**Figure 2A**) shows a poorly defined morphology, which supports uncomplete reaction and still poorly crystalline material, with large amorphous domains, embedding small particles of *c.a.* 5 nm and other domains containing larger particles of *ca.* 20-40 nm. To target a complete reaction, the temperature and dwell time were increased to 350 °C and 20 min, respectively (**Figure 2A**). The corresponding XRD pattern exhibits well defined reflections of nickel (0), with a slight fraction of LiI due to uncomplete washing. TEM (**Figure 2C**) shows roughly spherical particles with a size distribution (**Figure S-IA**) centered on 45 nm but spread out to 140 nm. These particles are also strongly coalesced. The composition determined by STEM-EDS confirms that only nickel (0) is present in proportions > 90 % at. if the oxygen content due to air exposure is taken out of the evaluation. Similar Ni contents are observed for all the syntheses described below.

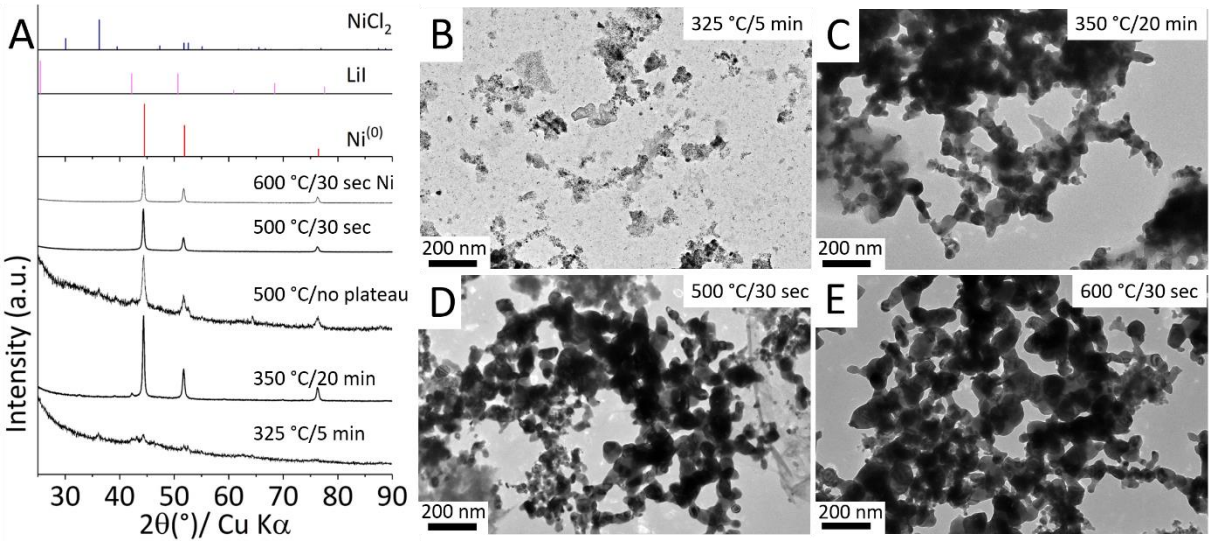

Figure 2. (A) XRD patterns and (B-E) TEM images of the powders obtained from mixtures $NiCl_2$:NaH (1:5 at.) reacted in the molten eutectic mixture LiI:KI heated by induction.

Then, to enhance size control and the dispersion state, we have sought to favor the nucleation step over the growth step, by increasing the temperature to 500 °C, but cancelling the dwell time. The X-ray diffraction peaks of $NiCl_2$ are still present when no dwell time is applied (**Figure 2A**). Hence, we have used a short plateau of 30 s. XRD indicates a complete disappearance of $NiCl_2$ at the benefit of nickel (0) formation. The particles are still aggregated (**Figure 2D**) with a slight narrowing of the size distribution (**Figure S-IB**) in the range 10-80 nm, which demonstrates the nanostructuration of the material. Finally, a synthesis performed at 600 °C for 30 s. to favor further nucleation shows again only Ni(0) according to XRD (**Figure 2A**) but a widening of the size distribution (**Figure S-IC**) from 10 to 120 nm.

According to the overall results obtained, further optimization of the morphology and dispersion state by only tuning the induction heating conditions. Further adjustment of the concentration of the precursor is limited by the amount of the final product. If we keep the nature of the eutectic salt mixture in order to ensure a low melting point, the reactivity of the precursors can be modulated. NaH is apparently sufficiently reducing to reduce in a short time all nickel species. So we modify the nature of the $Ni^{(II)}$ precursor by replacing $NiCl_2$ by NiI_2, which is less reactive. This modification is expected to delay the reduction, hence the nucleation to the temperature range of the molten salt, above 350 °C.

c) NiI_2 as precursor

Compared to $NiCl_2$, the reduction of NiI_2 to nickel (0) requires higher temperature/longer dwell time. Even at 500 °C for 10 min. (**Figure 3A**), the main diffraction peaks are attributed to the NiI_2 mixed with metallic nickel. TEM (**Figure B**) shows particles embedded in an amorphous matrix. The plateau duration was then increased to 30 min. According to XRD, we observe reaction of NiI_2 at the benefit of Ni(0) (**Figure 3 A**), with only small intensity diffraction peaks of NiI_2 still detected. Another diffraction peak at around 31° (2θ Cu Kα) could not be identified. TEM (**Figure 3C**) show similar morphologies and size distribution compared to particles obtained by using $NiCl_2$ as precursor at 350 °C for 20 min. As for $NiCl_2$, the temperature was increased and the plateau shortened. Among the conditions studied, even synthesis at 900 °C for 30 s (**Figure 3A**) yield uncomplete reduction of NiI_2, with also the formation of $Ni^{(0)}$ and NiO due to oxidation during the washing step. TEM (**Figure 3E**) highlights the same morphologies as the sample obtained at 500 °C for 10 min.

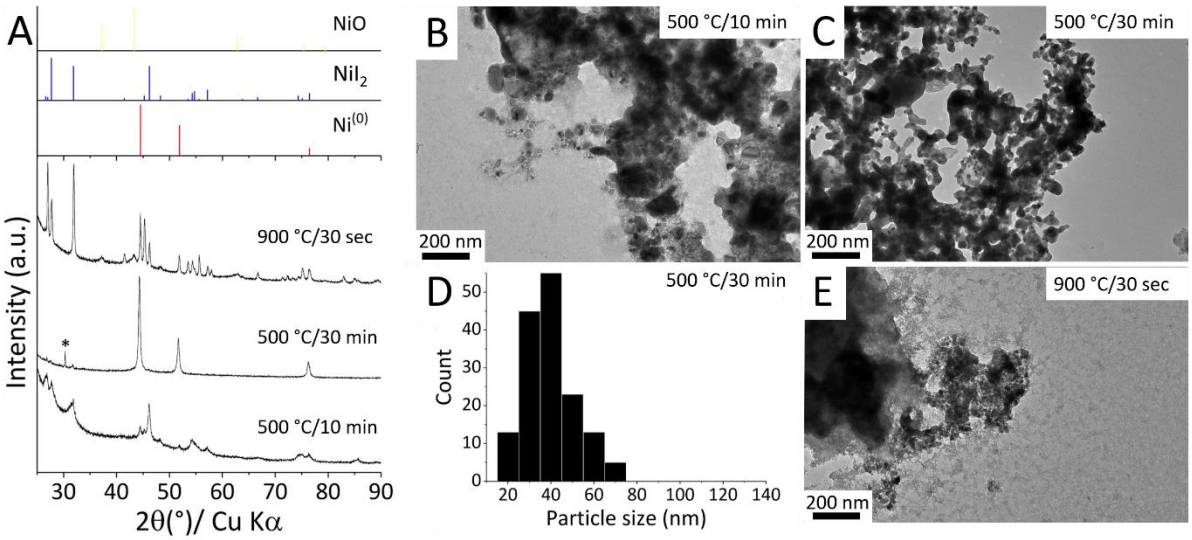

Figure 3. (A) XRD pattern and (B-E) TEM images of the powders obtained from mixtures NiI_2:NaH (1:5 at.) reacted in the molten eutectic mixture LiI:KI heated by induction.

The formation of nickel (0) from NiI_2 is then limited by the high stability of NiI_2 into the molten iodide salt and its slow reaction kinetics. Reversely, short dwell time but at a sufficiently high temperature allows the complete reduction of $NiCl_2$ into nickel. Attaining similar morphologies of particles for both cases mean that the conditions of heating does not account as first factor, but that the chemical reactivity of the precursors in the molten salt are a powerful experimental lever which should be investigated further.

Experimental methods

Reagents. Nickel (II) chloride ($NiCl_2$, 99%, Alfa Aesar), Nickel (II) iodide (NiI_2, 99.5 %, Alfa Aesar), lithium iodide (99%, Alfa Aesar), potassium iodide (99%, Sigma-Aldrich), sodium hydride (NaH, 90%, Sigma-Aldrich) were used as received, in an argon-filled glovebox.

Induction-assisted synthesis of nickel nanoparticles

In an argon filled glovebox, 5 g of the eutectic mixture LiI:KI (58:42 mass) as mixed with 71.30 mg $NiCl_2$ or 0.1719 g NiI_2 to achieve a concentration of 0.11 mmol of nickel per gram of salt and introduced in a ball milling jar. If $NiCl_2$ was used, 65 mg of NaH was added and respectively 66 mg for NiI_2 (atomic ratio NaH:Ni = 5:1). Ball milling was performed for 2 min at 20 Hz. Then, the mixed powder was placed in a molybdenum crucible in a quartz tube connecting to a Schlenk line under Ar flow, and adapted on an induction oven (**Figure 1**) from CEIA. The oven was equipped with a pyrometer that enables control of the temperature program. A emissivity value of ε = 0.1 is considered for molybdenum. As an indication, the heating time from room temperature to 900 °C did not exceed 12 s at an input power of 60 % W. After heating, the crucible was naturally cooled, which took about 4 min. Purification as performed by 10 cycles of dissolution/dispersion in methanol followed by centrifugation. The washing step was performed rapidly to avoid oxidation. The powder was then dried under vacuum and stored inside a glovebox.

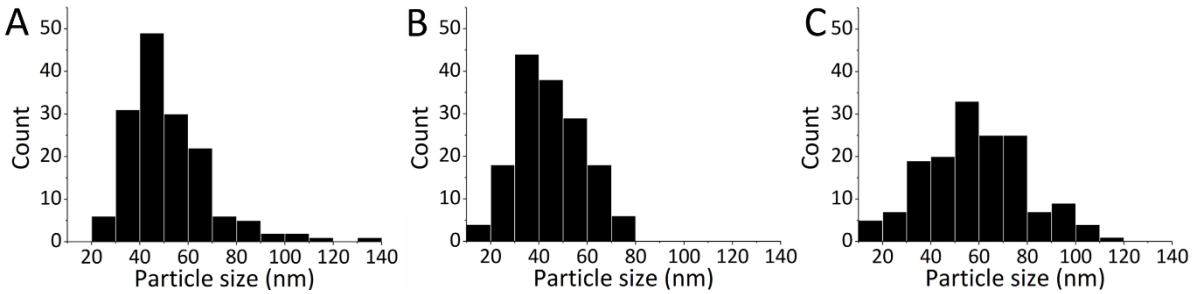

Figure S-I. Size distributions of nickel particles obtained by the reaction of $NiCl_2$ with NaH in molten LiI:KI (58:42 mass.) by induction heating at (A) 350 °C for 20 min, (B) 500 °C 30 s. and (C) 600 °C for 30 s.

References

(1) Wang, W.; Zhang, M.; Pan, Z.; Biesold, G. M.; Liang, S.; Rao, H.; Lin, Z.; Zhong, X. Colloidal Inorganic Ligand-Capped Nanocrystals: Fundamentals, Status, and Insights into Advanced Functional Nanodevices. *Chem. Rev.* **2022**, *122* (3), 4091–4162. https://doi.org/10.1021/acs.chemrev.1c00478.

(2) Lacroix, L. M.; Meffre, A.; Gatel, C.; Fazzini, P. F.; Lachaize, S.; Respaud, M.; Chaudret, B. Nanoparticle Ripening : A Versatile Approach for the Size and Shape Control of Metallic Iron Nanoparticles. *Chempluschem* **2019**, *84* (3), 302–306. https://doi.org/10.1002/cplu.201800665.

(3) Zhang, H.; Dasbiswas, K.; Ludwig, N. B.; Han, G.; Lee, B.; Vaikuntanathan, S.; Talapin, D. V. Stable Colloids in Molten Inorganic Salts. *Nature* **2017**, *542* (7641), 328–331. https://doi.org/10.1038/nature21041.

(4) Li, T.; Xu, Y.; Qian, X.; Yue, Q.; Kang, Y. Low-Temperature Molten Salt Synthesis for Ligand-Free Transition Metal Oxide Nanoparticles. *ACS Appl. Energy Mater.* **2020**, *3* (4), 3984–3990. https://doi.org/10.1021/acsaem.0c00403.

Instruments

Powder X-ray diffraction (XRD) was performed on a Bruker D8 Discover or Brucker D8 Advance diffractometer operating at the Cu Kα wavelength (λ = 1.5418 Å) in reflection mode and both equipped with an X-ray source working with Cu Kα radiation at an acceleration tension of 40 kV and a current of 30 mA. A linear detector LynxEye was used to record the diffracted intensity. Due to the air sensibility of the samples, the powders were loaded in an argon-filled glovebox on an airtight sample holder then capped with a protective plastic dome. A broad bump between 15-25° correspond to an unfiltered beam scattering on the dome. The Rietveld refinements were performed using the GSAS-II software.

***In situ* angular X-ray diffraction on synchrotron beamline** was acquired respectively at:
The ID11 beamline at the ESRF synchrotron, in the transmission mode at a fixed energy (wavelength) of 93.3159 keV (0.1329 Å). A double crystal monochromator equipped with two Si(111) crystals was used to tune the energy, and the beam size was set to 300 μm × 300 μm. The detector was a Frelon4M 2048 × 2048 16Bit fast CCD Camera.

The SOLEIL synchrotron on the DIFFABS beamline in transmission mode at a fixed energy (wavelength) of 18 keV. The beam size was set to 300 μm × 300 μm. A 2D circular detector (CIRPAD) was used to record the signal.

For both setups, a homemade capillary oven was used for the study of the samples. In brief, it enables performing transmission X-ray diffraction *in situ* during controlled heating of the reaction mixture in a 1.5 mm-diameter quartz capillary opened under argon flow to mimic the conditions of ex situ lab synthesis.

Total X-ray scattering diagrams for the Pair Distribution Function were recorded on a Bruker D8 Advance diffractometer equipped with a Göbel mirror and a LYNXEYE detector, with Mo Kα radiation (mean λ(Kα1α2) = 0.71073 Å) at room temperature at the Mo Kα radiation at room temperature. The samples were recorded in a Ø 1 mm sealed borosilicate capillary and placed in continuous rotation during the measurements. Additional scattering measure were performed with an empty capillary for background subtraction. The G(r) function was obtained suing the PDFgetX_3 program. The PDF refinement were performed using PDFGui[12].

Energy dispersive X-ray spectroscopy (EDX) for elemental analysis was operated on a Scanning Electron Microscope (SEM) on a SEM HITACHI S-3400N at 20 kV equipped with an Oxford Instruments- X-max. The powders samples were thin flatly smeared on a flat carbon adhesive tape, itself on a sample holder. The oxygen is subtracted for quantitative analyses.

X-ray photoelectron spectroscopy (XPS) analyses were performed on an Omicron Argus X-ray photoelectron spectrometer, equipped with a monochromated AlKα radiation source (1486.6 eV) and a 280 W electron beam power. Binding energies were calibrated against the C 1s (C-C) binding energy at 284.8 eV. Raw data were treated on CasaXPS software

Transmission electron microscopy (TEM) images were acquired with a Technai Spirit 2 microscope operating at 120 kV. The samples were prepared by depositing a drop of particles suspension in a solvent on a carbon coated Cu grid.

Résumé de thèse

Les borures et phosphures de métaux de transition présentent des propriétés intéressantes en électrocatalyse pour la production de dihydrogène[1–4]. Dans ces matériaux, l'élément du bloc p modifie la densité électronique portée par les atomes métalliques, ce qui rend non seulement ces matériaux résistants à l'oxydation et à la corrosion, mais améliore aussi les propriétés catalytiques. Alors que les synthèses couramment reportées se font en voie solide au-delà de 1000 °C[5,6], le développement de catalyseurs requiert la conception d'objets de rapport surface/volume élevé, donc à l'échelle nanométrique. Il est alors essentiel de développer des voies de synthèse adaptées à l'obtention de ces matériaux et à la recherche de nouveaux composés.

Notamment la combinaison du bore avec du phosphore et/ou un ou plusieurs métaux de transition au sein d'un même composé pourrait engendrer des modifications profondes, notamment de la densité électronique des sites métalliques et de la géométrie des sites de surface en raison de la formation de structures cristallines spécifiques, contraintes par la présence de liaisons covalentes. Au vu des propriétés des phases binaires, l'ensemble des modifications en termes de taille, morphologie et géométrie et composition permet d'envisager un contrôle de la réactivité et des propriétés (électro)catalytiques.

Les synthèses par voie liquide de borures à l'échelle nanométrique déjà reportées impliquent la formation d'une phase amorphe puis sa cristallisation, soit par une étape séparée de recuit à haute température,[5,7,8] soit par une élévation de température du milieu réactionnel[9]. Ces approches ne permettent cependant pas un contrôle fin de la morphologie et conduisent généralement à des particules agrégées ; ce qui induit une perte d'activité en catalyse.

La modification post-synthèse de nanomatériaux par incorporation d'éléments chimiques supplémentaires a été reportée pour la formation d'alliages metalliques[10], et pour l'incorporation de métaux alcalins, alcalino-terreux[11], de carbone[12], de phosphore[13] ou encore des chalcogènes oxygène, souffre et sélénium[14–16]. Cette approche permet en général un très bon contrôle morphologique, en utilisant les nano-objets initiaux comme des gabarits réactifs. Elle n'a jamais été abordées pour le bore. Elle permettrait pourtant, au-delà de la formation de borures, de combiner le bore avec le phosphore et/ou un ou plusieurs métaux de transition au sein d'un même composé. Cela pourrait engendrer des modifications profondes, notamment de

la densité électronique des sites métalliques et de la géométrie des sites de surface en raison de la formation de structures cristallines spécifiques, contraintes par la présence de liaisons covalentes. Au vu des propriétés des phases binaires, l'ensemble des modifications en termes de taille, morphologie, et composition permet d'envisager un contrôle de la réactivité et des propriétés (électro)catalytiques.

Dans ce manuscrit de thèse, nous développons le concept de post-modification de particules métalliques pour l'élaboration de borures et borophosphures de métaux de transition, avec pour objectifs un contrôle morphologique à l'échelle nanométrique, le développement de nouveaux composés, et l'élaboration d'électrocatalyseurs efficaces pour l'électrolyse de l'eau. Les approches de synthèse choisies reposent sur deux piliers. D'une part, l'utilisation de nanoparticules métalliques comme nano-réacteurs dans lesquels le bore et/ou le phosphore sont incorporés, de façon à maintenir la morphologie des particules. D'autre part, les milieux sels fondus, qui permettent de réaliser des synthèses à l'état liquide à des températures intermédiaires entre celles de la chimie du solide et celles des voies colloïdales, pour assurer des milieux réactionnels homogènes et permettre une réactivité accrue entre précurseurs solubles ou dispersés, et ainsi limiter la coalescence des particules. La compréhension des mécanismes de formation des composés et nano-objets a fait l'objet d'une attention particulière avec le suivi *in situ* des synthèses grâce à la diffraction des rayons X sous rayonnement synchrotron. Nous avons ainsi pu mettre en évidence des intermédiaires réactionnels sous forme de nanoparticules amorphes, dont la nature a été élucidée grâce à la diffusion totale des rayons X couplée à l'analyse par fonction de distribution de paires.

Le chapitre bibliographique (chapitre 1) présente les différentes voies de modification de nanostructures en milieu liquide, incluant les différents procédés d'élimination sélective, d'échange cationique, anionique et galvanique, de formation d'alliages et d'incorporation d'éléments supplémentaires. Au travers de ces procédés, nous retrouvons de manière récurrente les effets dits de Kirkendall décrivant les processus d'inter-diffusion entre les espèces insérées et les espèces expulsées des nanodomaines. Des gradients de concentration dans les nanoparticules peuvent induire des modifications sévères des structures internes des nanostructures telles que la formation de trous au centre des nanoparticules.

Par la suite, nous développons notre méthode de synthèse en utilisant le cas des borures de nickel comme preuve de concept. Nous montrons que l'utilisation de nanoparticules de nickel en tant que nano-réactifs dans lesquels nous insérons du bore élémentaire par décomposition thermique de $NaBH_4$ permet de former des nanocristaux de borures de nickel de phase et taille

contrôlée dans des sels fondus. Comparée à d'autres approches, la morphologie des nanoparticules est identique à celle des nanoparticules métalliques initiales malgré une légère coalescence sous forme de chaîne de particules cristallines. Une étude mécanistique a ensuite été réalisée par des techniques de diffraction des rayons X avec suivi en température (*in situ*) en synchrotron (ESRF ligne ID 11). Pour les deux phases borures étudiés, des intermédiaires amorphes d'après la DRX ont pu être détectés et par la suite isolés en laboratoire grâce aux conditions de température identifiés d'après les diagrammes obtenus au synchrotron. Par une technique de diffusion totale des rayons X couplée à la fonction de distribution de paires, nous avons pu discuter de la nature de ces intermédiaires et leurs évolutions pour l'obtention sélective de Ni_3B ou Ni_4B_3. Nous discutons ensuite la nature du mécanisme de cristallisation, en particulier son lien avec le phénomène d'agrégation.

Le chapitre suivant (chapitre 3) traite des propriétés électrocatalytiques des particules obtenues pour l'électrolyse de l'eau : production de dihydrogène et oxydation de l'eau. Pour ces deux demi-réactions, les nanocristaux rivalisent avec les matériaux de l'état-de-l'art en termes d'activité et stabilité. Nous discutons ensuite l'origine des propriétés de catalyse, en particulier les transformations de surface en conditions oxydantes, qui conduisent à la formation *in situ* d'un oxyhydroxide de surface, qui est l'espèce catalytique pour l'oxydation de l'eau en milieu alcalin.

Nous avons ensuite (chapitre 4) cherché à former des nanoparticules de borophosphures de métaux de transition. La combinaison des propriétés de covalence des borures avec celles de iono-covalence des phosphures pourrait modifier la densité électronique sur les sites métalliques et ainsi ajuster les propriétés catalytiques. L'intérêt de ces matériaux est d'autant plus important que seulement deux phases ont été reportées pour les borophosphure de nickel. Celles-ci ont été obtenues par des voies solides[17] qui n'ont pas permis d'obtenir des objets nanométriques. Nous avons développé plusieurs approches basées d'une part sur l'incorporation de/des hétéroélément(s) complémentaire(s) à partir de nanoparticules de phosphures et borures de nickel ou de nickel. Si ces voies ont permis de mettre en évidence de différences importante de réactivité entre phosphures et borures, elles n'ont pas permis d'obtenir des phases pures et des phases ternaires. Au contraire, l'approche basée sur la réduction d'un sel de nickel réduit en présence de sources de phosphore et de bore a permis de former une phase borophosphure, néanmoins mélangée à un phosphure. En parallèle, nous avons montré la possibilité de stabiliser une phase amorphe de composition en nickel, bore et

phosphore similaire à la composition introduite, ouvrant ainsi la voie à l'étude d'une famille de nanoparticles amorphes.

Ensuite (chapitre 5), nous avons consacré une étude sur les phases borures bimétalliques de nickel et cobalt. En effet, l'amélioration de l'activité électrocatalytique pour la dissociation de l'eau a été observée pour des borures bimétalliques notamment dans le cas de phases Co-Fe-B[18,19] ou Ni-Co-B[19,20], par rapport à leurs équivalents binaires. Tous ces matériaux ont été synthétisés par co-réduction de précurseur métalliques en milieu aqueux suivi d'un recuit pour la cristallisation. Avant notre étude, seule des phases bimétalliques $Co_{2(1-x)}Ni_xB$ avaient étés répertoriées, solution solide de Co_2B et Ni_2B[20,21]. Les phases CoB et NiB étant de structures proches, respectivement de type β-FeB and CrB, nous avons fait l'hypothèse qu'il serait possible d'obtenir un borure de cobalt substitué au nickel, ou au moins une intercroissance de CoB et NiB, comme notre équipe l'a récemment démontré pour α-FeB, une intercroissance des structures β-FeB and CrB à l'échelle nanométrique. L'approche que nous avons développée repose à nouveau sur la conversion de nanoparticules, en utilisant comme réactifs des nanoparticules cœur-coquille Ni-Co, dans lesquelles du bore est incorporé, de façon à contrôler la taille des objets et à s'affranchir des limitations liées aux réactions redox qui conduisent à une ségrégation Ni-Co lors la formation du borure. Le choix des domaines de composition d'intérêt a été guidé par l'apprentissage automatique pour la minimisation des énergies de formation[22]. En complément d'une étude mécanistique en diffraction RX *in situ* (Synchrotron SOLEIL/ ligne DIFFABS), ces études nous ont permis de former une phase unique Ni-Co-B de composition jamais reportée et d'une structure de type CoB distordue. La teneur en métaux des particules individuelles est restée similaire à celle des particules cœur-coquille initiales, confirmant l'absence de déplétion. Une étude des propriétés d'électrocatalyse pour l'oxydation de l'eau a été initiée, avec des premiers résultats encourageants.

Parmi les borures de métaux de transition développés pour l'électrocatalyse de l'eau, nous avons également étudié le cas de l'insertion de bore dans des nanoparticules de fer en milieu sels fondus (chapitre 6). La phase FeB présente deux formes structurales à l'échelle nanométrique, respectivement dénommés α- et β-FeB[23,24]. La forme α-FeB, dont notre groupe a récemment résolu la structure[23]; cristallise à plus basse température et donc limite davantage les phénomènes de mûrissement d'Ostwald, de coalescence et d'agrégation. Cependant, un contrôle de la nature des ligands de surface a été nécessaire pour guider l'insertion du bore et conduire au borure. Nous avons notamment identifié la formation potentielle de carbures en surface des nanoparticules de fer, bloquant la formation du borure. Nous avons donc abordé

une autre méthode de synthèse des nanoparticules de fer avec la présence de ligands amine[25]. Ce procédé a finalement permis de former la phase borure α-FeB recherchée. Une tendance des particules à la décomposition par ségrégation du bore lors de l'exposition à l'air a été mise en évidence, par la formation de coquilles creuses et de larges domaines ne montrant pas de cristallinité. Le mécanisme supposé est une oxydation des centres métalliques et éventuellement du bore sous forme de borate. A l'inverse, la morphologie des particules est maintenue en l'absence d'exposition à l'air, mettant ainsi en avant l'extrême sensibilité de ces nano-objets à leur environnement.

Enfin, nous avons débuté l'exploration d'une voie de synthèse de nanoparticules métalliques exemptes de ligands organiques de surface, afin d'éviter des réactions secondaires ou des mécanismes compétitifs de diffusion au sein des métaux à partir des ligands, lors des synthèses par incorporation d'éléments en sels fondus. En nous basant sur des travaux démontrant la stabilité colloïdale de nanoparticules dans des sels fondus[26], nous décrivons une méthode rapide et simple de synthèse de nanoparticules métalliques basés sur les sels fondus avec le nickel comme cas d'étude. Le chauffage est réalisé par induction afin de favoriser une nucléation rapide et homogène tout en maintenant des temps de palier court afin de limiter la croissance. Malgré des efforts d'optimisation des conditions de synthèse, les nanoparticules de nickel obtenues présentent une coalescence partielle et une diversité en taille importante.

Références

(1) Sun, L.; Luo, Q.; Dai, Z.; Ma, F. Material Libraries for Electrocatalytic Overall Water Splitting. *Coord. Chem. Rev.* **2021**, *444*, 214049. https://doi.org/10.1016/j.ccr.2021.214049.

(2) Gupta, S.; Patel, M. K.; Miotello, A.; Patel, N. Metal Boride-Based Catalysts for Electrochemical Water-Splitting: A Review. *Adv. Funct. Mater.* **2020**, *30* (1). https://doi.org/10.1002/adfm.201906481.

(3) Masa, J.; Piontek, S.; Wilde, P.; Antoni, H.; Eckhard, T.; Chen, Y. T.; Muhler, M.; Apfel, U. P.; Schuhmann, W. Ni-Metalloid (B, Si, P, As, and Te) Alloys as Water Oxidation Electrocatalysts. *Adv. Energy Mater.* **2019**, *9* (26), 1–8. https://doi.org/10.1002/aenm.201900796.

(4) Callejas, J. F.; Read, C. G.; Roske, C. W.; Lewis, N. S.; Schaak, R. E. Synthesis, Characterization, and Properties of Metal Phosphide Catalysts for the Hydrogen-Evolution Reaction. *Chem. Mater.* **2016**, *28* (17), 6017–6044. https://doi.org/10.1021/acs.chemmater.6b02148.

(5) Carenco, S.; Portehault, D.; Boissière, C.; Mézailles, N.; Sanchez, C. Nanoscaled Metal Borides and Phosphides: Recent Developments and Perspectives. *Chem. Rev.* **2013**, *113* (10), 7981–8065. https://doi.org/10.1021/cr400020d.

(6) Chen, H.; Zou, X. Intermetallic Borides: Structures, Synthesis and Applications in Electrocatalysis. *Inorg. Chem. Front.* **2020**, *7* (11), 2248–2264. https://doi.org/10.1039/d0qi00146e.

(7) Lee, E.; Fokwa, B. P. T. Nonprecious Metal Borides: Emerging Electrocatalysts for Hydrogen Production. *Acc. Chem. Res.* **2022**, *55* (1), 56–64. https://doi.org/10.1021/acs.accounts.1c00543.

(8) Dinh, K. N.; Liang, Q.; Du, C. F.; Zhao, J.; Tok, A. I. Y.; Mao, H.; Yan, Q. Nanostructured Metallic Transition Metal Carbides, Nitrides, Phosphides, and Borides for Energy Storage and Conversion. *Nano Today* **2019**, *25*, 99–121. https://doi.org/10.1016/j.nantod.2019.02.008.

(9) Portehault, D.; Devi, S.; Beaunier, P.; Gervais, C.; Giordano, C.; Sanchez, C.; Antonietti, M. A General Solution Route toward Metal Boride Nanocrystals. *Angew. Chemie - Int.*

Ed. **2011**, *50* (14), 3262–3265. https://doi.org/10.1002/anie.201006810.

(10) Chen, Y.; Zhan, X.; Bueno, S. L. A.; Shafei, I. H.; Ashberry, H. M.; Chatterjee, K.; Xu, L.; Tang, Y.; Skrabalak, S. E. Synthesis of Monodisperse High Entropy Alloy Nanocatalysts from Core@shell Nanoparticles. *Nanoscale Horizons* **2021**, *6* (3), 231–237. https://doi.org/10.1039/d0nh00656d.

(11) Li, C. H.; Nanba, Y.; Asakura, D.; Okubo, M.; Talham, D. R. Li-Ion and Na-Ion Insertion into Size-Controlled Nickel Hexacyanoferrate Nanoparticles. *RSC Adv.* **2014**, *4* (48), 24955–24961. https://doi.org/10.1039/c4ra03296a.

(12) Meffre, A.; Mehdaoui, B.; Kelsen, V.; Fazzini, P. F.; Carrey, J.; Lachaize, S.; Respaud, M.; Chaudret, B. A Simple Chemical Route toward Monodisperse Iron Carbide Nanoparticles Displaying Tunable Magnetic and Unprecedented Hyperthermia Properties. *Nano Lett.* **2012**, *12* (9), 4722–4728. https://doi.org/10.1021/nl302160d.

(13) Ha, D. H.; Moreau, L. M.; Bealing, C. R.; Zhang, H.; Hennig, R. G.; Robinson, R. D. The Structural Evolution and Diffusion during the Chemical Transformation from Cobalt to Cobalt Phosphide Nanoparticles. *J. Mater. Chem.* **2011**, *21* (31), 11498–11510. https://doi.org/10.1039/c1jm10337g.

(14) Anderson, B. D.; Tracy, J. B. Nanoparticle Conversion Chemistry: Kirkendall Effect, Galvanic Exchange, and Anion Exchange. *Nanoscale* **2014**, *6* (21), 12195–12216. https://doi.org/10.1039/c4nr02025a.

(15) Chen, J.; Jiang, F.; Yin, Y. Manipulation of Interfacial Diffusion for Controlling Nanoscale Transformation. *Acc. Chem. Res.* **2021**, *54* (5), 1168–1177. https://doi.org/10.1021/acs.accounts.0c00743.

(16) Yin, Y.; Rioux, R. M.; Erdonmez, C. K.; Hughes, S.; Somorjal, G. A.; Alivisatos, A. P. Formation of Hollow Nanocrystals Through the Nanoscale Kirkendall Effect. *Science (80-.).* **2004**, *304* (5671), 711–714. https://doi.org/10.1126/science.1096566.

(17) Mikhalenko, S.; Chernogorenko, V.; Kuz'ma, Y.; Lavrov, Y.; Muchnik, S. Phase Equilibria in the Ni-B-P System. *Inorg. Mater. (Engl. Transl.); (United States)*. 1985.

(18) Klemenz, S.; Schuch, J.; Hawel, S.; Zieschang, A. M.; Kaiser, B.; Jaegermann, W.; Albert, B. Synthesis of a Highly Efficient Oxygen-Evolution Electrocatalyst by Incorporation of Iron into Nanoscale Cobalt Borides. *ChemSusChem* **2018**, *11* (18),

3150–3156. https://doi.org/10.1002/cssc.201801547.

(19) Qiang, C.; Zhang, L.; He, H.; Liu, Y.; Zhao, Y.; Sheng, T.; Liu, S.; Wu, X.; Fang, Z. Efficient Electrocatalytic Water Splitting by Bimetallic Cobalt Iron Boride Nanoparticles with Controlled Electronic Structure. *J. Colloid Interface Sci.* **2021**, *604*, 650–659. https://doi.org/10.1016/j.jcis.2021.07.024.

(20) Schuch, J.; Klemenz, S.; Schuldt, P.; Zieschang, A. M.; Dolique, S.; Connor, P.; Kaiser, B.; Kramm, U. I.; Albert, B.; Jaegermann, W. Efficient Oxygen Evolution Electrocatalyst by Incorporation of Nickel into Nanoscale Dicobalt Boride. *ChemCatChem* **2021**, *13* (7), 1772–1780. https://doi.org/10.1002/cctc.202002030.

(21) Ma, X.; Zhao, K.; Sun, Y.; Wang, Y.; Yan, F.; Zhang, X.; Chen, Y. Direct Observation of Chemical Origins in Crystalline (Ni: XCo1- x)2B Oxygen Evolution Electrocatalysts. *Catal. Sci. Technol.* **2020**, *10* (7), 2165–2172. https://doi.org/10.1039/d0cy00099j.

(22) Peterson, G. G. C.; Brgoch, J. Materials Discovery through Machine Learning Formation Energy. *JPhys Energy* **2021**, *3* (2). https://doi.org/10.1088/2515-7655/abe425.

(23) Igoa Saldaña, F.; Defoy, E.; Janisch, D.; Rousse, G.; Autran, P. O.; Ghoridi, A.; Séné, A.; Baron, M.; Suescun, L.; Le Godec, Y.; Portehault, D. Revealing the Elusive Structure and Reactivity of Iron Boride α-FeB. *Inorg. Chem.* **2022**. https://doi.org/10.1021/acs.inorgchem.2c03709.

(24) Rades, S.; Kornowski, A.; Weller, H.; Albert, B. Wet-Chemical Synthesis of Nanoscale Iron Boride, XAFS Analysis and Crystallisation to α-FeB. *ChemPhysChem* **2011**, *12* (9), 1756–1760. https://doi.org/10.1002/cphc.201001072.

(25) Lacroix, L. M.; Frey Huls, N.; Ho, D.; Sun, X.; Cheng, K.; Sun, S. Stable Single-Crystalline Body Centered Cubic Fe Nanoparticles. *Nano Lett.* **2011**, *11* (4), 1641–1645. https://doi.org/10.1021/nl200110t.

(26) Zhang, H.; Dasbiswas, K.; Ludwig, N. B.; Han, G.; Lee, B.; Vaikuntanathan, S.; Talapin, D. V. Stable Colloids in Molten Inorganic Salts. *Nature* **2017**, *542* (7641), 328–331. https://doi.org/10.1038/nature21041.

Résumé:
Les borures et phosphures de métaux de transition présentent des propriétés intéressantes en électrocatalyse pour la production de dihydrogène. Dans ces matériaux, l'élément du bloc p modifie la densité électronique des atomes métalliques, ce qui rend non seulement ces matériaux résistants à l'oxydation et à la corrosion, mais modifie aussi les propriétés catalytiques. Le développement de catalyseurs requiert la conception d'objets de rapport surface/volume élevé, donc à l'échelle nanométrique. Il est alors essentiel de développer des voies de synthèse adaptées à l'obtention de ces matériaux et à la recherche de nouveaux composés. Notamment la combinaison du bore avec du phosphore et/ou un ou plusieurs métaux de transition au sein d'un même composé pourrait engendrer des modifications profondes, notamment de la densité électronique des sites métalliques et de la géométrie des sites de surface en raison de la formation de structures cristallines spécifiques, contraintes par la présence de liaisons covalentes. Au vu des propriétés des phases binaires, l'ensemble des modifications en termes de morphologie, géométrie et composition permet d'envisager un contrôle de la réactivité et des propriétés (électro)catalytiques.
Ce travail de thèse a ainsi porté sur le développement de borures et borophosphures de métaux de transition avec pour objectifs un contrôle morphologique à l'échelle nanométrique, le développement de nouveaux composés, y compris métastables, et la caractérisation de leurs propriétés électrocatalytiques. Les approches de synthèse choisies reposent sur deux piliers. D'abord les sels fondus, qui permettent de réaliser des synthèses à l'état liquide et à des températures intermédiaires entre celles de la chimie du solide et celles des voies colloïdales. Ainsi, les milieux réactionnels sont homogènes, permettent une réactivité accrue entre précurseurs solubles ou dispersés, et limitent la coalescence des particules. L'autre pilier est l'utilisation de nanoparticules métalliques comme nanoréacteurs dans lesquels le bore et/ou le phosphore sont incorporés, de façon à maintenir la morphologie des particules. Nous obtenons ainsi des nanomatériaux de phases pures dans le cas des borures de nickel et de fer, avec un contrôle de la composition et de la morphologie jamais obtenu auparavant. Ce contrôle n'a pu être atteint qu'en comprenant les mécanismes de formation des composés et nano-objets correspondant. Cette compréhension a pu être obtenue en développant le suivi in situ des synthèses grâce à la diffraction des rayons X sous rayonnement synchrotron. Nous avons ainsi pu mettre en évidence des intermédiaires réactionnels sous forme de nanoparticules amorphes, dont la nature a été élucidée grâce à la diffusion totale des rayons X couplée à la fonction de distribution de paires.
Par extension, cette voie particulière de synthèse permet aussi la recherche de phases rares ou jamais reportées et pouvant présenter une importante activité électrocatalytique pour la dissociation de l'eau. Le choix des domaines de composition d'intérêt, guidé par l'apprentissage automatique pour la minimisation des énergies de formation, a ainsi permis de réaliser la synthèse de nanoparticules d'un borure bimétallique de nickel et cobalt. Nous avons aussi progressé dans l'étude de nouvelles voies de synthèse de phases ternaires borophosphures de nickel, rares et difficilement atteignables.
Enfin, nous avons abordé l'exploration d'une voie de synthèse de nanoparticules métalliques exemptes de ligands organiques de surface, afin d'éviter des réactions secondaires ou des mécanismes compétitifs de diffusion au sein des métaux à partir des ligands, lors des synthèses en sels fondus. En nous basant sur des travaux démontrant la stabilité colloïdale de nanomatériaux dans des sels fondus, nous décrivons une méthode rapide et simple de synthèse de nanoparticules métalliques basés sur les sels fondus avec le nickel comme cas d'étude.

Mots clés : [nanomatériaux, borures de métaux de transition, borophosphures de métaux de transition, Sels fondus, modification post-synthèse, électrolyse de dissociation de l'eau]

Abstract:
Transition metal borides and phosphides present interesting properties in electrocatalysis for the production of dihydrogen. In these materials, the p-block element modifies the electron density of the metal atoms, which not only makes these materials resistant to oxidation and corrosion, but also modifies the catalytic properties. The development of catalysts requires the design of objects with a high surface/volume ratio, i.e. at the nanoscale. It is therefore essential to develop synthesis routes adapted to obtaining these materials and to the search for new compounds. In particular, combining boron with phosphorus and/or one or more transition metals in the same compound could lead to profound changes, notably in the electron density of the metal sites and the geometry of surface sites, due to the formation of specific crystalline structures constrained by the presence of covalent bonds. In view of the properties of the binary phases, all the modifications in terms of morphology, geometry and composition make it possible to control the reactivity and (electro)catalytic properties.
This thesis work focused on the development of transition metal borides and borophosphides, with the objectives of morphological control on the nanometric scale, the development of new compounds, including metastable ones, and the characterisation of their electrocatalytic properties. The synthesis approaches chosen are based on two pillars. Firstly, molten salts, which enable synthesis to be carried out in the liquid state and at temperatures intermediate between those of solid-state chemistry and those of colloidal routes. Thus, the reaction media are homogeneous, enabling greater reactivity between soluble or dispersed precursors, and limiting the coalescence of particles. The other pillar is the use of metallic nanoparticles as nanoreactors in which boron and/or phosphorus are incorporated, so as to maintain the morphology of the particles. In this way, we obtain pure-phase nanomaterials in the case of nickel and iron borides, with a degree of control over composition and morphology that has never been achieved before. This control could only be achieved by understanding the formation mechanisms of the corresponding compounds and nano-objects. This understanding was achieved by developing in situ monitoring of the syntheses using X-ray diffraction under synchrotron radiation. We were thus able to identify reaction intermediates in the form of amorphous nanoparticles, the nature of which was elucidated using total X-ray scattering coupled with the pair distribution function.
By extension, this particular synthesis route also enables us to search for rare or never reported phases that may exhibit significant electrocatalytic activity for the dissociation of water. The choice of compositional domains of interest, guided by machine learning to minimise formation energies, led to the synthesis of nanoparticles of a bimetallic boride of nickel and cobalt. We have also made progress in studying new synthesis routes for nickel borophosphide ternary phases, which are rare and difficult to obtain.
Finally, we explored a route for synthesising metal nanoparticles without organic surface ligands, in order to avoid secondary reactions or competitive diffusion mechanisms within the metals from the ligands during molten salt synthesis. Based on work demonstrating the colloidal stability of nanomaterials in molten salts, we describe a rapid and simple method for synthesising metal nanoparticles based on molten salts using nickel as a case study.

Keywords : [nanomaterials, transition metal borides, transition metal borophosphides, molten salts, post-synthesis modification, water spitting electrolysis]